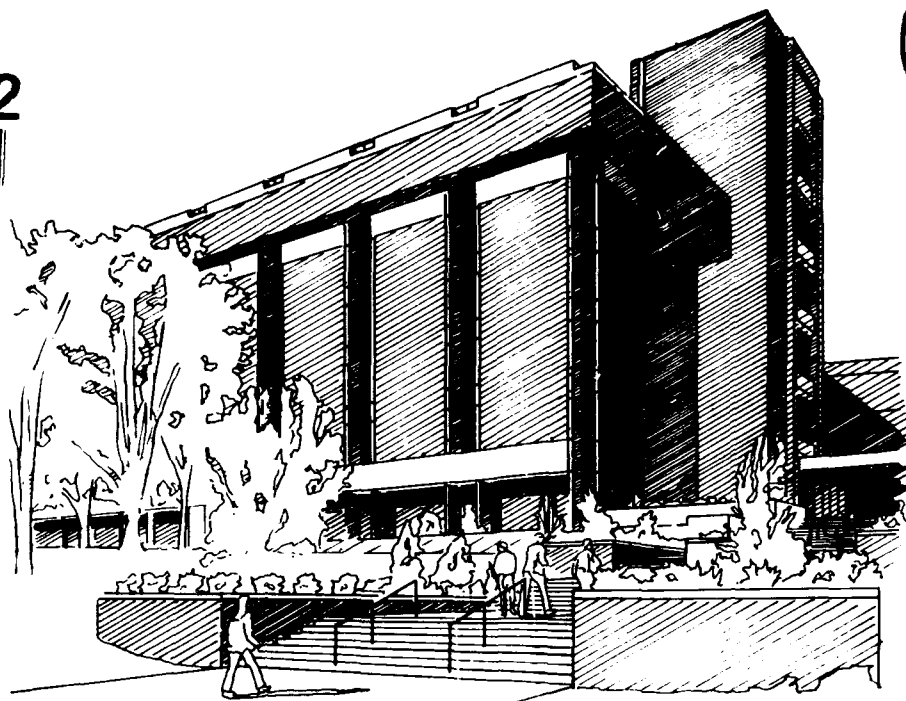


2

AD-A253 592



UNIVERSITY OF CINCINNATI
COLLEGE OF ENGINEERING

DTIC
ELECTE
AUG 5 1992
S C D

L.D.V. MEASUREMENTS OF UNSTEADY FLOW FIELDS
IN RADIAL TURBINE

FINAL REPORT

W. TABAKOFF AND M. PASIN

Under Contract No. DAAL03-90-G-0129
for

DEPARTMENT OF THE ARMY
United States Army Laboratory Command
Army Research Office
P.O. Box 12211
Research Triangle Park, NC 27709-2211



APPROVED FOR PUBLIC RELEASE;
DISTRIBUTION UNLIMITED.

92-20982



92 10 10 10

THE VIEWS, OPINIONS, AND/OR FINDINGS CONTAINED IN THIS REPORT ARE THOSE OF THE AUTHORS AND SHOULD NOT BE CONSTRUED AS AN OFFICIAL DEPARTMENT OF THE ARMY POSITION, POLICY, OR DECISION, UNLESS SO DESIGNATED BY OTHER DOCUMENTATION.

JULY 1992

AsE&EM REPORT NO. 92-105

DTIC QUALITY INSPECTED 5

DEPARTMENT OF AEROSPACE ENGINEERING
AND ENGINEERING MECHANICS

UNIVERSITY OF CINCINNATI

CINCINNATI, OHIO

Accession For	
NTIS GRA&I	<input checked="" type="checkbox"/>
DTIC TAB	<input type="checkbox"/>
Unannounced	<input type="checkbox"/>
Justification	
By	
Distribution/	
Availability Codes	
Dist	Avail and/or Special
A-1	

L.D.V. MEASUREMENTS OF UNSTEADY FLOW FIELDS
IN RADIAL TURBINE

FINAL REPORT

W. TABAKOFF AND M. PASIN

Under Contract No. DAAL03-90-G-0129

for

DEPARTMENT OF THE ARMY
United States Army Laboratory Command
Army Research Office
P.O. Box 12211
Research Triangle Park, NC 27709-2211

APPROVED FOR PUBLIC RELEASE;
DISTRIBUTION UNLIMITED.

REPORT DOCUMENTATION PAGE

Form Approved
OMB No. 0704-0188

Public reporting burden for this collection of information is estimated to average 1 hour per response, including the time for reviewing instructions, searching existing data sources, gathering and maintaining the data needed, and completing and reviewing the collection of information. Send comments regarding this burden estimate or any other aspect of this collection of information, including suggestions for reducing this burden, to Washington Headquarters Services, Directorate for Information Operations and Reports, 1215 Jefferson Davis Highway, Suite 1204, Arlington, VA 22202-4302, and to the Office of Management and Budget, Paperwork Reduction Project (0704-0188), Washington, DC 20503.

1. AGENCY USE ONLY (Leave blank)	2. REPORT DATE July 1992	3. REPORT TYPE AND DATES COVERED
----------------------------------	-----------------------------	----------------------------------

4. TITLE AND SUBTITLE LDV Measurements of Unsteady Flow Fields in Radial Turbine	5. FUNDING NUMBERS DAAL03-90-6-0129
--	--

6. AUTHOR(S) W. Tabakoff and M. Pasin	
--	--

7. PERFORMING ORGANIZATION NAME(S) AND ADDRESS(ES) Department of Aerospace Engineering & Engg. Mechanics University of Cincinnati, ML #70 University of Cincinnati Cincinnati, OH 45221	8. PERFORMING ORGANIZATION REPORT NUMBER AsE&EM Report No. 92-105
---	--

9. SPONSORING/MONITORING AGENCY NAME(S) AND ADDRESS(ES) U. S. Army Research Office P. O. Box 12211 Research Triangle Park, NC 27709-2211	10. SPONSORING/MONITORING AGENCY REPORT NUMBER ARO 27515.4-EG
---	---

11. SUPPLEMENTARY NOTES
The view, opinions and/or findings contained in this report are those of the author(s) and should not be construed as an official Department of the Army position, policy, or decision, unless so designated by other documentation.

12a. DISTRIBUTION/AVAILABILITY STATEMENT Approved for public release; distribution unlimited.	12b. DISTRIBUTION CODE
--	------------------------

13. ABSTRACT (Maximum 200 words)

Detailed measurements of an unsteady flow field within the inlet guide vanes (IGV) and the rotor of a radial inflow turbine were performed using a three component Laser Doppler Velocimeter (LDV) system together with a rotary encoder. The mean velocity, the flow angle and the turbulence contours for IGV passages are presented at four blade-to-blade planes for different rotor positions to give three dimensional, unsteady behavior of the IGV flow field. These results are compared with the measurements obtained in the same passage in the absence of the rotor. The flow field of the IGV passage was found to be affected by the presence of the rotor. The ratio of the tangential normal stresses to the radial normal stresses at the exit of the IGV was found to be more than doubled when compared to the case without the rotor.

The rotor flow field measurements are presented as relative mean velocity and turbulence stress contours at various cross section planes throughout the rotor. The cross flow and turbulence stress levels were found to be influenced by the incidence angle. Transportation of the high turbulence fluid by the cross flow was observed downstream in the rotor blade passages.

14. SUBJECT TERMS Radial Turbine Aerodynamics LDV Unsteady Flow Measurements	15. NUMBER OF PAGES 163
	16. PRICE CODE

17. SECURITY CLASSIFICATION OF REPORT UNCLASSIFIED	18. SECURITY CLASSIFICATION OF THIS PAGE UNCLASSIFIED	19. SECURITY CLASSIFICATION OF ABSTRACT UNCLASSIFIED	20. LIMITATION OF ABSTRACT UL
--	---	--	----------------------------------

FOREWORD

This is the final report covering the technical work performed by the Department of Aerospace Engineering and Engineering Mechanics under contract No. DAAL03-90-G-0129 (Army Research Office, Research Triangle Park, NC 27709). The authors are very grateful and wishes to extend sincere appreciation to Director, Dr. Robert R. Singleton and Dr. Thomas Doligalski, Chief, Fluid Dynamics Branch of the Army Research Office for their continued interest and suggestions during the course of this work. Appendix A includes a listing of the scientific and technical personnel participating in this research project, and the students obtaining degrees, as well as a list of technical publications.

TABLE OF CONTENTS

	<u>Page</u>
FOREWORD	iii
TABLE OF CONTENTS	iv
LIST OF FIGURES	v
NOMENCLATURE	xii
ABSTRACT	1
INTRODUCTION	2
EXPERIMENTAL SET-UP	5
DATA ACQUISITION SYSTEM	9
ANALOG REFERENCE INPUT SIGNAL ROTARY ENCODER	9
ROTOR SHAFT-ANGLE ENCODER	10
SYNCHRONIZATION OF THE ANALOG REFERENCE INPUT SIGNAL WITH THE ROTOR	11
VELOCITY AND TURBULENCE MEASUREMENTS	12
ERROR ANALYSIS	16
RESULTS AND DISCUSSION	19
CONCLUSIONS AND RECOMMENDATIONS	32
REFERENCES	34
FIGURES	36
APPENDIX	151

LIST OF FIGURES

<u>Fig.</u>		<u>Page</u>
1	SCHEMATIC SHOWING THE TEST RIG AND LDV SYSTEM	36
2	SCHEMATIC SHOWING THE EXPERIMENTAL TURBINE CONFIGURATION	37
3	VARIATION OF UNCERTAINTY OF MEAN VELOCITY AS A FUNCTION OF SAMPLE SIZE (AT THE EXIT OF THE INLET GUIDE VANE)	38
4	SCHEMATIC SHOWING OF THE FLOW PASSAGE GEOMETRY	39
5	NORMALIZED RADIAL VELOCITY CONTOURS ON THE BLADE-TO-BLADE PLANE, $Z=0.50$ (ROTOR BLADE ENTERING THE PASSAGE)	40
6	NORMALIZED RADIAL VELOCITY CONTOURS ON THE BLADE-TO-BLADE PLANE, $Z=0.50$ (ROTOR BLADE AT THE CENTER OF THE PASSAGE)	41
7	NORMALIZED RADIAL VELOCITY CONTOURS ON THE BLADE-TO-BLADE PLANE, $Z=0.50$ (ROTOR BLADE LEAVING THE PASSAGE)	42
8	NORMALIZED TANGENTIAL VELOCITY CONTOURS ON THE BLADE-TO-BLADE PLANE, $Z=0.50$ (ROTOR BLADE ENTERING THE PASSAGE)	43
9	NORMALIZED TANGENTIAL VELOCITY CONTOURS ON THE BLADE-TO-BLADE PLANE, $Z=0.50$ (ROTOR BLADE AT THE CENTER OF THE PASSAGE)	44
10	NORMALIZED TANGENTIAL VELOCITY CONTOURS ON THE BLADE-TO-BLADE PLANE, $Z=0.50$ (ROTOR BLADE LEAVING THE PASSAGE)	45
11	NORMALIZED RADIAL VELOCITY CONTOURS ON THE BLADE-TO-BLADE PLANE, $Z=0.10$ (ROTOR BLADE ENTERING THE PASSAGE)	46
12	NORMALIZED RADIAL VELOCITY CONTOURS ON THE BLADE-TO-BLADE PLANE, $Z=0.10$ (ROTOR BLADE AT THE CENTER OF THE PASSAGE)	47
13	NORMALIZED RADIAL VELOCITY CONTOURS ON THE BLADE-TO-BLADE PLANE, $Z=0.10$ (ROTOR BLADE LEAVING THE PASSAGE)	48
14	NORMALIZED TANGENTIAL VELOCITY CONTOURS ON THE BLADE-TO-BLADE PLANE, $Z=0.10$ (ROTOR BLADE ENTERING THE PASSAGE)	49
15	NORMALIZED TANGENTIAL VELOCITY CONTOURS ON THE BLADE-TO-BLADE PLANE, $Z=0.10$ (ROTOR BLADE AT THE CENTER OF THE PASSAGE)	50
16	NORMALIZED TANGENTIAL VELOCITY CONTOURS ON THE BLADE-TO-BLADE PLANE, $Z=0.10$ (ROTOR BLADE LEAVING THE PASSAGE)	51
17	NORMALIZED RADIAL VELOCITY CONTOURS ON THE BLADE-TO-BLADE PLANE, $Z=0.25$ (ROTOR BLADE ENTERING THE PASSAGE)	52

<u>Fig.</u>	<u>Page</u>
18 NORMALIZED RADIAL VELOCITY CONTOURS ON THE BLADE-TO-BLADE PLANE, Z=0.25 (ROTOR BLADE AT THE CENTER OF THE PASSAGE)	53
19 NORMALIZED RADIAL VELOCITY CONTOURS ON THE BLADE-TO-BLADE PLANE, Z=0.25 (ROTOR BLADE LEAVING THE PASSAGE)	54
20 NORMALIZED TANGENTIAL VELOCITY CONTOURS ON THE BLADE-TO-BLADE PLANE, Z=0.25 (ROTOR BLADE ENTERING THE PASSAGE)	55
21 NORMALIZED TANGENTIAL VELOCITY CONTOURS ON THE BLADE-TO-BLADE PLANE, Z=0.25 (ROTOR BLADE AT THE CENTER OF THE PASSAGE)	56
22 NORMALIZED TANGENTIAL VELOCITY CONTOURS ON THE BLADE-TO-BLADE PLANE, Z=0.25 (ROTOR BLADE LEAVING THE PASSAGE)	57
23 NORMALIZED RADIAL VELOCITY CONTOURS ON THE BLADE-TO-BLADE PLANE, Z=0.70 (ROTOR BLADE ENTERING THE PASSAGE)	58
24 NORMALIZED RADIAL VELOCITY CONTOURS ON THE BLADE-TO-BLADE PLANE, Z=0.70 (ROTOR BLADE AT THE CENTER OF THE PASSAGE)	59
25 NORMALIZED RADIAL VELOCITY CONTOURS ON THE BLADE-TO-BLADE PLANE, Z=0.70 (ROTOR BLADE LEAVING THE PASSAGE)	60
26 NORMALIZED TANGENTIAL VELOCITY CONTOURS ON THE BLADE-TO-BLADE PLANE, Z=0.70 (ROTOR BLADE ENTERING THE PASSAGE)	61
27 NORMALIZED TANGENTIAL VELOCITY CONTOURS ON THE BLADE-TO-BLADE PLANE, Z=0.70 (ROTOR BLADE AT THE CENTER OF THE PASSAGE)	62
28 NORMALIZED TANGENTIAL VELOCITY CONTOURS ON THE BLADE-TO-BLADE PLANE, Z=0.70 (ROTOR BLADE LEAVING THE PASSAGE)	63
29 PITCH AVERAGED MEAN VELOCITY PROFILES.	64
30 β -FLOW ANGLE CONTOURS ON THE BLADE-TO-BLADE PLANE, Z=0.10 (ROTOR BLADE ENTERING THE PASSAGE)	65
31 β -FLOW ANGLE CONTOURS ON THE BLADE-TO-BLADE PLANE, Z=0.10 (ROTOR BLADE AT THE CENTER OF THE PASSAGE)	66
32 β -FLOW ANGLE CONTOURS ON THE BLADE-TO-BLADE PLANE, Z=0.10 (ROTOR BLADE LEAVING THE PASSAGE)	67
33 β -FLOW ANGLE CONTOURS ON THE BLADE-TO-BLADE PLANE, Z=0.25 (ROTOR BLADE ENTERING THE PASSAGE)	68
34 β -FLOW ANGLE CONTOURS ON THE BLADE-TO-BLADE PLANE, Z=0.25 (ROTOR BLADE AT THE CENTER OF THE PASSAGE)	69

<u>Fig.</u>	<u>Page</u>
35 β -FLOW ANGLE CONTOURS ON THE BLADE-TO-BLADE PLANE, $Z=0.25$ (ROTOR BLADE LEAVING THE PASSAGE)	70
36 β -FLOW ANGLE CONTOURS ON THE BLADE-TO-BLADE PLANE, $Z=0.50$ (ROTOR BLADE ENTERING THE PASSAGE)	71
37 β -FLOW ANGLE CONTOURS ON THE BLADE-TO-BLADE PLANE, $Z=0.50$ (ROTOR BLADE AT THE CENTER OF THE PASSAGE)	72
38 β -FLOW ANGLE CONTOURS ON THE BLADE-TO-BLADE PLANE, $Z=0.50$ (ROTOR BLADE LEAVING THE PASSAGE)	73
39 β -FLOW ANGLE CONTOURS ON THE BLADE-TO-BLADE PLANE, $Z=0.70$ (ROTOR BLADE ENTERING THE PASSAGE)	74
40 β -FLOW ANGLE CONTOURS ON THE BLADE-TO-BLADE PLANE, $Z=0.70$ (ROTOR BLADE AT THE CENTER OF THE PASSAGE)	75
41 β -FLOW ANGLE CONTOURS ON THE BLADE-TO-BLADE PLANE, $Z=0.70$ (ROTOR BLADE LEAVING THE PASSAGE)	76
42 NORMALIZED AXIAL VELOCITY CONTOURS ON THE BLADE-TO-BLADE PLANE, $Z=0.50$ (ROTOR BLADE ENTERING THE PASSAGE)	77
43 NORMALIZED AXIAL VELOCITY CONTOURS ON THE BLADE-TO-BLADE PLANE, $Z=0.50$ (ROTOR BLADE AT THE CENTER OF THE PASSAGE)	78
44 NORMALIZED AXIAL VELOCITY CONTOURS ON THE BLADE-TO-BLADE PLANE, $Z=0.50$ (ROTOR BLADE LEAVING THE PASSAGE)	79
45 NORMALIZED AXIAL VELOCITY CONTOURS ON THE BLADE-TO-BLADE PLANE, $Z=0.25$ (ROTOR BLADE ENTERING THE PASSAGE)	80
46 NORMALIZED AXIAL VELOCITY CONTOURS ON THE BLADE-TO-BLADE PLANE, $Z=0.25$ (ROTOR BLADE AT THE CENTER OF THE PASSAGE)	81
47 NORMALIZED AXIAL VELOCITY CONTOURS ON THE BLADE-TO-BLADE PLANE, $Z=0.25$ (ROTOR BLADE LEAVING THE PASSAGE)	82
48 NORMALIZED AXIAL VELOCITY CONTOURS ON THE BLADE-TO-BLADE PLANE, $Z=0.70$ (ROTOR BLADE ENTERING THE PASSAGE)	83
49 NORMALIZED AXIAL VELOCITY CONTOURS ON THE BLADE-TO-BLADE PLANE, $Z=0.70$ (ROTOR BLADE AT THE CENTER OF THE PASSAGE)	84
50 NORMALIZED AXIAL VELOCITY CONTOURS ON THE BLADE-TO-BLADE PLANE, $Z=0.70$ (ROTOR BLADE LEAVING THE PASSAGE)	85
51 TURBULENT NORMAL STRESS IN THE RADIAL DIRECTION ON THE BLADE-TO-BLADE PLANE, $Z=0.10$ ($U_r'^2/V_{cr}^2$) (ROTOR BLADE ENTERING THE PASSAGE)	86

<u>Fig.</u>	<u>Page</u>
52 TURBULENT NORMAL STRESS IN THE RADIAL DIRECTION ON THE BLADE-TO-BLADE PLANE, $Z=0.10$ ($U_r'^2/V_{cx}^2$) (ROTOR BLADE AT THE CENTER OF THE PASSAGE)	87
53 TURBULENT NORMAL STRESS IN THE RADIAL DIRECTION ON THE BLADE-TO-BLADE PLANE, $Z=0.10$ ($U_r'^2/V_{cx}^2$) (ROTOR BLADE LEAVING THE PASSAGE)	88
54 TURBULENT NORMAL STRESS IN THE RADIAL DIRECTION ON THE BLADE-TO-BLADE PLANE, $Z=0.25$ ($U_r'^2/V_{cx}^2$) (ROTOR BLADE ENTERING THE PASSAGE)	89
55 TURBULENT NORMAL STRESS IN THE RADIAL DIRECTION ON THE BLADE-TO-BLADE PLANE, $Z=0.25$ ($U_r'^2/V_{cx}^2$) (ROTOR BLADE AT THE CENTER OF THE PASSAGE)	90
56 TURBULENT NORMAL STRESS IN THE RADIAL DIRECTION ON THE BLADE-TO-BLADE PLANE, $Z=0.25$ ($U_r'^2/V_{cx}^2$) (ROTOR BLADE LEAVING THE PASSAGE)	91
57 TURBULENT NORMAL STRESS IN THE RADIAL DIRECTION ON THE BLADE-TO-BLADE PLANE, $Z=0.50$ ($U_r'^2/V_{cx}^2$) (ROTOR BLADE ENTERING THE PASSAGE)	92
58 TURBULENT NORMAL STRESS IN THE RADIAL DIRECTION ON THE BLADE-TO-BLADE PLANE, $Z=0.50$ ($U_r'^2/V_{cx}^2$) (ROTOR BLADE AT THE CENTER OF THE PASSAGE)	93
59 TURBULENT NORMAL STRESS IN THE RADIAL DIRECTION ON THE BLADE-TO-BLADE PLANE, $Z=0.50$ ($U_r'^2/V_{cx}^2$) (ROTOR BLADE LEAVING THE PASSAGE)	94
60 TURBULENT NORMAL STRESS IN THE RADIAL DIRECTION ON THE BLADE-TO-BLADE PLANE, $Z=0.70$ ($U_r'^2/V_{cx}^2$) (ROTOR BLADE ENTERING THE PASSAGE)	95
61 TURBULENT NORMAL STRESS IN THE RADIAL DIRECTION ON THE BLADE-TO-BLADE PLANE, $Z=0.70$ ($U_r'^2/V_{cx}^2$) (ROTOR BLADE AT THE CENTER OF THE PASSAGE)	96
62 TURBULENT NORMAL STRESS IN THE RADIAL DIRECTION ON THE BLADE-TO-BLADE PLANE, $Z=0.70$ ($U_r'^2/V_{cx}^2$) (ROTOR BLADE LEAVING THE PASSAGE)	97
63 TURBULENT NORMAL STRESS IN THE TANGENTIAL DIRECTION ON THE BLADE-TO-BLADE PLANE, $Z=0.10$ ($U_\theta'^2/V_{cx}^2$) (ROTOR BLADE ENTERING THE PASSAGE)	98
64 TURBULENT NORMAL STRESS IN THE TANGENTIAL DIRECTION ON THE BLADE-TO-BLADE PLANE, $Z=0.10$ ($U_\theta'^2/V_{cx}^2$) (ROTOR BLADE AT THE CENTER OF THE PASSAGE)	99
65 TURBULENT NORMAL STRESS IN THE TANGENTIAL DIRECTION ON THE BLADE-TO-BLADE PLANE, $Z=0.10$ ($U_\theta'^2/V_{cx}^2$) (ROTOR BLADE LEAVING THE PASSAGE)	100
66 TURBULENT NORMAL STRESS IN THE TANGENTIAL DIRECTION ON THE BLADE-TO-BLADE PLANE, $Z=0.25$ ($U_\theta'^2/V_{cx}^2$) (ROTOR BLADE ENTERING THE PASSAGE)	101
67 TURBULENT NORMAL STRESS IN THE TANGENTIAL DIRECTION ON THE BLADE-TO-BLADE PLANE, $Z=0.25$ ($U_\theta'^2/V_{cx}^2$) (ROTOR BLADE AT THE CENTER OF THE PASSAGE)	102
68 TURBULENT NORMAL STRESS IN THE TANGENTIAL DIRECTION ON THE BLADE-TO-BLADE PLANE, $Z=0.25$ ($U_\theta'^2/V_{cx}^2$) (ROTOR BLADE LEAVING THE PASSAGE)	103

<u>Fig.</u>		<u>Page</u>
69	TURBULENT NORMAL STRESS IN THE TANGENTIAL DIRECTION ON THE BLADE-TO-BLADE PLANE, $Z=0.50$ ($U_{\theta}'^2/V_{\infty}^2$) (ROTOR BLADE ENTERING THE PASSAGE)	104
70	TURBULENT NORMAL STRESS IN THE TANGENTIAL DIRECTION ON THE BLADE-TO-BLADE PLANE, $Z=0.50$ ($U_{\theta}'^2/V_{\infty}^2$) (ROTOR BLADE AT THE CENTER OF THE PASSAGE)	105
71	TURBULENT NORMAL STRESS IN THE TANGENTIAL DIRECTION ON THE BLADE-TO-BLADE PLANE, $Z=0.50$ ($U_{\theta}'^2/V_{\infty}^2$) (ROTOR BLADE LEAVING THE PASSAGE)	106
72	TURBULENT NORMAL STRESS IN THE TANGENTIAL DIRECTION ON THE BLADE-TO-BLADE PLANE, $Z=0.70$ ($U_{\theta}'^2/V_{\infty}^2$) (ROTOR BLADE ENTERING THE PASSAGE)	107
73	TURBULENT NORMAL STRESS IN THE TANGENTIAL DIRECTION ON THE BLADE-TO-BLADE PLANE, $Z=0.70$ ($U_{\theta}'^2/V_{\infty}^2$) (ROTOR BLADE AT THE CENTER OF THE PASSAGE)	108
74	TURBULENT NORMAL STRESS IN THE TANGENTIAL DIRECTION ON THE BLADE-TO-BLADE PLANE, $Z=0.70$ ($U_{\theta}'^2/V_{\infty}^2$) (ROTOR BLADE LEAVING THE PASSAGE)	109
75	TURBULENT REYNOLDS STRESS ON THE BLADE-TO-BLADE PLANE, $Z=0.10$ ($U_r'U_{\theta}'/V_{\infty}^2$) (ROTOR BLADE ENTERING THE PASSAGE)	110
76	TURBULENT REYNOLDS STRESS ON THE BLADE-TO-BLADE PLANE, $Z=0.10$ ($U_r'U_{\theta}'/V_{\infty}^2$) (ROTOR BLADE AT THE CENTER OF THE PASSAGE)	111
77	TURBULENT REYNOLDS STRESS ON THE BLADE-TO-BLADE PLANE, $Z=0.10$ ($U_r'U_{\theta}'/V_{\infty}^2$) (ROTOR BLADE LEAVING THE PASSAGE)	112
78	TURBULENT REYNOLDS STRESS ON THE BLADE-TO-BLADE PLANE, $Z=0.25$ ($U_r'U_{\theta}'/V_{\infty}^2$) (ROTOR BLADE ENTERING THE PASSAGE)	113
79	TURBULENT REYNOLDS STRESS ON THE BLADE-TO-BLADE PLANE, $Z=0.25$ ($U_r'U_{\theta}'/V_{\infty}^2$) (ROTOR BLADE AT THE CENTER OF THE PASSAGE)	114
80	TURBULENT REYNOLDS STRESS ON THE BLADE-TO-BLADE PLANE, $Z=0.25$ ($U_r'U_{\theta}'/V_{\infty}^2$) (ROTOR BLADE LEAVING THE PASSAGE)	115
81	TURBULENT REYNOLDS STRESS ON THE BLADE-TO-BLADE PLANE, $Z=0.50$ ($U_r'U_{\theta}'/V_{\infty}^2$) (ROTOR BLADE ENTERING THE PASSAGE)	116
82	TURBULENT REYNOLDS STRESS ON THE BLADE-TO-BLADE PLANE, $Z=0.50$ ($U_r'U_{\theta}'/V_{\infty}^2$) (ROTOR BLADE AT THE CENTER OF THE PASSAGE)	117
83	TURBULENT REYNOLDS STRESS ON THE BLADE-TO-BLADE PLANE, $Z=0.50$ ($U_r'U_{\theta}'/V_{\infty}^2$) (ROTOR BLADE LEAVING THE PASSAGE)	118
84	TURBULENT REYNOLDS STRESS ON THE BLADE-TO-BLADE PLANE, $Z=0.70$ ($U_r'U_{\theta}'/V_{\infty}^2$) (ROTOR BLADE ENTERING THE PASSAGE)	119
85	TURBULENT REYNOLDS STRESS ON THE BLADE-TO-BLADE PLANE, $Z=0.70$ ($U_r'U_{\theta}'/V_{\infty}^2$) (ROTOR BLADE AT THE CENTER OF THE PASSAGE)	120

<u>Fig.</u>	<u>Page</u>
86 TURBULENT REYNOLDS STRESS ON THE BLADE-TO-BLADE PLANE, Z=0.70 ($U_r'U_\theta'/V_\infty^2$) (ROTOR BLADE LEAVING THE PASSAGE)	121
87 MEASUREMENT LOCATIONS IN THE ROTOR.	122
88 STREAMWISE RELATIVE VELOCITY CONTOURS (m/s) CROSS SECTION 1	123
89 TANGENTIAL RELATIVE VELOCITY CONTOURS (m/s) CROSS SECTION 1	124
90 STREAMWISE RELATIVE VELOCITY CONTOURS (m/s) CROSS SECTION 2	125
91 TANGENTIAL RELATIVE VELOCITY CONTOURS (m/s) CROSS SECTION 2	126
92 STREAMWISE RELATIVE VELOCITY CONTOURS (m/s) CROSS SECTION 3	127
93 TANGENTIAL RELATIVE VELOCITY CONTOURS (m/s) CROSS SECTION 3	128
94 STREAMWISE RELATIVE VELOCITY CONTOURS (m/s) CROSS SECTION 4	129
95 TANGENTIAL RELATIVE VELOCITY CONTOURS (m/s) CROSS SECTION 4	130
96 STREAMWISE RELATIVE VELOCITY CONTOURS (m/s) CROSS SECTION 5	131
97 TANGENTIAL RELATIVE VELOCITY CONTOURS (m/s) CROSS SECTION 5	132
98 STREAMWISE RELATIVE VELOCITY CONTOURS (m/s) CROSS SECTION 6	133
99 TANGENTIAL RELATIVE VELOCITY CONTOURS (m/s) CROSS SECTION 6	134
100 TURBULENT NORMAL STRESS IN THE STREAMWISE DIRECTION CROSS SECTION 1, ($U_r'^2/V_\infty^2$)	135
101 TURBULENT NORMAL STRESS IN THE TANGENTIAL DIRECTION CROSS SECTION 1, ($U_\theta'^2/V_\infty^2$)	136
102 TURBULENT NORMAL STRESS IN THE STREAMWISE DIRECTION CROSS SECTION 2, ($U_r'^2/V_\infty^2$)	137
103 TURBULENT NORMAL STRESS IN THE TANGENTIAL DIRECTION CROSS SECTION 2, ($U_\theta'^2/V_\infty^2$)	138
104 TURBULENT NORMAL STRESS IN THE STREAMWISE DIRECTION CROSS SECTION 3, ($U_r'^2/V_\infty^2$)	139
105 TURBULENT NORMAL STRESS IN THE TANGENTIAL DIRECTION CROSS SECTION 3, ($U_\theta'^2/V_\infty^2$)	140
106 TURBULENT NORMAL STRESS IN THE STREAMWISE DIRECTION CROSS SECTION 4, ($U_r'^2/V_\infty^2$)	141

<u>Fig.</u>	<u>Page</u>
107 TURBULENT NORMAL STRESS IN THE TANGENTIAL DIRECTION CROSS SECTION 4, $(U_t'^2/V_\infty^2)$	142
108 TURBULENT NORMAL STRESS IN THE STREAMWISE DIRECTION CROSS SECTION 5, $(U_s'^2/V_\infty^2)$	143
109 TURBULENT NORMAL STRESS IN THE TANGENTIAL DIRECTION CROSS SECTION 5, $(U_t'^2/V_\infty^2)$	144
110 TURBULENT NORMAL STRESS IN THE STREAMWISE DIRECTION CROSS SECTION 6, $(U_s'^2/V_\infty^2)$	145
111 TURBULENT NORMAL STRESS IN THE TANGENTIAL DIRECTION CROSS SECTION 6, $(U_t'^2/V_\infty^2)$	146
112 SPANWISE RELATIVE VELOCITY CONTOURS (m/s) CROSS SECTION 1	147
113 SPANWISE RELATIVE VELOCITY CONTOURS (m/s) CROSS SECTION 2	148
114 SPANWISE RELATIVE VELOCITY CONTOURS (m/s) CROSS SECTION 3	149
115 SPANWISE RELATIVE VELOCITY CONTOURS (m/s) CROSS SECTION 4	150

NOMENCLATURE

N	number of data.
$U_b, U_g,$ U_p	transverse (blue), vertical (green), and inclined (purple) velocity components.
U	average total velocity.
$U_r, U_\theta,$ U_{ax}	radial, tangential and axial velocity components.
$U_{rj}^{\prime 2}$	turbulence normal stress in radial direction.
$U_{\theta j}^{\prime 2}$	turbulence normal stress in tangential direction.
$(U_r' U_\theta')_{ij}$	Reynolds shear stress.
V_{ex}	passage and time averaged velocity at inlet guide vane exit.
β	flow angle with respect to circumferential direction.
σ, S	standard deviation.

Subscripts:

i	refers to a measurement location in the IGV passage.
j	refers to a rotor blade position.
k	datum number.
1	inlet conditions.
2	exit conditions.

ABSTRACT

Detailed measurements of an unsteady flow field within the inlet guide vanes (IGV) and the rotor of a radial inflow turbine were performed using a three component Laser Doppler Velocimeter (LDV) system together with a rotary encoder. The mean velocity, the flow angle and the turbulence contours for IGV passages are presented at four blade-to-blade planes for different rotor positions to give three dimensional, unsteady behavior of the IGV flow field. These results are compared with the measurements obtained in the same passage in the absence of the rotor. The flow field of the IGV passage was found to be affected by the presence of the rotor. The ratio of the tangential normal stresses to the radial normal stresses at the exit of the IGV was found to be more than doubled when compared to the case without the rotor.

The rotor flow field measurements are presented as relative mean velocity and turbulence stress contours at various cross section planes throughout the rotor. The cross flow and turbulence stress levels were found to be influenced by the incidence angle. Transportation of the high turbulence fluid by the cross flow was observed downstream in the rotor blade passages.

INTRODUCTION

Radial gas turbines have been used for many years in special applications because of their high power/weight ratio, good starting capability, small size, quietness, low level vibration and efficiency advantage over the axial small size turbines [1]. Therefore, radial inflow turbine finds wide range of applications from automotive turbocharger to aircraft auxiliary power units, and has recently been given serious consideration for primary powerplants applications for both automobiles and rotocrafts [2].

Increasing application of radial gas turbines necessitates a better understanding of the flow behavior to improve the performance characteristics. Past research efforts have been concentrated on One Dimensional flows with the combination of a loss model [1-3].

However, typical geometries in the radial turbines which turn the flow through 90° angle of deflection in the meridional plane and simultaneously in the blade-to-blade plane naturally induce large three-dimensional flows even in the absence of viscous effects [4]. It is further complicated by the interaction between the scroll, nozzles and the rotor. Three dimensional flow fields in the scroll and nozzle sections have been reported in ref[5-8].

Tabakoff et al.[9-11] obtained hot wire anemometer measurements in the scrolls of different cross-sectional geometries that revealed the presence of the two counter rotating vortices. The total pressure, Mach number and the flow angle were obtained

with pressure probe measurements at the inlet and the exit of the radial nozzle. These results are reported by Khalil, Tabakoff and Hamed [12]. It showed strong end wall cross flow and large mixing effect at the nozzle exit. Hashemi et al. [13] presented the results of total and static pressure measurements at three radii downstream of the radial nozzle cascades. They also conducted flow visualizations in air and water test rigs which showed that secondary flows in radial turbines are different than that in the axial machines because of the radial pressure gradients and the incidence effects. I. Ariga et al. [14] reported relative velocity distribution within the radial section of the radial turbine rotor for various rotor speeds. They showed the effect of the rotor speed on the cross flow within the rotor passages.

The errors introduced by the presence of the measuring probe can be very serious in the radial machines because they have narrow blade passages and low aspect ratios. A non-intrusive technique such as Laser Doppler Velocimeter (LDV) avoids these difficulties. Malak et al. [15] reported the measurements of the detailed flow field through a rectangular cross-section scroll using LDV, and observed only one vortex. H. Eroglu [16] reported detailed flow measurements in the inlet guide vanes. He observed lack of periodicity between flow passages due to the scroll geometry and also rapid mixing at the exit of the Inlet Guide Vanes (IGV), caused by the converging nature of the cross-section. Rapid mixing was also confirmed by A.N. Laksiminarasimha [17]. The studies mentioned above were performed without the rotor which was replaced

by an aluminum body of revolution to provide flow path.

In the present study, the three dimensional flow field through the inlet guide vanes(IGV) of the radial inflow turbine was obtained with the corresponding rotor. Flow measurements within the rotor blades were carried out. A three dimensional, three color LDV system was used. The effect of the rotor on the upstream IGV flow field was investigated through unsteady measurements. The variation of the mean velocities in the IGV passage with respect to the rotor blade position is reported. It was observed that the flow field within the IGV passage exhibits periodicity with the rotor blade rotation. The flow angle at the exit of the IGV indicated underturning caused by the presence of the rotor and leading edge vortices were observed. The flow was found to be unsymmetrical due to the unsymmetrical scroll geometry. Flow separation at the blade pressure surface was observed, and the measurements indicated strong cross flow at the end wall. The turbulence results indicated that the presence of the rotor increases the tangential turbulence stresses. In addition it was found that the ratio of the radial normal stresses to the tangential normal stresses were more than doubled when compared to the data obtained without the rotor.

The rotor measurements showed that the cross flow direction is from the suction to the pressure side at the inlet because of the incidence angle. This direction later changes from the pressure to the suction side when passage pressure field becomes more dominant.

EXPERIMENTAL SET-UP

The experimental set-up consists of the following: a) the radial turbine, b) the seeding atomizer, c) the 3-D Laser Doppler Velocimeter (LDV) optical system, d) the data acquisition hardware and e) the software. (Fig.1).

Test Rig

The pressurized air stored in a high pressure tank is supplied through four inch diameter pipes and adjusted by a pressure regulator. The inlet total pressure to the turbine can be set up to 20 psi by the pressure regulator. The mass flow rate is measured by a standard orifice-meter connected to an inclined manometer filled with standard manometer red oil with 0.827 specific density. A flow regulating valve is used to change the air mass flow rate. The air flow enters a settling chamber with 10" diameter followed by a flow adapter which converges the flow from 10" diameter to 5" diameter. Because the scroll entrance has a square cross section, another adapter is provided. A honeycomb is placed at the end of the second adapter, before the air flow enters the scroll.

The scroll has nearly a square cross section over most of the circumference. The details of the scroll can be found in ref [18].

The cross section of the scroll is positioned unsymmetrically such that one side of the square cross section lines up with one of the nozzle end walls. The nozzle end walls are parallel and 0.5" apart. There is a vaneless section between the exit of the scroll and the entrance of the nozzle. This vaneless section starts at 5.41" radius and ends at 4.41" radius which is also the entrance of

the nozzles. The nozzles are between 4.41" and 3.35" radii. After the exit of the inlet guide vanes (IGV), the air flow goes through a vaneless section and enters the rotor. The rotor inlet radius is 3.22", while the exit shroud and hub radii are 1.7" and 0.87" respectively (Fig.2).

Flow Seeding

A commercial six-jet atomizer was used to seed the flow with two micrometer mean diameter propylene glycol particles at 100000 Particles/cm³

Laser and Optics

A three component Laser Doppler Velocimeter (LDV) system was used to measure the velocity field through the inlet guide vanes and the rotor section. The LDV system is shown in Fig.1 schematically. A five Watt argon-ion Spectra Physics, model 164-09 laser is used as the light source. The laser beam is separated in the components by the dispersion prism. The three beams with the highest intensities are used for the measurements. These beams have 0.5145, 0.4880, 0.4765 micrometer wavelengths and are green, blue and purple respectively. Green and blue beams are sent through the optical train which is in the axial direction where as the purple beam goes through another train whose beam expander and focusing lens are inclined 30 deg. to the axial direction. Each beam is polarized by the polarization rotator and split into two beams with equal intensities. After passing through the beam expander, the two beams for each color are focused by the focusing lens to produce a set of fringes. Three sets of fringes are obtained for the three

colors. The blue and green colors are used to measure two orthogonal velocity components on the plane perpendicular to the optical axis. The non-orthogonal purple component is used along with the blue beam to obtain the velocity component perpendicular to this plane.

The beam expanders reduce the measurement volume diameter 3.75 times and improve the signal-to-noise ratio. Scattered lights from the particles in the measurement volume are collected in the off-axis backward scatter mode to reduce the noise during the wall proximity measurements. Frequency shifters are used for each component to reduce the fringe bias and to determine the flow direction. Two separate collimators are installed to ensure that the focused beams are intersected at their beam waist. This maximizes the signal quality and eliminates the frequency broadening effects.

The LDV signal are collected through photo multipliers and sent to the three TSI 1990 counter type signal processors. The entire LDV system is on a milling machine table which can traverse 10" in the axial, 18" in the transverse and 22" in the vertical direction with 0.001" accuracy.

Measurement Window

Transparent window is required to allow the laser beams to penetrate in the measurement region. The window that was manufactured for the velocity measurements in the IGV passage was flat because it replaced a part of one of the endwall. Therefore, it did not cause any deflection problem since it deflected the

laser beams with the same angle at all measurement locations. Plexiglass with 0.25 inches thickness was chosen as window material.

However, the window for the velocity measurements in the rotor has to follow the rotor shroud contour which requires curved window shape. Different window materials were tried to investigate the optical effect of the window material and thickness on the laser beam. Also several models of the section at which the window was planned was molded and these different window materials were tried with the molded models to understand the effect of the curvature. Finally, Lexan was selected as the window material, because it has good transmitting properties and its thickness is 0.05 inches which allowed us to fit the window to the rotor shroud curvature. The molded window model with Lexan was tested with laser beam and magnifier optics at various beam incidence angles to investigate the possible distortions of the laser beam which can be caused by the curved window. The highest distortion was found to be within the location uncertainty which is limited by the accuracy of the traverse mechanism.

After the shape, location and material of the window were selected, the rotor section of the turbine was machined and the window was mounted to replace the shroud wall of the rotor. The width of the window was calculated so that laser beams are not blocked at the deepest penetration.

DATA ACQUISITION SYSTEM

The LDV signal coming from the photo detectors are processed by three counter type signal processors. The signal processors send the data to a TSI MI-990 interface which is mounted into one of the signal processors. The interface combines these data with the rotor shaft information coming from TSI 1999 rotary encoder and sends then to an IBM PC/AT compatible computer through a DMA card. The data are collected with a rotating machinery software and stored for further calculations.

Because the data rate from the purple component was low, the measurement were obtained from that component separately. However, the data from the blue and green components are collected simultaneously with coincidence requirement set to 20 micro seconds which is detected by the MI-990 interface, set through the data acquisition software.

ANALOG REFERENCE INPUT SIGNAL FOR ROTARY ENCODER

The TSI 1999 Rotary Encoder is used to obtain the position information of the rotor shaft. The rotary encoder requires an input signal coming from the rotor to indicate the shaft position.

The rotor has eight full blades and eight splitters. Therefore a disc with 16 teeth was machined to generate 16 pulses with each revolution. This disc was mounted to the turbine shaft with a light emitting diode (LED) and a light detector assembly. The LED and the light detector produce a signal whenever a tooth passes between them. This signal is then sent to a circuit which was designed and manufactured in the propulsion lab of the University of Cincinnati.

The circuit conditions the coming signal and generates clean pulse signal with constant width. The width and the slope of the signal can be adjusted with two adjustable resistances mounted on the circuit.

The output signal of the circuit has an amplitude of 1.75V. This pulse is fed to the rotary encoder as the reference input signal.

ROTOR SHAFT-ANGLE ENCODER

The TSI 1999 Rotary Encoder is used to tag each velocity measurement with the corresponding angular position of the rotor.

The encoder operation is based on phase-locking of the voltage-controlled oscillator. The oscillator runs n times (selected by the operator) faster than the frequency of the pulse train which is fed to the encoder as analog reference input. A 14-bit counter is started at the arrival of every input pulse and it counts up to number n . Whenever a velocity data is received by the MI-990 interface from the three processors, the number on this counter is latched and sent to the computer together with the velocity information. Between every input pulses, the time at which the n th count is reached, is compared with the time of the arrival of the next pulse. If the difference between any consecutive pulses are smaller than a preset number of counts (set by the lock-detector sensitivity switch), the rotary encoder adjusts the oscillator so that the counter can follow small changes in the input frequency hence in the rotor speed. If the difference is

larger than the set lock-detector sensitivity value, the rotor is identified as being out-of-lock.[19]

During the experiments, the number n was set to 8000, and the lock-detector sensitivity was set to 16. Since the circuit sends 16 pulses for every revolution, each pulse corresponds to a rotor blade passage. For the measurements through the IGV passage, the rotor blade passage was divided to 10 blade positions so that each shaft position has 2 deg of rotor revolution interval length. The velocity measurements were obtained in the Inlet Guide Vanes (IGV) of the turbine for these 10 rotor positions.

SYNCHRONIZATION OF THE ANALOG REFERENCE INPUT SIGNAL WITH THE ROTOR IGV MEASUREMENTS:

The TSI 1999 is set such that it starts the counter as soon as the rotor blade is at the trailing edge of the upper blade of the interested passage. It is accomplished by adjusting the delay setting of the encoder.

First the measurement volume of the LDV is positioned at the rotor tip when it passes the trailing edge of the upper blade. The rotor blades generate laser signal when they pass from the measurement volume. The pulses coming from the circuit and the signals coming from the LDV are observed with an oscilloscope. These two signals are overlapped by playing with the delay setting of the rotary encoder. The synchronization is accomplished by repeating this procedure to assure the accuracy.

ROTOR MEASUREMENTS:

During the velocity measurements in the rotor, the rotor blade passes from the LDV measurement volume. This creates strong signal which causes saturation in the photo multipliers, and also introduces error in the measurements process. Therefore, the data acquisition process is halted when rotor blade passes from the measurement volume. This was accomplished with TSI 1999 rotary encoder. The first, LDV measurement volume positioned on the axis of the rotor at the interested cross section. The pulse coming from the circuit and the laser signal obtained from the rotor blade were observed on an oscilloscope and delay was adjusted to coincide the pulse and the rising location of the laser signal. The second step was to observe the laser signal coming from the blade, along with the signal coming from the window output of the rotary encoder. The window count on the TSI 1999 determines the time span during which the data acquisition is halted. This value was adjusted to cover the time required for each blade to pass through the measurement volume. Because rotor blade has constant thickness resulting in greater blockage for the locations downstream at smaller radii, the value of the window count was determined at every measurement cross section.

VELOCITY AND TURBULENCE MEASUREMENTS

The measurements of the flow field in the IGV passages are limited to the passage of the seventh and the eighth blades according to the numbering in Fig.2. This passage was chosen to minimize the blockage of the laser beams by the blades. The

measurements are taken on four blade-to-blade planes. These planes are located at 0.1, 0.25, 0.50 and 0.7 span distances from the plexiglass window.

The experiments were performed at 0.12 lb/s air mass flow and 900 rpm rotor speed. The horizontal (blue) and the vertical (green) velocities are measured directly, and the on-axis velocity U_{ax} is calculated from the blue and purple components according to the following equation:

$$U_{ax} = \frac{U_b \cos\theta - U_p}{\sin\theta}$$

where U_b and U_p are the blue and the purple velocities respectively and θ is the angle between the two optical trains. In this LDV system, " θ " is 30 deg.

Due to the presence of the rotor, the velocity in the IGV is divided into two components. The first component is the deterministic component of the flow which varies with the disturbances coming from the rotor. This component is the mean velocity calculated from the data taken for a given rotor position at a measurement point. The undeterministic component of the velocity is calculated from the standard deviation of the data, which is also taken for a given rotor position at a measurement point.

In this report, the mean velocity will be defined as the mean velocity calculated for a given rotor position, and the turbulence velocity will be defined as the standard deviation of the data for

the same rotor position.

For the rotor position j and the measurement point i , the mean velocity is;

$$\bar{U}_{ij} = \frac{\sum_k U_{ij,k}}{N_{ij}} \quad k = 1 \text{ to } N_{ij}$$

N_{ij} = The number of data points for the rotor position j and the measurement point i .

The standard deviation of the velocity for the same rotor position j , at the measurement point i is as follows:

$$\sigma_{ij}^2 = \frac{\sum_k (U_{ij,k} - \bar{U}_{ij})^2}{N_{ij} - 1} \quad k=1 \text{ to } N_{ij}$$

σ_{ij} is the turbulence level of the resultant velocity.

Turbulence results are presented in terms of non-dimensionalized turbulence normal stresses in radial and tangential directions are:

$$\frac{U_{ij}^2}{V_{ex}^2} = \frac{\sigma_{ij}^2 \sin^2 \beta_{ij}}{V_{ex}^2}$$

$$\frac{U_{\theta ij}^2}{V_{ex}^2} = \frac{\sigma_{ij}^2 \cos^2 \beta_{ij}}{V_{ex}^2}$$

where β_{ij} is the angle of the resultant velocity with respect to tangential direction for the rotor position j and at the measurement point i . V_{ex} is the time and passage averaged exit velocity. For the mass flow rate the turbine was tested, V_{ex} was 22.35 m/s.

Since the data coming from the blue and the green beams are acquired with coincidence requirement, which assures that they come from the same particle, Reynolds shear stress $U_r'U_\theta'$ can be calculated by the following equation:

$$\frac{(U_r'U_\theta')_{ij}}{V_{ex}^2} = \frac{\sum_k (U_{ijk} \cos \beta_{ijk} - U_{ij} \cos \beta_{ij}) (U_{ijk} \sin \beta_{ijk} - U_{ij} \sin \beta_{ij})}{(N_{ij} - 1) V_{ex}^2}$$

where $U_{ij,k}$ and $\beta_{ij,k}$ are the velocity and the angle of the resultant velocity with respect to tangential direction for k th datum at measurement location i and rotor position j .

N_{ij} is the number of data for that measurement. U_{ij} and β_{ij} are the averaged velocity and angle of that particular location and rotor position.

The rotor measurements were performed at the same operation conditions on six cross section planes which are perpendicular to the main streamline. Total four measurement locations were chosen in the spanwise direction at every measurement cross section which

were at 0.1, 0.25, 0.50 and 0.70 span distances from the window. The mean velocity data are presented with relative velocity contours in tangential and streamwise directions which were calculated from the measured absolute velocities.

ERROR ANALYSIS

As with any other techniques, the measurement of flow velocity with LDV has some uncertainty. However, it offers non-intrusive measurement capability, linear response and wider dynamic range as compared to other more conventional techniques.

The use of LDV system introduces some bias errors due to the nature of the LDV as well as some statistical uncertainties. The bias errors have been investigated and correction methods have been studied by many researchers. There are three groups of bias errors. These are filter, directional (angle) and velocity bias.

The Doppler burst is filtered by a band-pass filter before being sent to the counter processors to remove the DC pedestal and high frequency noise, as well as to reduce the noise coming from the outside of the frequency region containing the Doppler signal. Different settings of the filters were tried to avoid any cut-off of the Doppler signal to eliminate the filter biasing. Also, the filter band widths were kept as small as possible to reduce the noise.

The counter signal processor requires a minimum number of fringes that a particle should cross to validate the measurement. Therefore, the particles with the normal directions to the fringes have a higher chance to meet this requirement. This creates a

directional bias which can be reduced by decreasing the ratio of the number of required fringes to the number of the total fringes in the measurement volume.

For the LDV system used, the number of total fringes is 19 and the number of cycles to validate the data was set to 4. The directional bias can also be reduced by using frequency shifters. Frequency shifters were used for all the three beams mostly in the opposite direction of the flow. Hence, the directional bias was reduced to a great extent.

The particles with higher velocities have a higher chance of crossing the measurement volume. This creates a velocity bias in the measurements. Various averaging techniques were used to reduce the measurement bias by using different weight functions. It is shown that the ensemble average of the velocity gives very close results to the weighted averaging in the investigated IGV passage [20]. Ensemble averaging was used along with the frequency shifters which also reduce the velocity bias.

The random error was also investigated at the upstream and downstream of the IGV blades. The uncertainty interval of the measured mean velocities is related to the sample size by the following relation [21];

$$\Delta U = \frac{z S_u}{N^{1/2}}$$

for 95% confidence level, $z=0.96$. S_u is an estimator for the true standard deviation and N is the sample size.

The experiments at the upstream and at the exit of the IGV channel were performed to investigate the effect of the sample size for different turbulence levels.

Total 8000 data were taken at each point to determine the value of the standard deviation. This value then was used to calculate the variation of the uncertainty limits with the sample size. The velocity survey results at the exit of the IGV passage is presented in Fig.3. The uncertainty improves with increasing sample size. However, the improvement is not significant when the sample size is above 400. Therefore the sample size was chosen 400 data for every rotor position. For 400 sample size, the statistical uncertainties were calculated 0.60% and 2.65% for transverse and vertical velocities respectively at the inlet of the IGV passage whereas the same uncertainties were 1.31% and 5.58% at the exit plane of the IGV. Since there are total 10 rotor positions, 4000 data were collected at every measurement point in the IGV. Total 7 positions were chosen for the rotor along the circumferential direction. Therefore 3000 data collected in the rotor for a given spanwise measurement location.

Also systematic uncertainties were calculated using the procedure given by Snyder et al.[21]. Relative uncertainties were found to be 1.63%.

RESULTS AND DISCUSSION

The measurements were taken at mass flow rate of 0.12 lb/s and 900 rpm rotor speed. The Reynolds number and Mach number were 0.69×10^5 and 0.084 respectively based on the time and passage averaged velocity at the exit of the Inlet Guide Vane(IGV), the IGV chord length and cold air properties at 70°F.

INLET GUIDE VANE RESULTS:

The velocity results are presented for normalized radial, tangential and axial velocity components of the mean velocity and the angle of the total mean velocity with respect to the circumferential direction (Fig.4) on 4 blade-to-blade planes. These planes are located at 0.10, 0.25, 0.50 and 0.70 blade span distances from the plexiglass window. The velocity results are normalized with passage and time averaged velocity at the IGV exit which was 22.35 m/s for the test condition. Velocity and mean flow angle contours are presented for three different rotor positions which are rotor blade entering the IGV passage at downstream of the IGV, rotor blade at the center of the IGV passage and rotor blade leaving the IGV passage.

The contours of normalized radial and tangential mean velocities at 0.5 span (mid-span) plane are given in Figs 5 through 10. The effect of the rotor on the flow field of the IGV passage can be clearly seen by comparing Fig.5 and Fig.6. The radial velocities reduce as the rotor blade travels from the entrance of the passage (Fig.5) to the center of the passage (Fig.6). Then they

increase when the rotor blade is about to leave the IGV passage (Fig.7). Figs 8-10 are the contours for the normalized tangential velocities on mid-span plane. The tangential velocities also decrease when the rotor blade is at the center of the passage. The decrease is more significant for the tangential velocities. Similarities between Figs.5 and 7 of radial velocity contours and Figs.8 and 10 of tangential velocity contours indicate the periodicity of the flow field within the IGV passage with the rotor blade revolution. The change in the velocity values with the rotor revolution is more pronounced closer to the trailing edge where it reaches up to 15%. The effect of the rotor reduces at the upstream in the IGV passage, and velocity decrease becomes around 5%. This behavior of the radial and the tangential velocities is observed at the other 3 blade-to-blade planes. These contours are presented in Figs.11 through 28.

Due to the high negative incidence, the flow turns and accelerates near the pressure surface close to the leading edge, then it decreases which indicates a possible separation at this region as can be seen from the velocities on the mid-span plane (Figs.5-10). This separation character can also be observed at 0.25 span (Figs.17-22), and 0.70 span (Figs.23-28) planes, but it can not be seen as clearly on the plane at 0.10 span (Figs.11-16), because of the slower moving flow resulted from the end wall boundary layer. While tangential velocities increase downstream in the passage, radial velocities remain at the same order of magnitude. Both radial and tangential velocities have smaller

values at the planes close to the end walls because of the end wall boundary layer. This is more notable for the plane close to the plexiglass window (0.1 span plane). Velocity decrease closer to the end walls becomes more significant downstream, because end wall boundary layer further develops. The development of the end wall boundary layer is apparent from the spanwise variation of the pitch averaged velocity at the inlet and exit cross sections presented in Fig. 29. The end wall boundary layer effect on the exit velocity profile can be seen more significantly at the plexiglass end wall. The velocity profile is not symmetrical, its maximum value is not located at the mid-channel, but it has shifted towards to the plexiglass side. This profile is resulted from the 90° bend that flow experiences at the exit of the scroll. In general, the flow velocity on the suction surface is higher than the pressure surface throughout the IGV passage at all blade-to-blade planes.

The low velocity region on the suction surface downstream from the leading edge indicates the stagnation point. This low velocity region is observed at all blade-to-blade planes.

Mean flow angle contours are presented in Figs.30 through 40 at 4 blade-to-blade planes for 3 rotor blade positions. Beta angle is defined with respect to circumferential direction. The flow angle at the entrance of the passage is almost uniform at all 4 planes, but they have higher values on the planes at 0.1 span (Figs.30-32) and 0.7 span (Figs.39-41). Because the end wall boundary layer decreases the flow velocity, and the radial pressure gradient resultant from the passage geometry becomes more dominant

hence this increases the flow angles. Upstream of the passage on the 0.70 span plane (Figs.39-41), the flow angles are slightly higher than the flow angles on 0.25 span plane (Figs.33-35) although 0.7 span plane is further away from the end wall. This indicates that radial pressure field is more dominant at the plane closer to the back wall due to the smaller velocities, which are caused by 90° turning at the scroll exit. Also the flow angles are higher at the measurement points close to the pressure and suction surfaces because of the blade boundary layer. Beta angle decreases with the accelerating flow along the blade passage. The exit flow angle is higher than the blade trailing edge solid angle which is 11 deg. This indicates an underturning of the flow at the exit. The flow angle at the exit of the passage at 0.1 span plane (Figs.30-32) is higher, which shows that the radial pressure field at the exit is stronger than the passage pressure field when it approaches the end wall, and it further turns the flow in radial direction.

The normalized axial velocity contours are given in Figs. 42 through 50 at 0.25, 0.50 and 0.70 span planes for 3 different rotor positions. Axial velocity measurements could not be obtained on 0.10 span plane due to low signal-to-noise ratio for the purple component. Positive values indicate velocities towards the plexiglass window. The axial velocities are generally low in the IGV passage with the exception of the separation region explained previously. In addition to that, axial velocities are higher at the stagnation point on 0.7 span plane which can be caused by the end

wall boundary layer collapsing at the stagnation point.

Turbulence results are presented with turbulent normal stresses in radial and tangential directions and the Reynolds shear stresses on the cross section planes in Figs 51 through 86 at 4 blade-to-blade planes and for 3 rotor blade positions. Figs 51-53 are the contours of turbulent normal stress in radial direction at 0.1 span plane. Radial normal stresses vary from 0.4 to 0.8 percent through out the passage, and they do not show an increase towards downstream. The region at the pressure surface closer to the leading edge is the only exception where the turbulence stresses increase up to 5 percent. This region is the flow separation region as explained previously. The radial normal turbulence stress contours at 0.25 span plane are shown in Figs. 54-56. The turbulence stress levels are at the same order as the results presented on 0.1 span plane. The high turbulence region at the separation point is also shown at the blade pressure surface with the maximum stress levels reaching 4 percent. The stagnation point as pointed out before is at the suction surface downstream from the leading edge. The turbulence stresses on this plane are high at that stagnation point. It can be due to the inlet end wall boundary layer collapsing on the blade hence creating high turbulence region. This high turbulence region is not present at mid-span plane presented in Figs.57-59. The turbulent normal stresses in the radial direction on the mid-span plane show the same behavior as the ones at the two previous planes. The only high turbulence values are at the separation region close to the pressure surface.

The turbulence stress values at that region are reaching 2.5 percent. Besides the separation zone, the normal stress values vary from 0.1 to 0.4 percent over the IGV passage. The same turbulence contours at 0.7 span plane are given in Figs.60-62. The normal stresses are 0.3-0.4 percent in the blade passage with the exception of the two familiar regions which are the separation region at the pressure surface and the stagnation point on the suction surface. The stress levels at the separation zone increases up to 4 percent. When compare the stress levels at the separation region for all the planes, 0.1 span plane has the highest stress levels at this region although the stress levels at other locations on this plane are at the same order. This indicates that high turbulence flow is transported from mid-channel towards to plexiglass end wall. This conclusion is supported by the axial velocity contours which have high values in that region. Second high turbulence zone at the stagnation point on 0.7 span plane experiences much higher turbulence levels than 0.25 span plane. This shows that the back end wall boundary layer is thicker than the end wall boundary layer at the plexiglass side which was also concluded previously. In general, the radial normal turbulence values do not vary with the rotor revolution.

The turbulent normal stresses in the tangential direction are given in the Figs.63-74. The tangential stresses on the 0.1 span plane are presented in Figs.63-65. Inspection of these figures shows that the separation region at the pressure surface are also increased, reaching up to 7 percent. The tangential stress levels

at other locations vary from 0.5 to 1 percent. Figs.66-68 show tangential normal stresses on 0.25 span plane. Similar to the other planes, the stress levels are high at the separation zone. Also stagnation point shows increased turbulence levels which is consistent to the results presented for radial turbulent stresses on the same plane. Downstream after the reattachment, the stress levels are higher across to passage than the stresses on the mid-span plane presented in Figs.69-71. This indicates that, the cross flow driven by the blade pressure gradient is transporting high turbulence fluid from the pressure blade surface to the suction blade surface. Further downstream at the trailing edge of the pressure surface, the tangential stresses are at 2 percent level in Fig.66 which gives the turbulence contours when the rotor blade is at the trailing edge of the pressure surface. These stress levels drops after the rotor blade passes as shown in Fig.67. This shows the effect of the rotor blade on the tangential stress levels at the trailing edge region of the IGV passage. The same behavior can be observed on the mid-span plane by comparing Figs.69 and 70, on 0.7 span plane by comparing Figs.72 and 73. Mid-span blade-to-blade tangential normal turbulence levels (Figs.69-71) are lower than the levels on 0.25 plane as explained before. With exception of the similar high turbulence values at the separation region, the stress levels vary between 0.1 and 1 percent. There is not a high turbulence region present at the stagnation point, because the end wall inlet boundary layer does not extent to the mid-span. Figs.72-74 show the tangential normal turbulence contours on 0.7

span plane. The separation region as well as the stagnation point exhibit high turbulence levels. The stress levels at the stagnation point are higher than the stress levels at the same point on 0.25 plane which also indicates that back end wall boundary layer is more developed than the plexiglass side end wall boundary layer. This results are consistent with the radial normal turbulence results.

When compared the tangential normal stresses with the radial normal stresses at the trailing edge on the mid-span plane (Figs.57-59,69-71), it can be seen that the tangential normal stresses are approximately seven times larger than the radial normal stresses at the same region. The turbulence measurements obtained in the same passage without the rotor at the mass flow rates 0.2 and 0.3 lb/s are reported by Eroglu and Tabakoff. The tangential normal stresses at the trailing edge were measured only three times larger than the radial normal stresses for both mass flow rates, which indicates that the mass flow rate did not have an effect on this ratio. Therefore it can be concluded that the presence of the rotor increases tangential turbulent stresses at the trailing edge in the IGV passage.

The Reynolds stresses on blade-to-blade plane are given in Figs.75-86 on four planes and for three rotor blade positions. Reynolds stresses are positive through out the passage. Similar to the tangential and the radial stresses, the separation region has higher Reynolds stress levels at all four planes. In addition to that, high Reynolds stresses are present at the stagnation point on

0.25 span (Figs.78-80) and 0.7 span (Figs.84-86) planes which are also consistent with the tangential and radial stress contours presented previously for these planes.

ROTOR RESULTS:

The velocity measurements through the rotor of the radial inflow turbine were also carried out at the same mass flow rate and rotor speed. The LDV measurements were performed at six cross section planes which were perpendicular to the main streamline (Fig.87). Four measurement locations were chosen in the spanwise direction. These measurement points were at 0.1, 0.25, 0.5, and 0.7 span distances from the tip of the rotor blade. Mean velocity results are presented as relative velocity contours in streamwise, tangential, and spanwise directions within the rotor blade passages. The turbulence results are given as normalized normal stresses in streamwise and tangential directions. The normal stresses are normalized with passage averaged relative velocity at the rotor inlet which was 10.8 m/s for the test condition.

The first cross section is at 0.05 inches downstream from the rotor tip. The streamwise and the tangential velocity contours are shown in Figs 88 and 89 respectively. The averaged incidence angle at the entrance of the rotor was calculated from the measured velocity values and found to be 40 deg. with respect to the tangential direction. The tangential velocities are high closer to the suction blade surface, and they decrease rapidly when they approach the blade pressure surface. Streamwise velocities show the same behavior as they are higher at the suction side. The

second cross section is located at 0.10 inches downstream from the rotor tip. The streamwise velocity is still higher at the suction surface due to the turning (Fig.90). The tangential velocities significantly decrease as the flow adjust itself to the rotor blade passage as shown in Fig.91. But the tangential velocity component is still from the suction surface to the pressure surface. This indicates that the initial inertia that the flow has at the entrance of the rotor due to the incidence angle is still a dominating factor over the pressure field of the rotor blade passage. Figs.92 and 93 are streamwise and tangential velocity contours at the third cross section which is located at the point the flow starts turning from radial direction to axial direction in the rotor. The streamwise velocity is higher at the pressure surface as shown in Fig.92. This can be due to transportation of higher energy flow from the suction to the pressure surface with the tangential velocity component. Tangential velocity at this cross section is very low throughout the passage (Fig.93). Fig. 94 and 95 give streamwise and tangential velocities in the fourth cross section which is located at the point at which the flow is at the half way of the turning from the radial to the axial direction. Streamwise velocities are higher towards to the hub, because the flow has larger turning at that region than the flow at the shroud section. The tangential velocities change direction in the passage, and they are from pressure to suction surface at the fourth cross section, because the pressure field within the blade passage becomes more dominant. The section five is at the region

when the flow turns completely to the axial direction. The streamwise and the tangential velocities are presented in Figs.96 and 95. The streamwise velocity is almost uniform in the cross section, but it decreases closer to the suction surface which indicates boundary layer development. Also high velocity gradients are experienced closer to the shroud. The tangential velocities are relatively low across the rotor blade passage (Fig.97). The sixth cross section is at the exit of the rotor. The streamwise and the tangential velocity contours at this cross section are presented in Figs.98 and 99. The streamwise velocity is slightly higher in the hub section. The tangential velocities are uniform in the rotor passage as shown in Fig.99.

The turbulent normal stresses in the streamwise and the tangential directions in the rotor are presented in Figs.100 through 111. The streamwise and tangential normal turbulence stress contours on the first cross section are shown in Figs.100 and 100. Both normal stresses are high near the suction surface because of the possible separation caused by high incidence angle. Turbulence stresses at the second cross section increase considerably at the same region (Figs.102 and 103). This indicates further development of the separation at the rotor entrance closer to the suction surface. The turbulence stresses at the third cross section are given in Figs.104 and 105. The high turbulence stress region is shifted to the pressure blade surface. This indicates a cross flow that transported high turbulence flow from the blade suction to the blade pressure surface. The fourth cross section

which is where the flow turns from the radial to the axial direction has high turbulence stresses close to the back wall due to that turning (Figs.106 and 107). Also relatively higher tangential turbulence stresses are present closer to the blade suction surface. This is because of the further transportation of high turbulence flow from the third cross section at this region. The turbulence stresses on the fifth plane are given in Figs.108 and 109. The stresses do not vary in the tangential direction but generally they are higher at the mid passage and lower close to the end walls because of the end wall boundary layer. Figs.110 and 111 are the contours of the streamwise and the tangential turbulence stresses at the cross section six which is located at 0.05 inches before the rotor exit. The flow closer to the hub has higher turbulence stresses. This is because of the adjustment of the flow to the exit geometry which does not have the blockage caused by the rotor shaft.

Spanwise velocity measurements were obtained at the first 4 cross sections. Measurements at cross sections 5 and 6 for the spanwise velocity are rejected due to low signal to noise ratio. Spanwise velocity contours for planes 1 through 4 are presented in Figs.112-115. Velocity values are low for all 4 cross sections, but the spanwise component increases at the cross section 4, because the flow starts turning from the radial to the axial direction which introduces three dimensional character. Also at all cross sections, spanwise velocity component is relatively higher at the rotor blade pressure surface close to the hub. This indicates a

possible transportation of the boundary flow from the end wall section towards to mid channel.

CONCLUSIONS AND RECOMMENDATIONS

The flow fields of the IGV and the rotor blade passages were measured with three component LDV system. The IGV flow field was found to be affected by the presence of the rotor. The periodicity of the flow field in the passage with the rotor revolution was observed. It was observed that the flow field in the IGV passage was strongly influenced by the upstream scroll geometry. A separation region at the inlet pressure surface due to high negative incidence angle was detected. The high turbulence flow generated by the separation region is further transported to the downstream suction surface. Turbulent stress levels at the trailing edge of the IGV are affected by the presence of the rotor. The ratio of the tangential normal stresses to the radial normal stresses at the exit of the IGV were more than doubled when compared to the case without the rotor. The measurement in the rotor blade passages revealed a separation region at the suction surface at the inlet due to incidence angle. The cross flow and turbulence levels were found to be affected by the incidence angle. Transportation of the high turbulence fluid downstream in the passage was observed.

For future work, the flow field at the exit of the rotor should be investigated for better understanding of the mixing mechanism and corresponding losses at the exit region of the radial inflow turbine. Also an unsteady computer code can be used to

obtain the potential flow solution throughout the radial inflow turbine. Analysis of the experimental results and the potential flow will enable to understand the secondary flows in the radial turbine in greater detail.

REFERENCES

1. Rohlik, H.E., "Current and Future Technology in Radial and Axial Gas Turbines", NASA-TM- 83414, August 1983.
2. Meitner, P.L. and Glassman, A.J., "Computer Code for Off-Design Performance Analysis of Radial-Inflow Turbines with Rotor Blade Sweep", NASA-TP-2199, 1983.
3. Meitner, P.L. and Glassman, A.J., "Loss Model for Off-Design Performance Analysis of Radial Turbines with Pivoting-Vane, Variable-Area Stators", SAE Aerospace Congress & Exposition, October 13-16, 1980, Los Angeles Convention Center, Paper No. 801135.
4. Choo, Y.K. and Civinskas, K.C., "Three-Dimensional Inviscid Analysis of Radial-Turbine Flow and a Limited Comparison with Experimental Data", Proceedings of the ASME on Three-Dimensional Flow Phenomena in Fluid Machinery, Miami Beach, Florida, Nov. 1985.
5. Hamed, A. and Abou Ghantous, C., "Three-Dimensional Flow Computations in a Turbine Scroll", NASA CR 168003, August 1982.
6. Hamed, A., Tabakoff, W. and Malak, M., "The Three-Dimensional Compressible Flow in a Radial Inflow Turbine Scroll", GTSJ Paper 83-TOKYO-IGTC-66.
7. Hamed, A. and Baskharone, E., "Analysis of the Three-Dimensional Flow in a Turbine Scroll", Journal of Fluids Engineering, Vol. 102, No.3, pp.297-301, 1980.
8. Hamed, A., Baskharone, E. and Tabakoff, W., "A Flow Study in Radial Inflow Turbine Scroll-Nozzle Assembly," Journal of Fluids Engineering, Vol.100, pp.31-36, March 1978.
9. Tabakoff, W., Vittal, B.V.R. and Wood, B., "Three-Dimensional Flow Measurements in a Turbine Scroll, NASA CR-167920, 1982.
10. Tabakoff, W., Wood, B. and Vittal, B.V.R., "Three-Dimensional Flow Measurements in a Vaneless Radial Turbine", NASA CR-167994, August 1982.
11. Tabakoff, W., Vittal, B.V.R., and Wood, B, "Three-Dimensional Flow Measurements in a Turbine Scroll", ASME Paper 83-GT-128, 1983.
12. Khalil, I., Tabakoff, W., and Hamed, A., "Losses in Radial Inflow Turbines", Journal of Fluids Engineering, Vol.98, pp.364-373, September 1976.

13. Hashemi, S.G.R., Lemak, R.J. and Owczarek, J.A., "An Investigation of the Flow Characteristics and of Losses in Radial Nozzle Cascades", Journal of Engineering for Gas Turbine Power, April 1984, Vol. 106, pp. 502-510.
14. Ariga, I., Watanabe, I. and Fujie, K., "Investigations Concerning Flow Patterns Within the Impeller Channels of Radial Inflow Turbines, With Some Reference to the Influence of the Splitter Vanes", Journal of Engineering for Power, October, 1967, pp.463-476.
15. Malak, M.F., Hamed, A. and Tabakoff, W., "3-D Flow Field Measurements in a Radial Inflow Turbine Scroll Using LDV", Journal of Engineering for Gas Turbine Power, April 1987, Vol. 109, pp. 163-169.
16. Eroglu, H. and Tabakoff W., "LDV Measurements and Investigation of Flow Field Through Radial Turbine Guide Vanes", ASME 34th International Gas Turbine Conference, Toronto, 1989.
17. Laksiminarasimha, A.N., Tabakoff, W., and Metwally, M.A., "LDV Measurements and the Flow Analysis in the Vaneless Region of a Radial Inflow Turbine", ASME 34th International Gas Turbine Conference, Toronto, 1989.
18. Malak, M.F., "Laser Doppler Velocimeter Measurements and the Theoretical Investigation of Three Dimensional Scroll Flow", Ph.D. Thesis, Dept. of Aerospace Engineering and Engineering Mechanics, University of Cincinnati, 1986.
19. TSI Incorporated, Model 1999 Rotary Encoder Manual.
20. Eroglu, H., "LDV Measurements and Investigation of Flow Field Through Radial Turbine Guide Vanes", Ph.D. Thesis, Dept. of Aerospace Engineering and Engineering Mechanics, University of Cincinnati, 1988.
21. Snyder, P.K. et al., "Performance and Analysis of a Three-Dimensional Nonorthogonal Laser Doppler Anemometer" NASA-TM-81293, July 1981.

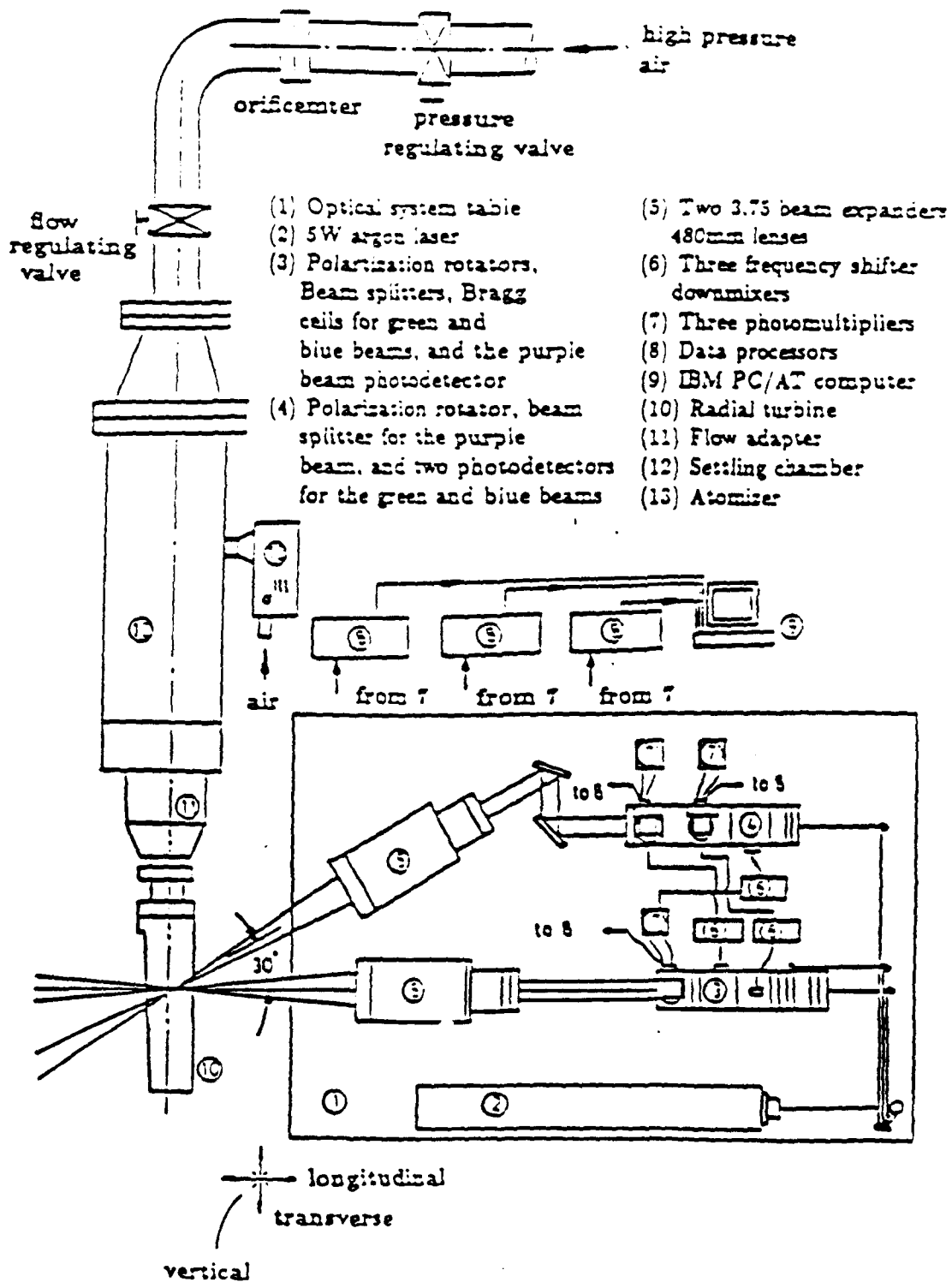


FIG. 1 SCHEMATIC SHOWING THE TEST RIG AND LDV SYSTEM

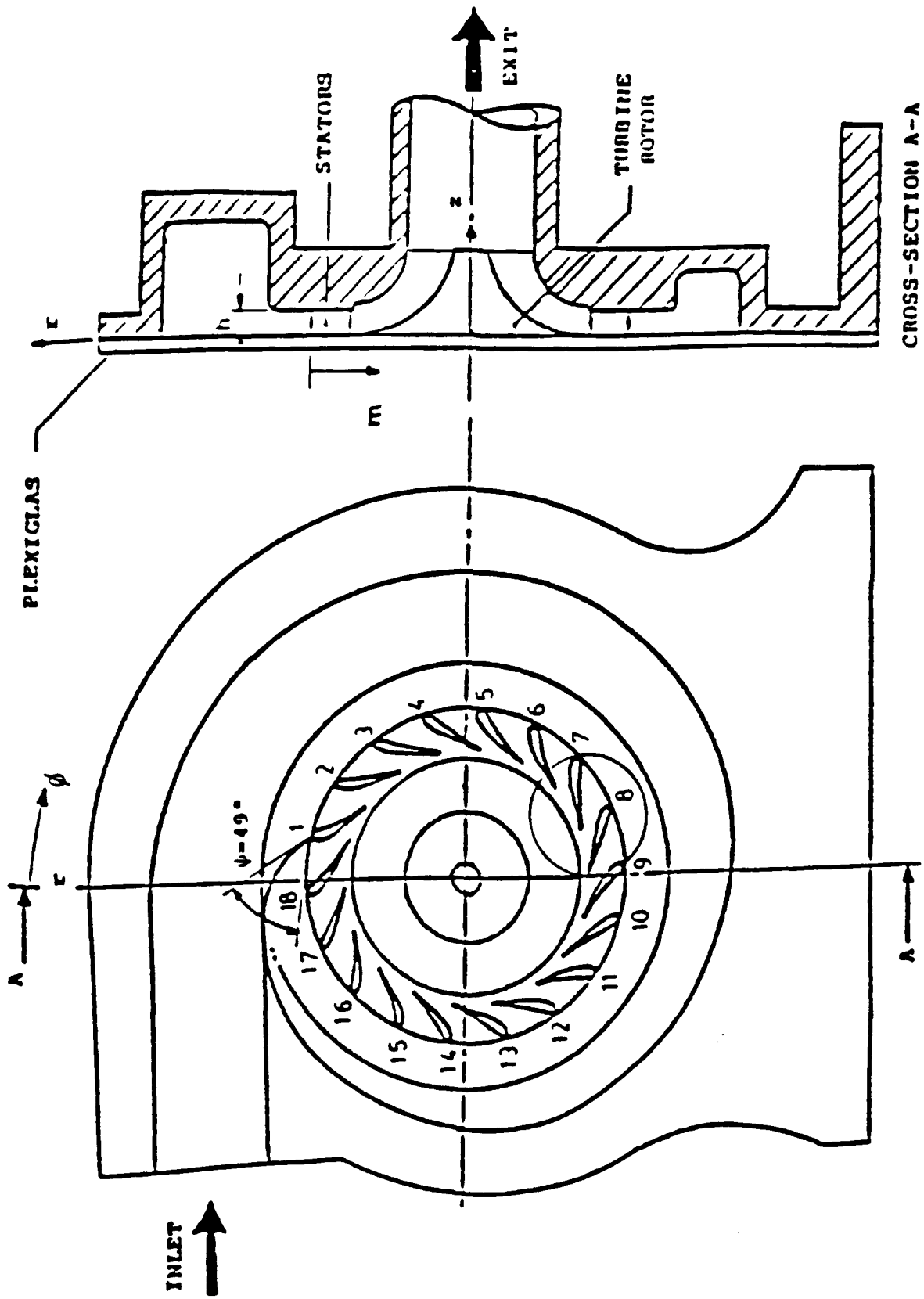


FIG. 2 SCHEMATIC SHOWING THE EXPERIMENTAL TURBINE CONFIGURATION.

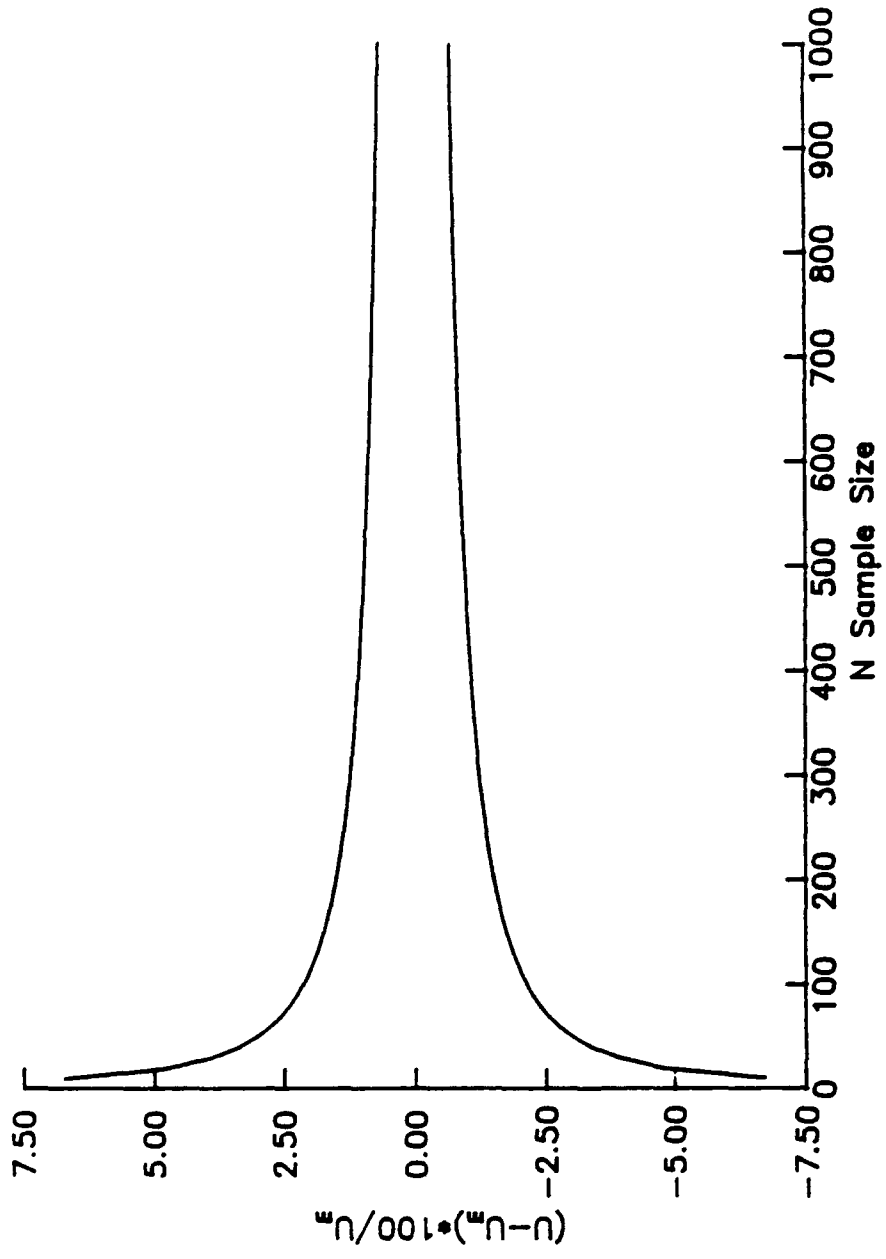


FIG. 3 VARIATION OF UNCERTAINTY OF MEAN VELOCITY
 AS A FUNCTION OF SAMPLE SIZE
 (AT THE EXIT OF THE INLET GUIDE VANE)

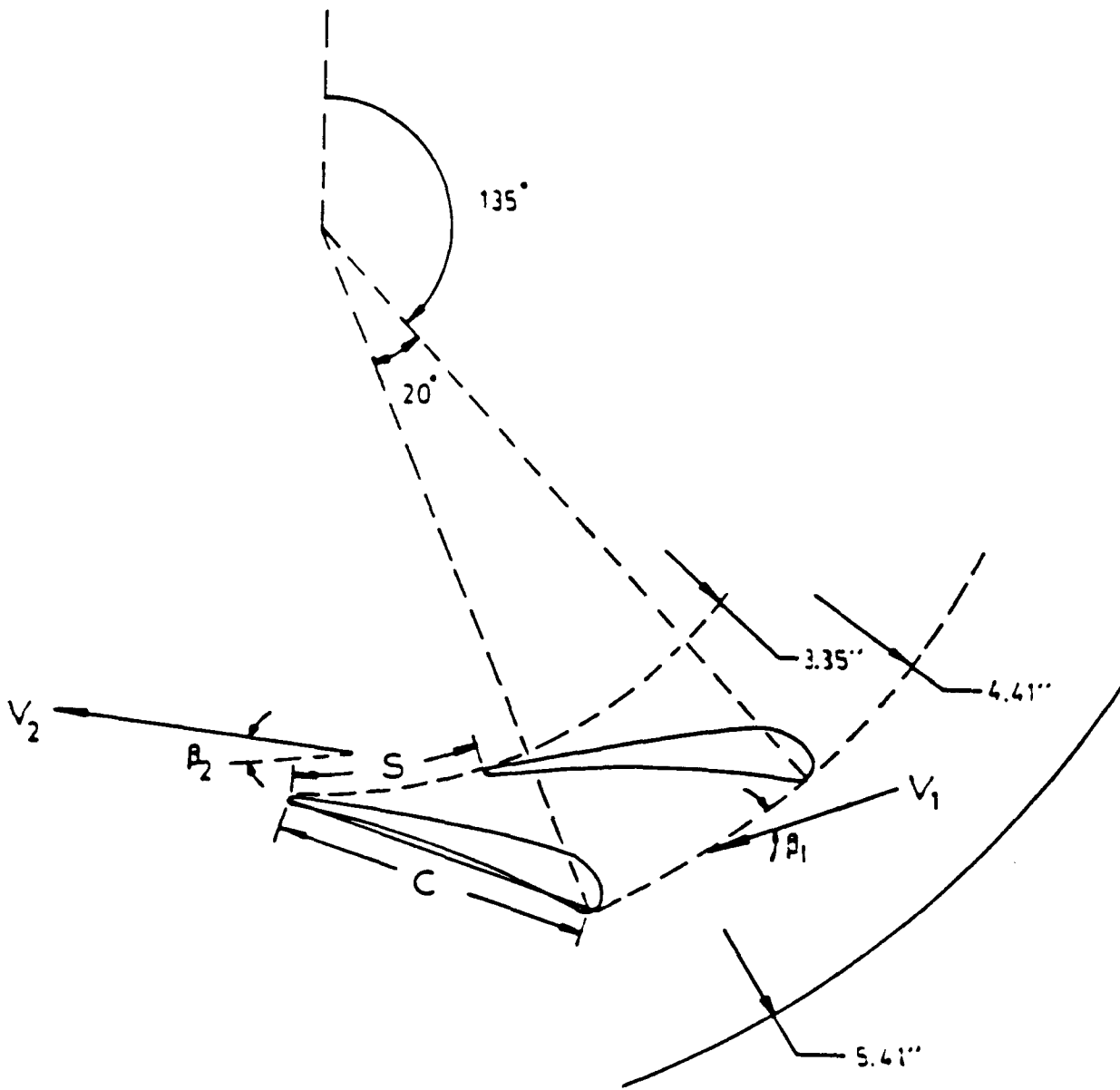


FIG. 4 SCHEMATIC SHOWING THE FLOW PASSAGE GEOMETRY

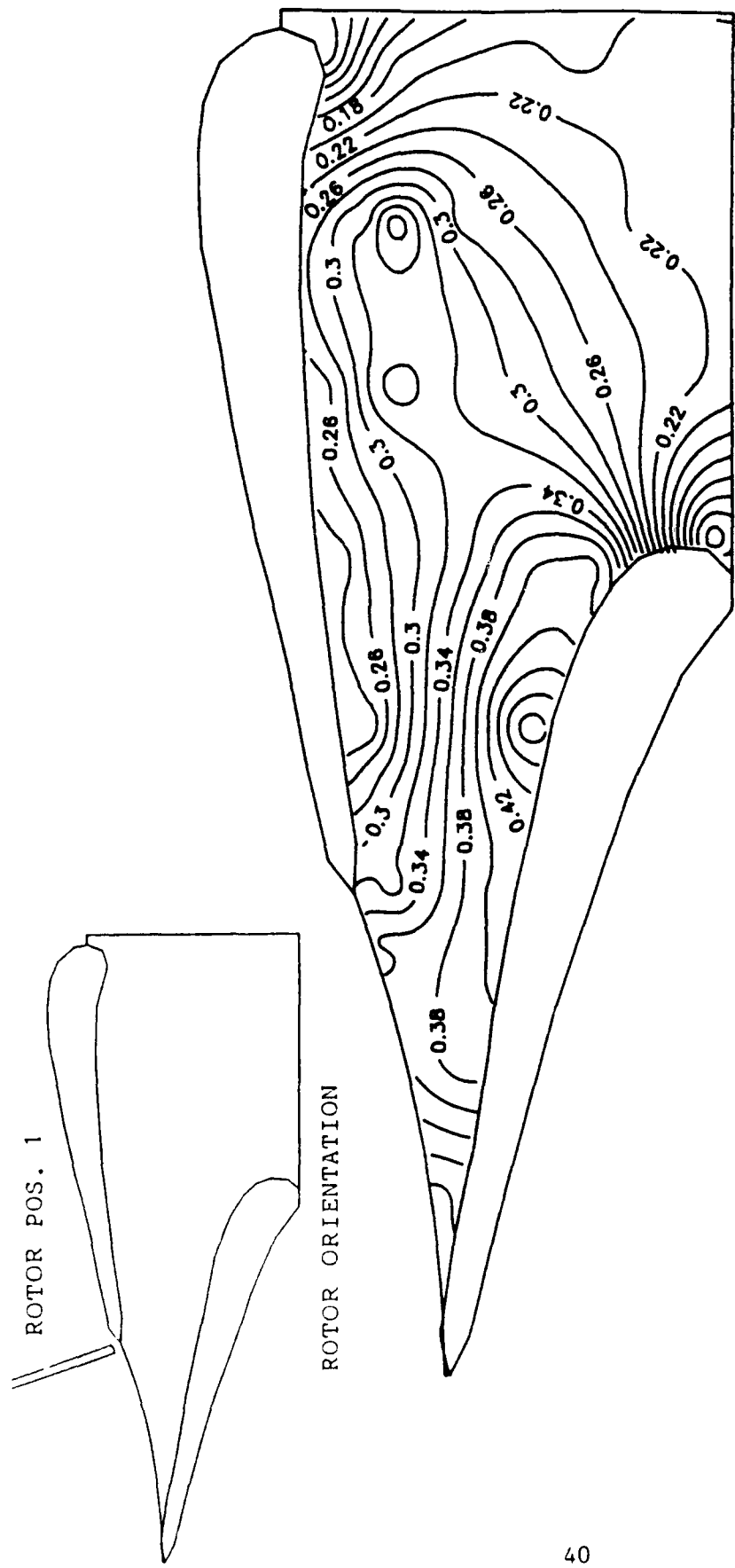


FIG. 5 NORMALIZED RADIAL VELOCITY CONTOURS ON THE
 BLADE-TO-BLADE PLANE, $Z=0.50$
 (ROTOR BLADE ENTERING THE PASSAGE)

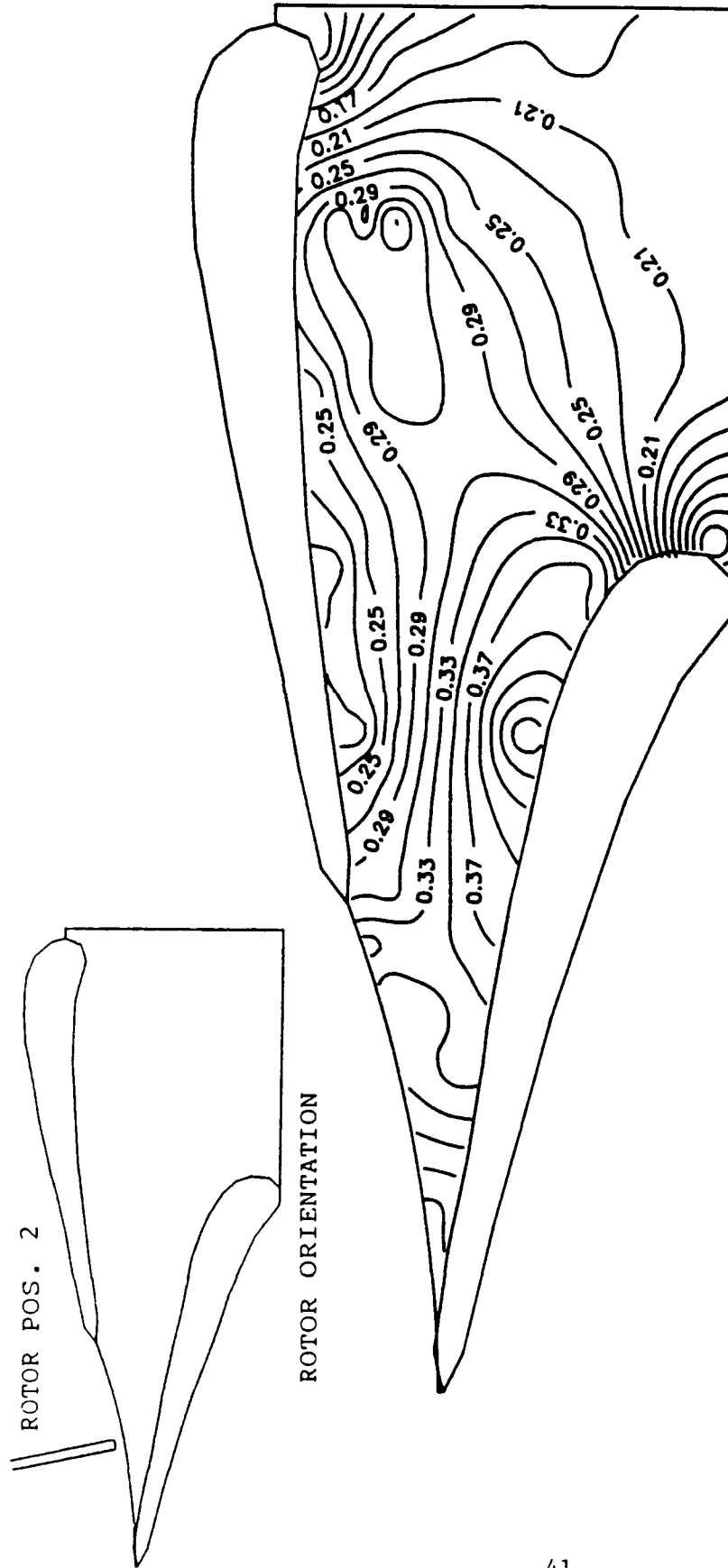
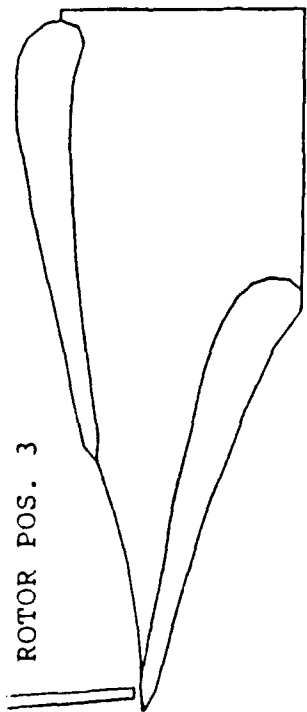


FIG. 6 NORMALIZED RADIAL VELOCITY CONTOURS ON THE
 BLADE-TO-BLADE PLANE, $Z=0.50$
 (ROTOR BLADE AT THE CENTER OF THE PASSAGE)

ROTOR POS. 3



ROTOR ORIENTATION

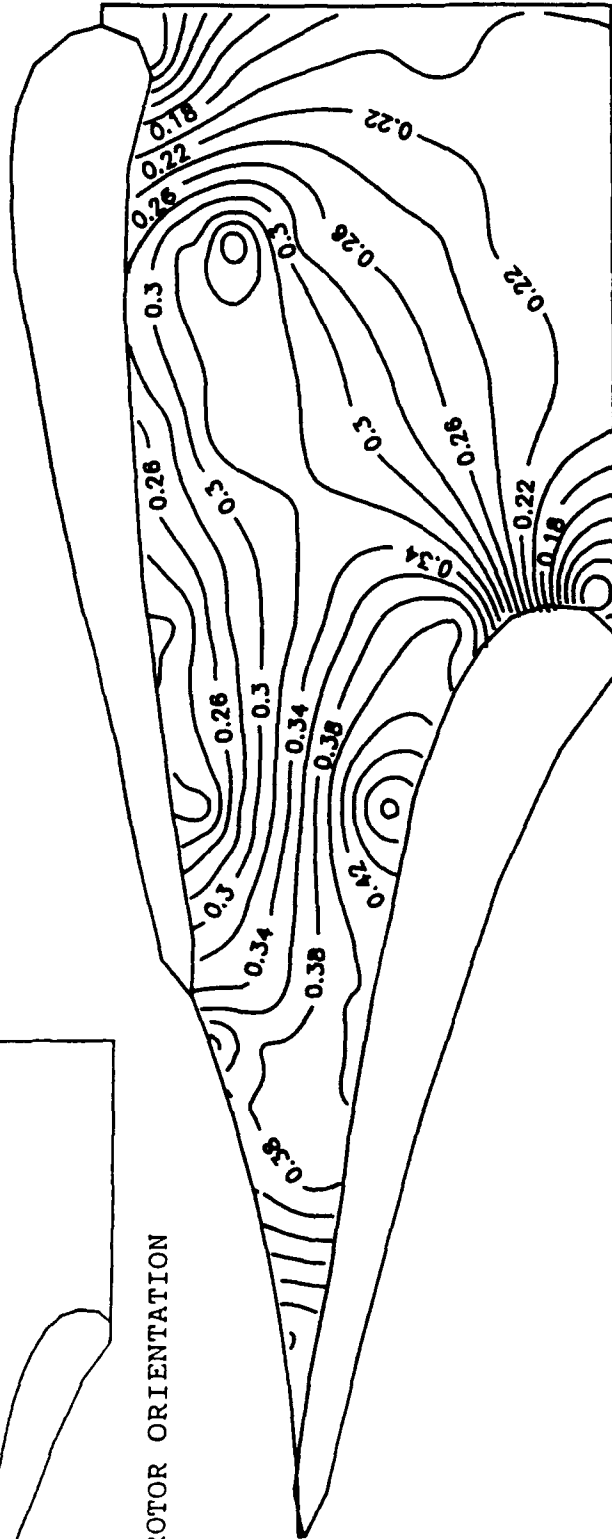


FIG. 7 NORMALIZED RADIAL VELOCITY CONTOURS ON THE
BLADE-TO-BLADE PLANE, $Z=0.50$
(ROTOR BLADE LEAVING THE PASSAGE)

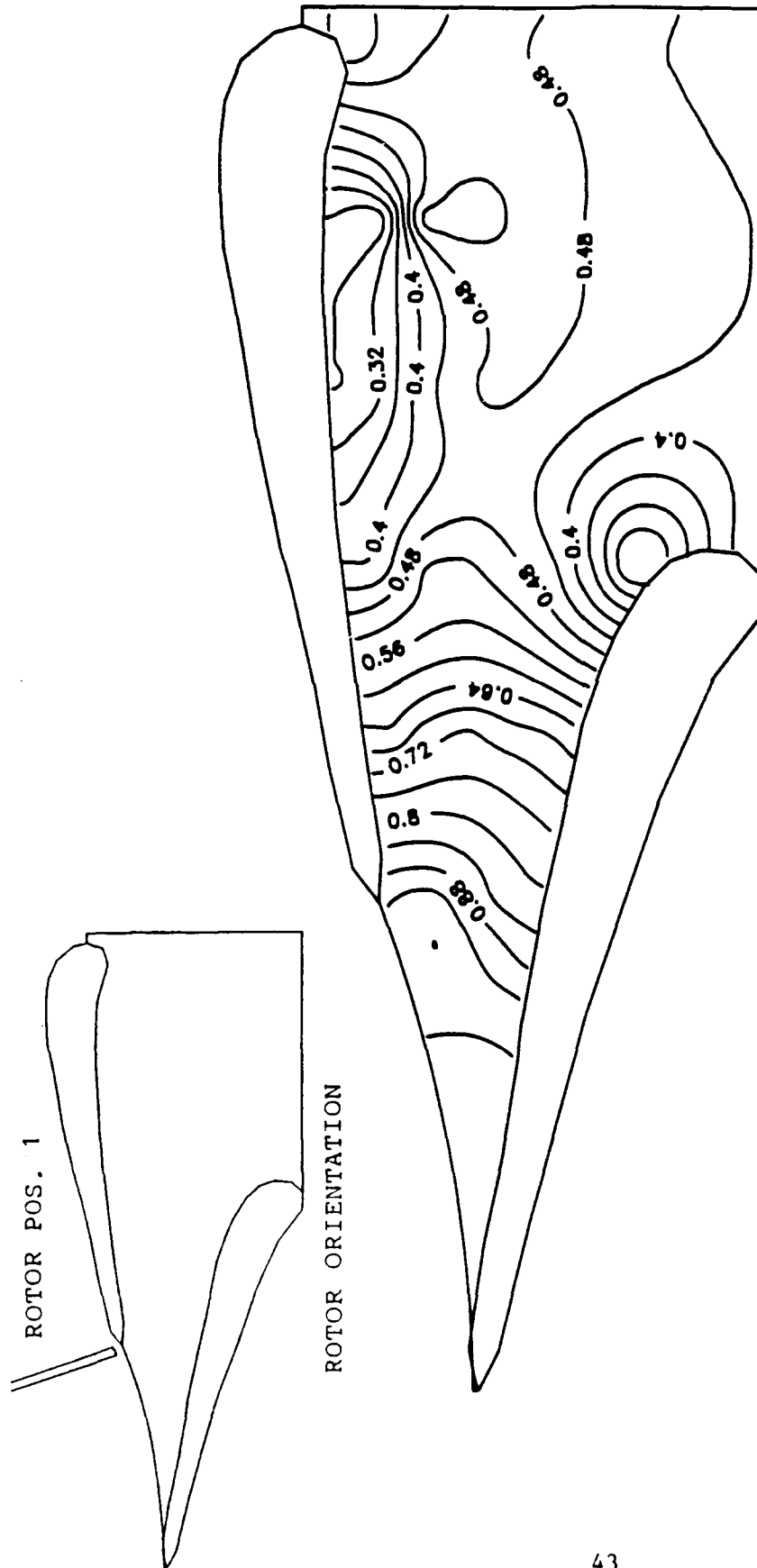


FIG. 8 NORMALIZED TANGENTIAL VELOCITY CONTOURS ON THE BLADE-TO-BLADE PLANE, $Z=0.50$ (ROTOR BLADE ENTERING THE PASSAGE)

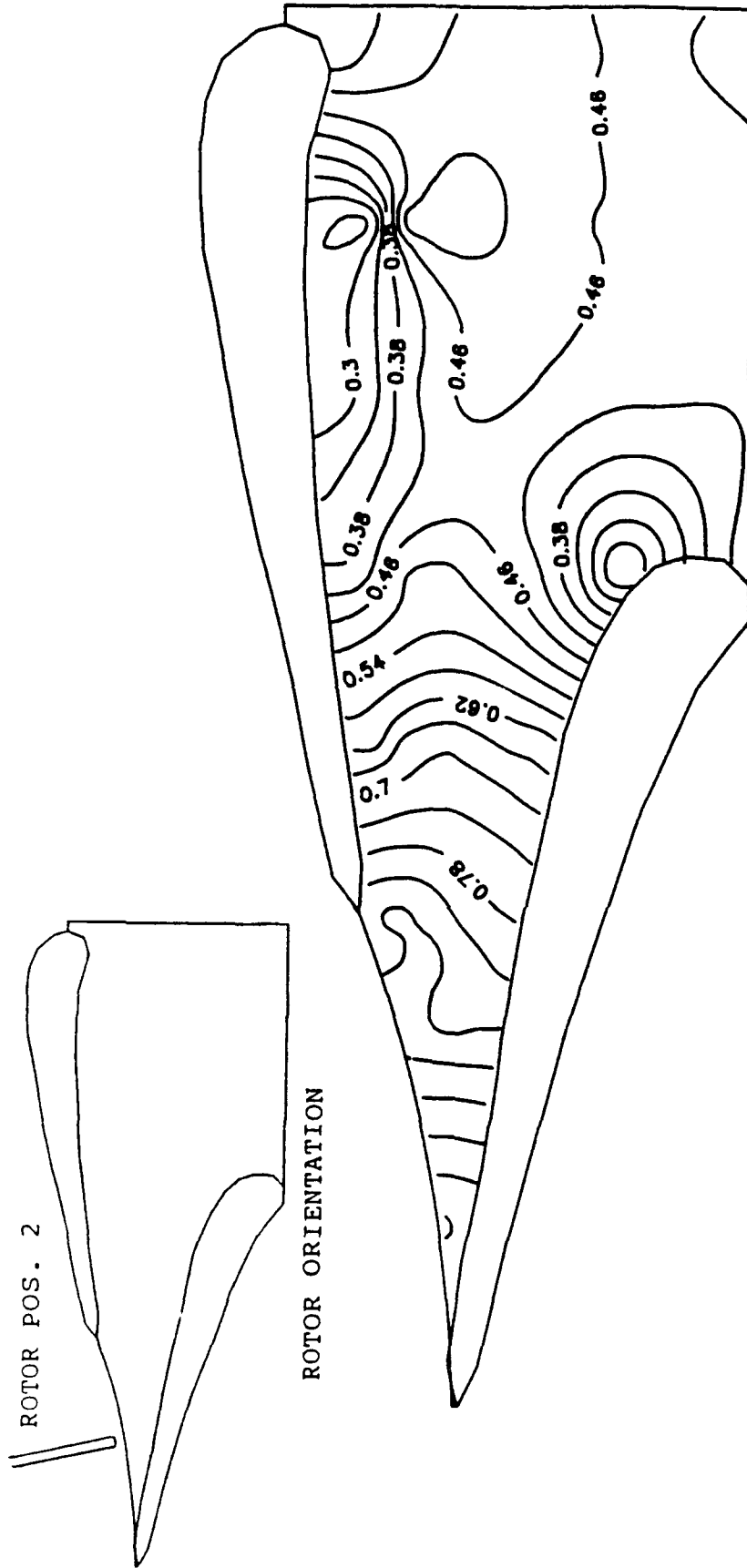


FIG. 9 NORMALIZED TANGENTIAL VELOCITY CONTOURS ON THE BLADE-TO-BLADE PLANE, $Z=0.50$ (ROTOR BLADE AT THE CENTER OF THE PASSAGE)

ROTOR POS. 3

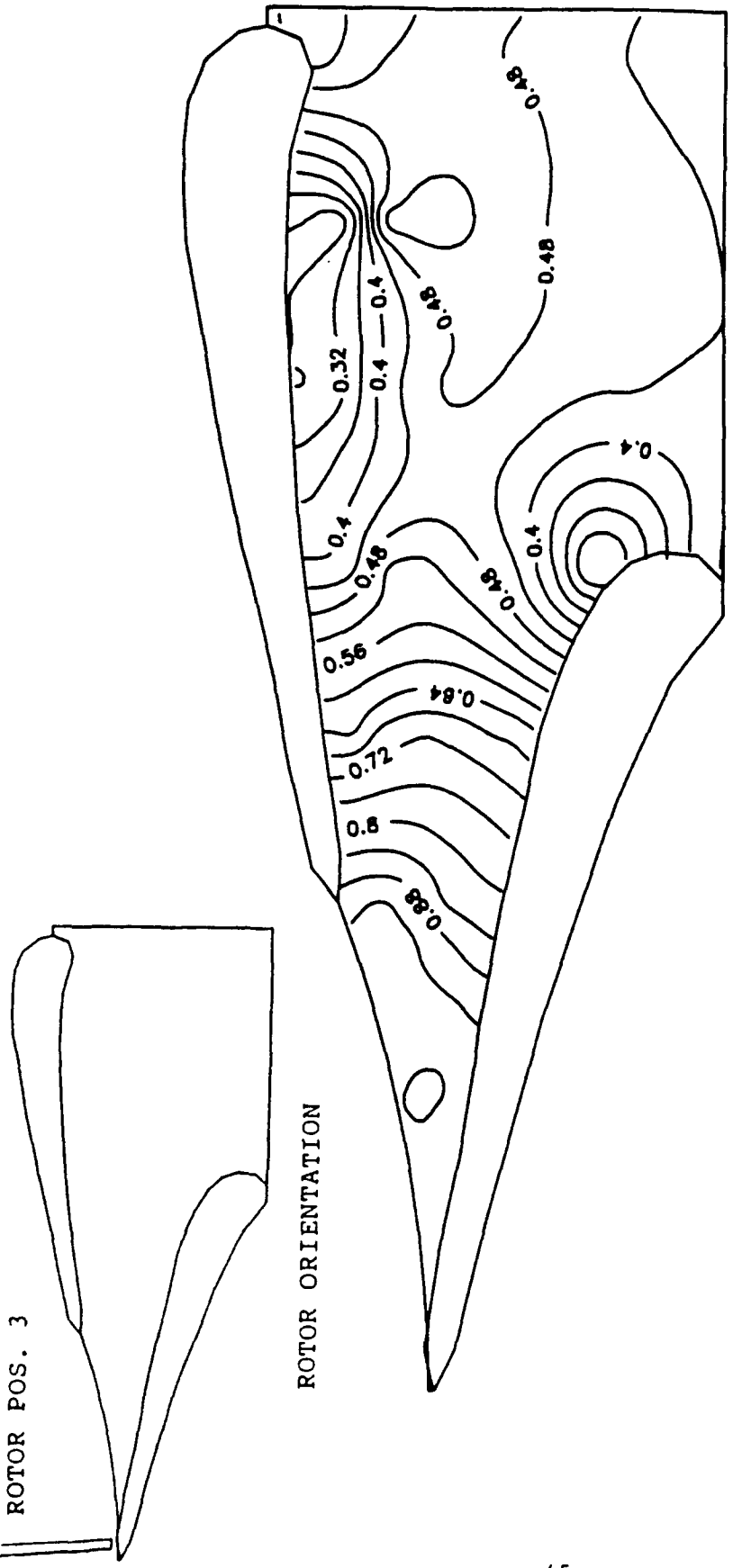


FIG. 10 NORMALIZED TANGENTIAL VELOCITY CONTOURS ON THE BLADE-TO-BLADE PLANE, $Z=0.50$ (ROTOR BLADE LEAVING THE PASSAGE)

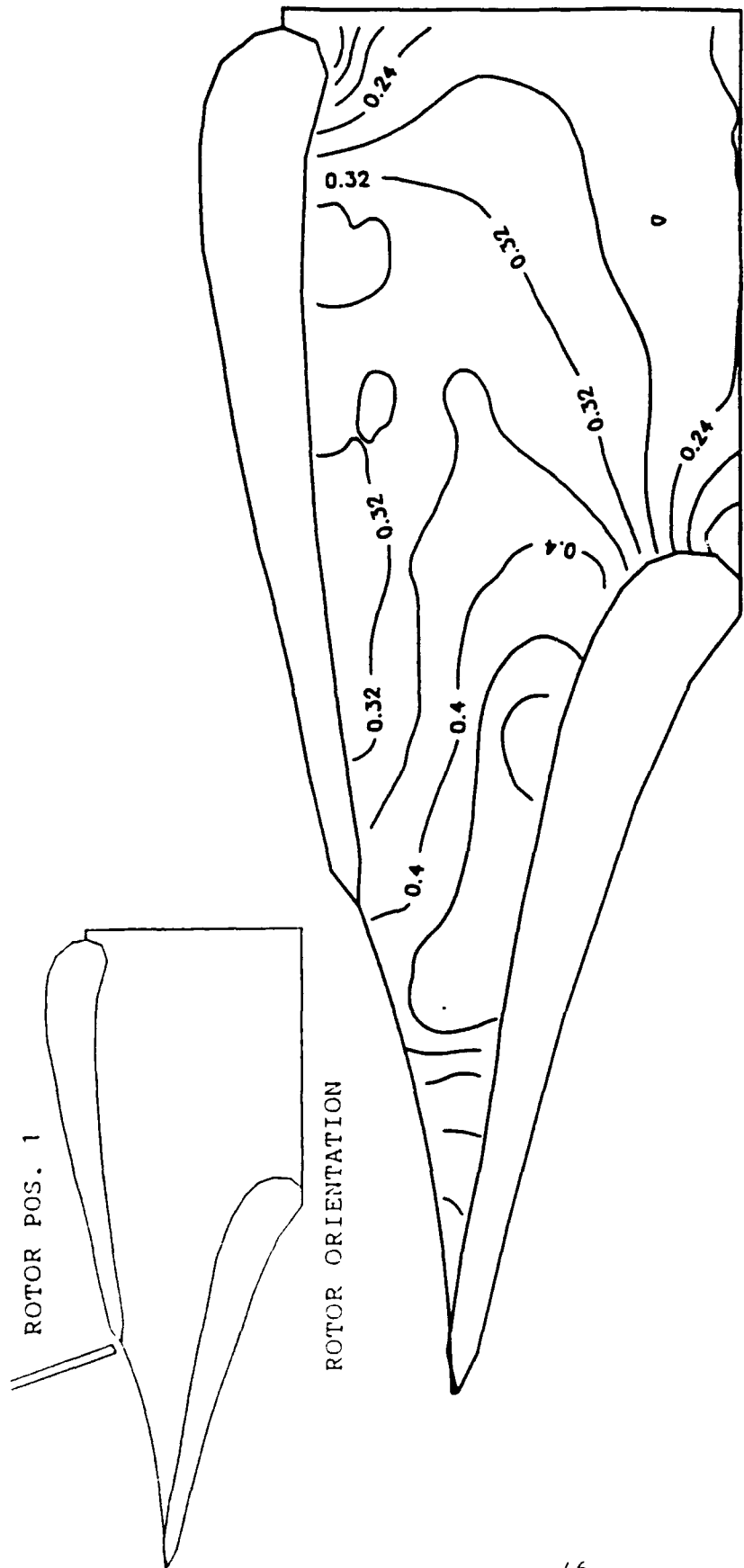


FIG. 11 NORMALIZED RADIAL VELOCITY CONTOURS ON THE
 BLADE-TO-BLADE PLANE, $Z=0.10$
 (ROTOR BLADE ENTERING THE PASSAGE)

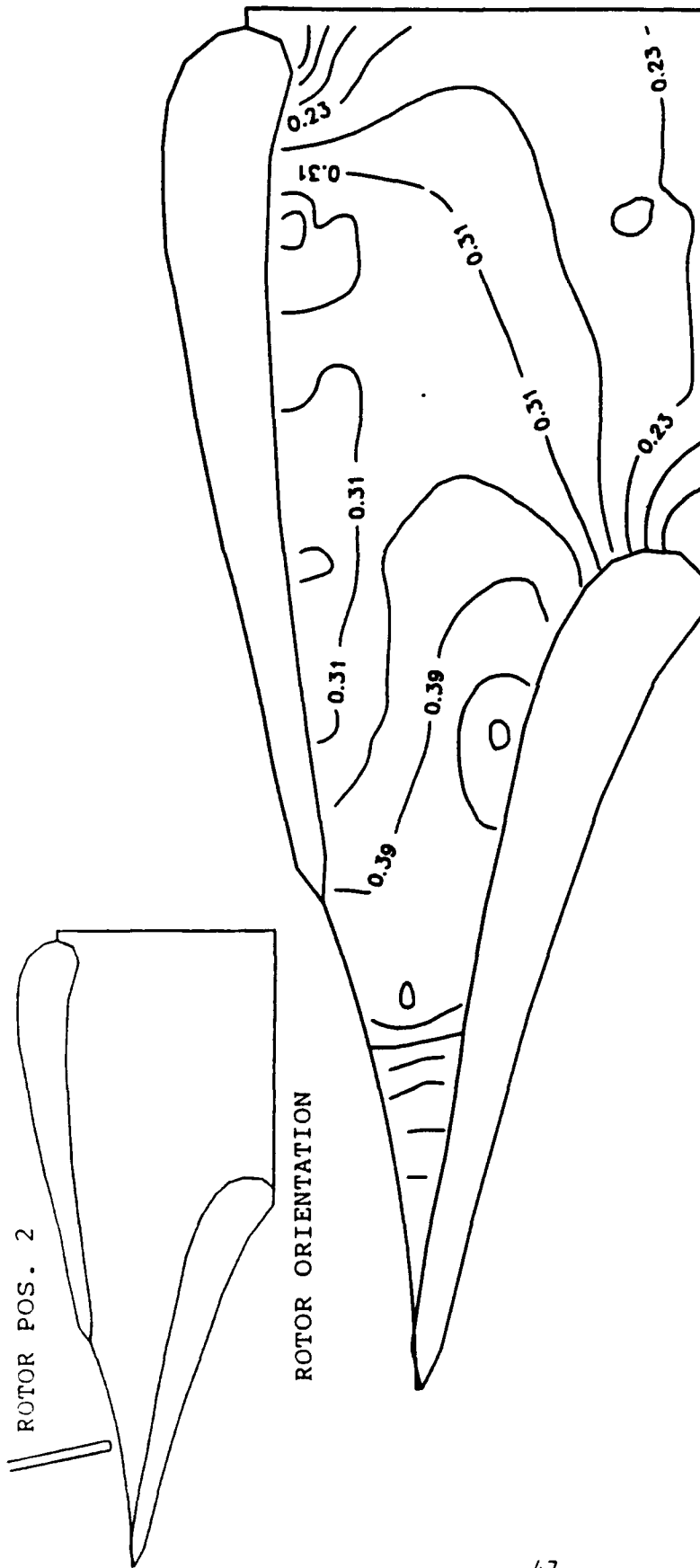


FIG. 12 NORMALIZED RADIAL VELOCITY CONTOURS ON THE
 BLADE-TO-BLADE PLANE, $Z=0.10$
 (ROTOR BLADE AT THE CENTER OF THE PASSAGE)

ROTOR POS. 3

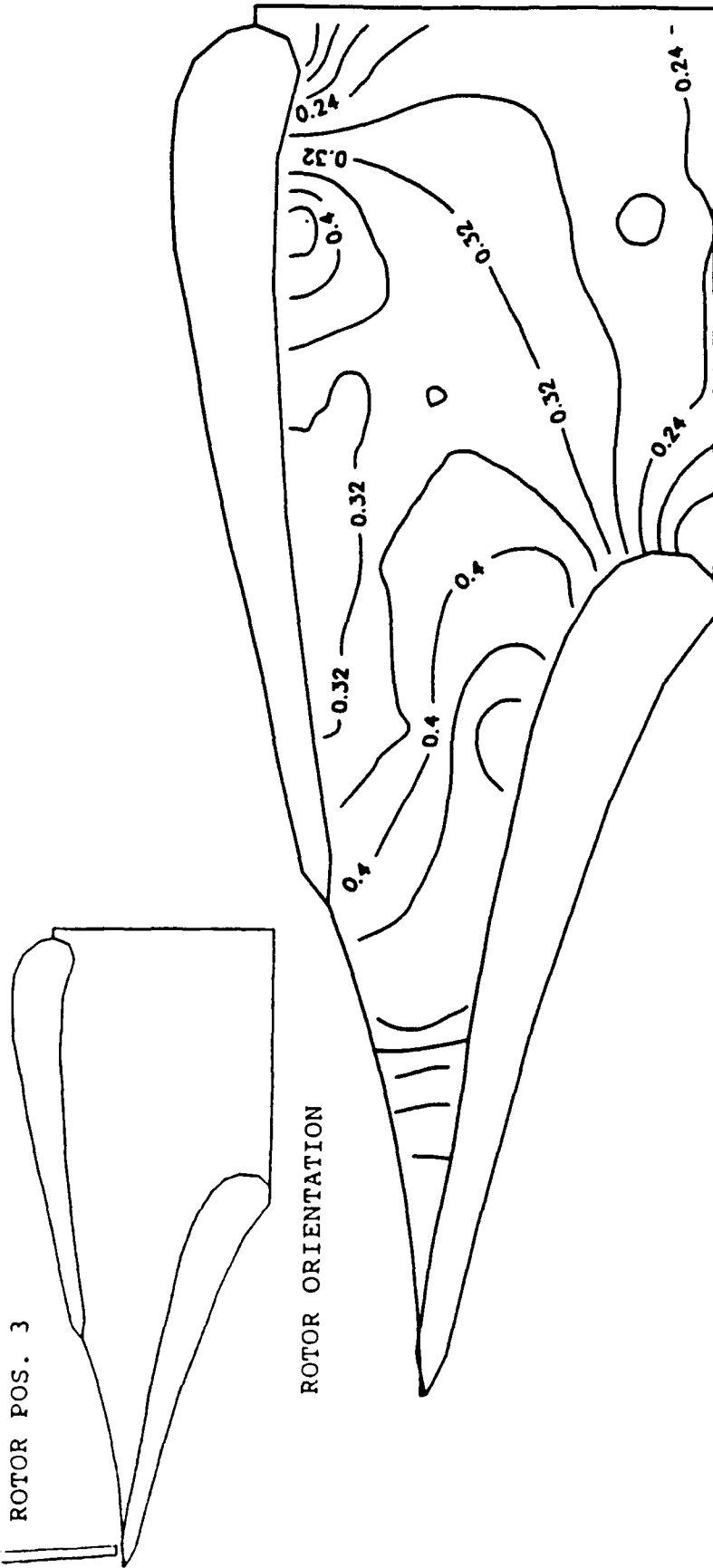


FIG. 13 NORMALIZED RADIAL VELOCITY CONTOURS ON THE
BLADE-TO-BLADE PLANE, $Z=0.10$
(ROTOR BLADE LEAVING THE PASSAGE)

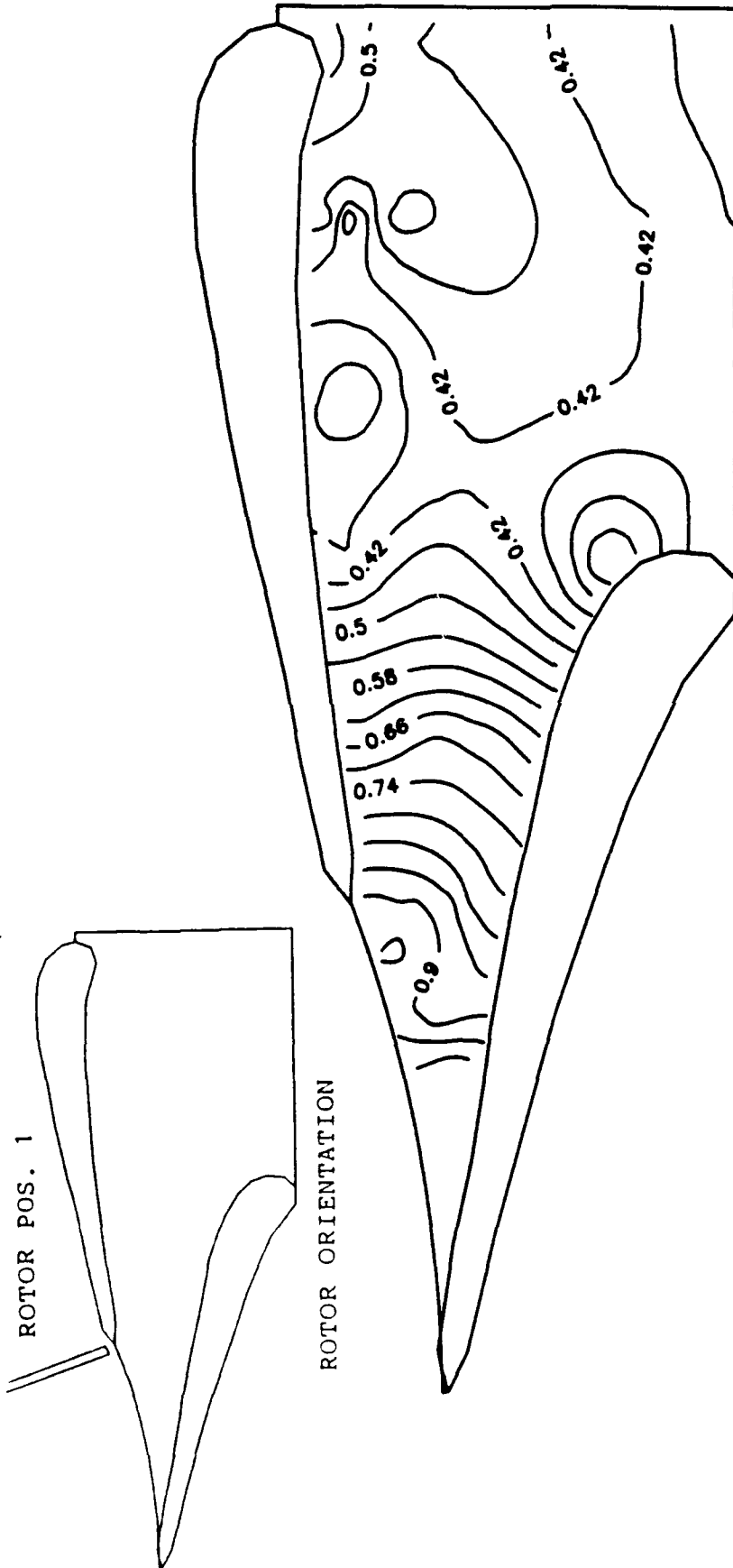


FIG. 14 NORMALIZED TANGENTIAL VELOCITY CONTOURS ON THE BLADE-TO-BLADE PLANE, $z=0.10$ (ROTOR BLADE ENTERING THE PASSAGE)

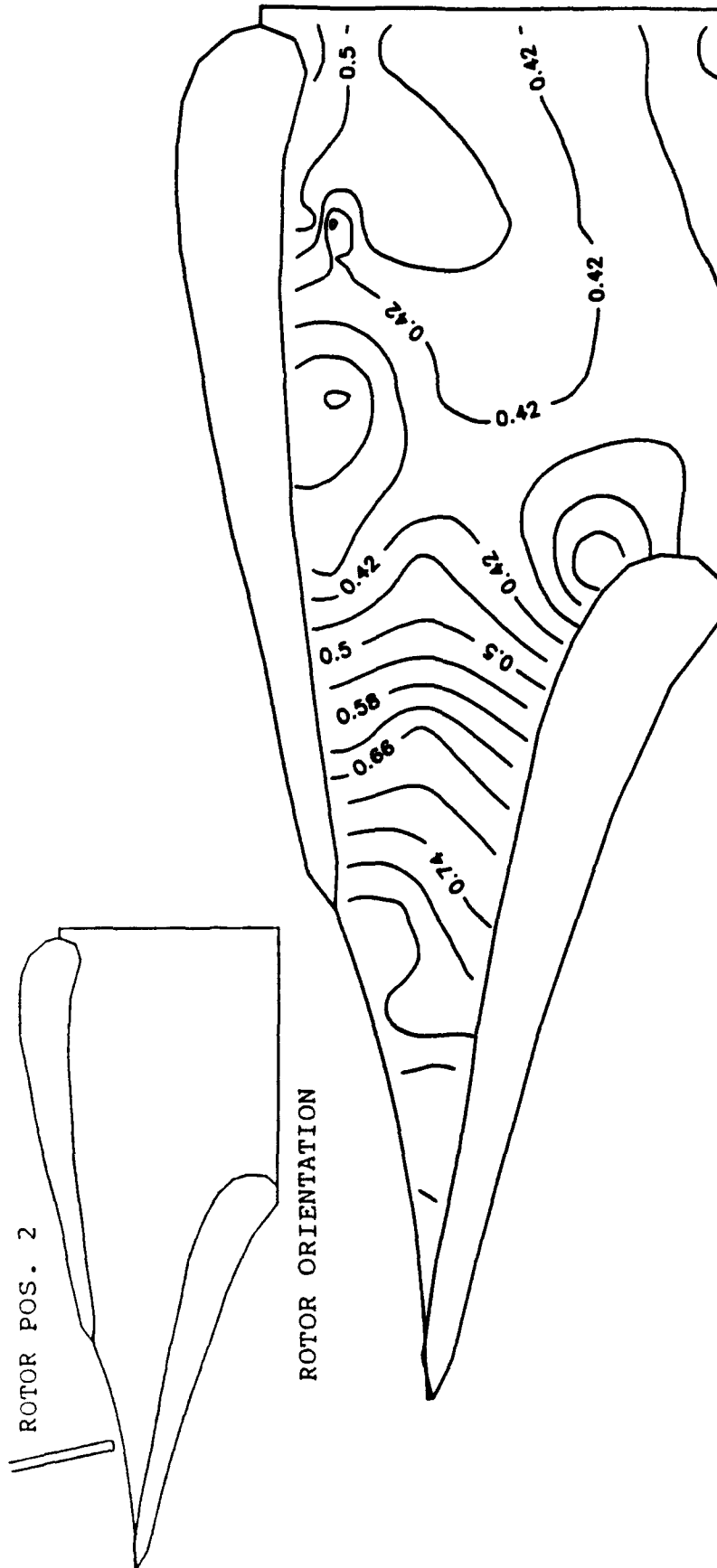


FIG.15 NORMALIZED TANGENTIAL VELOCITY CONTOURS ON THE BLADE-TO-BLADE PLANE, $Z=0.10$ (ROTOR BLADE AT THE CENTER OF THE PASSAGE)

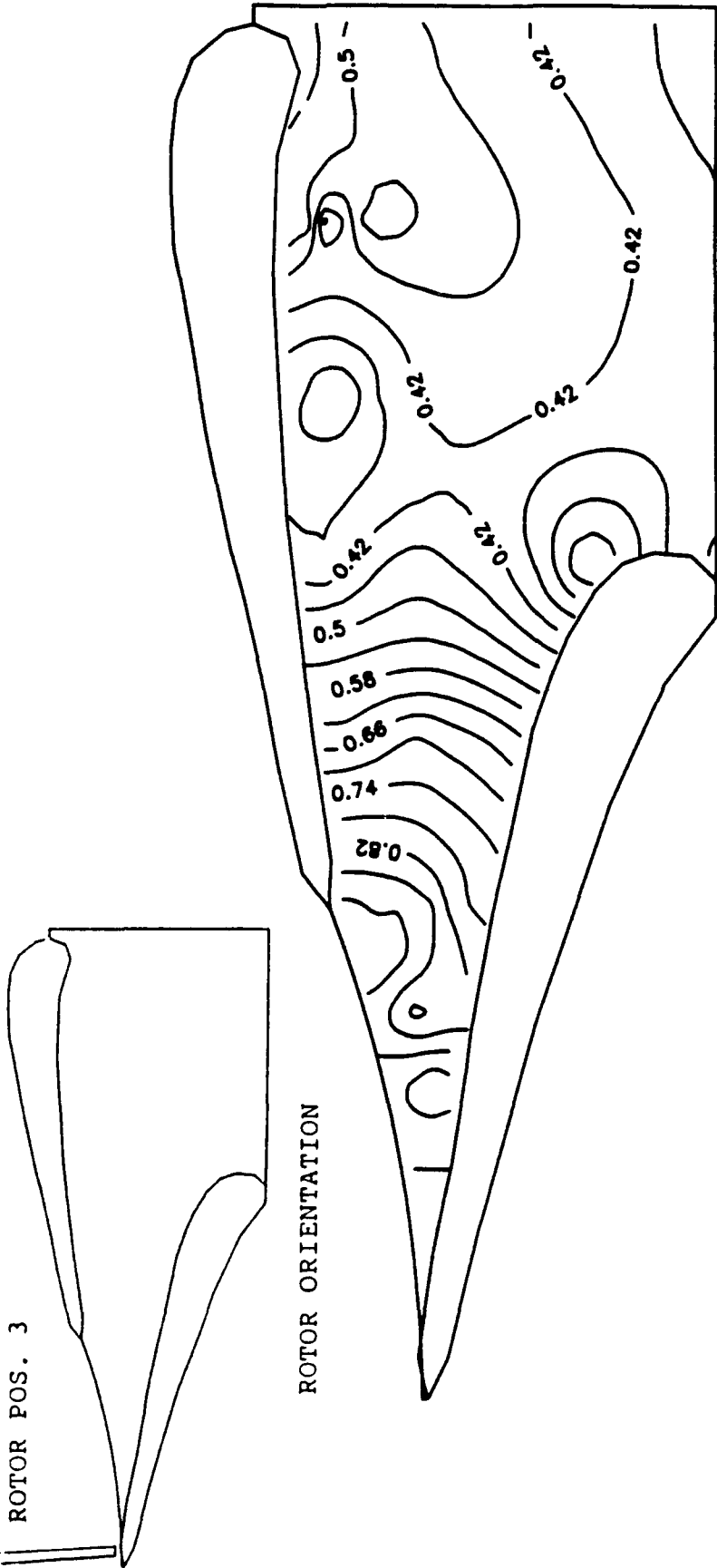


FIG. 16 NORMALIZED TANGENTIAL VELOCITY CONTOURS ON THE BLADE-TO-BLADE PLANE, $z=0.10$ (ROTOR BLADE LEAVING THE PASSAGE)

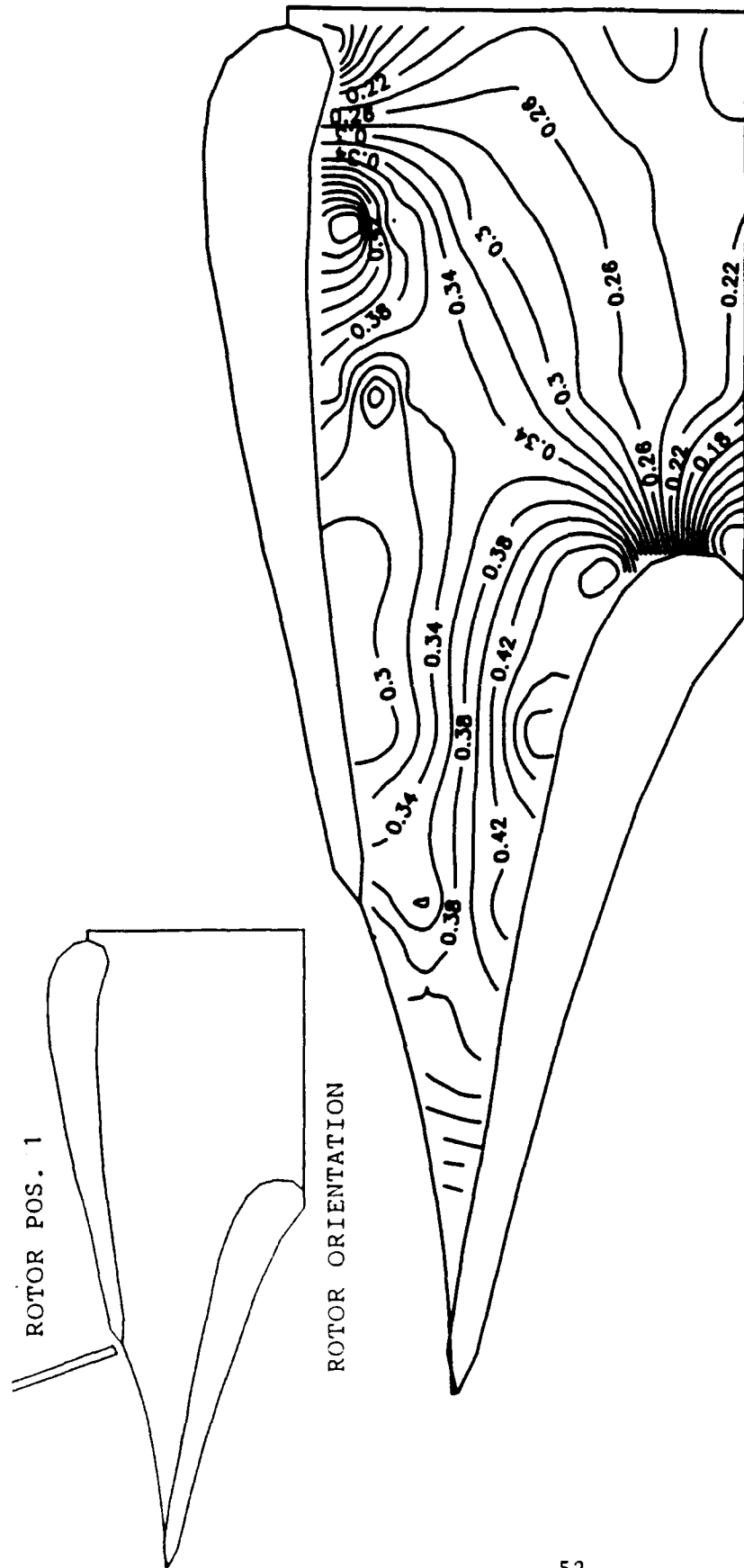


FIG. 17 NORMALIZED RADIAL VELOCITY CONTOURS ON THE
 BLADE-TO-BLADE PLANE, $Z=0.25$
 (ROTOR BLADE ENTERING THE PASSAGE)

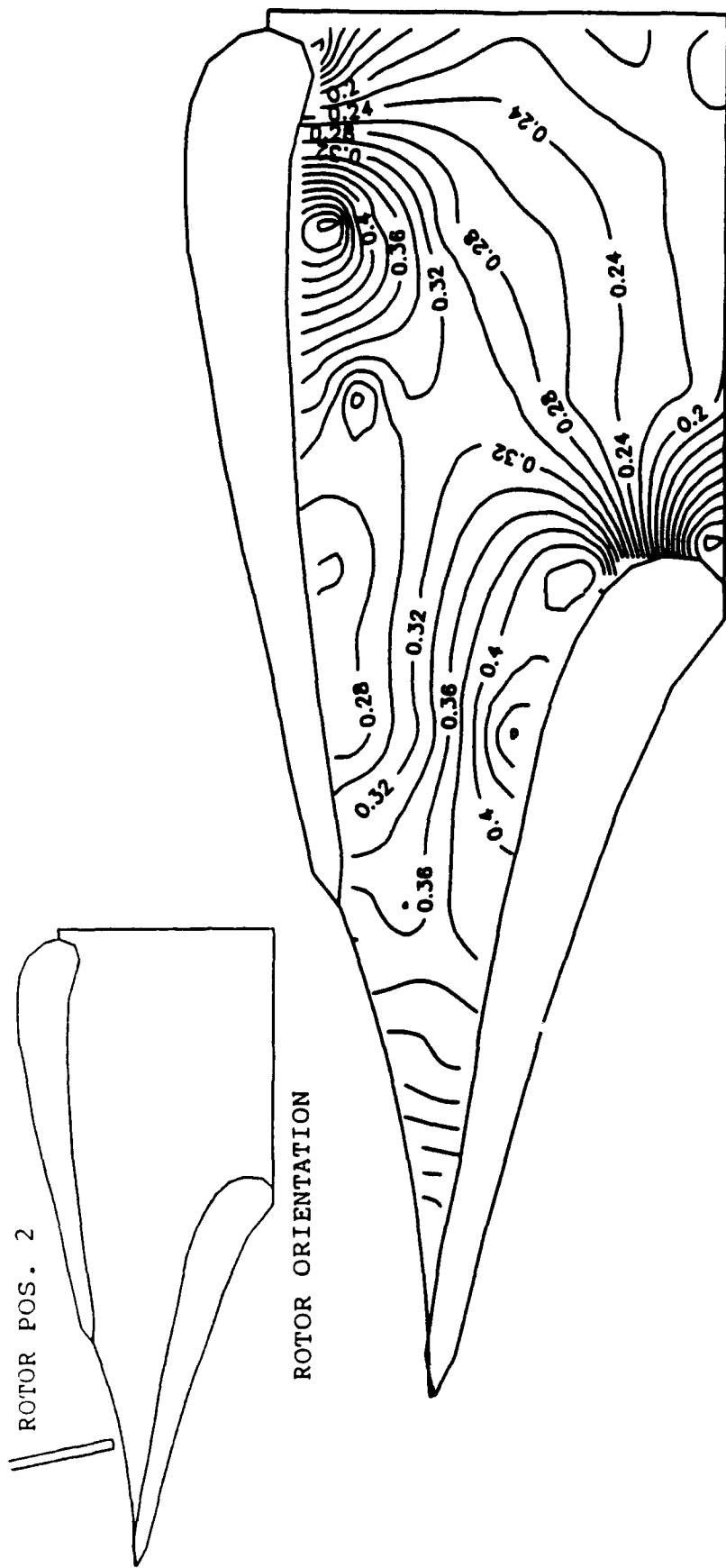


FIG. 18 NORMALIZED RADIAL VELOCITY CONTOURS ON THE
 BLADE-TO-BLADE PLANE, $Z=0.25$
 (ROTOR BLADE AT THE CENTER OF THE PASSAGE)

ROTOR POS. 3

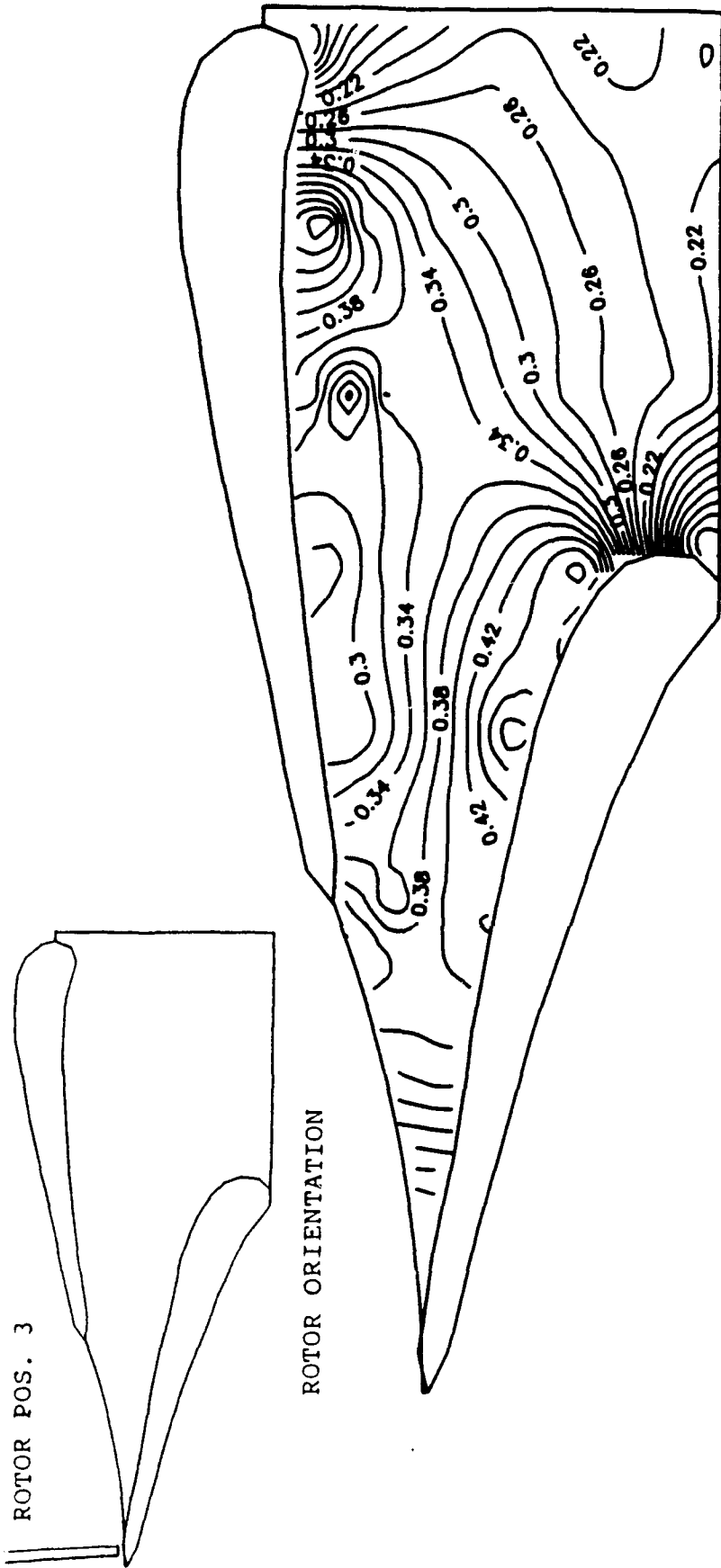


FIG. 19 NORMALIZED RADIAL VELOCITY CONTOURS ON THE
BLADE-TO-BLADE PLANE, $Z=0.25$
(ROTOR BLADE LEAVING THE PASSAGE)

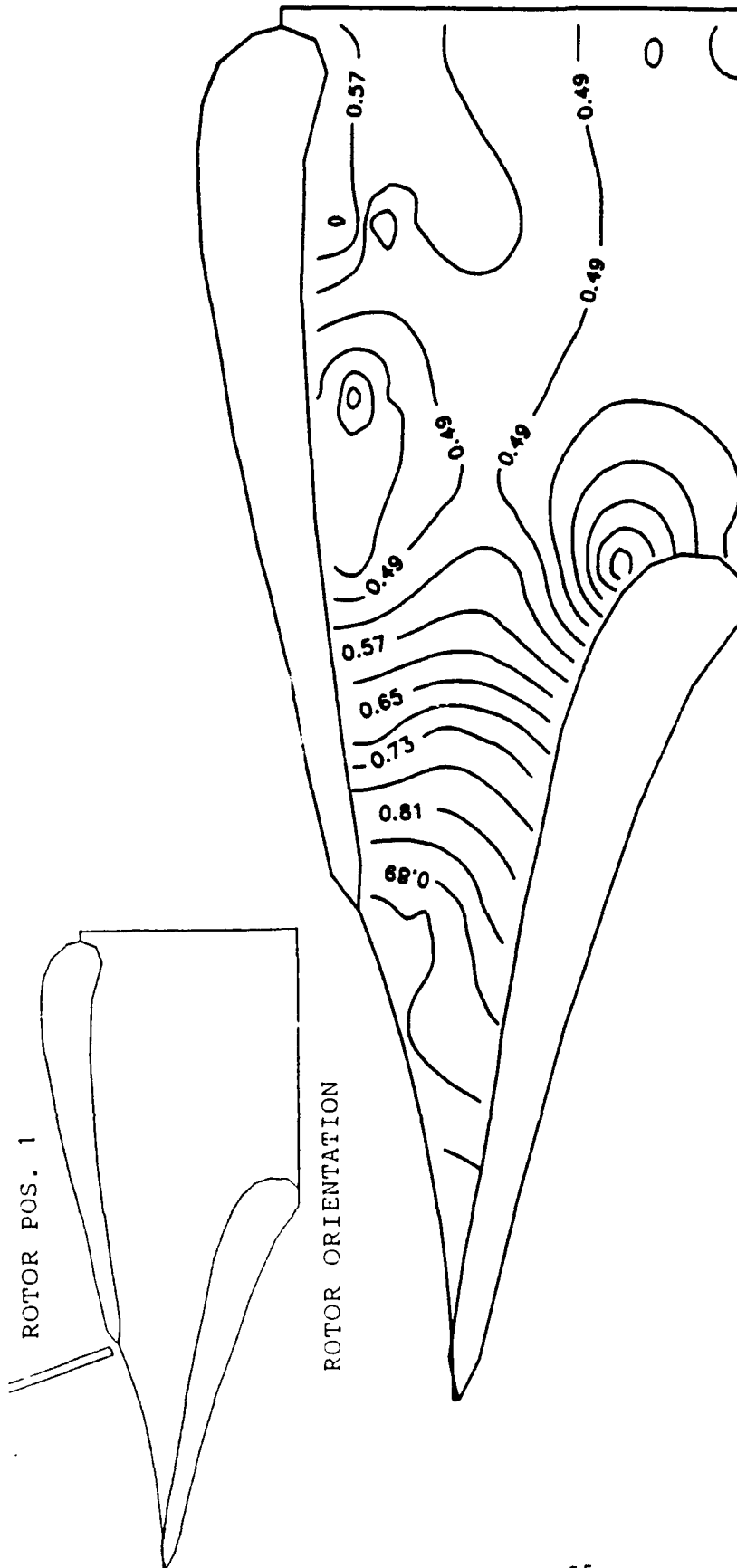


FIG. 20 NORMALIZED TANGENTIAL VELOCITY CONTOURS ON THE BLADE-TO-BLADE PLANE, $Z=0.25$ (ROTOR BLADE ENTERING THE PASSAGE)

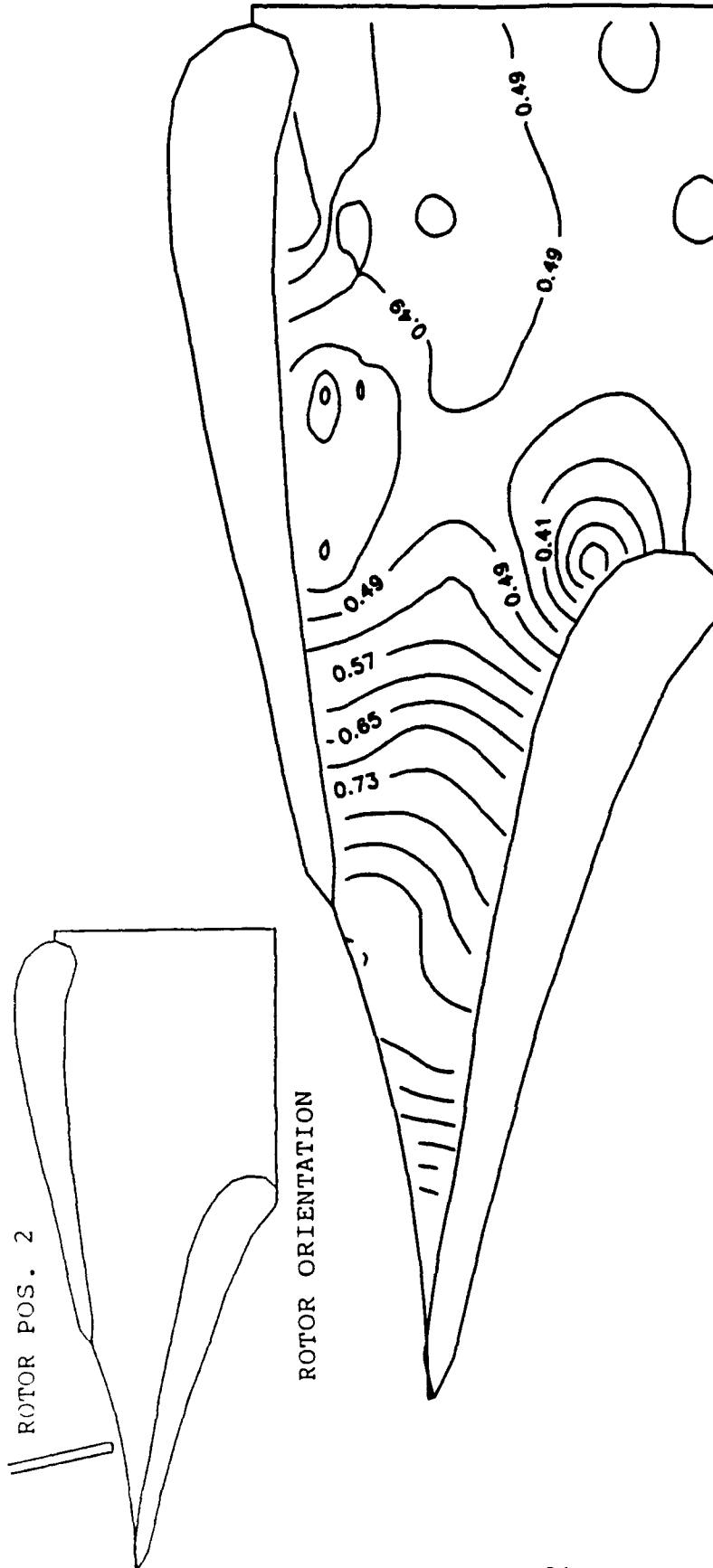


FIG. 21 NORMALIZED TANGENTIAL VELOCITY CONTOURS ON THE BLADE-TO-BLADE PLANE, $z=0.25$ (ROTOR BLADE AT THE CENTER OF THE PASSAGE)

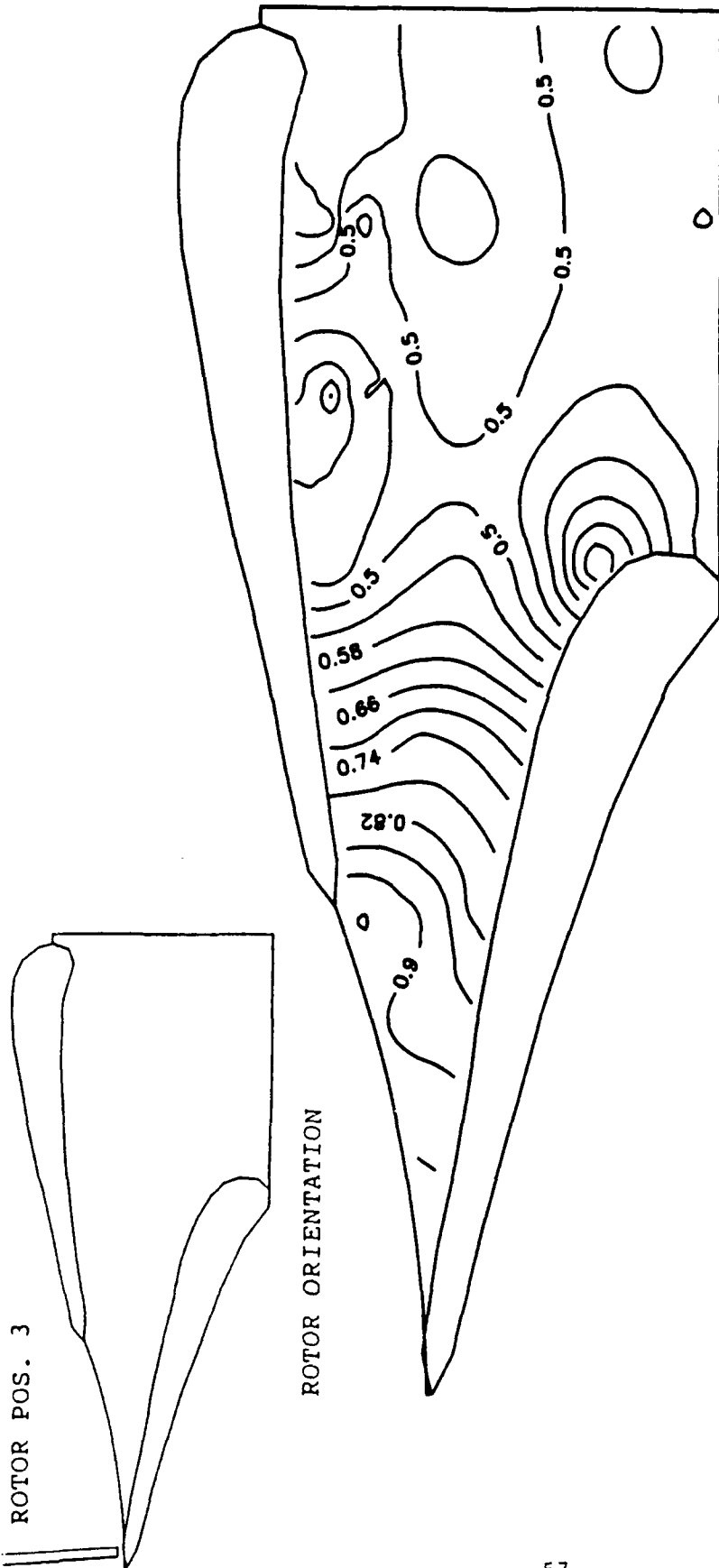


FIG. 22 NORMALIZED TANGENTIAL VELOCITY CONTOURS ON THE BLADE-TO-BLADE PLANE, $Z=0.25$ (ROTOR BLADE LEAVING THE PASSAGE)

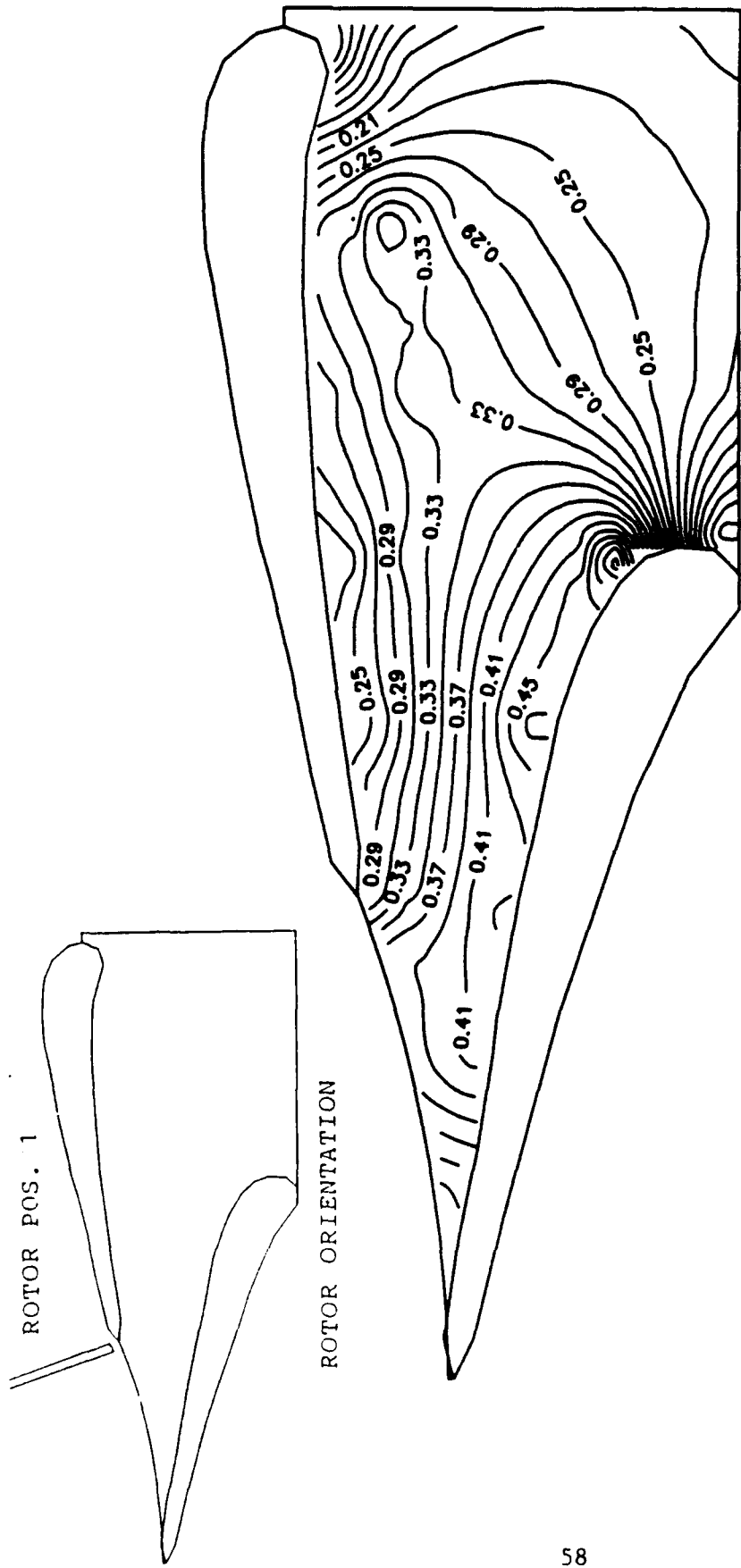


FIG. 23 NORMALIZED RADIAL VELOCITY CONTOURS ON THE
 BLADE-TO-BLADE PLANE, $z=0.70$
 (ROTOR BLADE ENTERING THE PASSAGE)

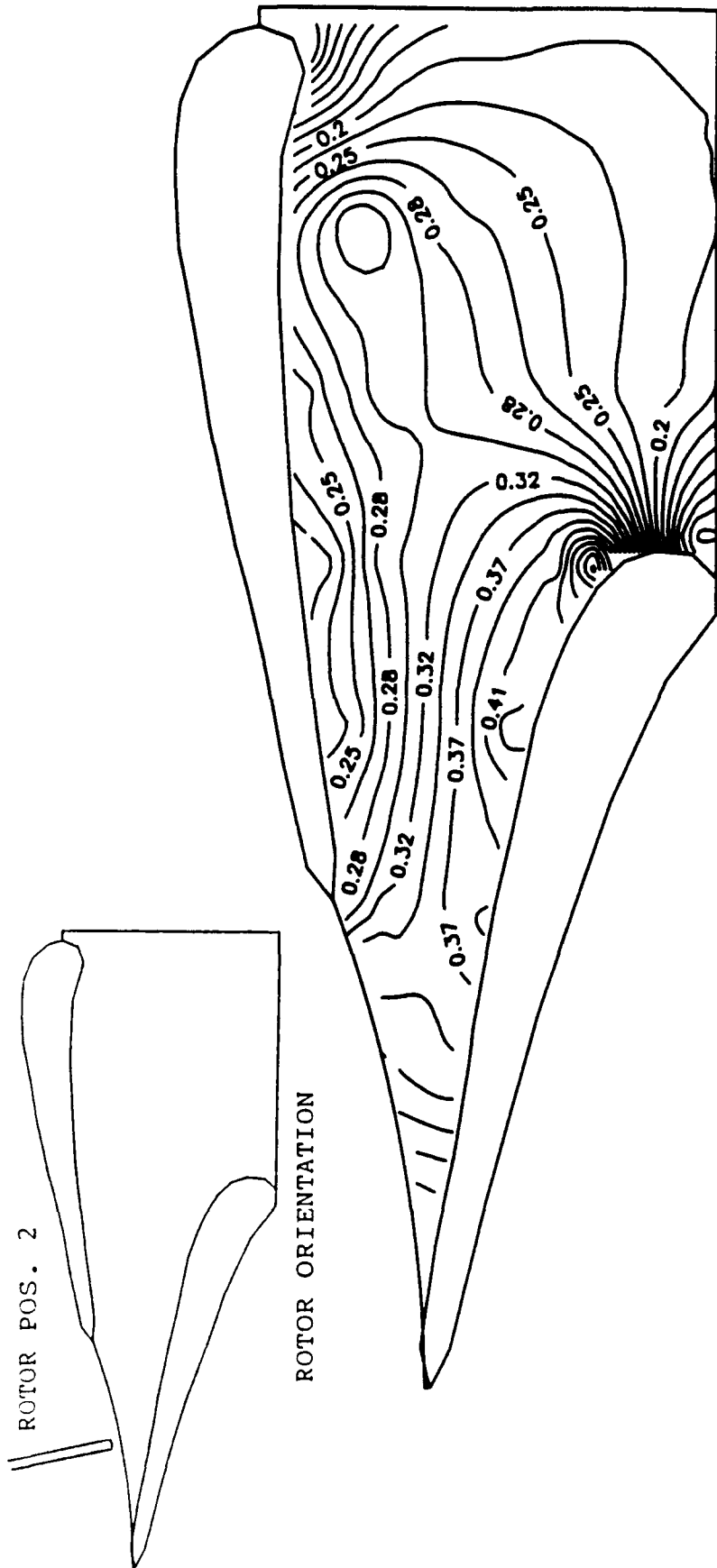
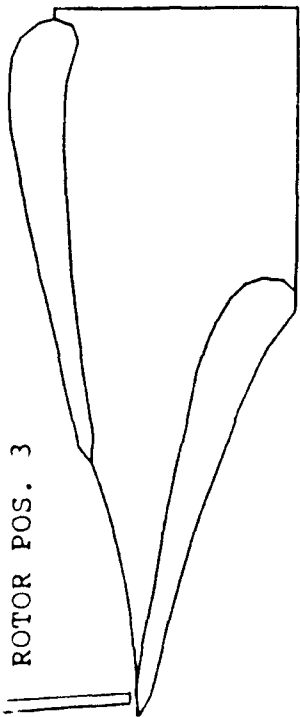


FIG. 24 NORMALIZED RADIAL VELOCITY CONTOURS ON THE
 BLADE-TO-BLADE PLANE, $z=0.70$
 (ROTOR BLADE AT THE CENTER OF THE PASSAGE)

ROTOR POS. 3



ROTOR ORIENTATION

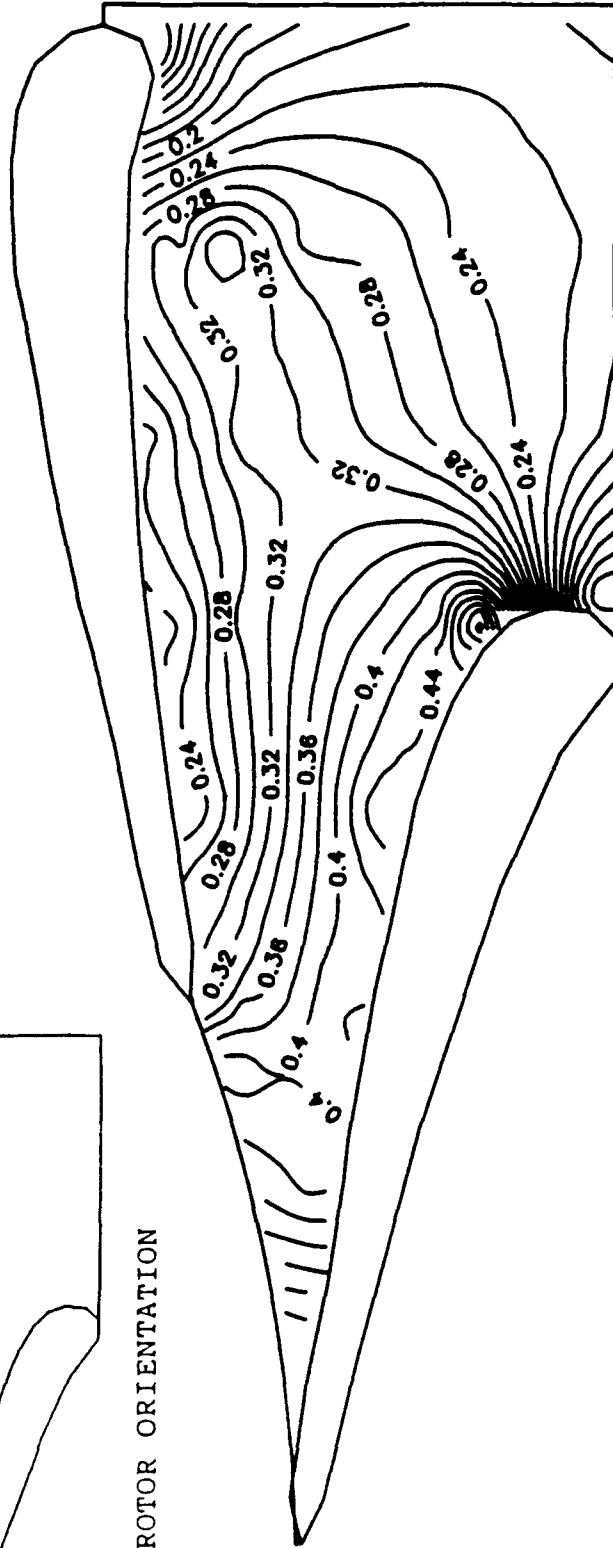


FIG. 25 NORMALIZED RADIAL VELOCITY CONTOURS ON THE
BLADE-TO-BLADE PLANE, $Z=0.70$
(ROTOR BLADE LEAVING THE PASSAGE)

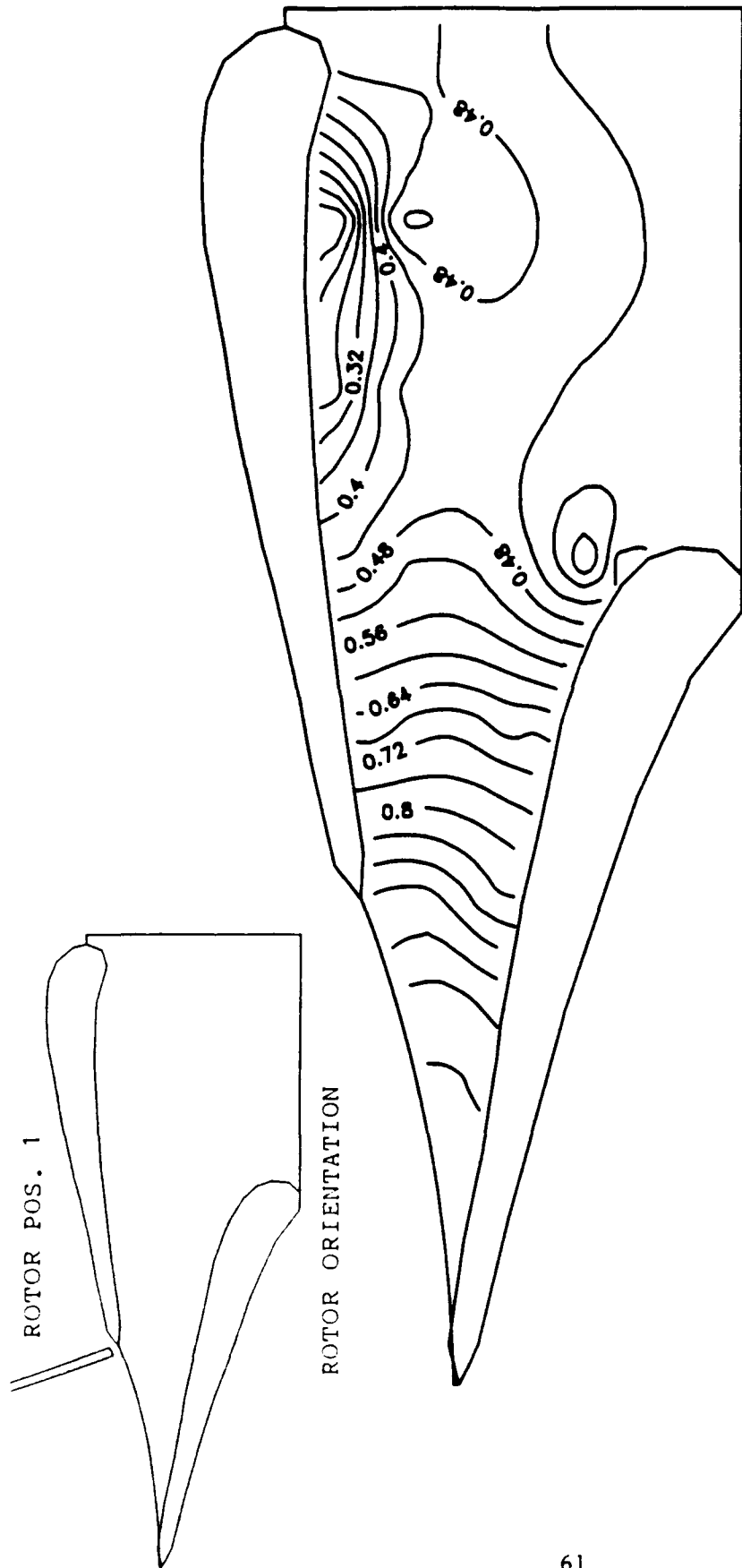


FIG. 26 NORMALIZED TANGENTIAL VELOCITY CONTOURS ON THE BLADE-TO-BLADE PLANE, $z=0.70$ (ROTOR BLADE ENTERING THE PASSAGE)

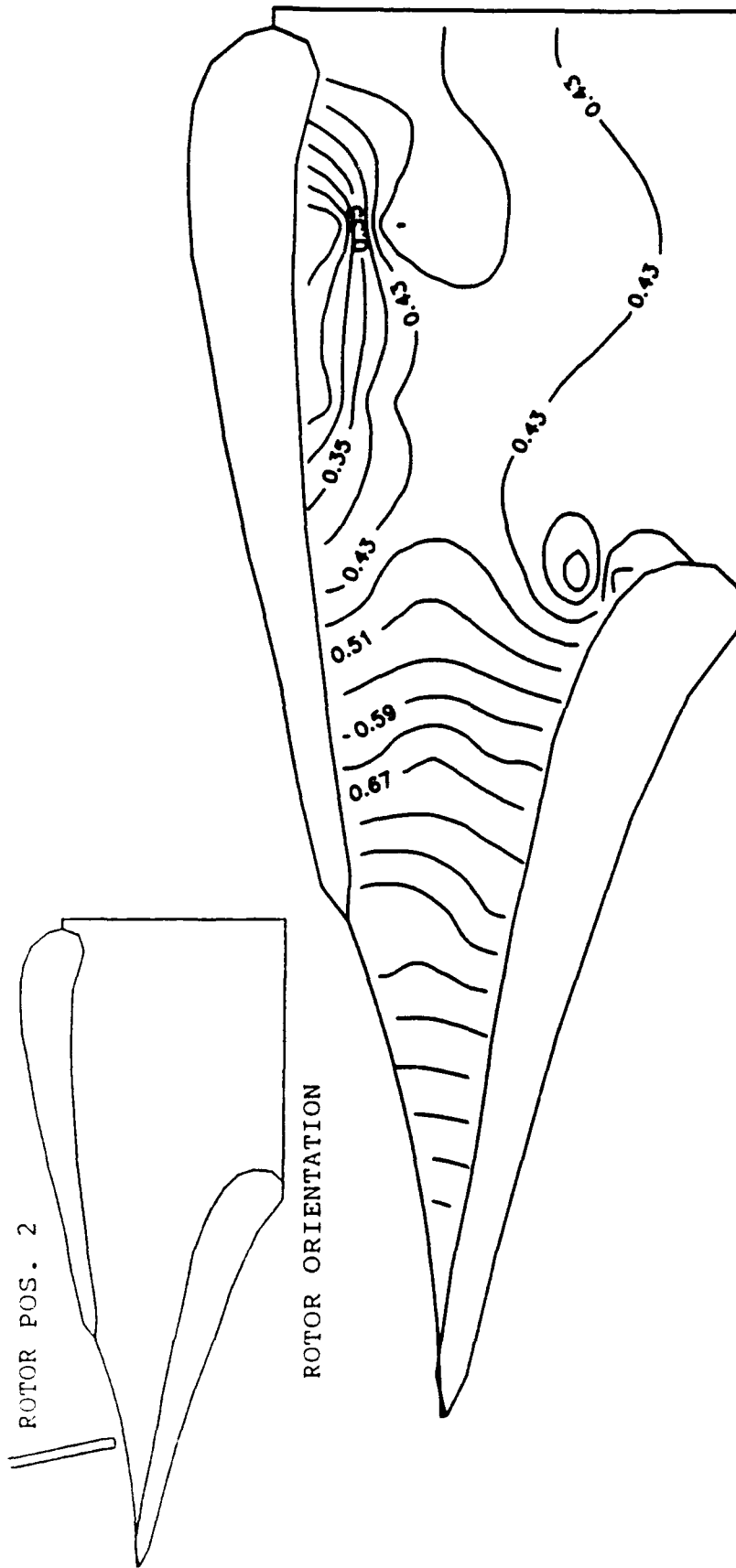


FIG. 27 NORMALIZED TANGENTIAL VELOCITY CONTOURS ON THE BLADE-TO-BLADE PLANE, $Z=0.70$ (ROTOR BLADE AT THE CENTER OF THE PASSAGE)

ROTOR POS. 3

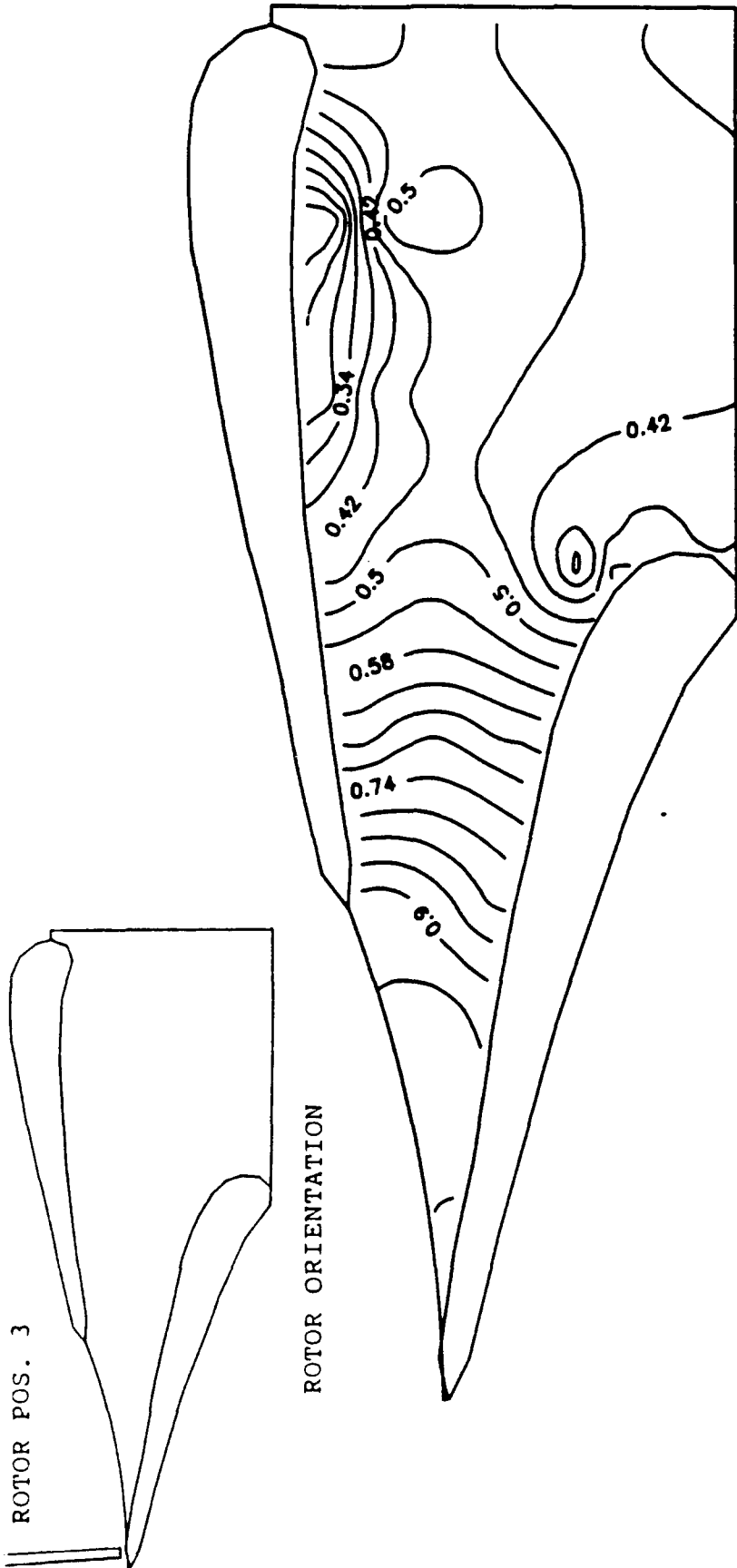


FIG. 28 NORMALIZED TANGENTIAL VELOCITY CONTOURS ON THE BLADE-TO-BLADE PLANE, $Z=0.70$ (ROTOR BLADE LEAVING THE PASSAGE)

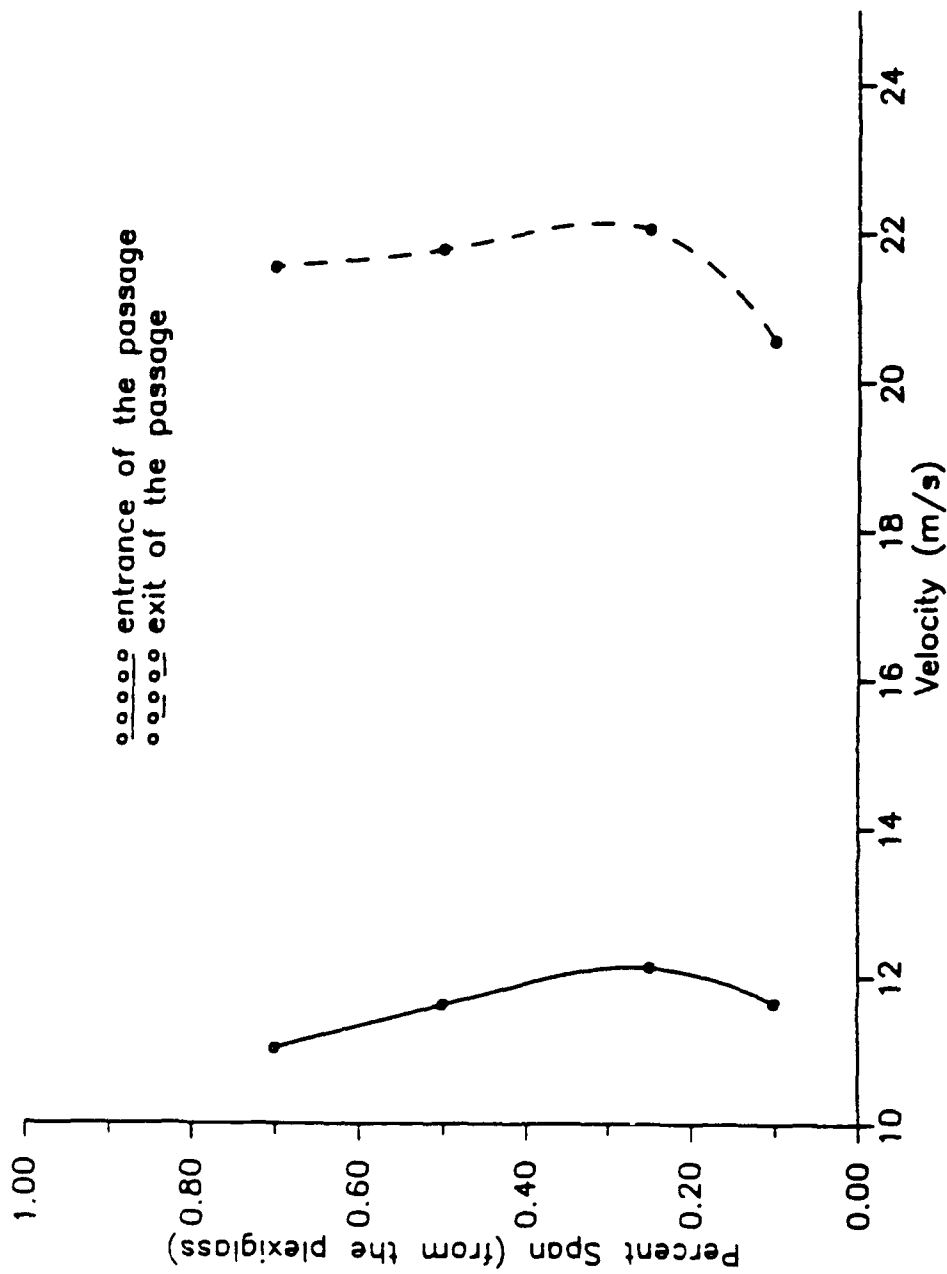


FIG. 29 PITCH AVERAGED MEAN VELOCITY PROFILES

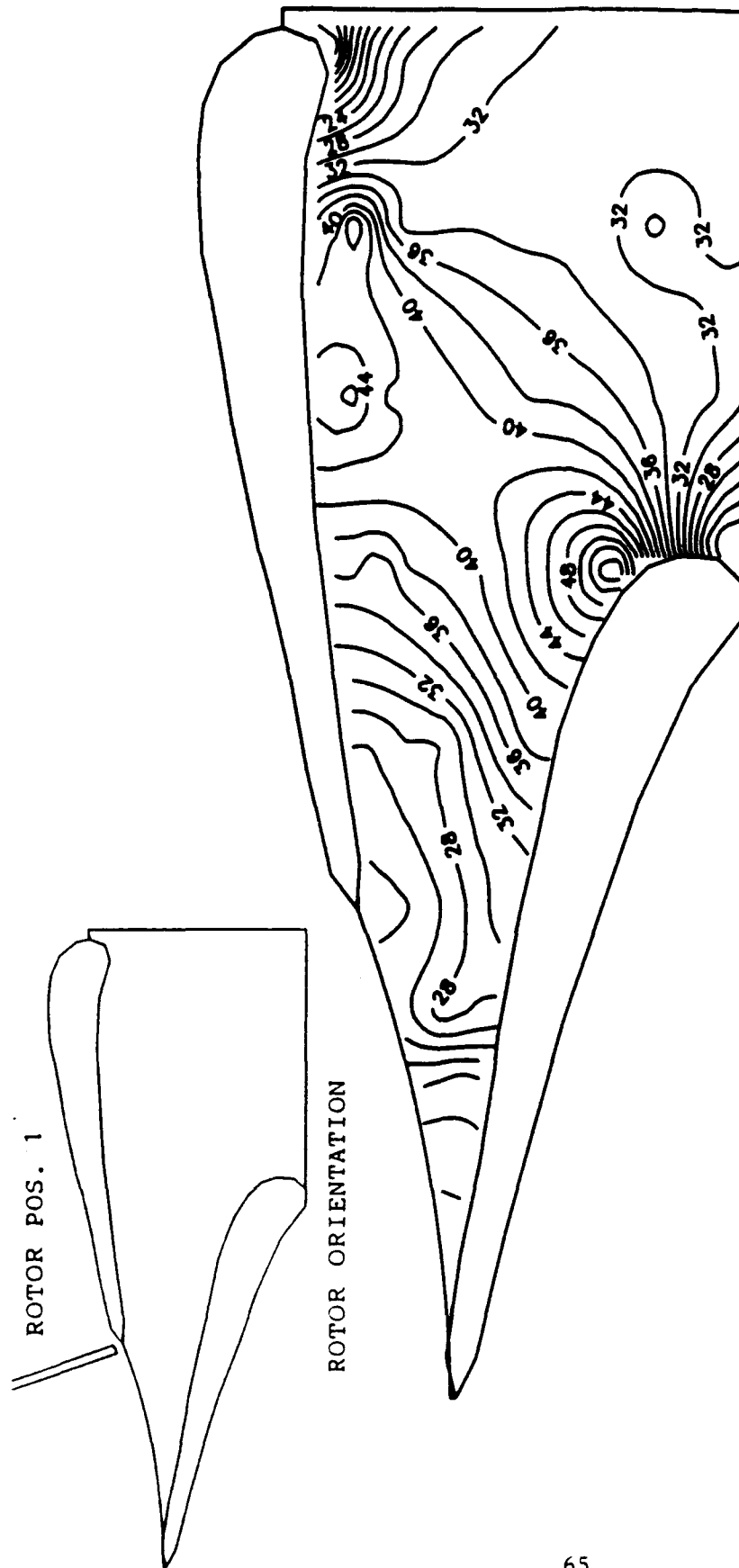


FIG. 30 β -FLOW ANGLE CONTOURS ON THE BLADE-TO-BLADE PLANE, $Z=0.10$
 (ROTOR BLADE ENTERING THE PASSAGE)

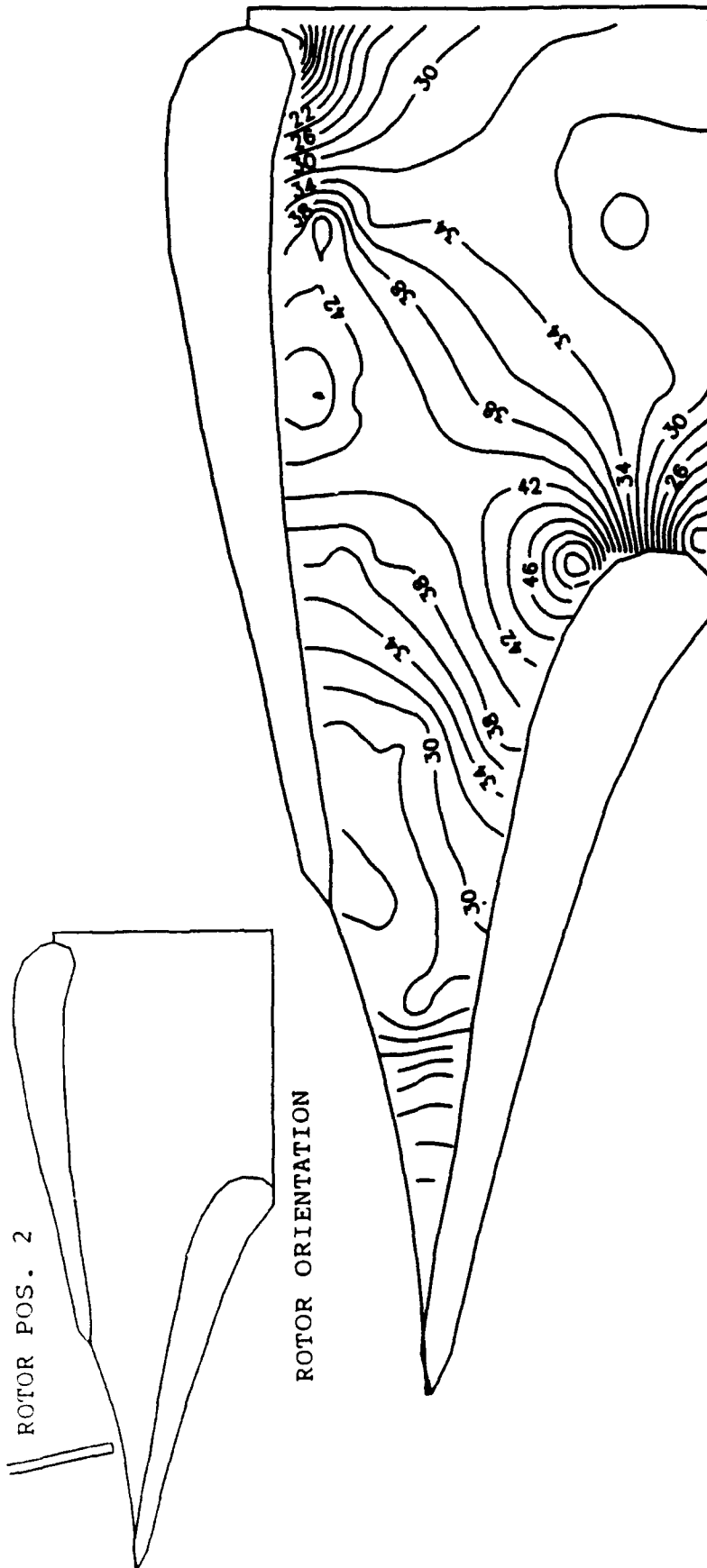


FIG. 31 β -FLOW ANGLE CONTOURS ON THE BLADE-TO-BLADE PLANE, $Z=0.10$ (ROTOR BLADE AT THE CENTER OF THE PASSAGE)

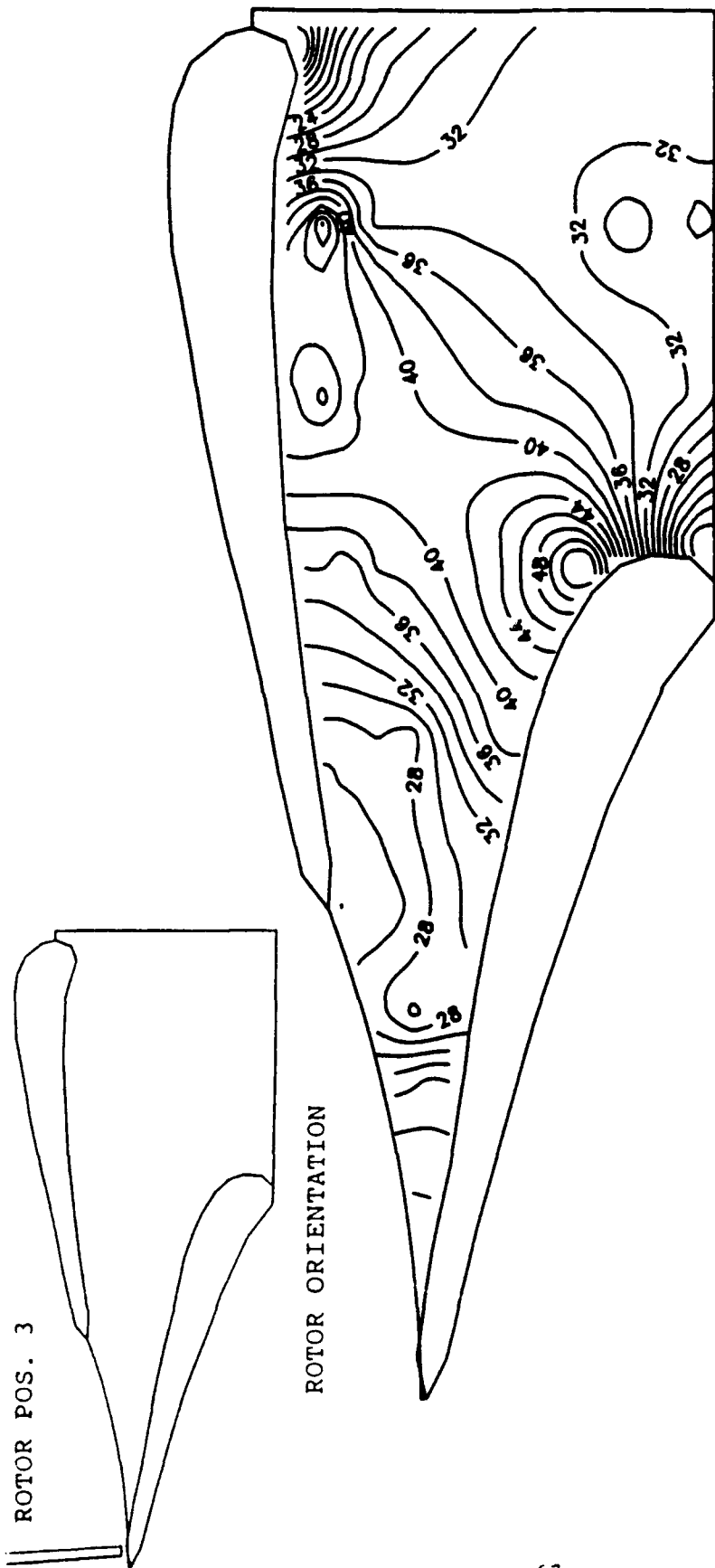


FIG. 32 β -FLOW ANGLE CONTOURS ON THE BLADE-TO-BLADE PLANE, $Z=0.10$ (ROTOR BLADE LEAVING THE PASSAGE)

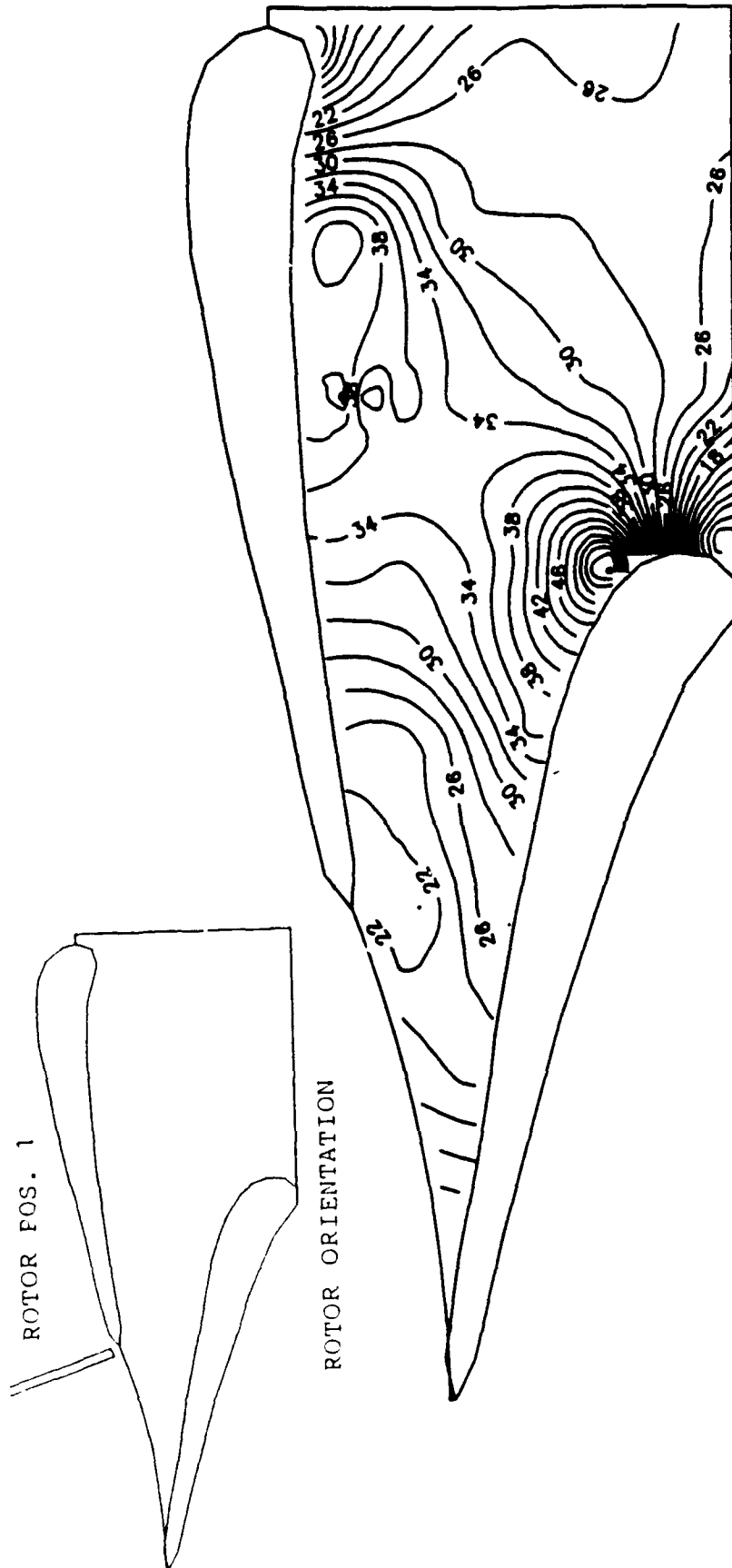


FIG. 33 β -FLOW ANGLE CONTOURS ON THE BLADE-TO-BLADE PLANE, $Z=0.25$
 (ROTOR BLADE ENTERING THE PASSAGE)

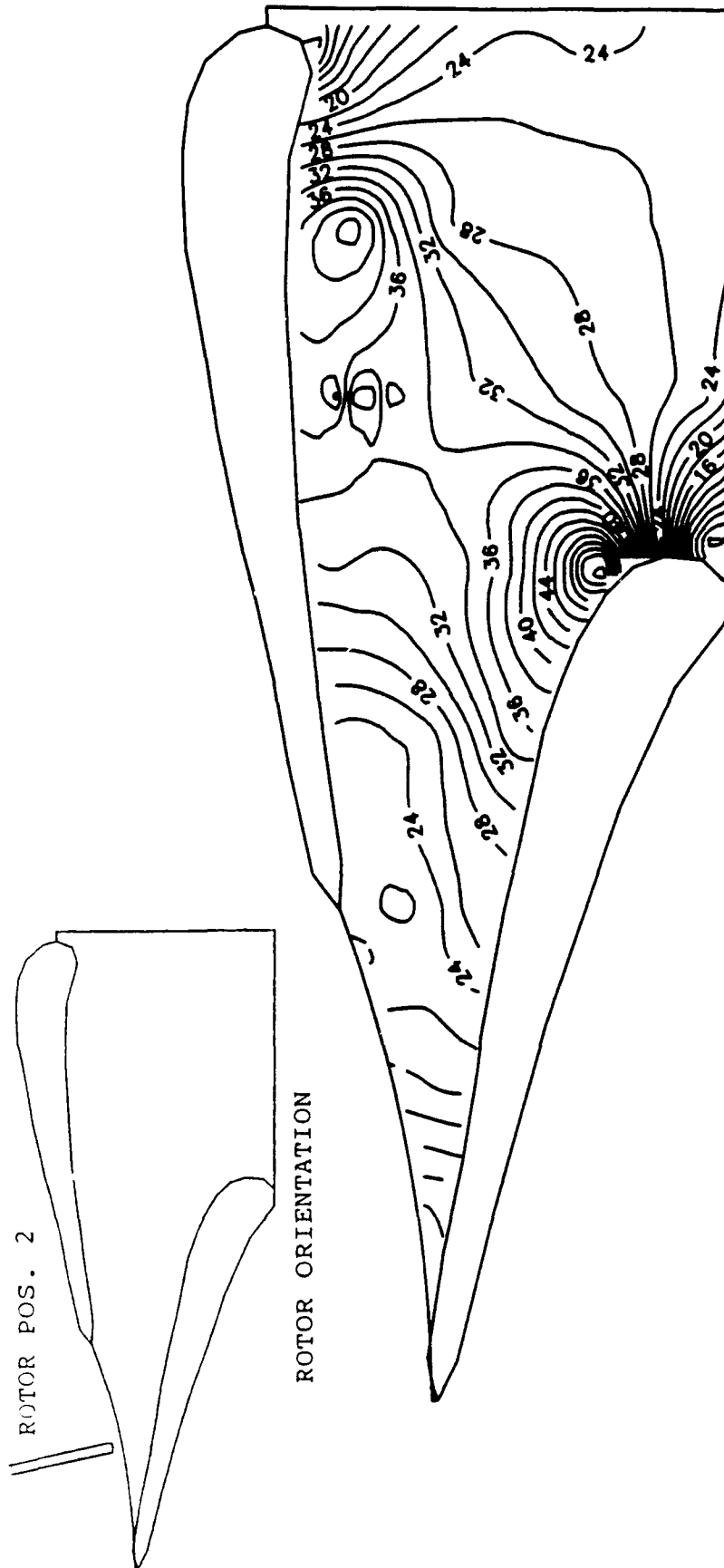


FIG. 34 β -FLOW ANGLE CONTOURS ON THE BLADE-TO-BLADE PLANE, $Z=0.25$
(ROTOR BLADE AT THE CENTER OF THE PASSAGE)

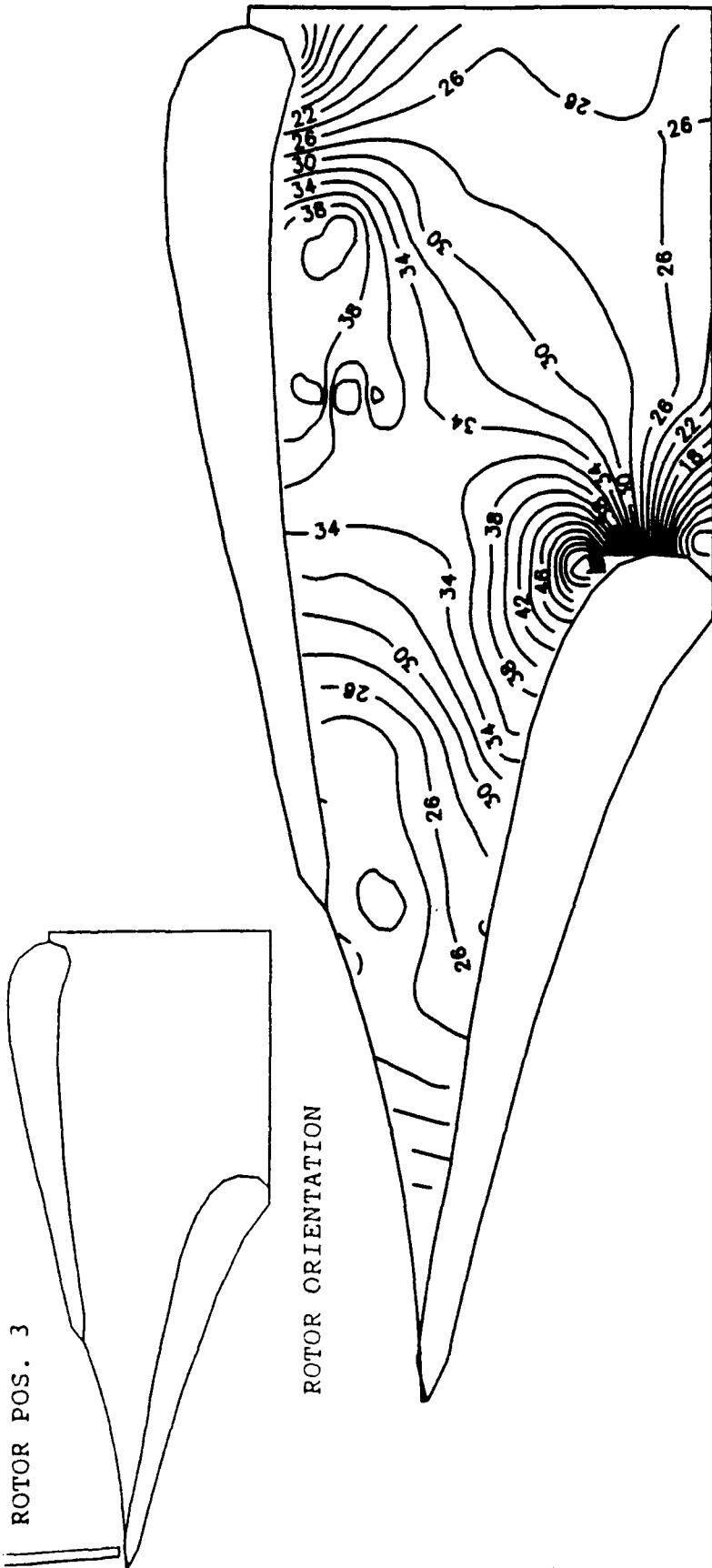


FIG. 35 β -FLOW ANGLE CONTOURS ON THE BLADE-TO-BLADE PLANE, $Z=0.25$
 (ROTOR BLADE LEAVING THE PASSAGE)

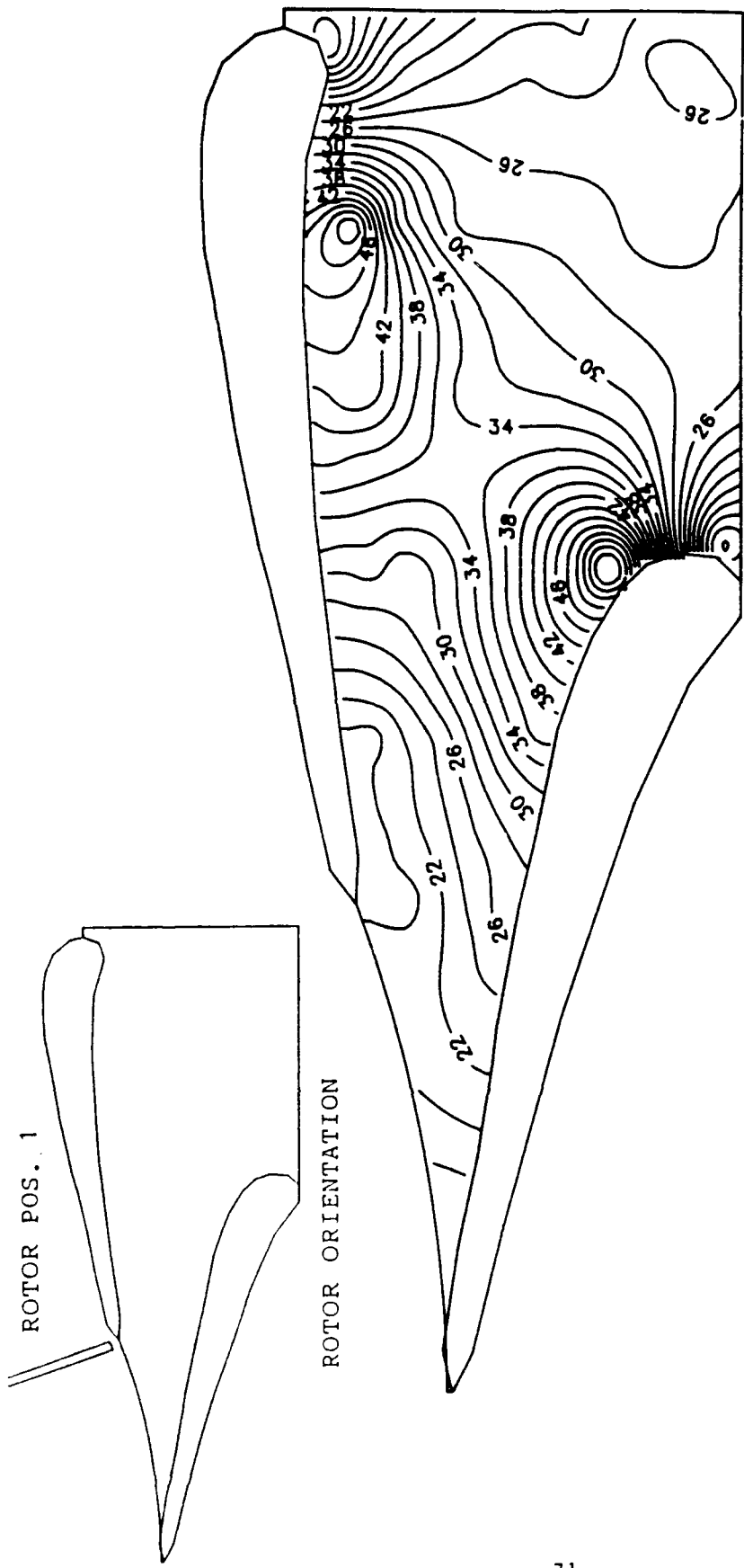


FIG. 36 β -FLOW ANGLE CONTOURS ON THE BLADE-TO-BLADE PLANE, $Z=0.50$ (ROTOR BLADE ENTERING THE PASSAGE)

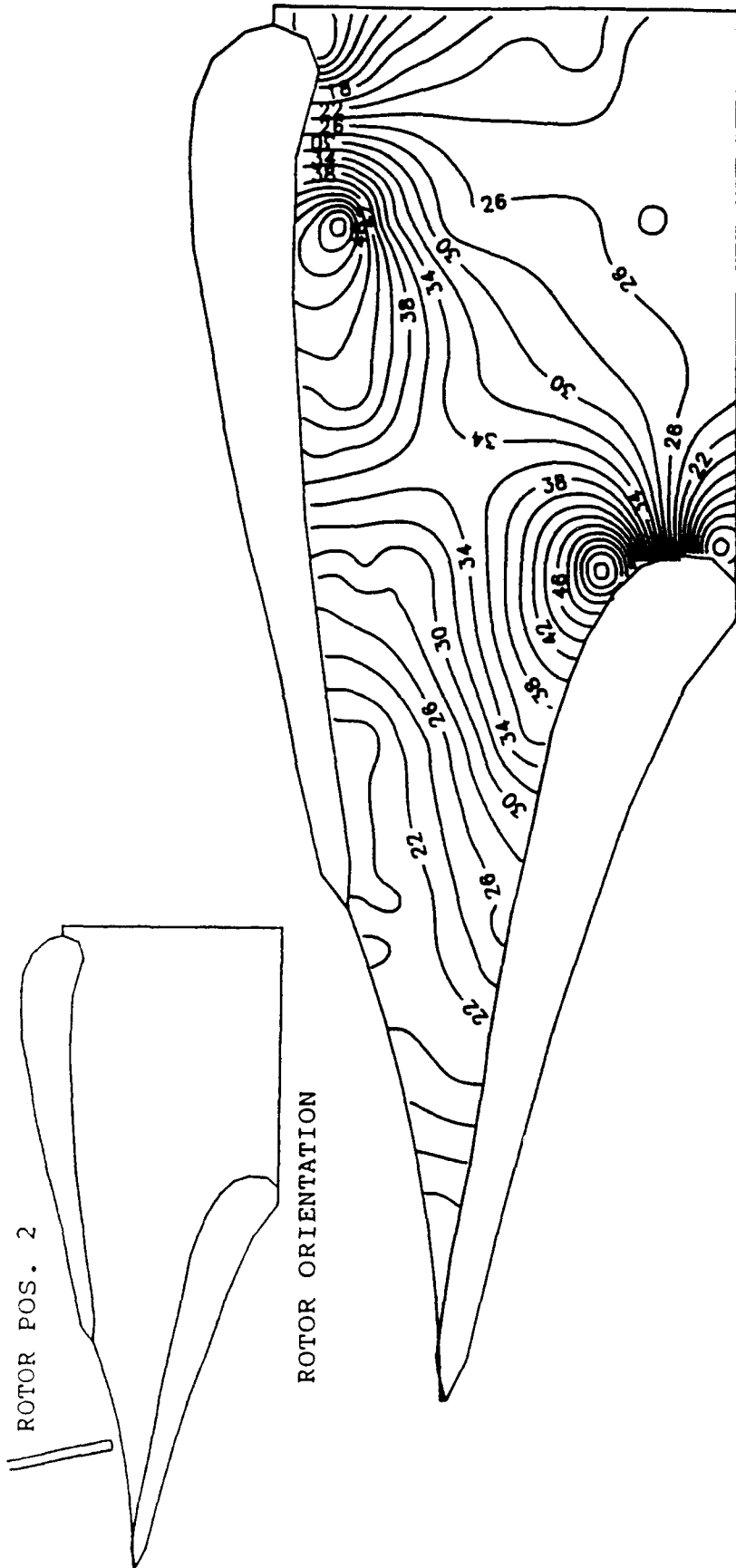
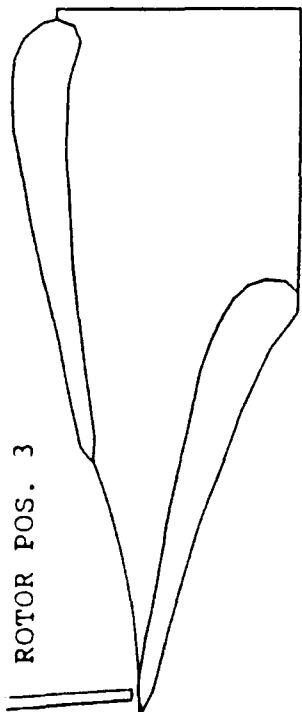


FIG. 37 β -FLOW ANGLE CONTOURS ON THE BLADE-TO-BLADE PLANE, $Z=0.50$ (ROTOR BLADE AT THE CENTER OF THE PASSAGE)

ROTOR POS. 3



ROTOR ORIENTATION

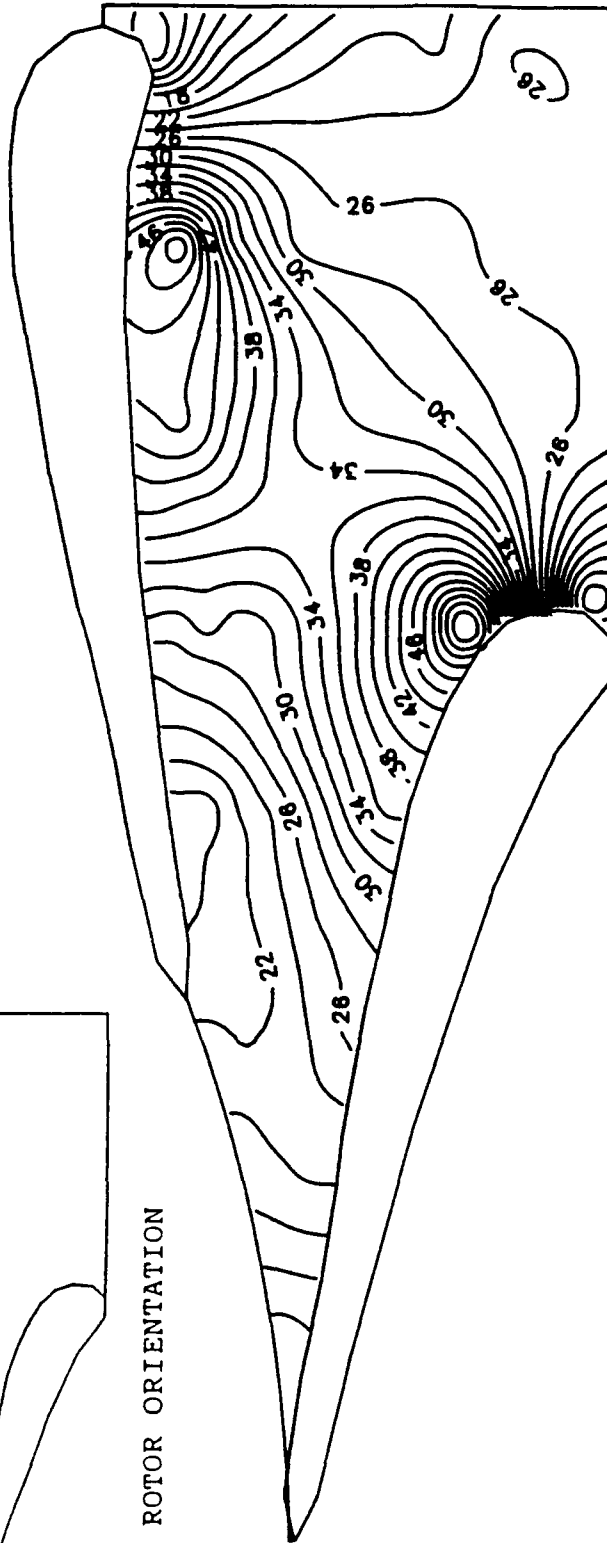


FIG. 38 β -FLOW ANGLE CONTOURS ON THE BLADE-TO-BLADE PLANE, $Z=0.50$
(ROTOR BLADE LEAVING THE PASSAGE)

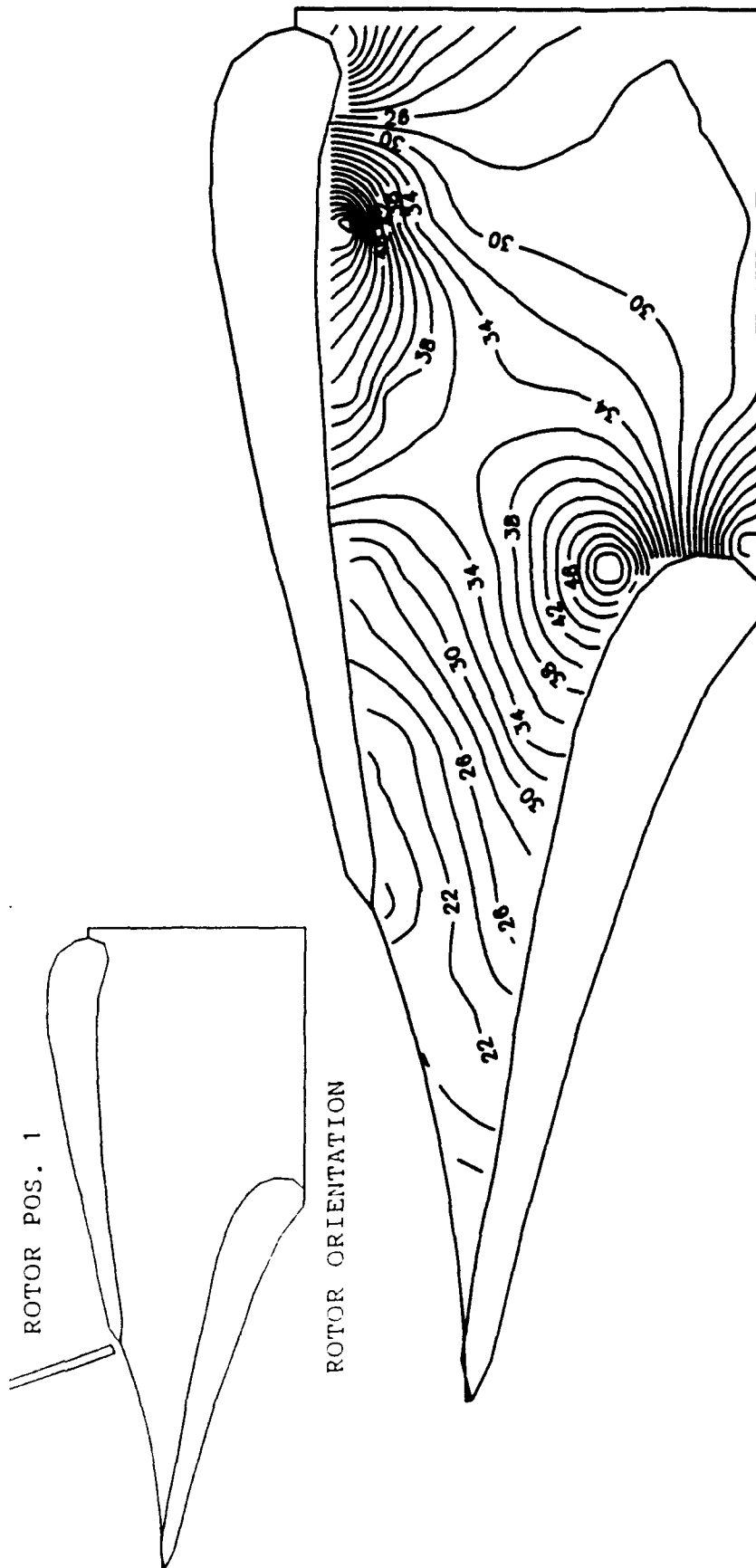


FIG. 39 β -FLOW ANGLE CONTOURS ON THE BLADE-TO-BLADE PLANE, $Z=0.70$ (ROTOR BLADE ENTERING THE PASSAGE)

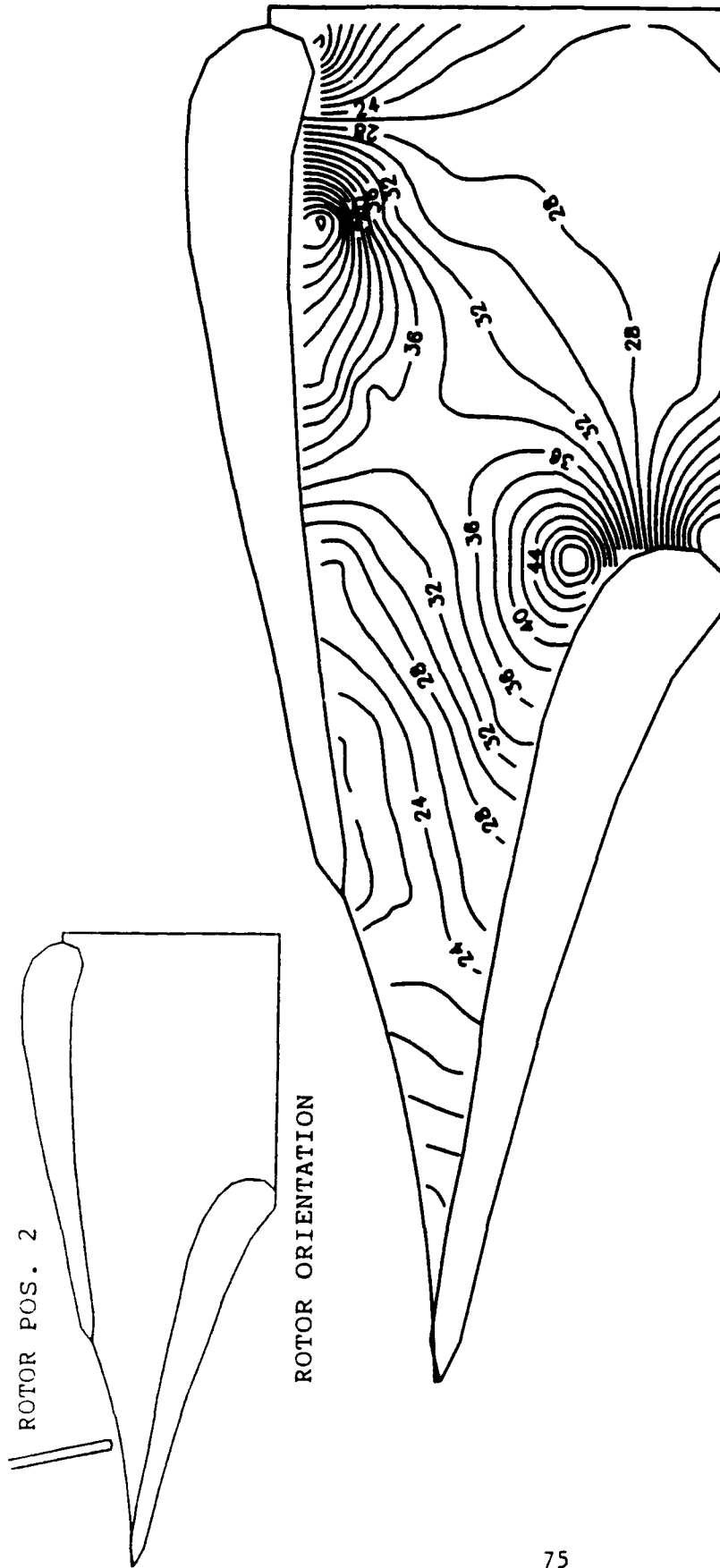
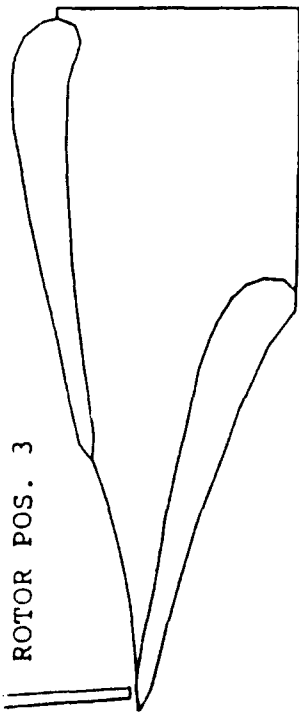


FIG. 40 β -FLOW ANGLE CONTOURS ON THE BLADE-TO-BLADE PLANE, $Z=0.70$ (ROTOR BLADE AT THE CENTER OF THE PASSAGE)

ROTOR POS. 3



ROTOR ORIENTATION

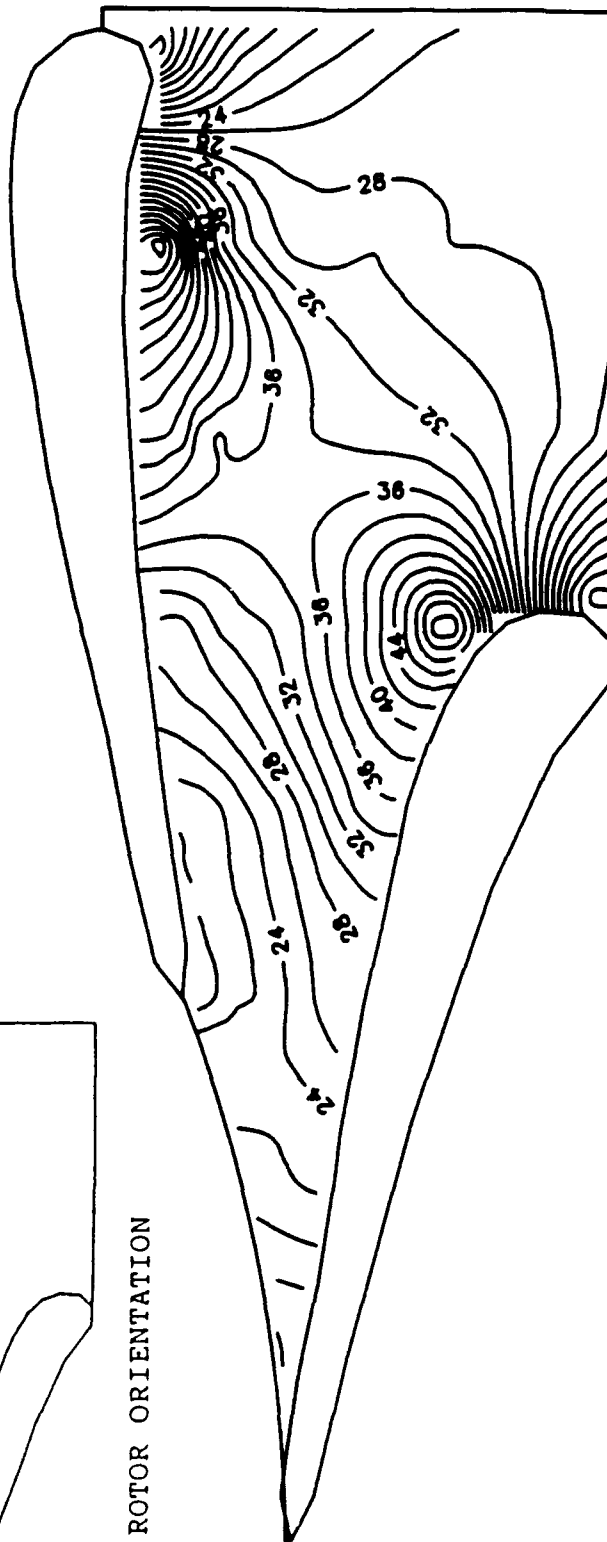


FIG. 41 β -FLOW ANGLE CONTOURS ON THE BLADE-TO-BLADE
PLANE, $Z=0.70$
(ROTOR BLADE LEAVING THE PASSAGE)

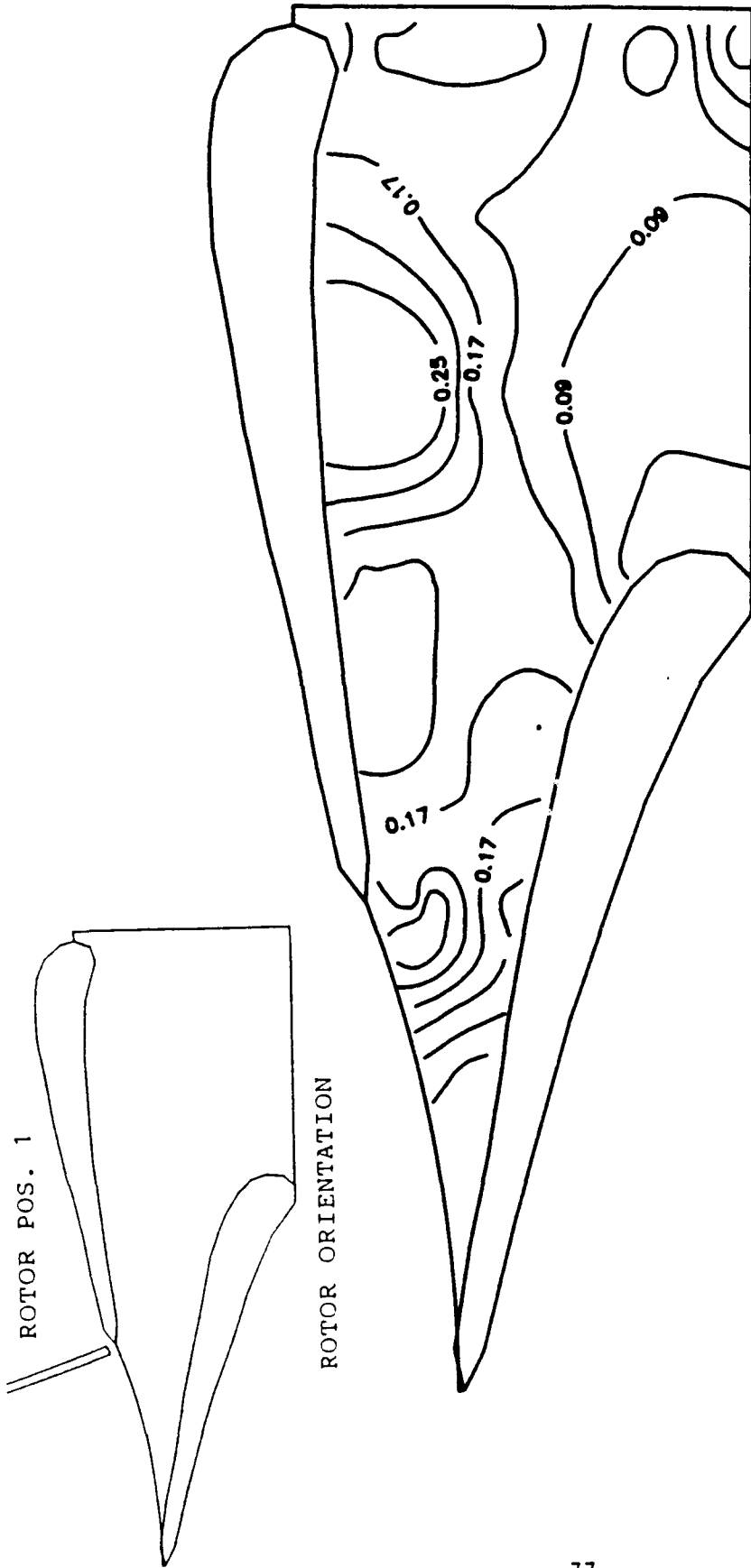


FIG. 42 NORMALIZED AXIAL VELOCITY CONTOURS ON THE
 BLADE-TO-BLADE PLANE, $Z=0.25$
 (ROTOR BLADE ENTERING THE PASSAGE)

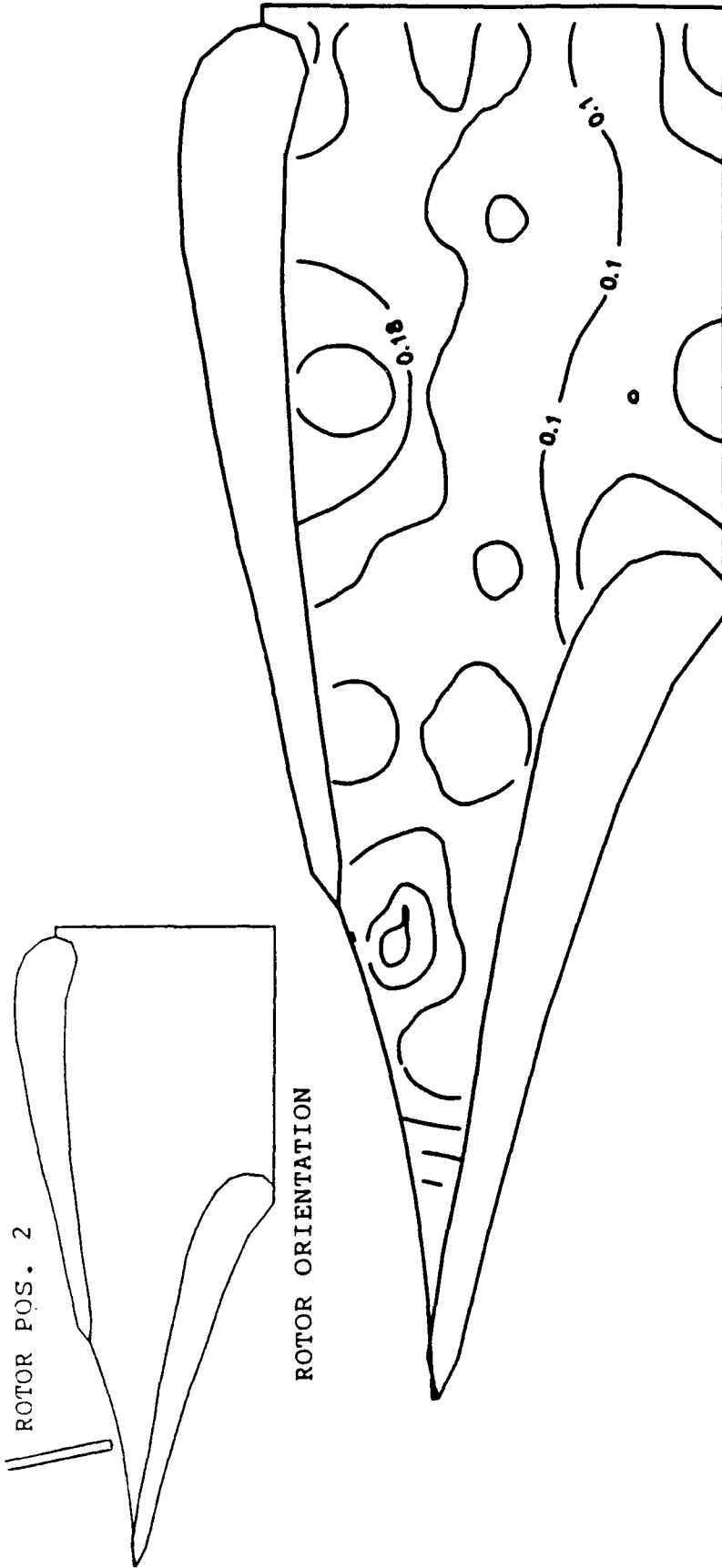


FIG. 43 NORMALIZED AXIAL VELOCITY CONTOURS ON THE
 BLADE-TO-BLADE PLANE, $Z=0.25$
 (ROTOR BLADE AT THE CENTER OF THE PASSAGE)

ROTOR POS. 3

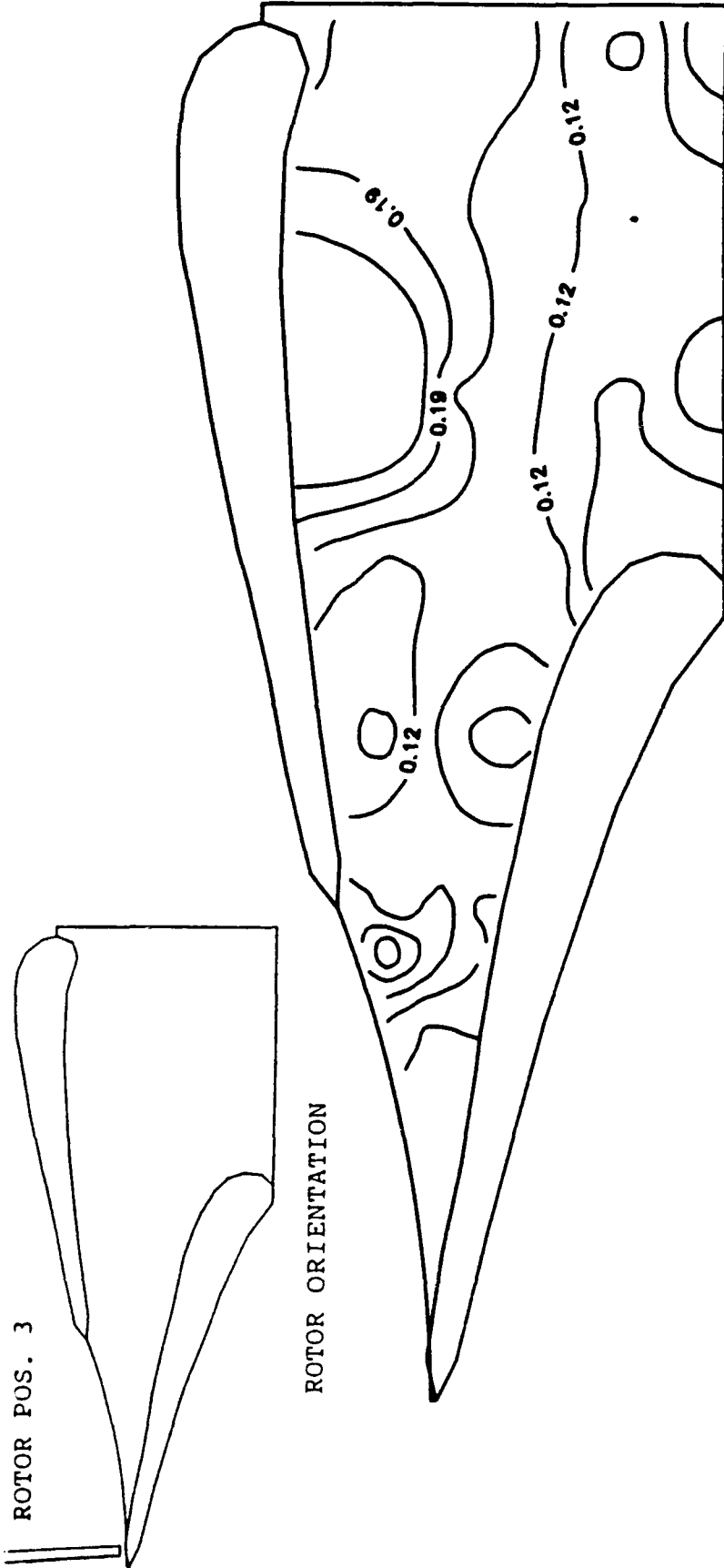


FIG. 44 NORMALIZED AXIAL VELOCITY CONTOURS ON THE
BLADE-TO-BLADE PLANE, $Z=0.25$
(ROTOR BLADE LEAVING THE PASSAGE)

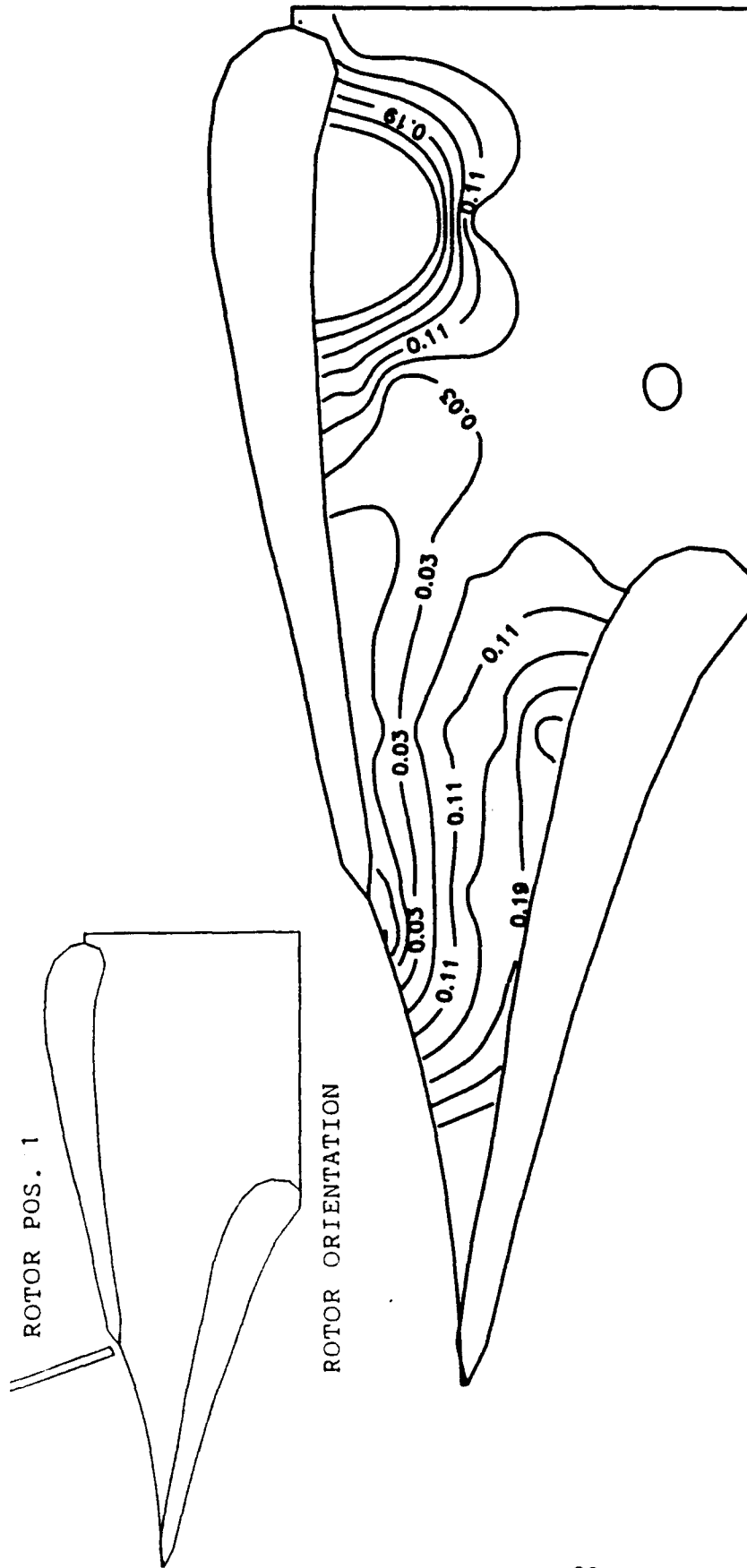


FIG. 45 NORMALIZED AXIAL VELOCITY CONTOURS ON THE
 BLADE-TO-BLADE PLANE, $Z=0.50$
 (ROTOR BLADE ENTERING THE PASSAGE)

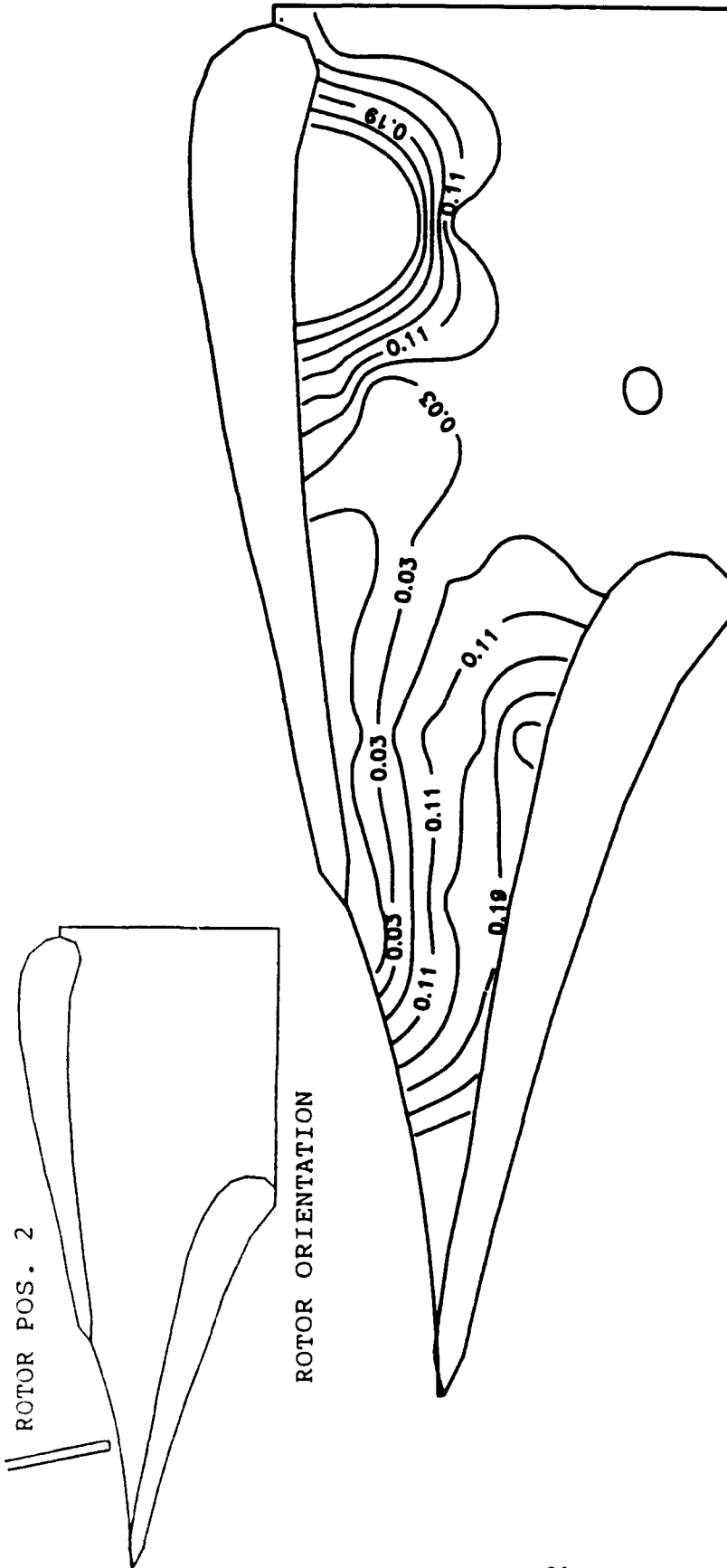


FIG. 46 NORMALIZED AXIAL VELOCITY CONTOURS ON THE
 BLADE-TO-BLADE PLANE, $Z=0.50$
 (ROTOR BLADE AT THE CENTER OF THE PASSAGE)

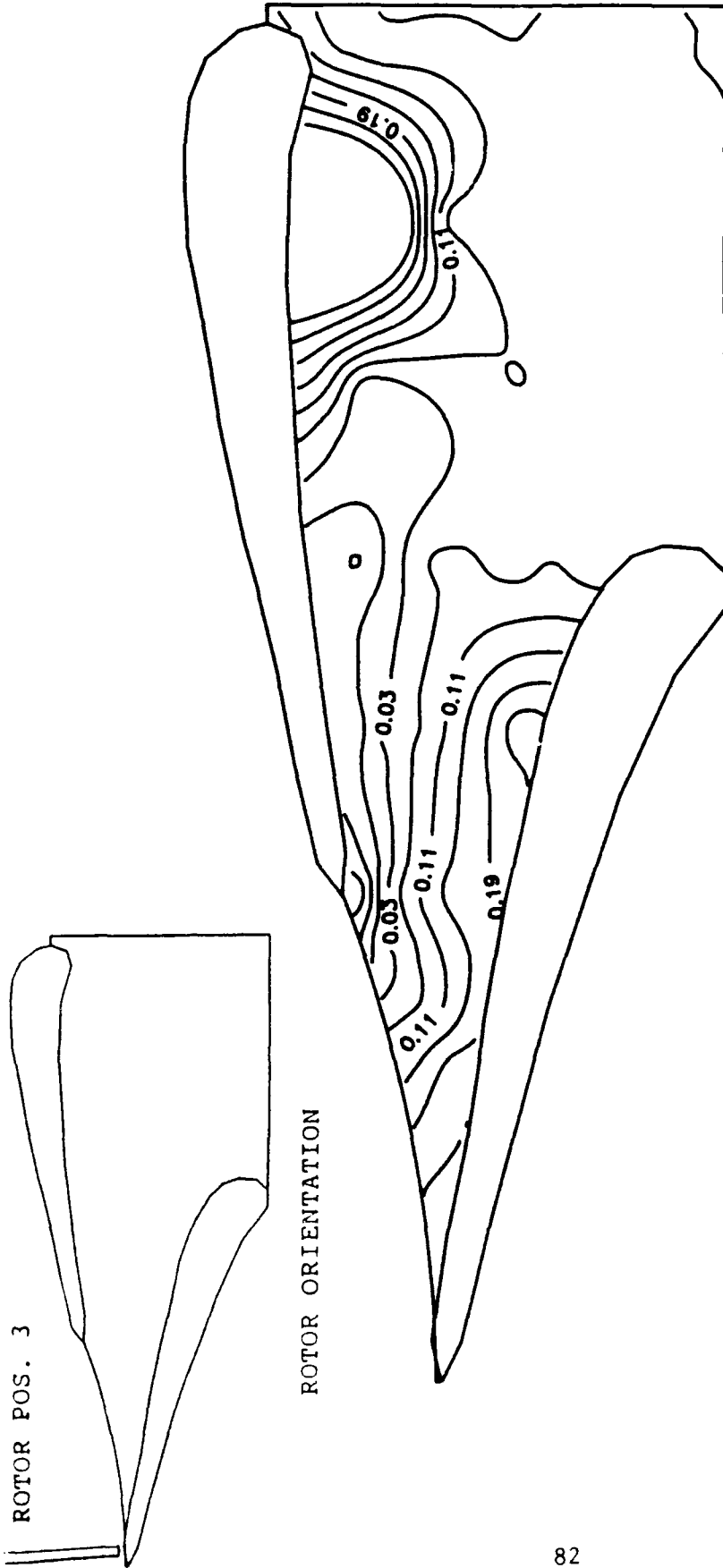


FIG. 47 NORMALIZED AXIAL VELOCITY CONTOURS ON THE
 BLADE-TO-BLADE PLANE, $Z=0.50$
 (ROTOR BLADE LEAVING THE PASSAGE)

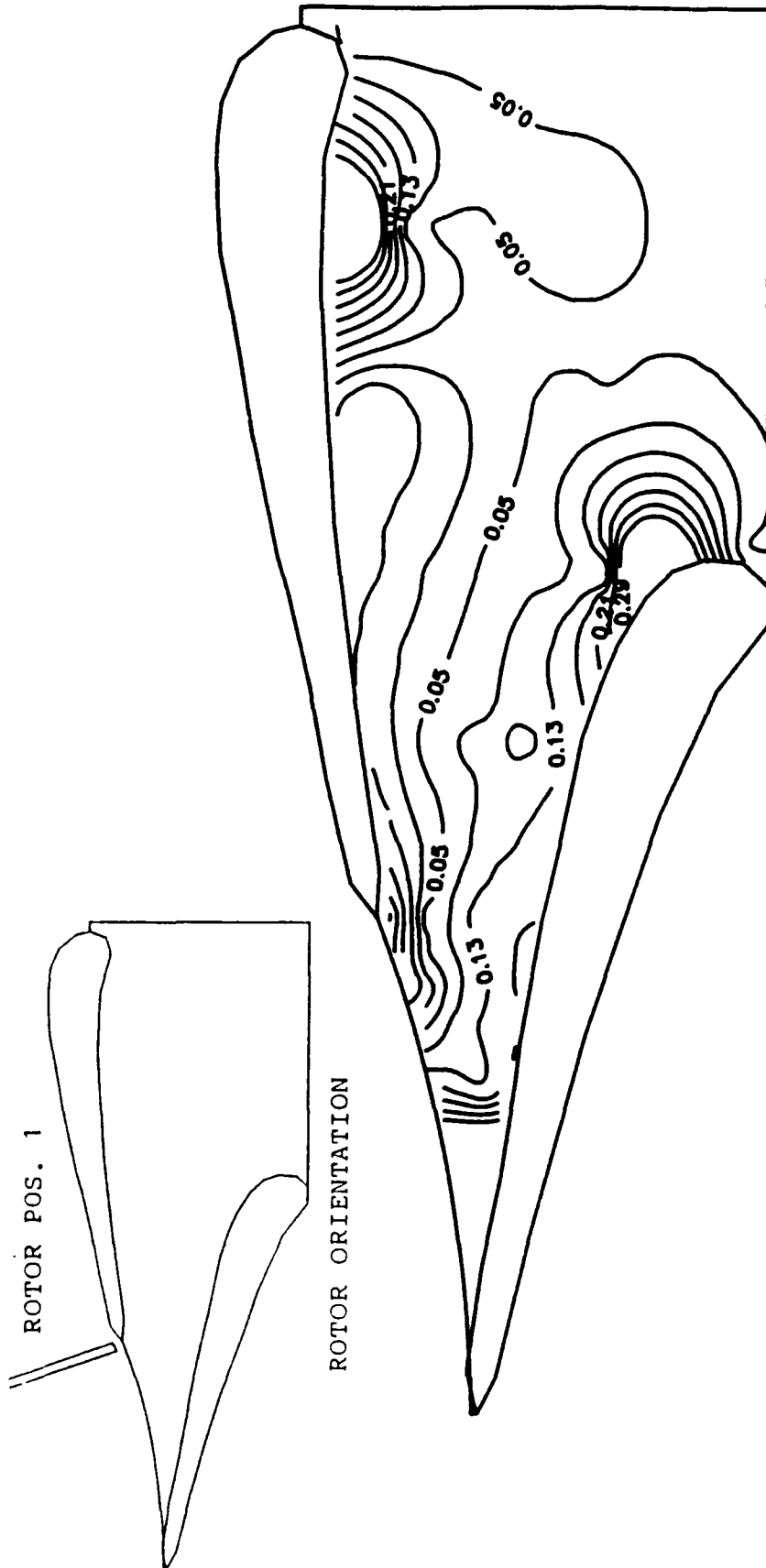


FIG. 48 NORMALIZED AXIAL VELOCITY CONTOURS ON THE
 BLADE-TO-BLADE PLANE, $Z=0.70$
 (ROTOR BLADE ENTERING THE PASSAGE)

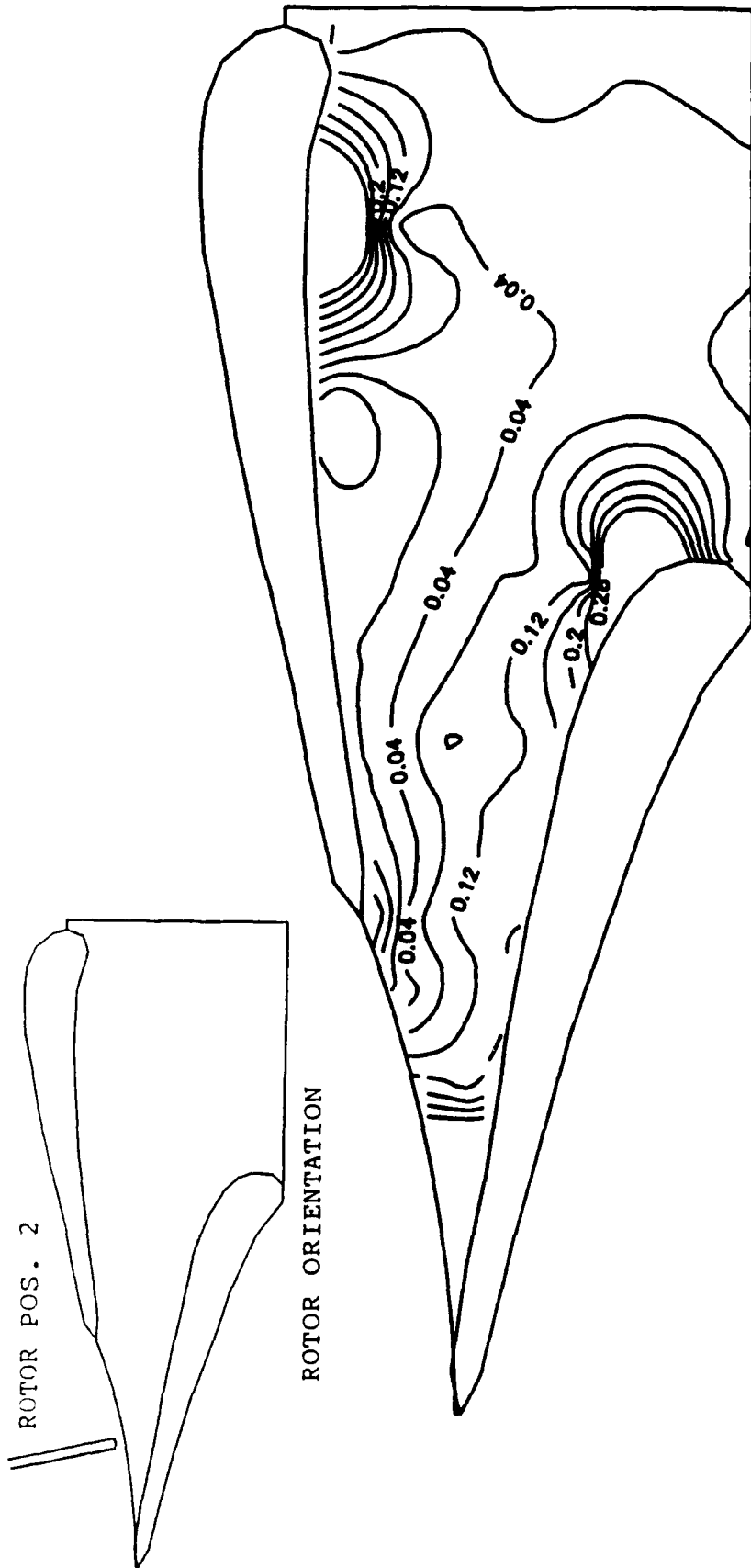


FIG. 49 NORMALIZED AXIAL VELOCITY CONTOURS ON THE
 BLADE-TO-BLADE PLANE, $z=0.70$
 (ROTOR BLADE AT THE CENTER OF THE PASSAGE)

ROTOR POS. 3

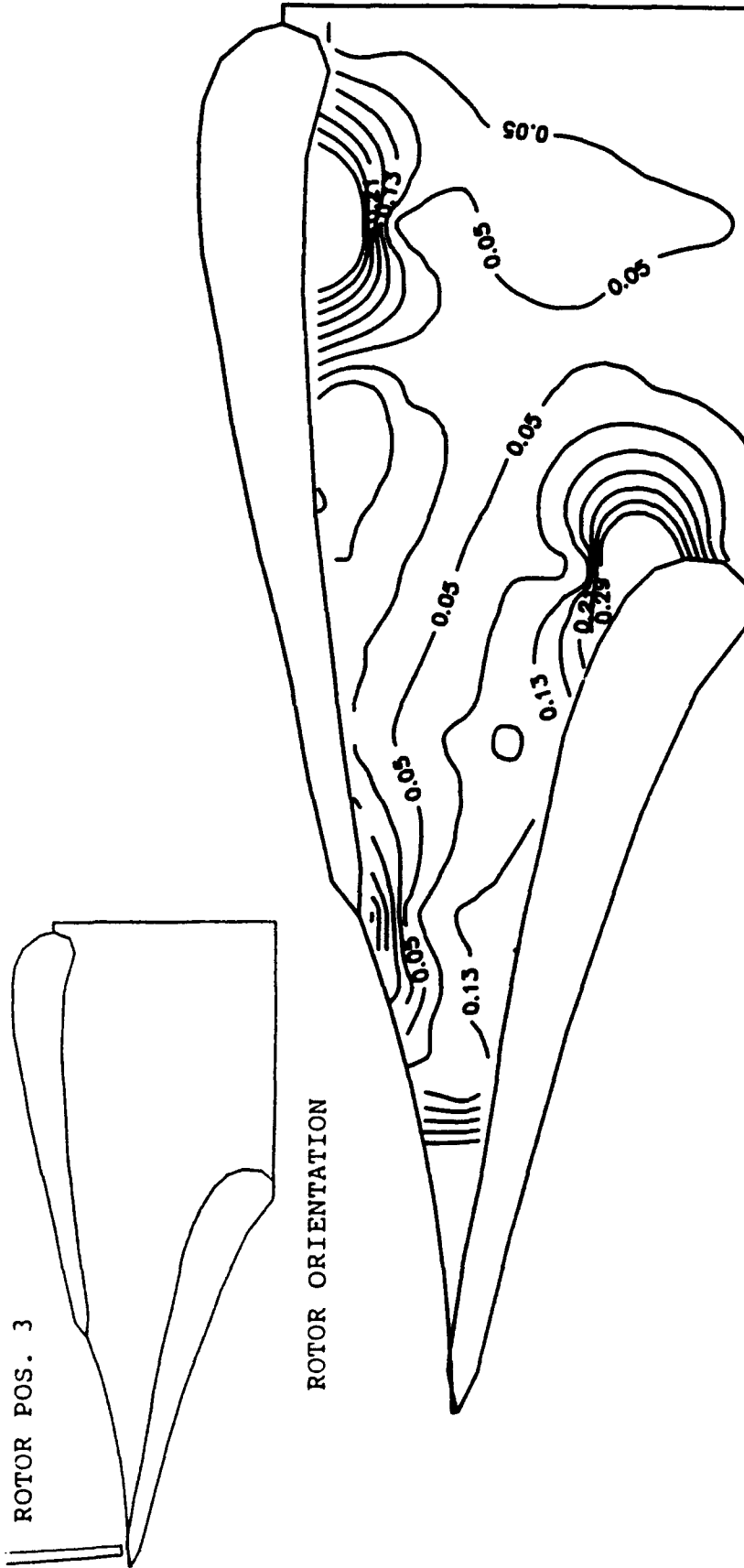


FIG. 50 NORMALIZED AXIAL VELOCITY CONTOURS ON THE
BLADE-TO-BLADE PLANE, $Z=0.70$
(ROTOR BLADE LEAVING THE PASSAGE)

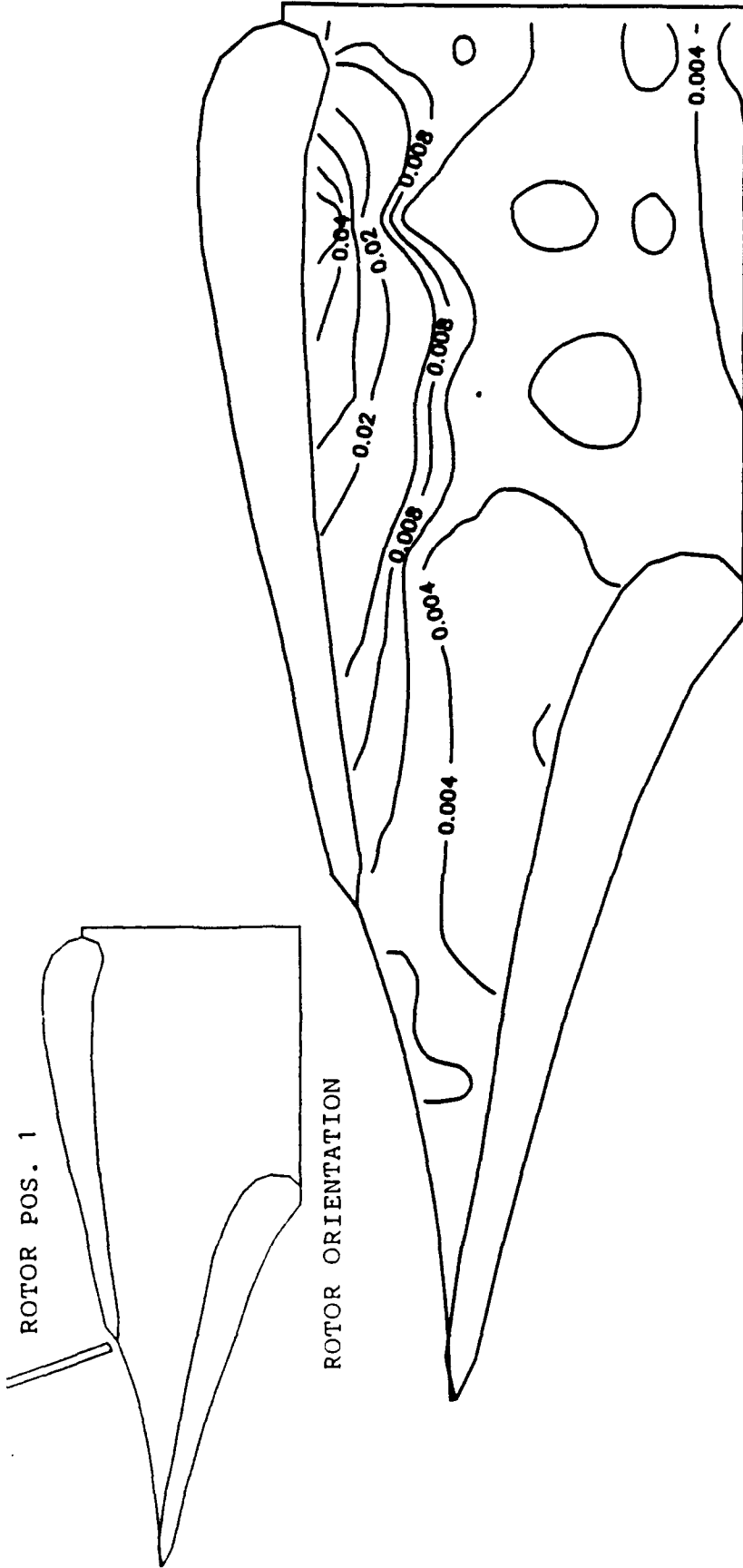


FIG. 51 TURBULENT NORMAL STRESS IN THE RADIAL DIRECTION
 ON THE BLADE-TO-BLADE PLANE, $Z=0.10$ ($U_r'^2/V_{ex}^2$)
 (ROTOR BLADE ENTERING THE PASSAGE)

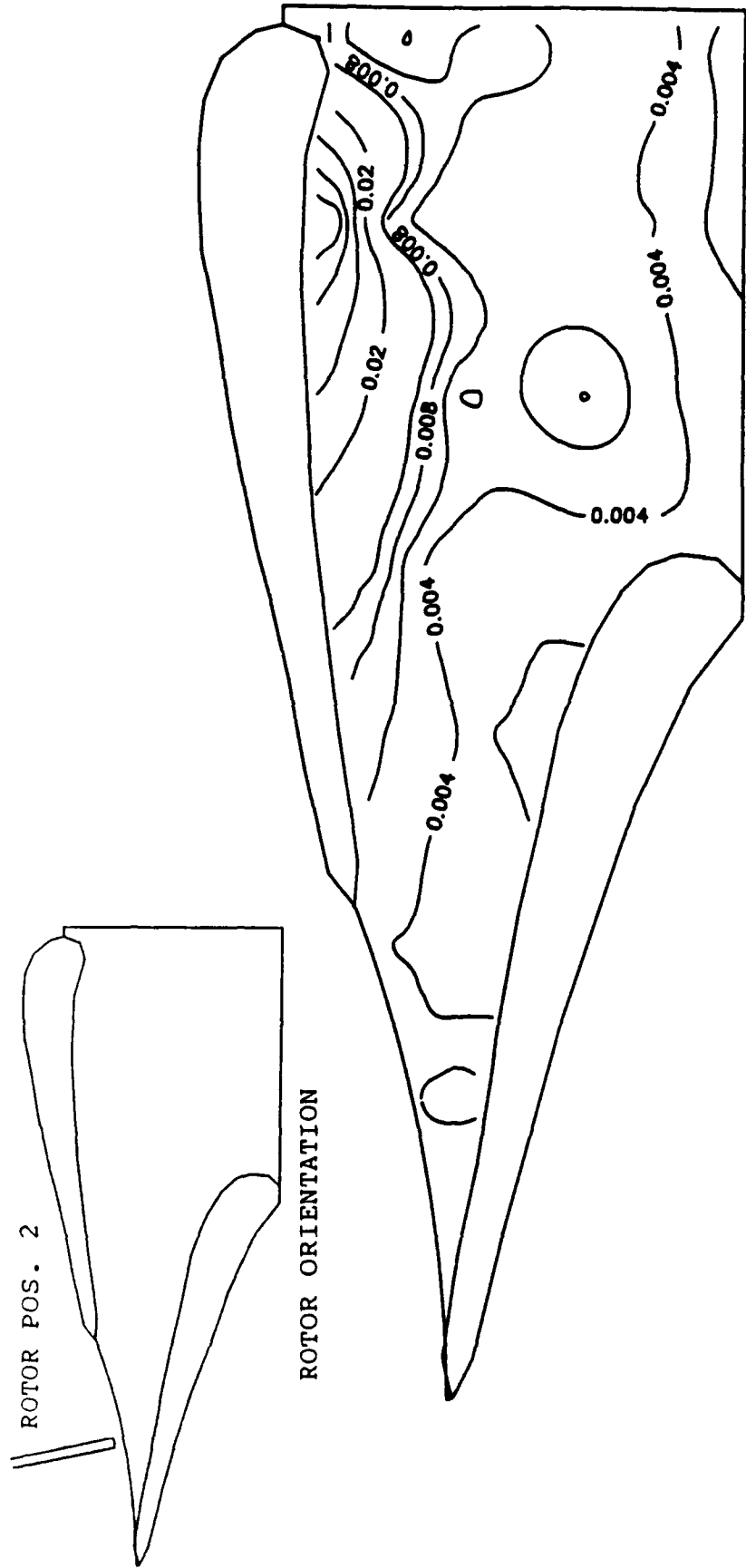


FIG. 52 TURBULENT NORMAL STRESS IN THE RADIAL DIRECTION ON THE BLADE-TO-BLADE PLANE, $Z=0.10$ ($U_r'^2/V_{ex}^2$) (ROTOR BLADE AT THE CENTER OF THE PASSAGE)

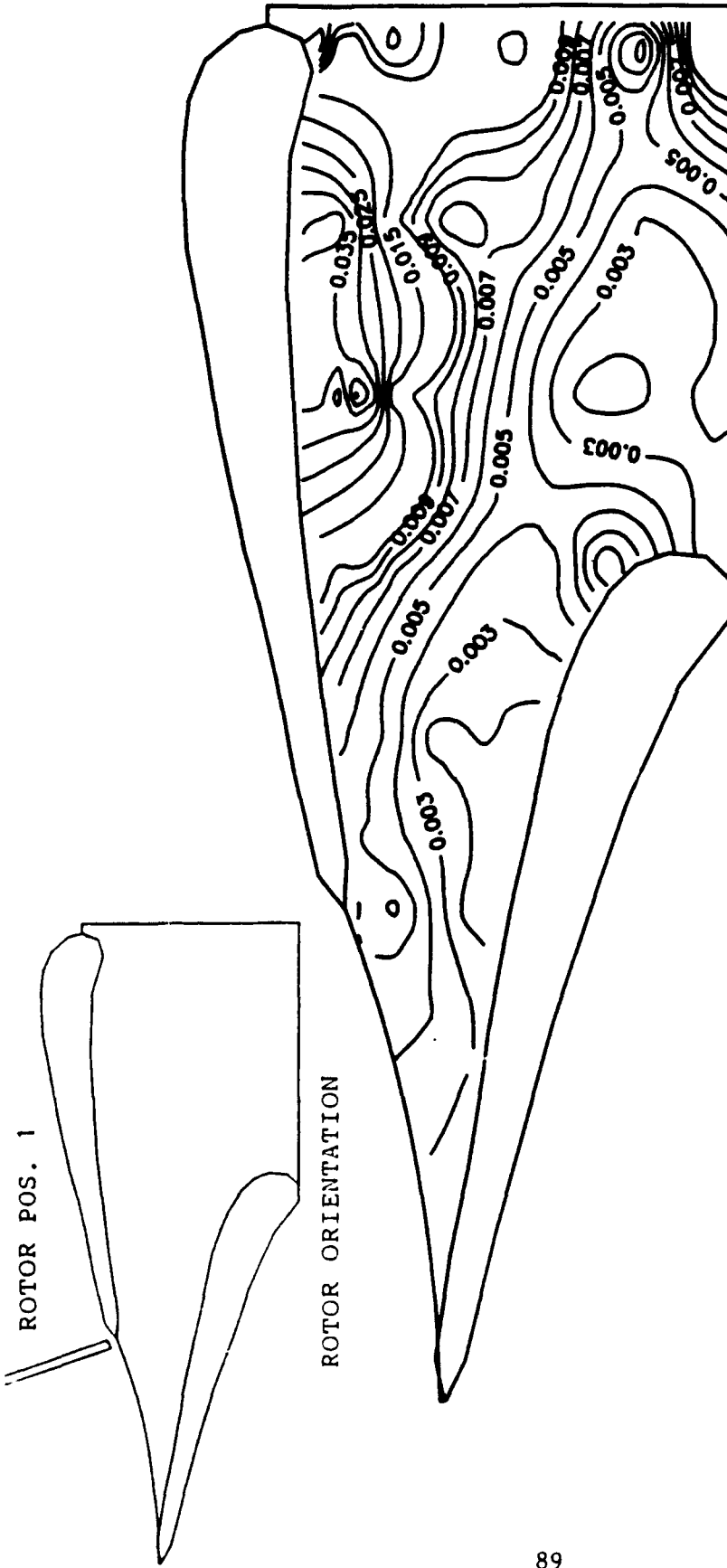


FIG. 54 TURBULENT NORMAL STRESS IN THE RADIAL DIRECTION
 ON THE BLADE-TO-BLADE PLANE, $Z=0.25$ ($U_r'^2/V_{ex}^2$)
 (ROTOR BLADE ENTERING THE PASSAGE)

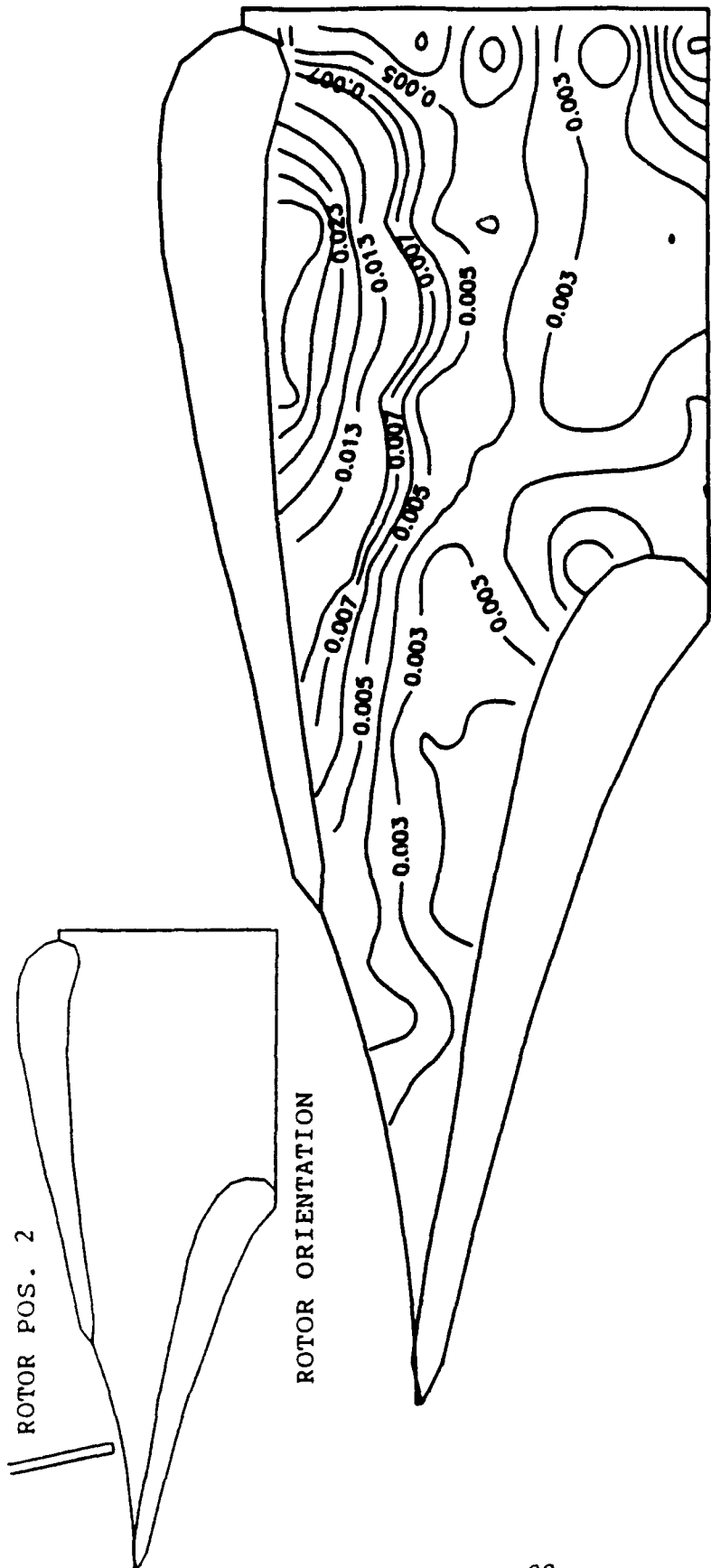
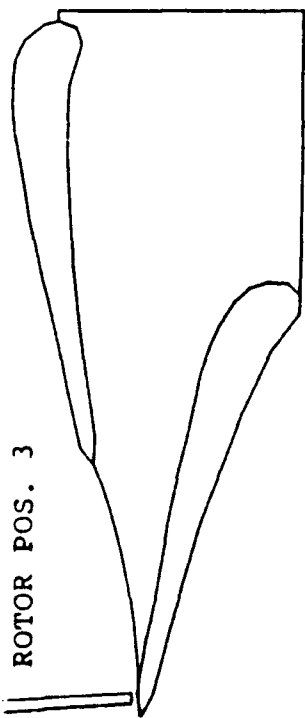


FIG. 55 TURBULENT NORMAL STRESS IN THE RADIAL DIRECTION ON THE BLADE-TO-BLADE PLANE, $Z=0.25$ (U_r^2/V_{ex}^2) (ROTOR BLADE AT THE CENTER OF THE PASSAGE)

ROTOR POS. 3



ROTOR ORIENTATION

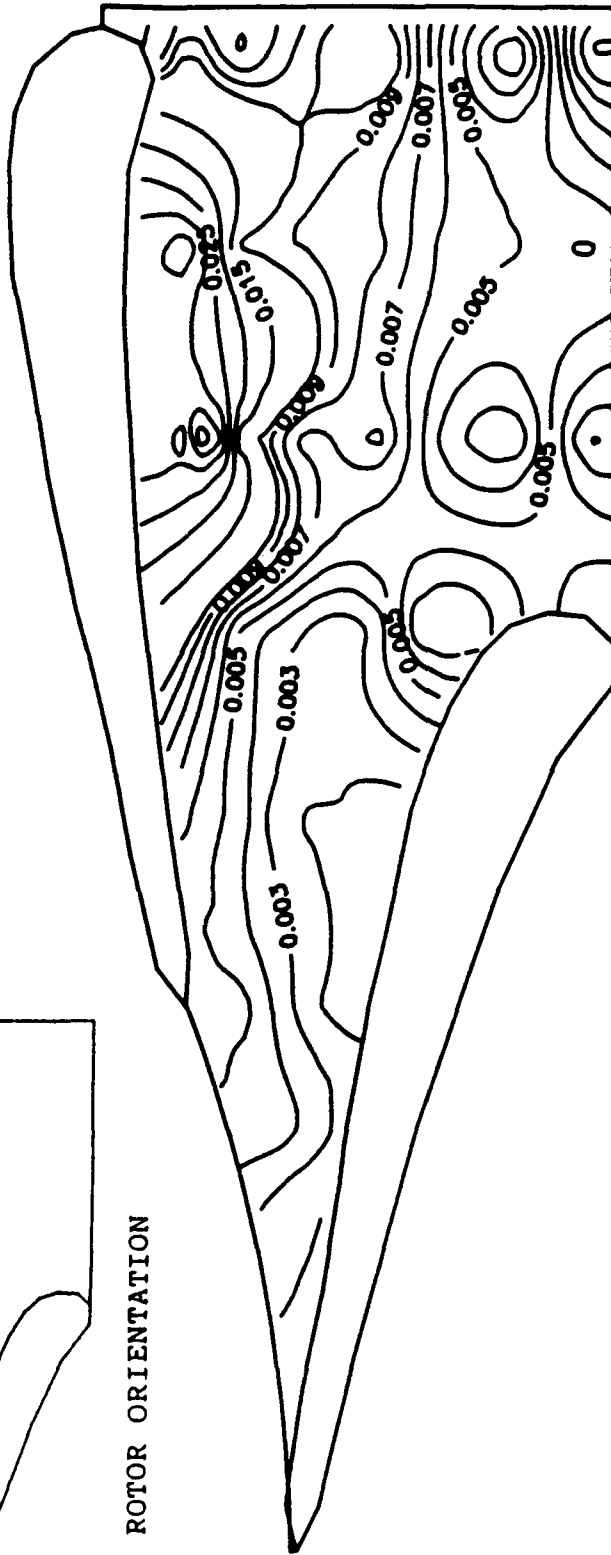


FIG. 56 TURBULENT NORMAL STRESS IN THE RADIAL DIRECTION
ON THE BLADE-TO-BLADE PLANE, $Z=0.25$ ($U_r'^2/V_{ax}^2$)
(ROTOR BLADE LEAVING THE PASSAGE)

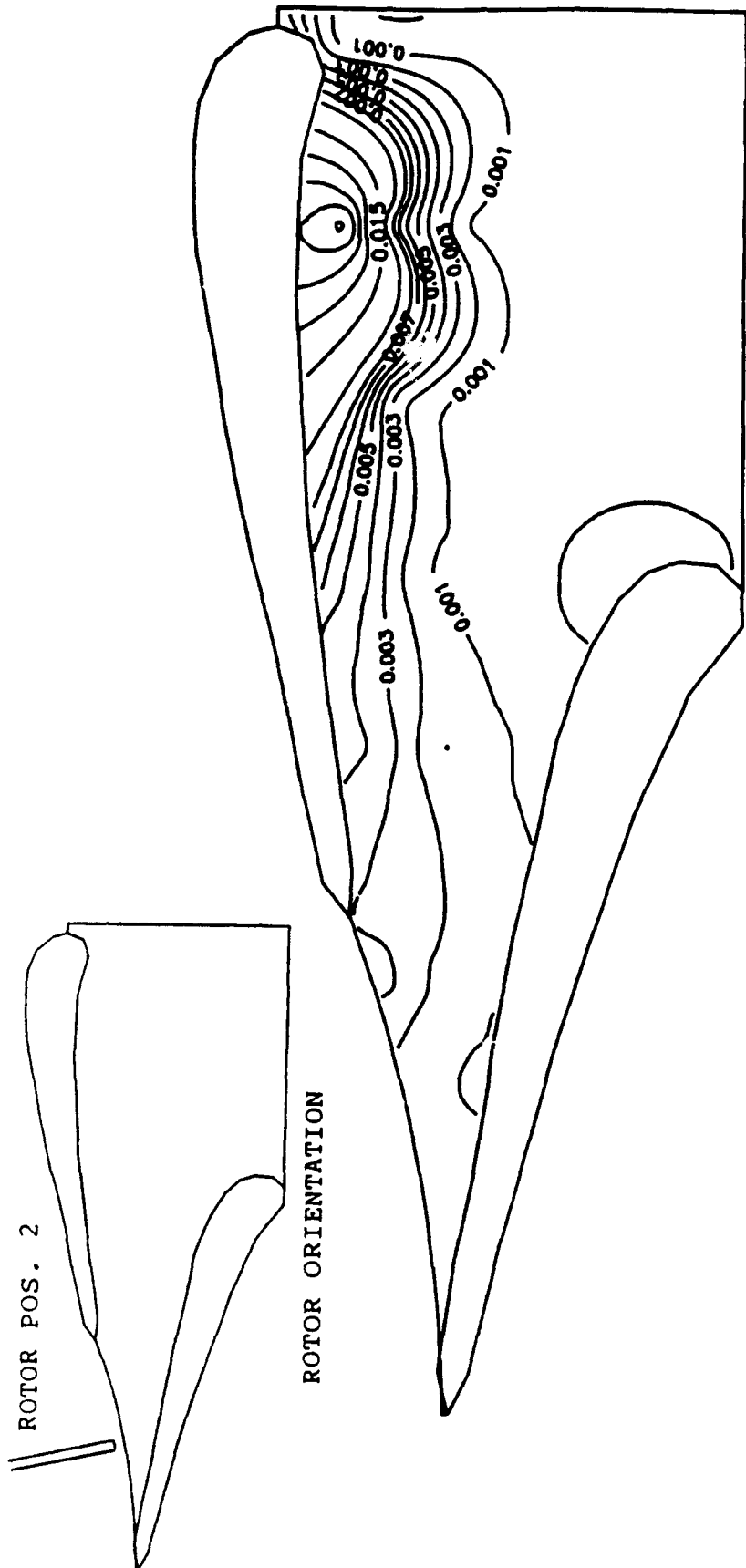


FIG. 58 TURBULENT NORMAL STRESS IN THE RADIAL DIRECTION
 ON THE BLADE-TO-BLADE PLANE, $z=0.50$ ($U_r'^2/V_{ex}^2$)
 (ROTOR BLADE AT THE CENTER OF THE PASSAGE)

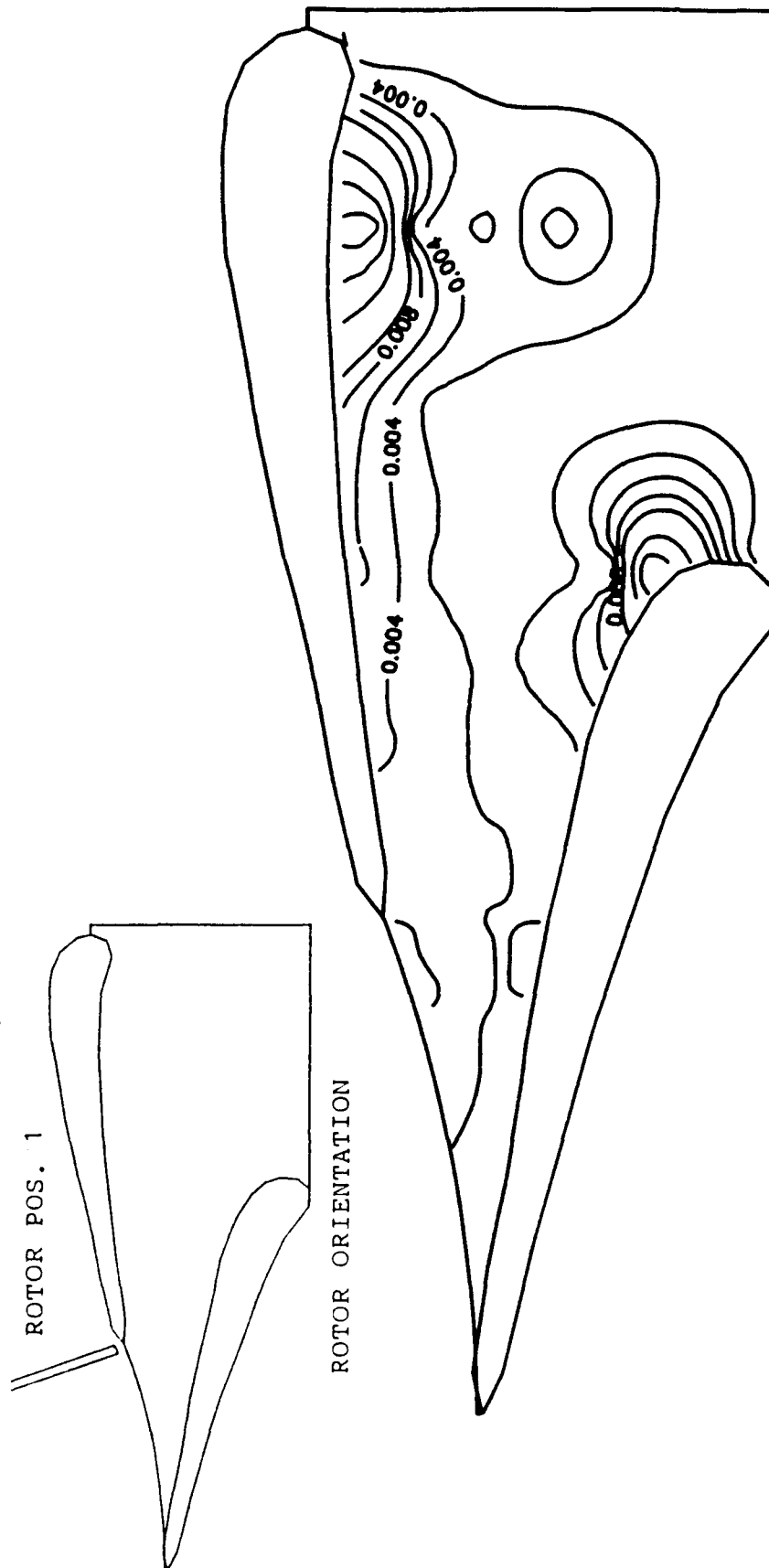


FIG. 60 TURBULENT NORMAL STRESS IN THE RADIAL DIRECTION
ON THE BLADE-TO-BLADE PLANE, $z=0.70$ ($U_r'^2/V_{ex}^2$)
(ROTOR BLADE ENTERING THE PASSAGE)

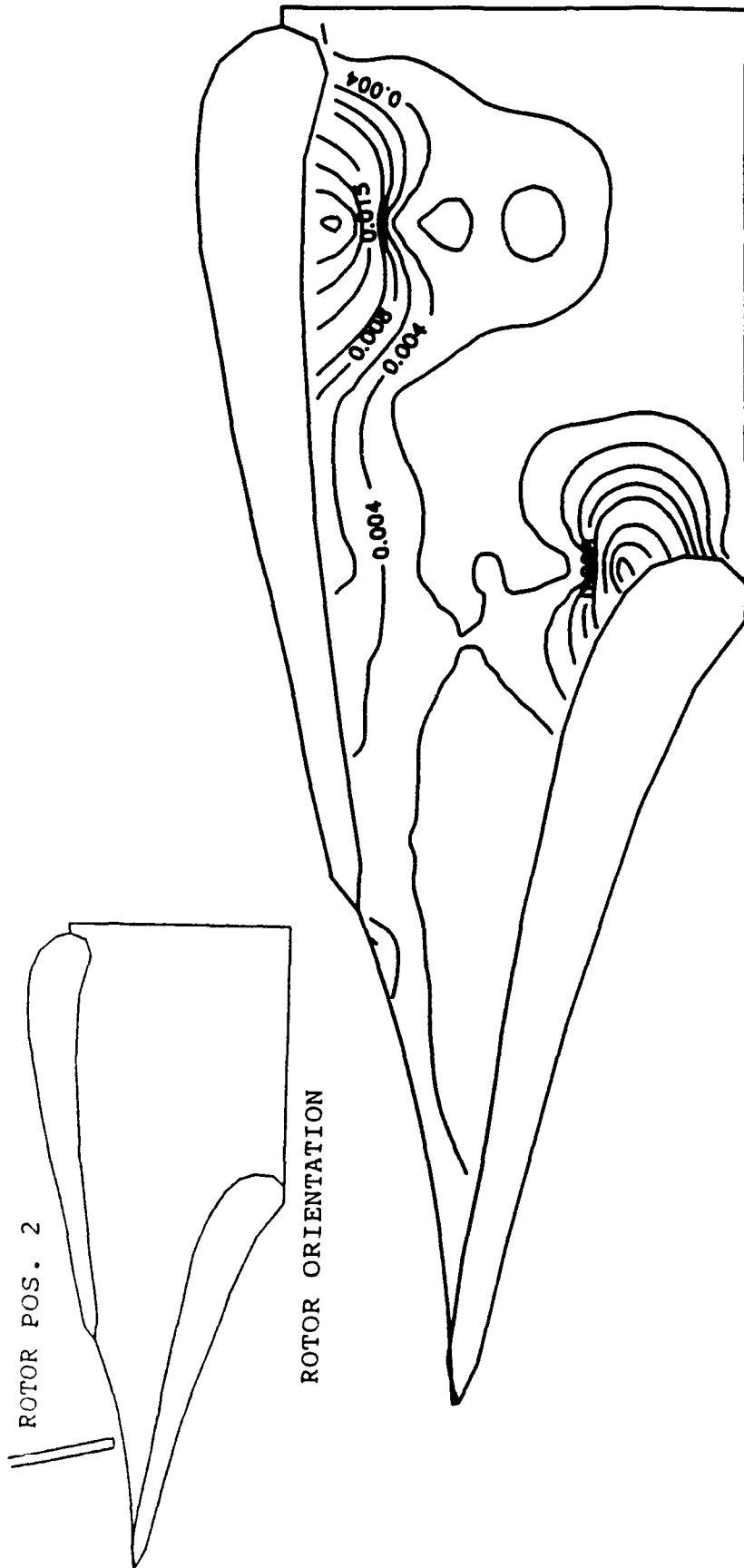


FIG. 61 TURBULENT NORMAL STRESS IN THE RADIAL DIRECTION
 ON THE BLADE-TO-BLADE PLANE, $z=0.70$ ($U_r'^2/V_{ex}^2$)
 (ROTOR BLADE AT THE CENTER OF THE PASSAGE)

ROTOR POS. 3

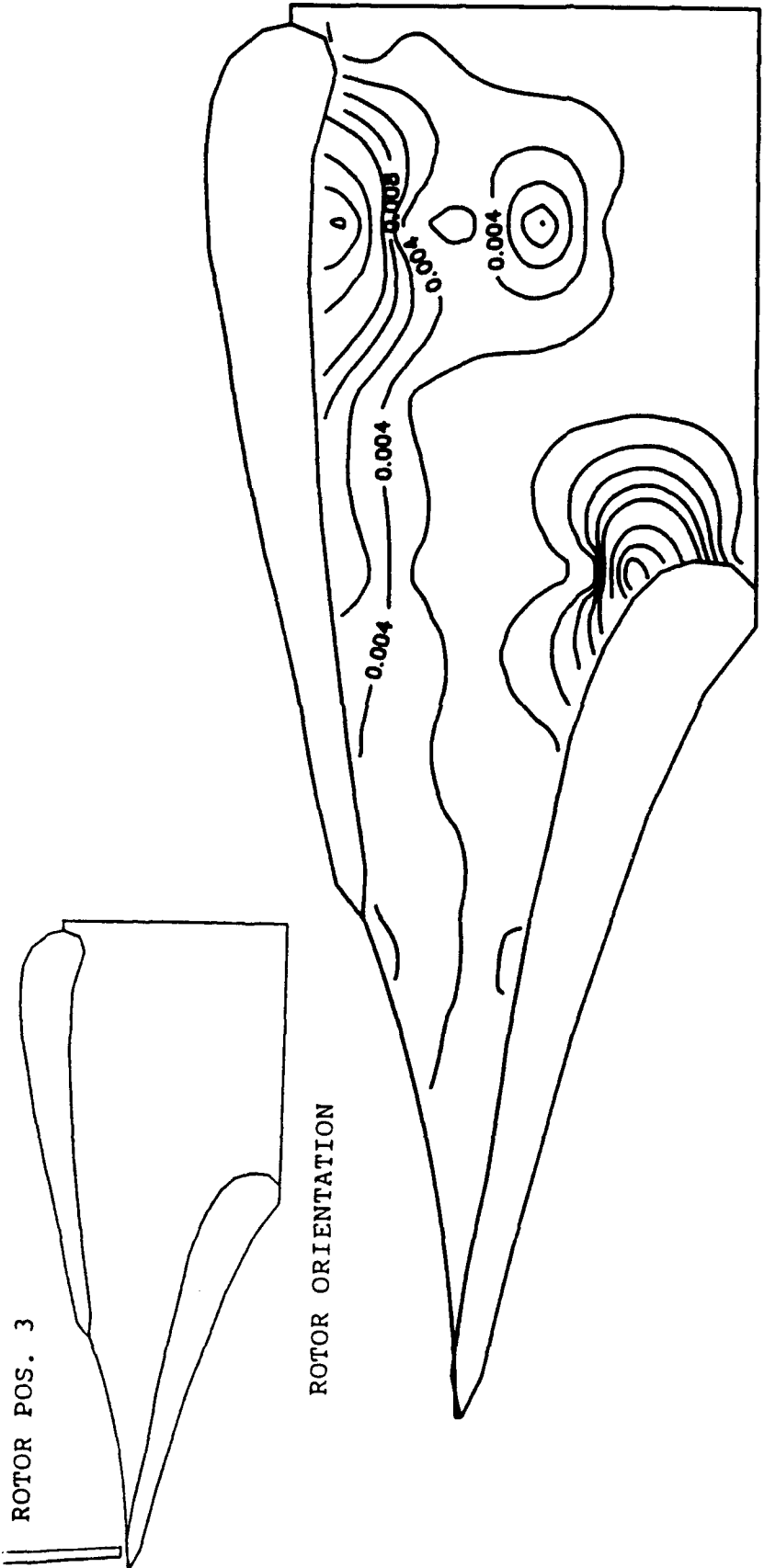


FIG. 62 TURBULENT NORMAL STRESS IN THE RADIAL DIRECTION
ON THE BLADE-TO-BLADE PLANE, $z=0.70$ ($U_t'^2/V_{ex}^2$)
(ROTOR BLADE LEAVING THE PASSAGE)

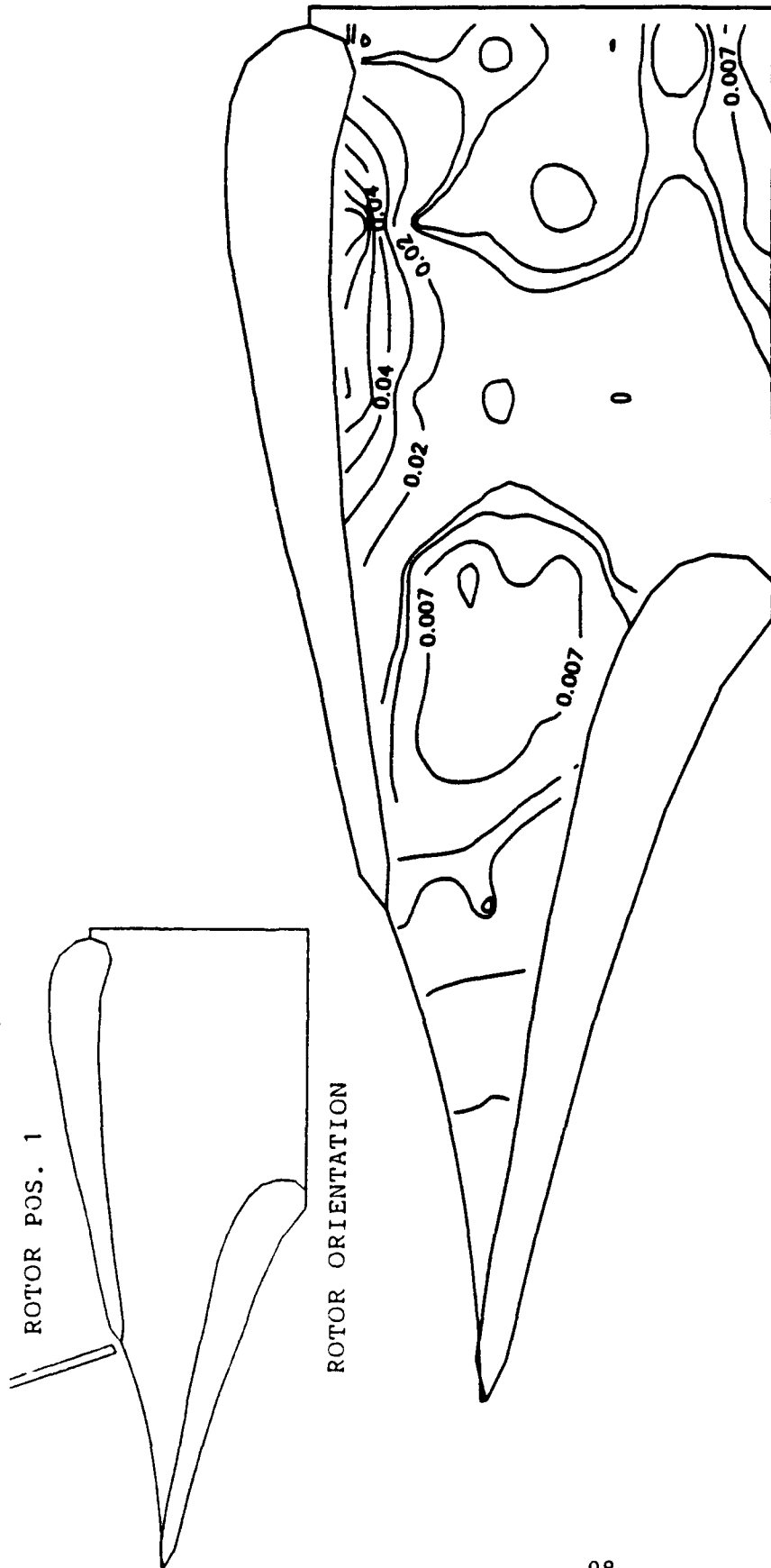


FIG. 63 TURBULENT NORMAL STRESS IN THE TANGENTIAL DIRECTION
 ON THE BLADE-TO-BLADE PLANE, $Z=0.10$ (U_{θ}^2/V_{ex}^2)
 (ROTOR BLADE ENTERING THE PASSAGE)

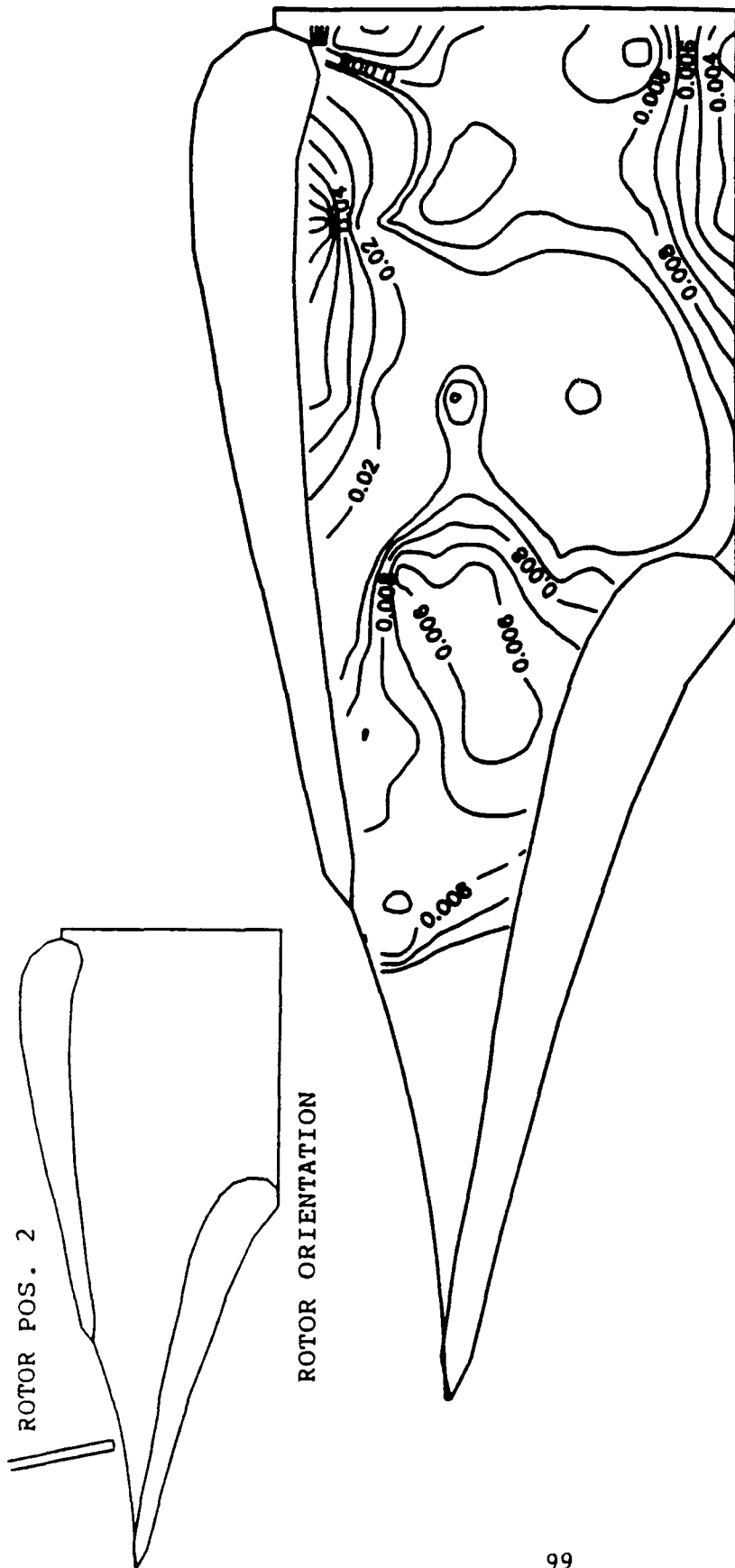


FIG. 64 TURBULENT NORMAL STRESS IN THE TANGENTIAL DIRECTION
 ON THE BLADE-TO-BLADE PLANE, $Z=0.10$ ($U_0'^2/V_{ex}^2$)
 (ROTOR BLADE AT THE CENTER OF THE PASSAGE)

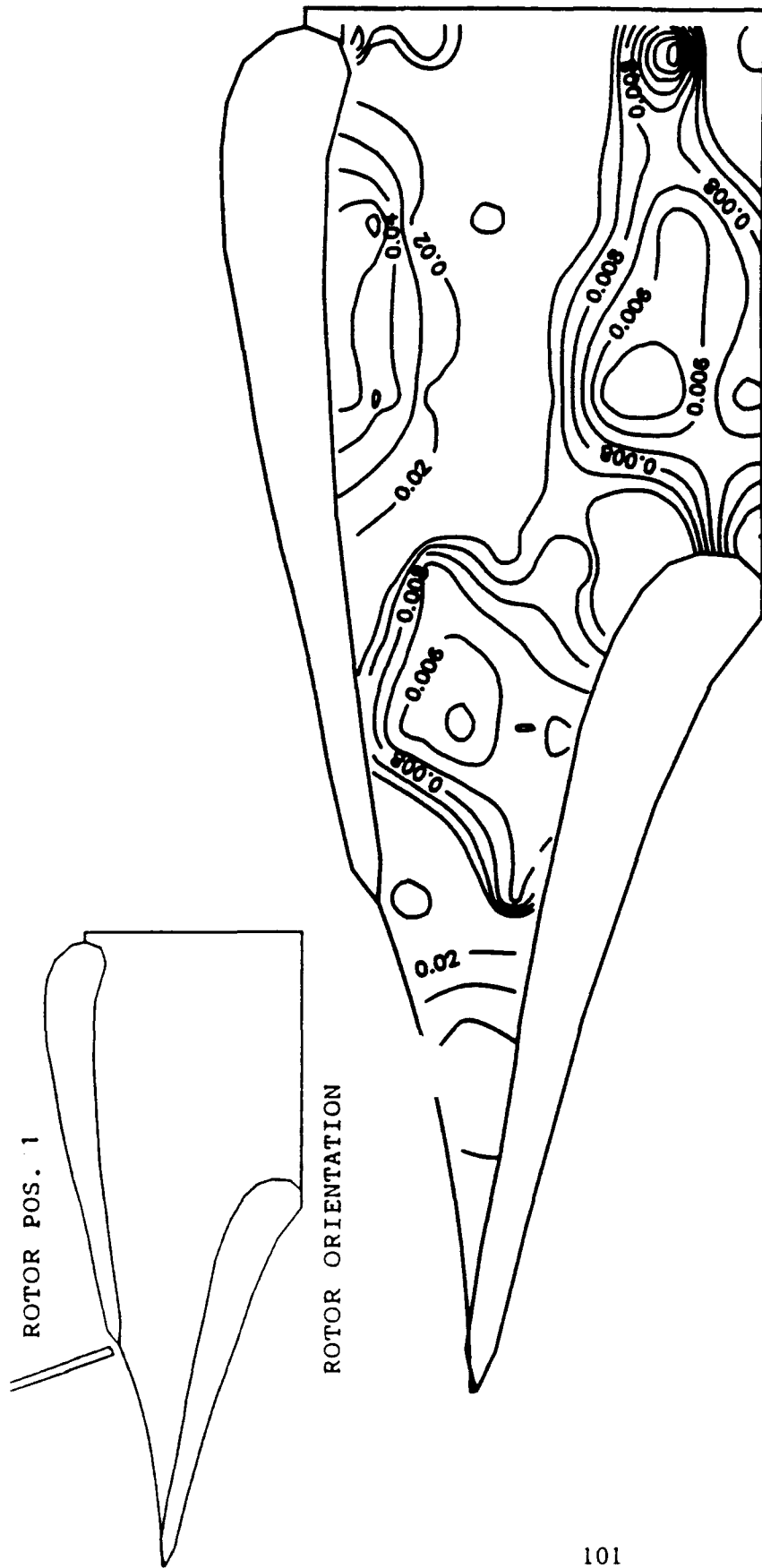


FIG. 66 TURBULENT NORMAL STRESS IN THE TANGENTIAL DIRECTION
 ON THE BLADE-TO-BLADE PLANE, $Z=0.25$ ($U_{\theta}'^2/V_{ex}^2$)
 (ROTOR BLADE ENTERING THE PASSAGE)

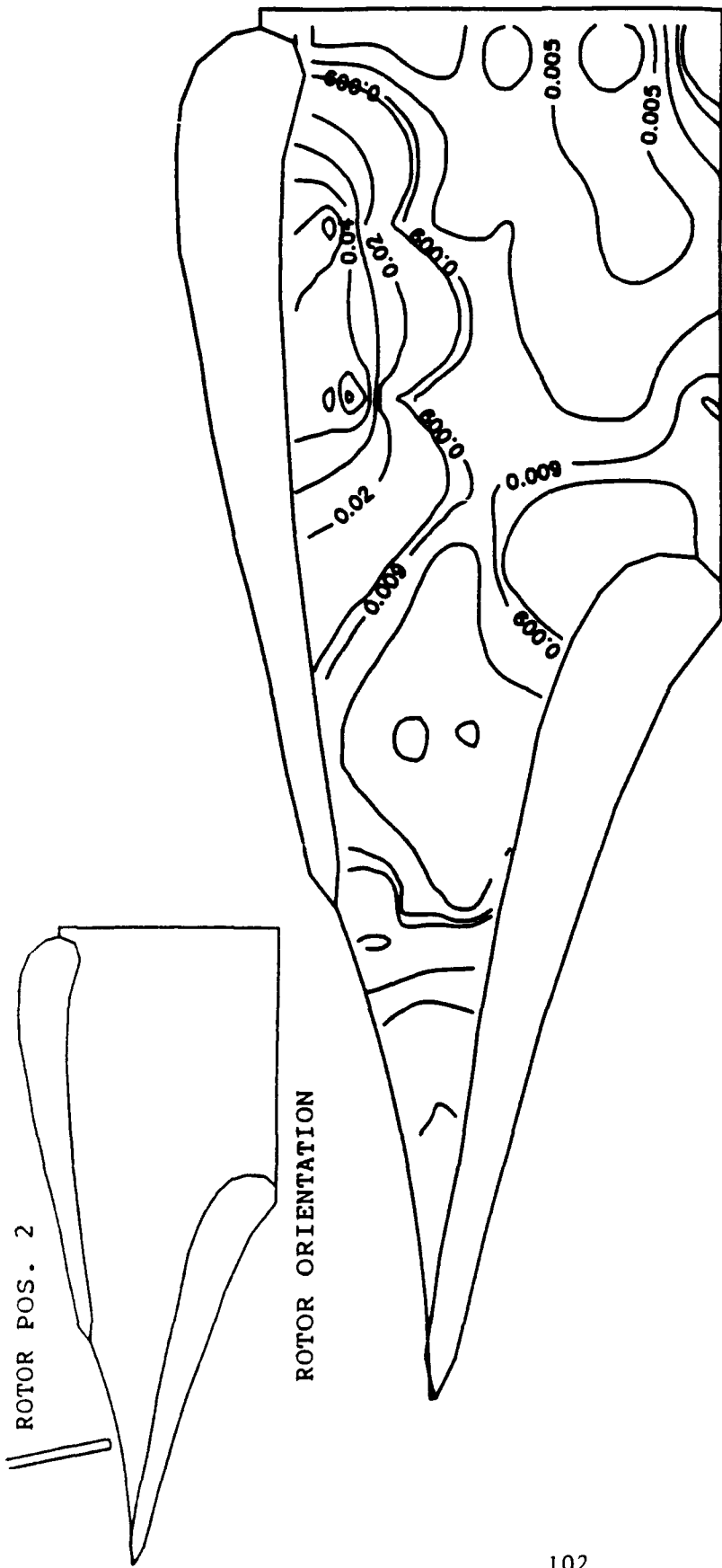
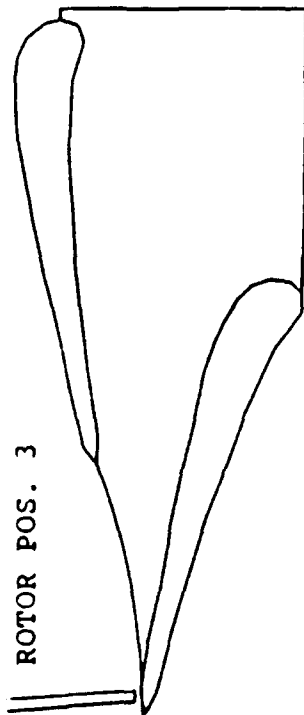


FIG. 67 TURBULENT NORMAL STRESS IN THE TANGENTIAL DIRECTION
 ON THE BLADE-TO-BLADE PLANE, $z=0.25$ ($U_{\theta}^{1/2}/V_{ex}^2$)
 (ROTOR BLADE AT THE CENTER OF THE PASSAGE)

ROTOR POS. 3



ROTOR ORIENTATION

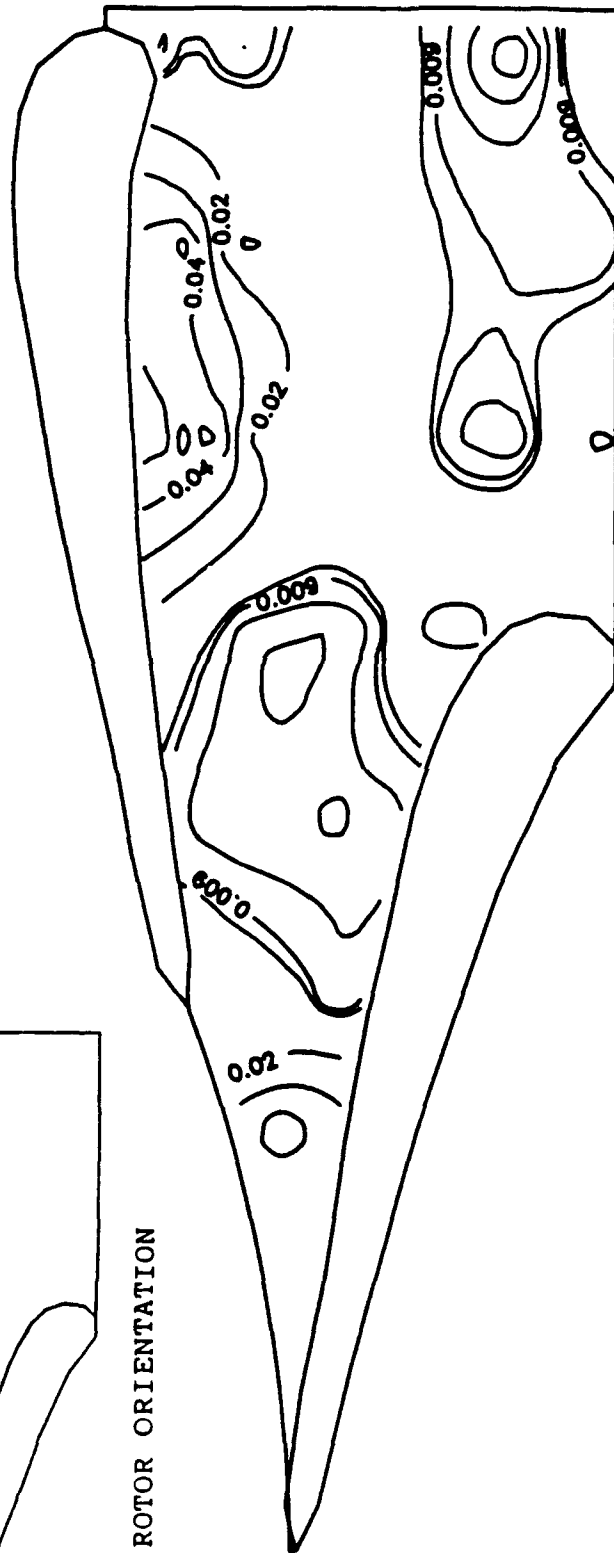


FIG. 68 TURBULENT NORMAL STRESS IN THE TANGENTIAL DIRECTION ON THE BLADE-TO-BLADE PLANE, $Z=0.25$ (U_{θ}^2/V_{ex}^2) (ROTOR BLADE LEAVING THE PASSAGE)

ROTOR POS. 1

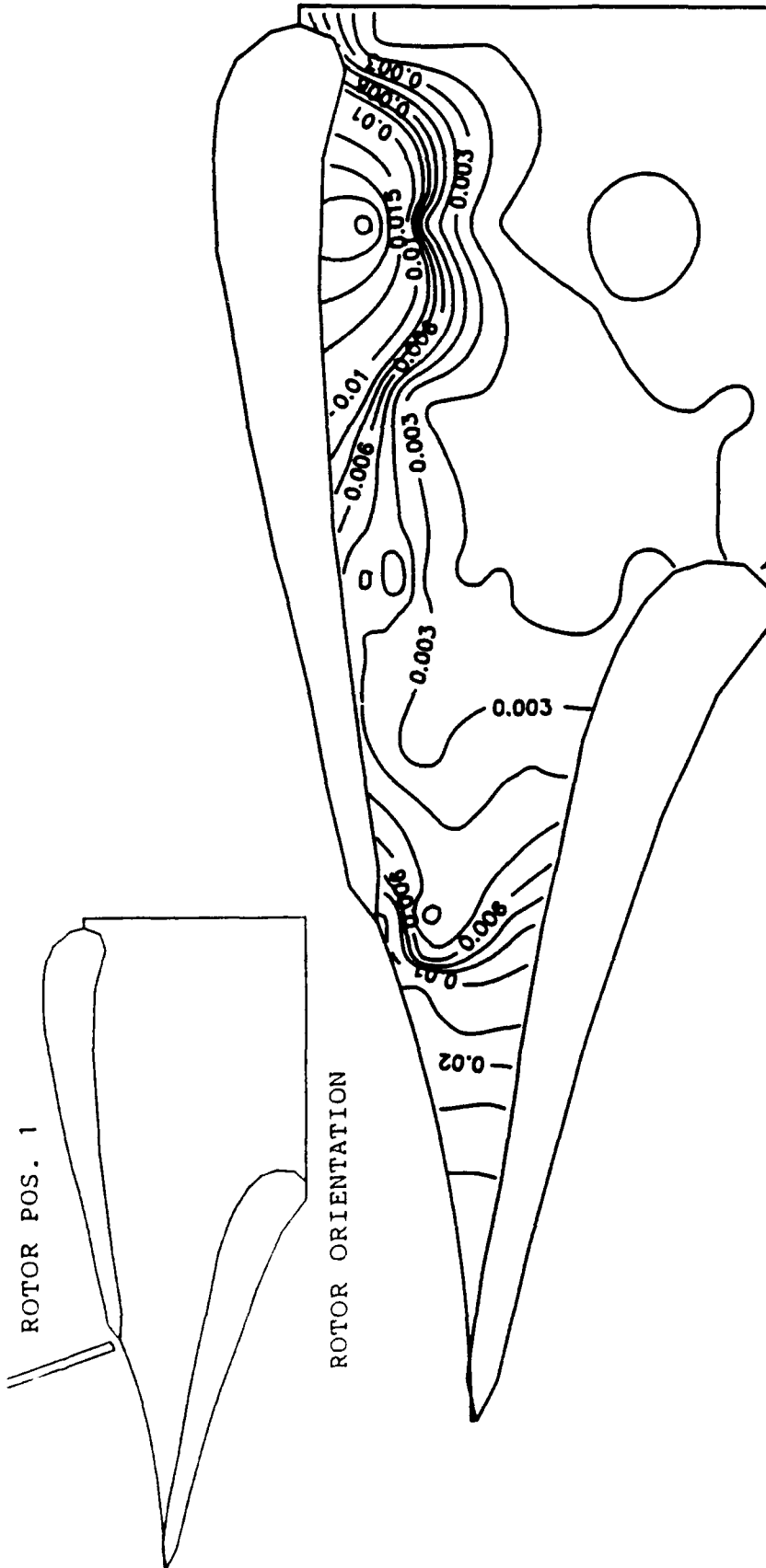


FIG. 69 TURBULENT NORMAL STRESS IN THE TANGENTIAL DIRECTION ON THE BLADE-TO-BLADE PLANE, $z=0.50$ (U_{θ}^2/V_{ex}^2) (ROTOR BLADE ENTERING THE PASSAGE)

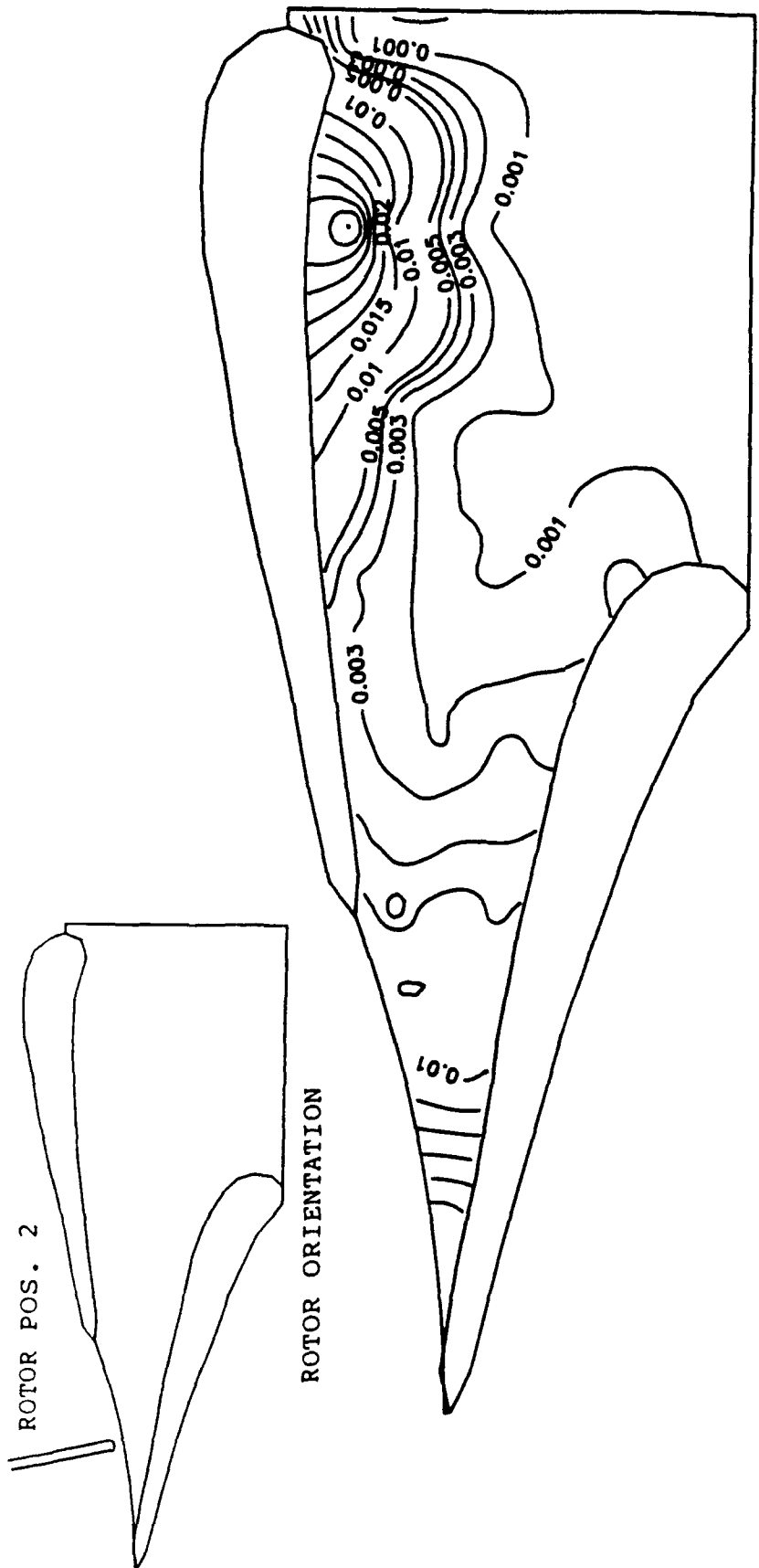


FIG. 70 TURBULENT NORMAL STRESS IN THE TANGENTIAL DIRECTION ON THE BLADE-TO-BLADE PLANE, $Z=0.50$ ($U_0'^2/V_{ex}^2$) (ROTOR BLADE AT THE CENTER OF THE PASSAGE)

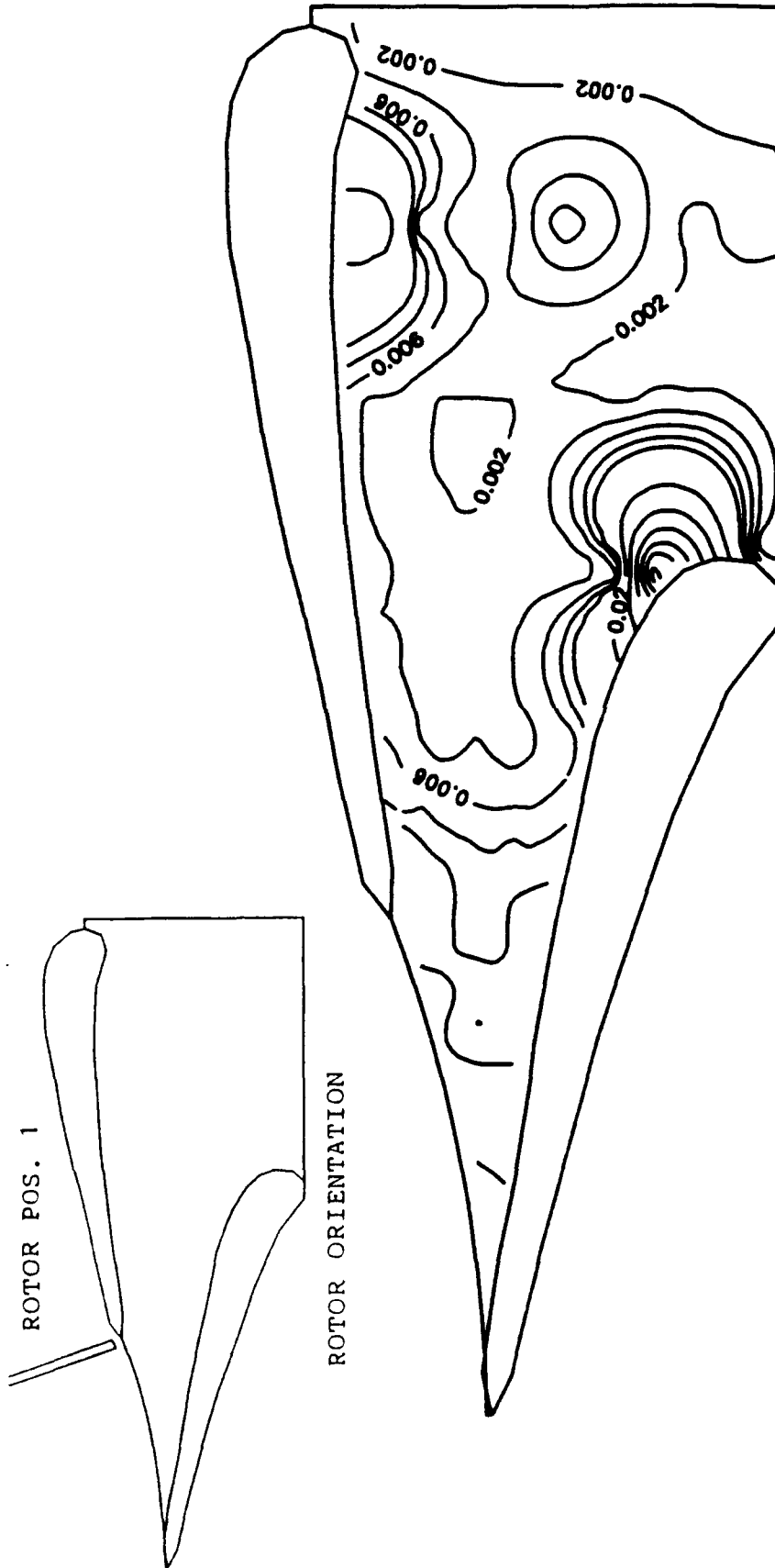


FIG. 72 TURBULENT NORMAL STRESS IN THE TANGENTIAL DIRECTION
 ON THE BLADE-TO-BLADE PLANE, $Z=0.70$ ($U_\theta'^2/V_{ex}^2$)
 (ROTOR BLADE ENTERING THE PASSAGE)

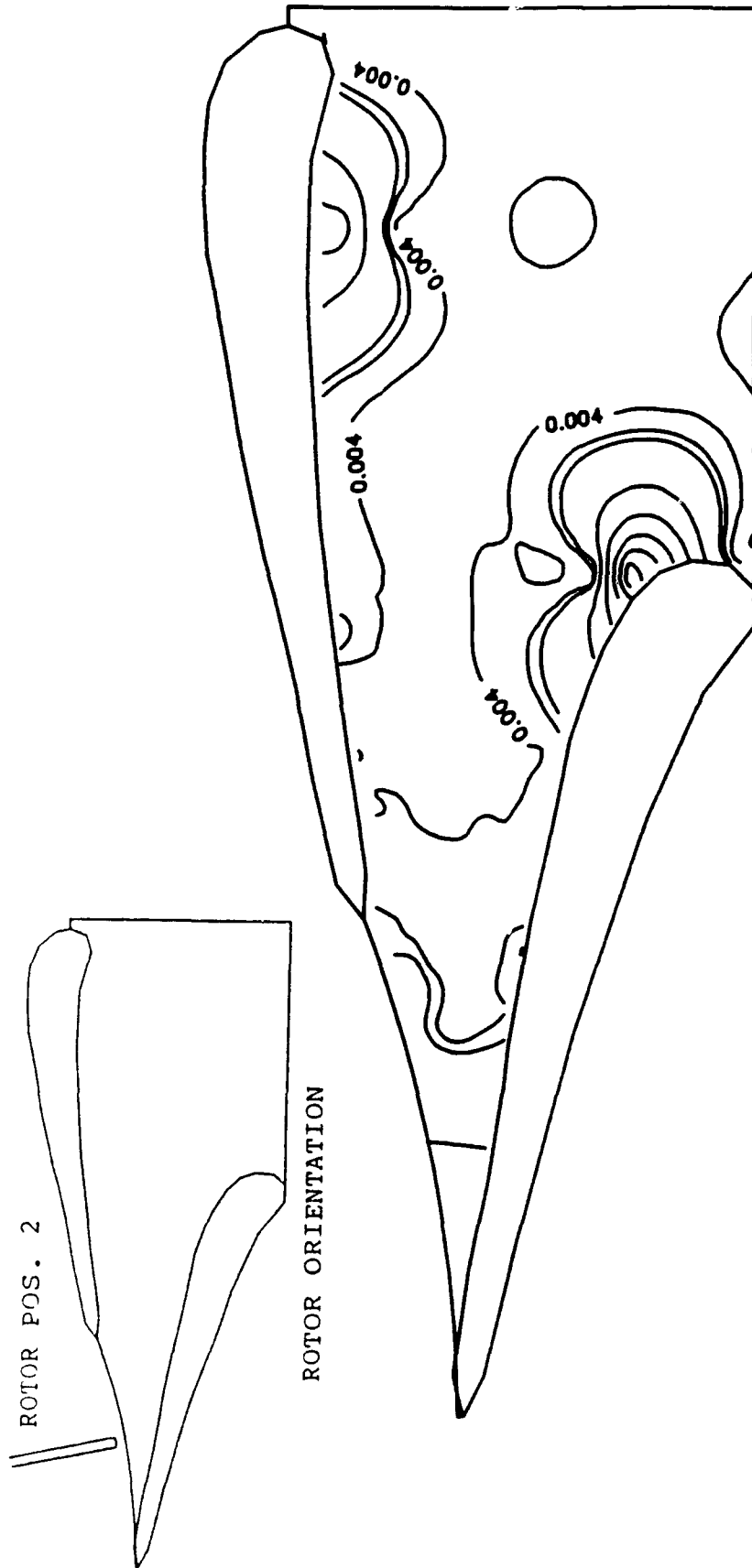
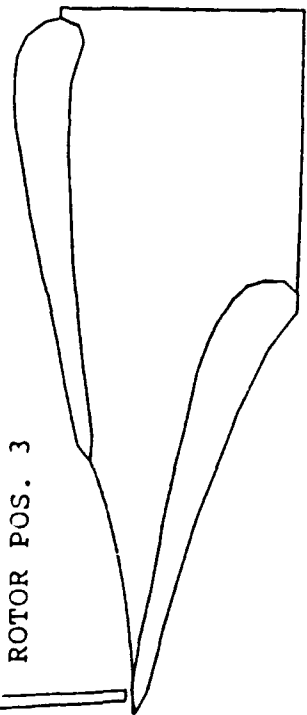


FIG. 73 TURBULENT NORMAL STRESS IN THE TANGENTIAL DIRECTION
 ON THE BLADE-TO-BLADE PLANE, $Z=0.70$ (U_{θ}^2/V_{ex}^2)
 (ROTOR BLADE AT THE CENTER OF THE PASSAGE)

ROTOR POS. 3



ROTOR ORIENTATION

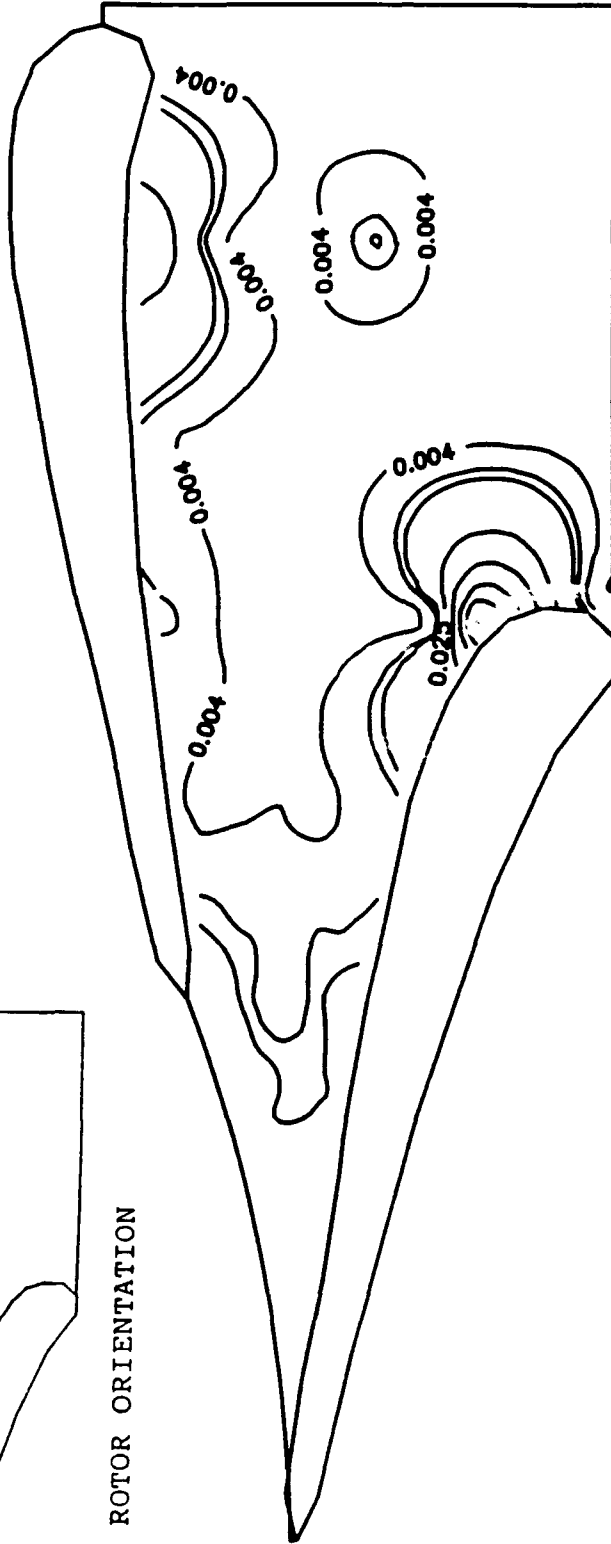


FIG. 74 TURBULENT NORMAL STRESS IN THE TANGENTIAL DIRECTION ON THE BLADE-TO-BLADE PLANE, $Z=0.70$ (U_{θ}^2/V_{ex}^2) (ROTOR BLADE LEAVING THE PASSAGE)

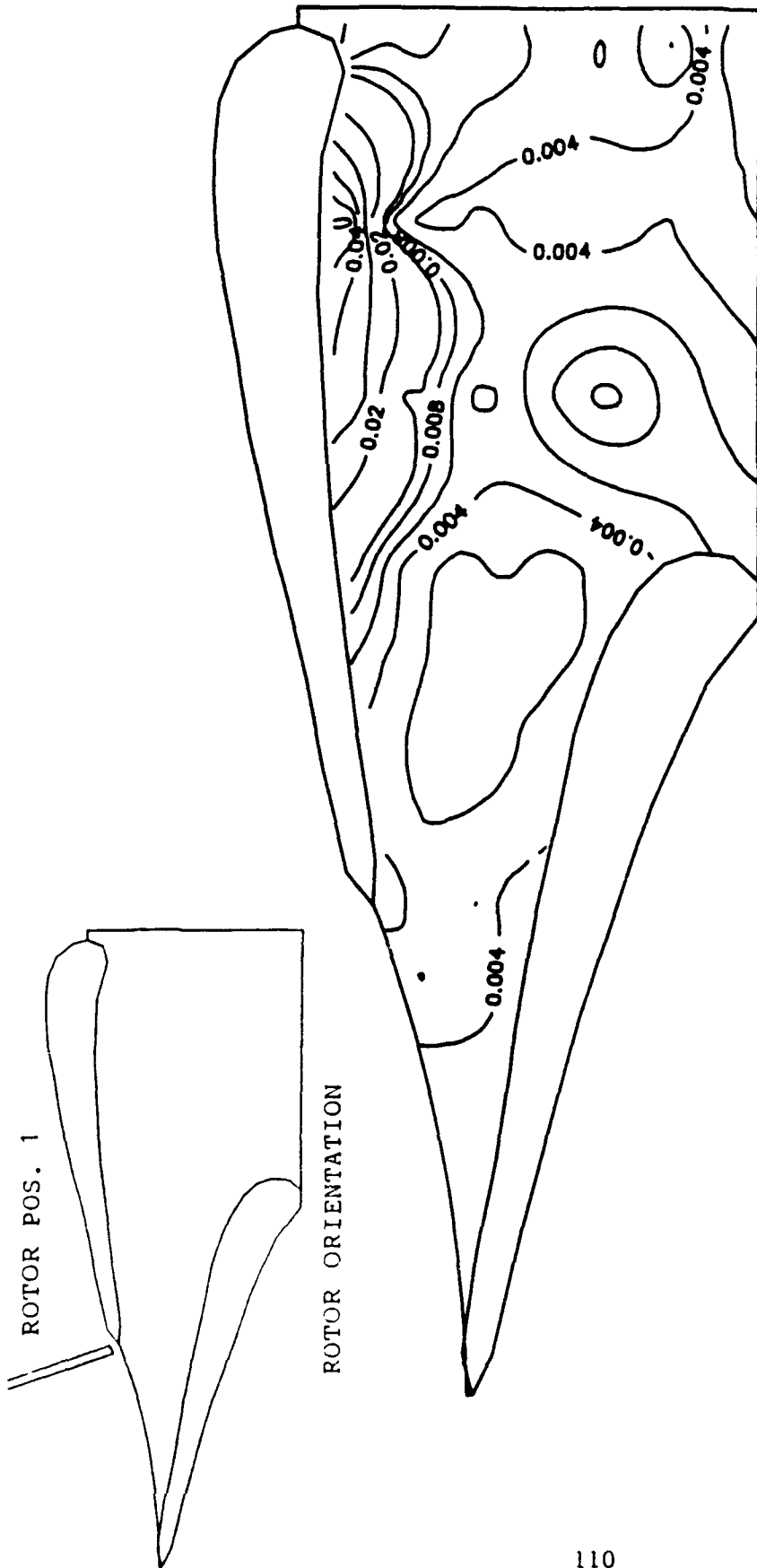


FIG. 75 TURBULENT REYNOLDS STRESS ON THE BLADE-TO-BLADE PLANE, $Z=0.10$ ($U'U_{\theta}'/V^2$) (ROTOR BLADE ENTERING THE PASSAGE)

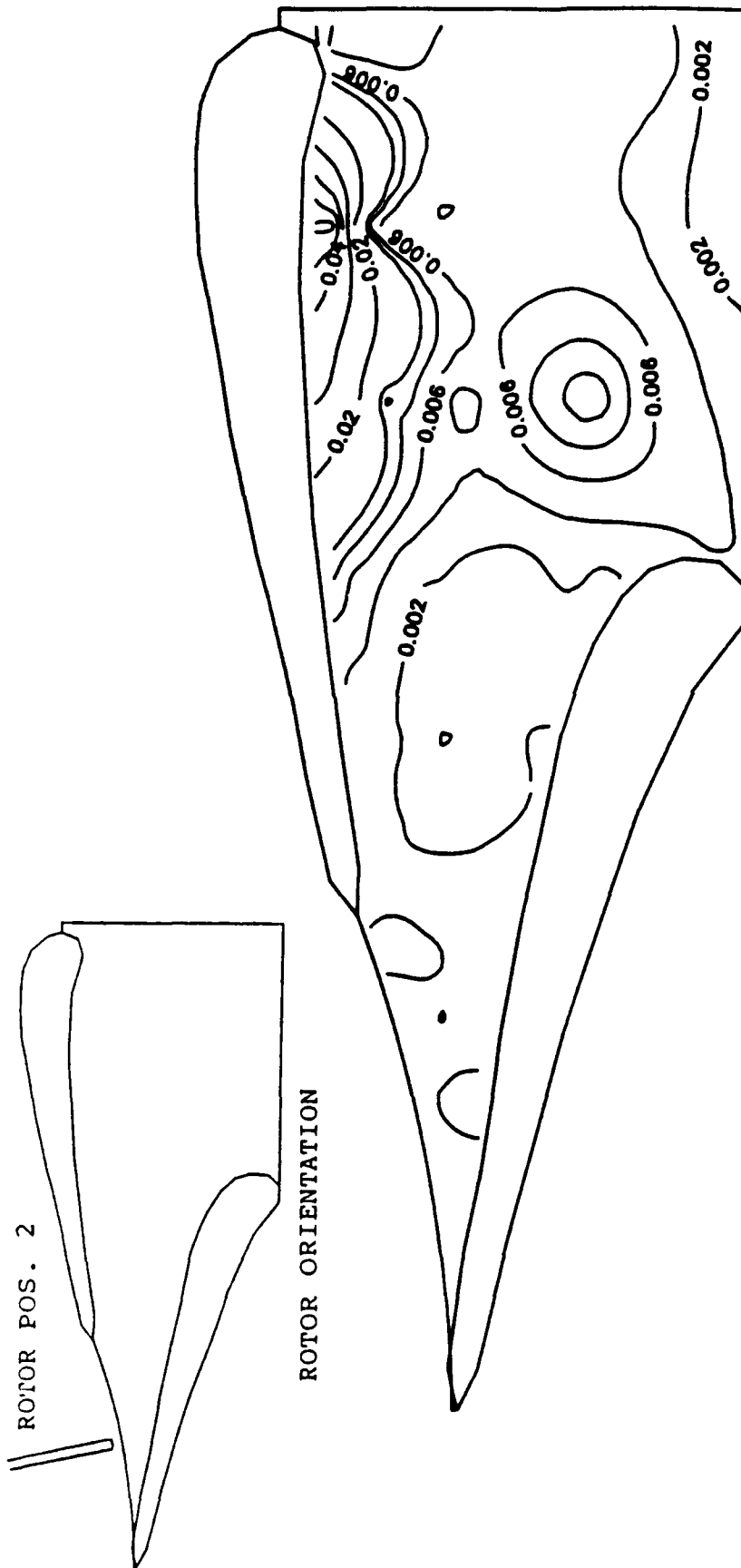


FIG. 76 TURBULENT REYNOLDS STRESS ON THE BLADE-TO-BLADE PLANE, $Z=0.10$ ($U_r'U_\theta'/V_{ex}^2$) (ROTOR BLADE AT THE CENTER OF THE PASSAGE)

ROTOR POS. 3

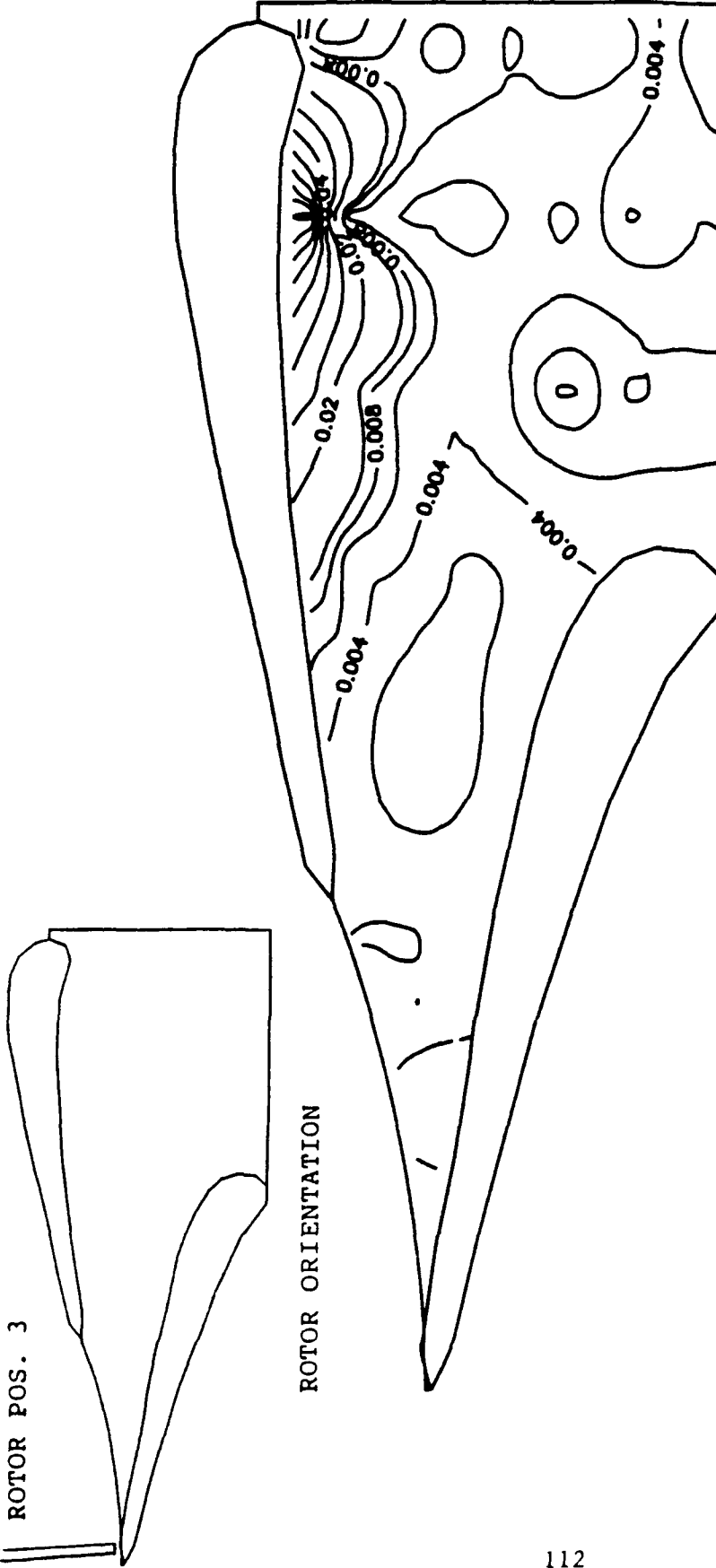


FIG. 77 TURBULENT REYNOLDS STRESS ON THE BLADE-TO-BLADE
PLANE, $Z=0.10$ ($U'U'_\theta/V^2$)
(ROTOR BLADE LEAVING THE PASSAGE)

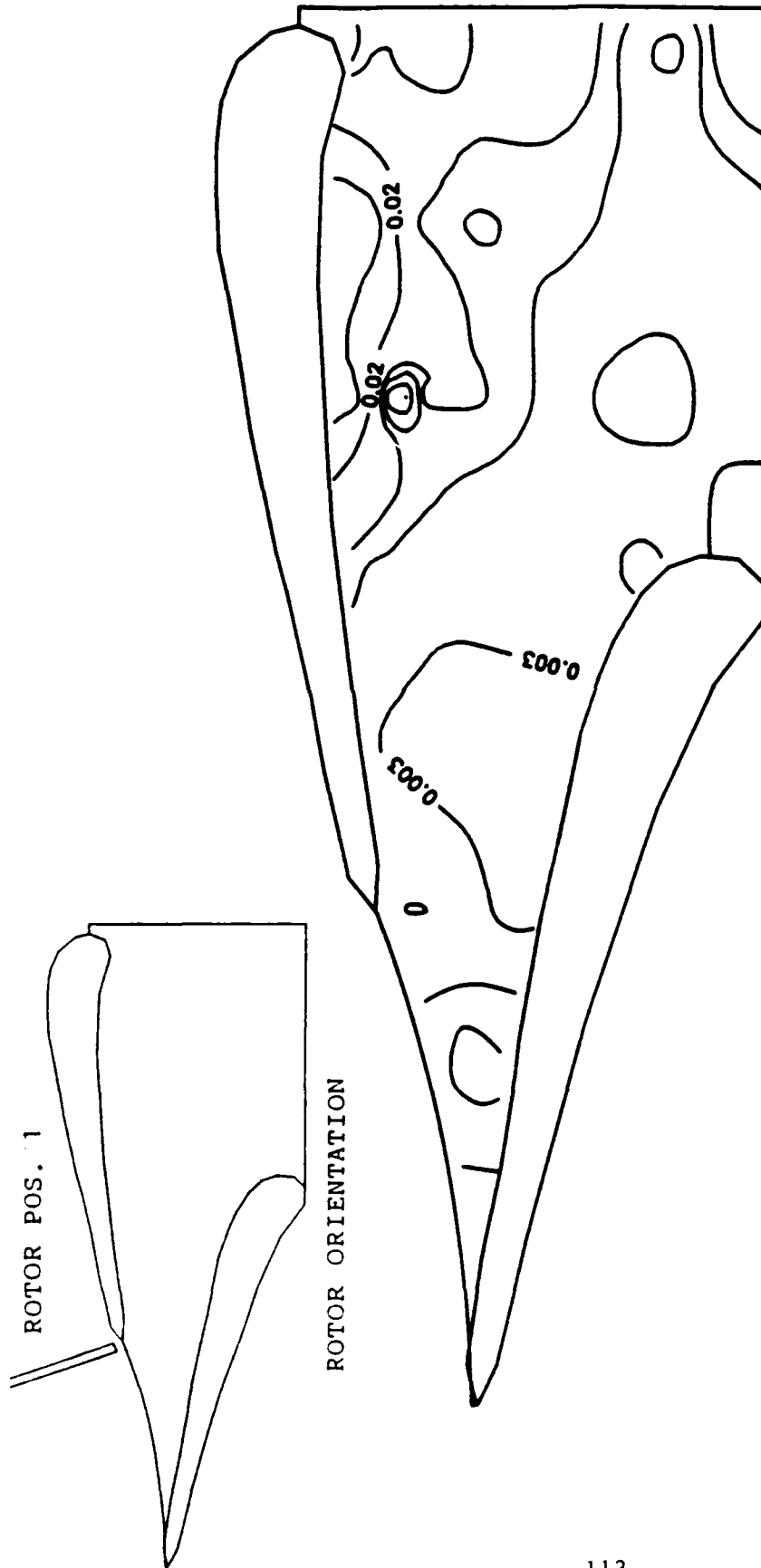


FIG. 78 TURBULENT REYNOLDS STRESS ON THE BLADE-TO-BLADE PLANE, $Z=0.25$ ($U_f U_\theta' / V_{ex}^2$) (ROTOR BLADE ENTERING THE PASSAGE)

ROTOR POS. 3

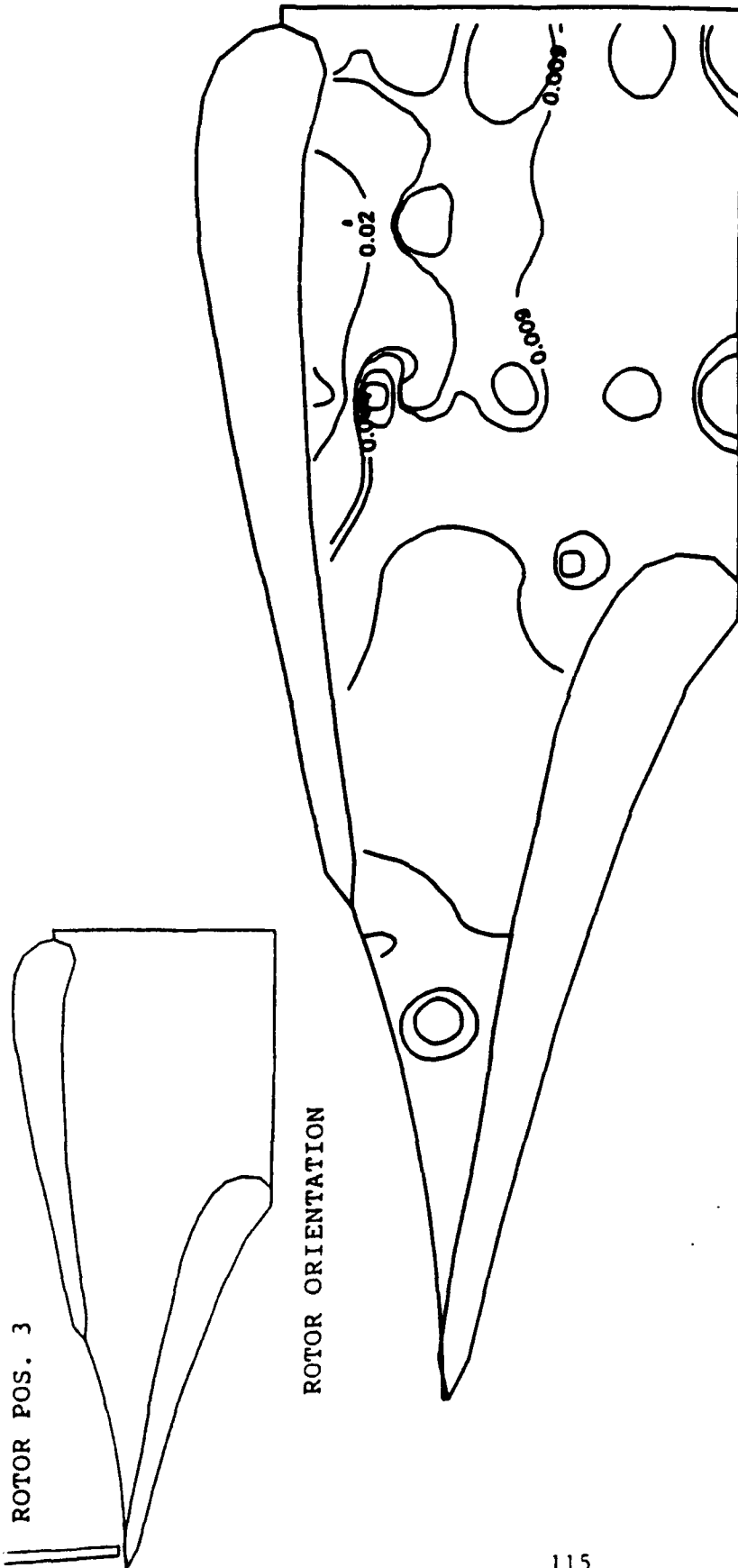


FIG. 80 TURBULENT REYNOLDS STRESS ON THE BLADE-TO-BLADE PLANE, $Z=0.25$ ($U'U_{\theta}'/V_{ex}^2$) (ROTOR BLADE LEAVING THE PASSAGE)

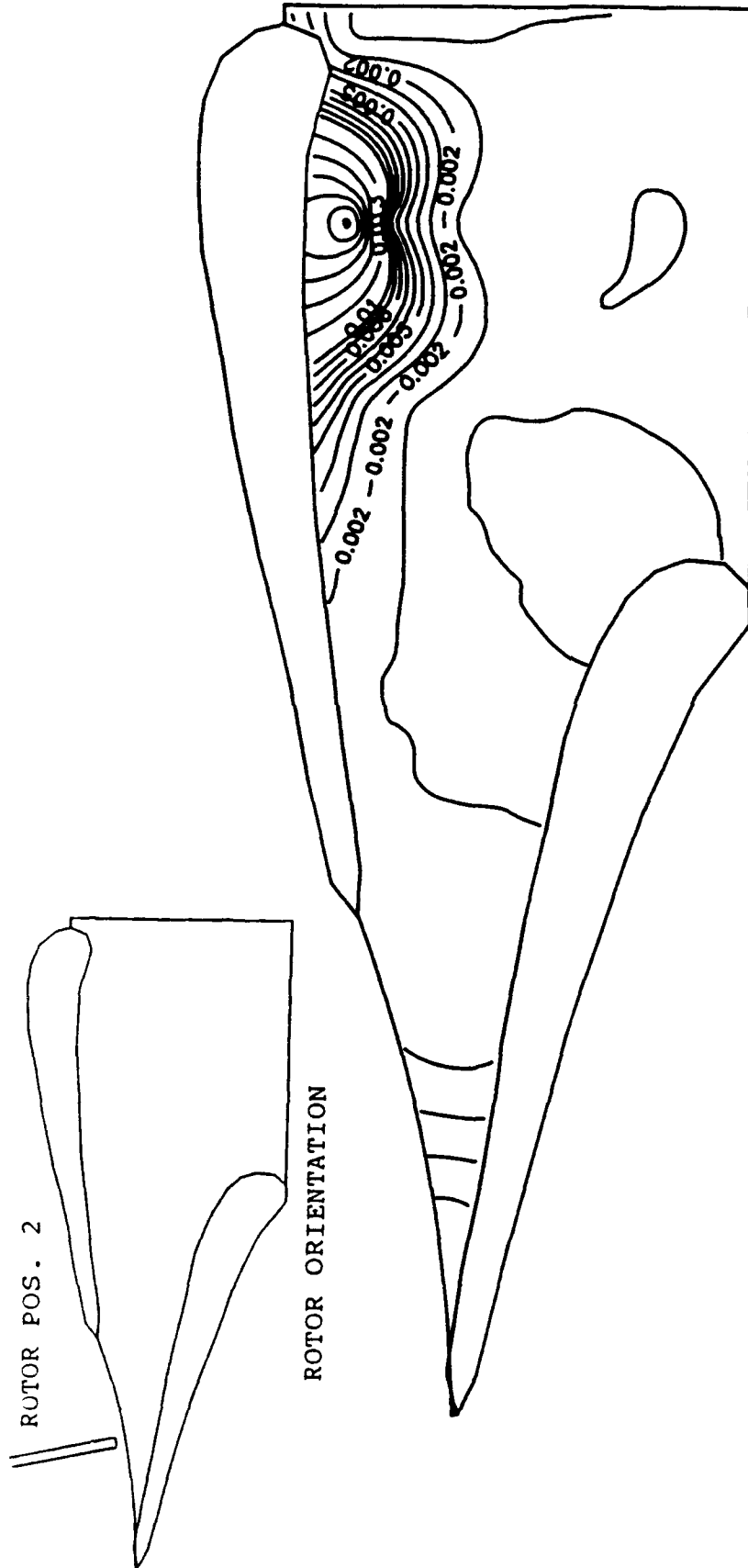
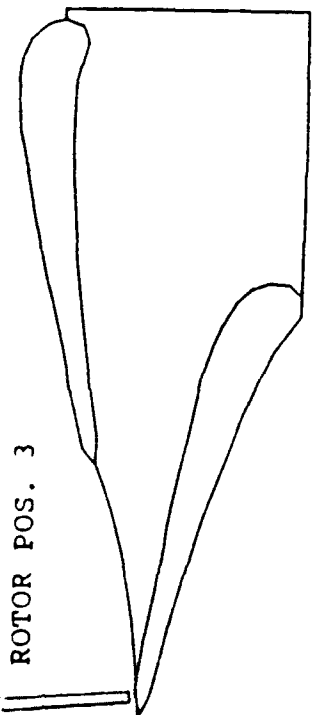


FIG. 82 TURBULENT REYNOLDS STRESS ON THE BLADE-TO-BLADE
 PLANE, $Z=0.50$ ($U_i'U_j'/V_{ex}^2$)
 (ROTOR BLADE AT THE CENTER OF THE PASSAGE)

ROTOR POS. 3



ROTOR ORIENTATION

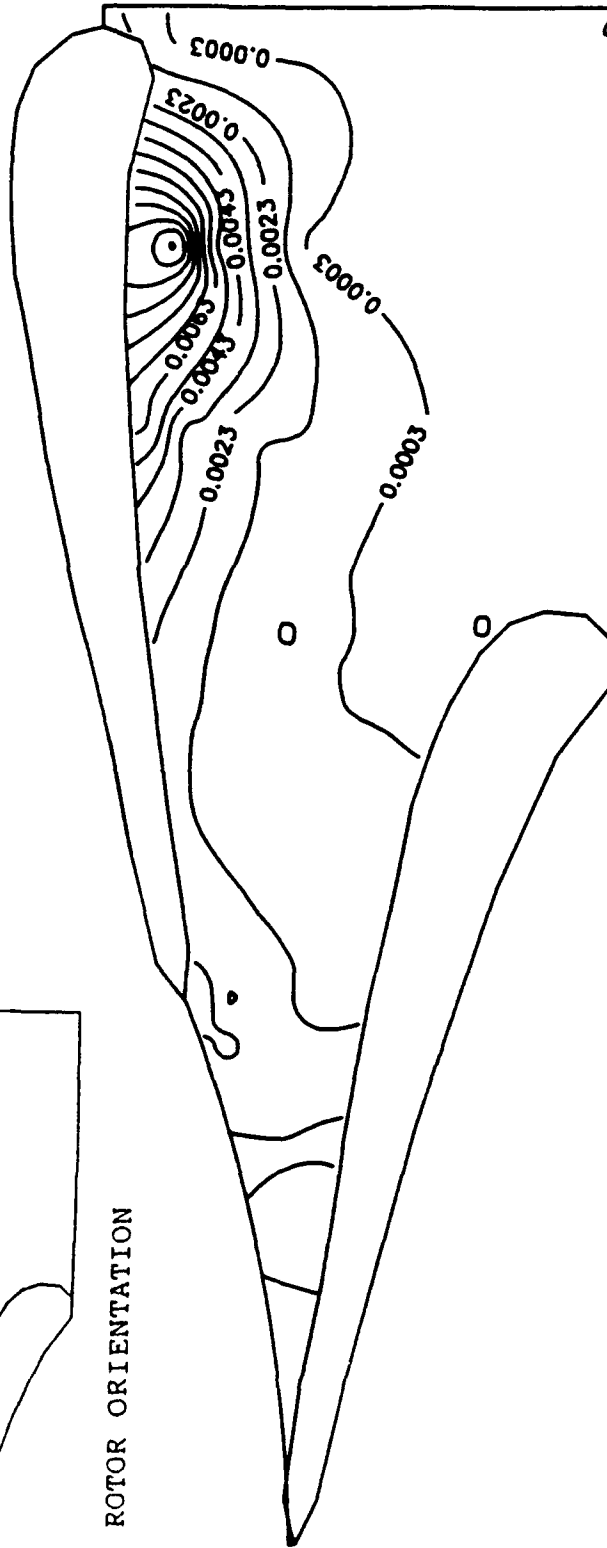


FIG. 83 TURBULENT REYNOLDS STRESS ON THE BLADE-TO-BLADE
PLANE, $Z=0.50$ ($U_1'U_2'/V^2$)
(ROTOR BLADE LEAVING THE PASSAGE)

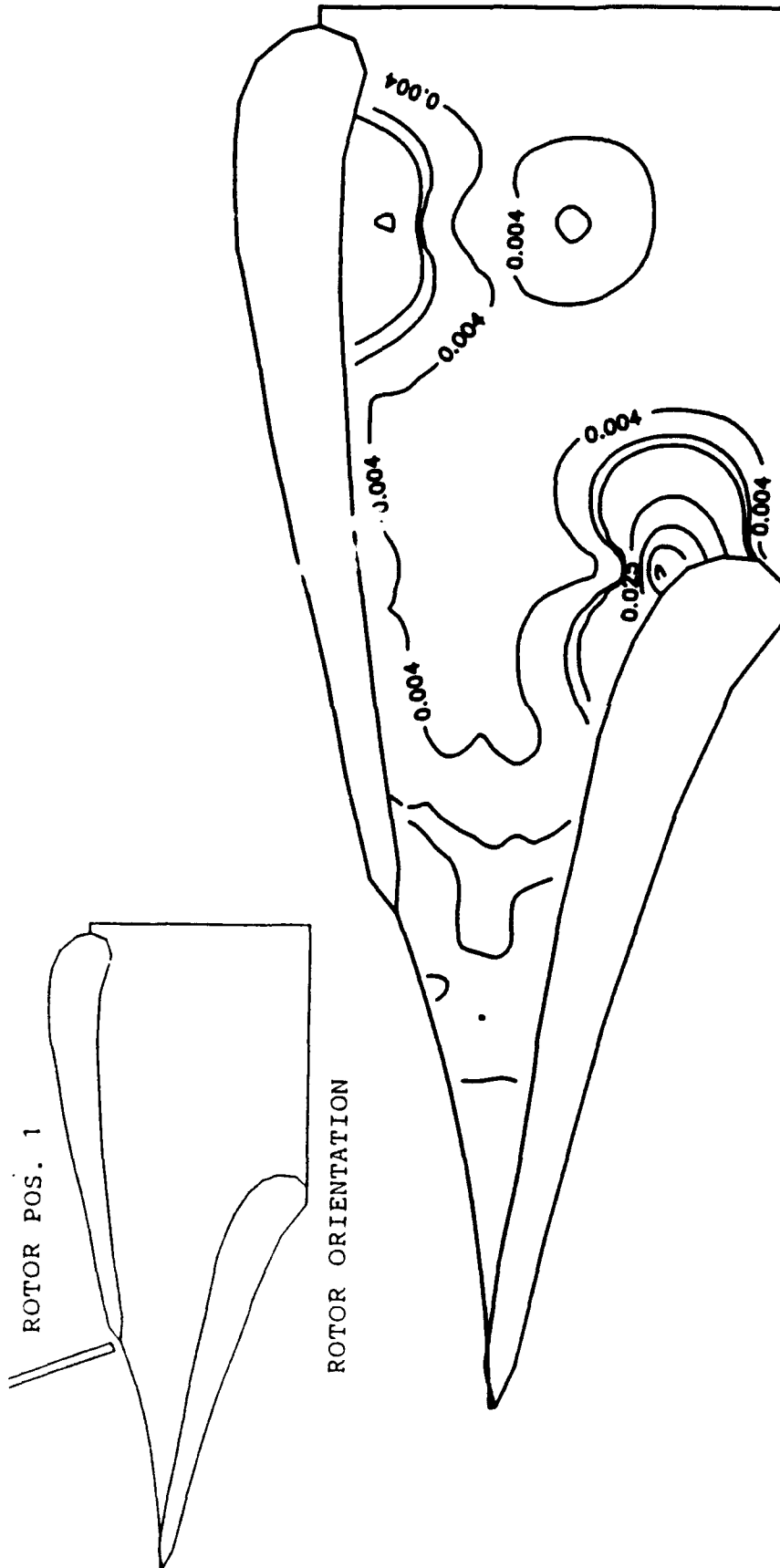


FIG. 84 TURBULENT REYNOLDS STRESS ON THE BLADE-TO-BLADE PLANE, $Z=0.70$ ($U'U'_x/V^2$) (ROTOR BLADE ENTERING THE PASSAGE)

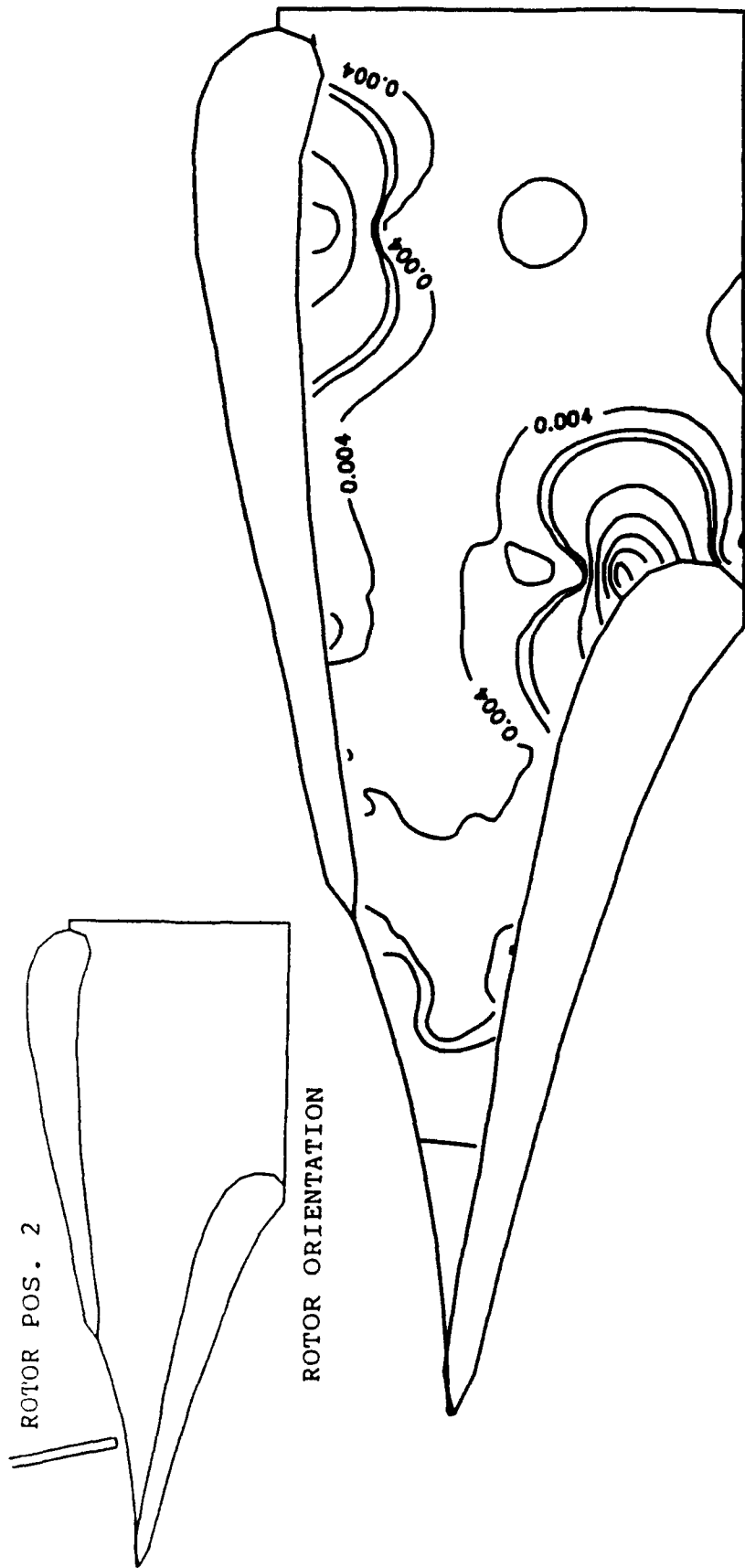


FIG. 85 TURBULENT REYNOLDS STRESS ON THE BLADE-TO-BLADE PLANE, $z=0.70$ ($U'U'_\theta / V^2$) (ROTOR BLADE AT THE CENTER OF THE PASSAGE)

ROTOR POS. 3

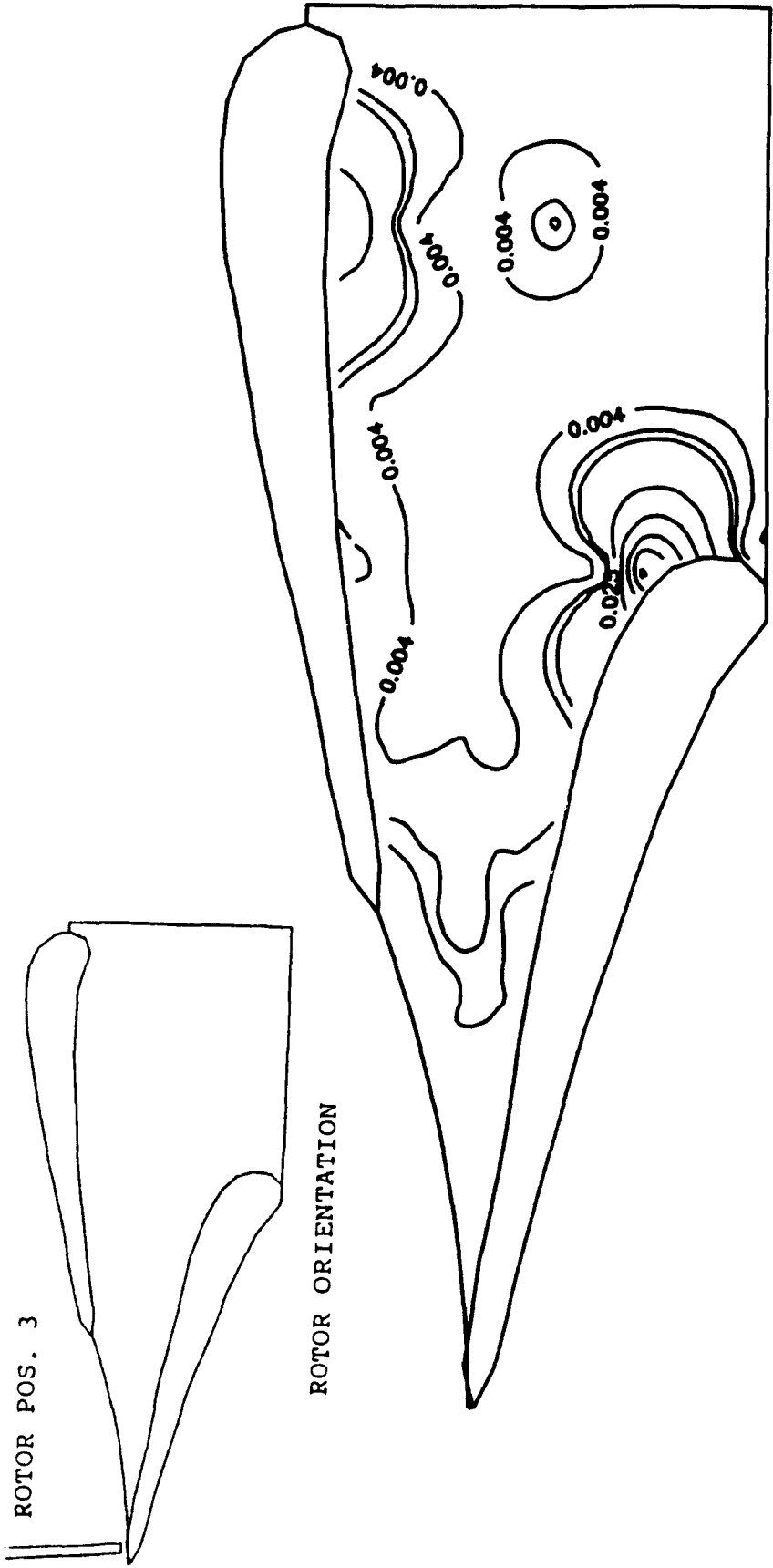


FIG. 86 TURBULENT REYNOLDS STRESS ON THE BLADE-TO-BLADE PLANE, $Z=0.70$ ($U'U'_\theta / V^2$) (ROTOR BLADE LEAVING THE PASSAGE)

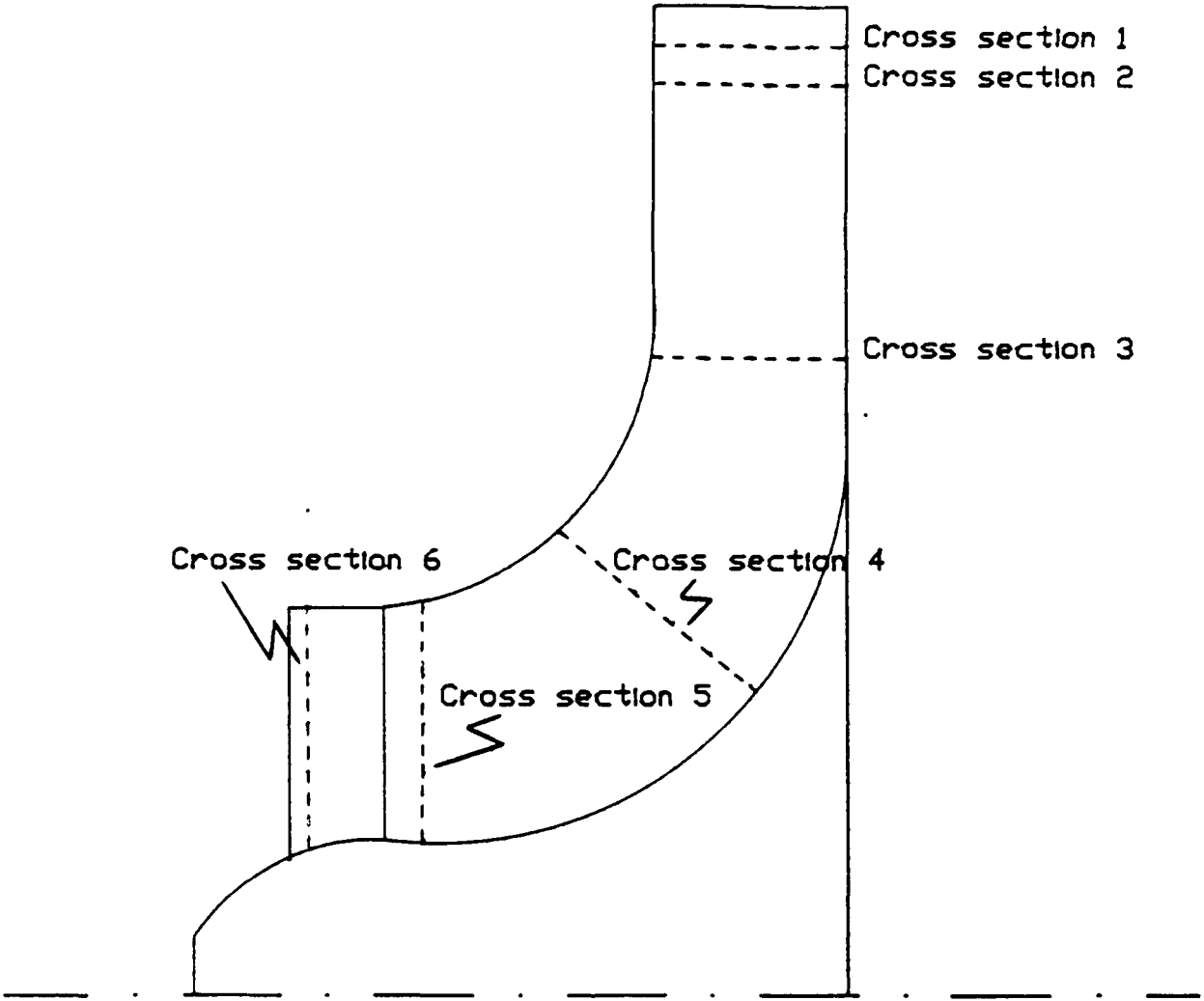


FIG. 87 MEASUREMENT LOCATIONS IN THE ROTOR

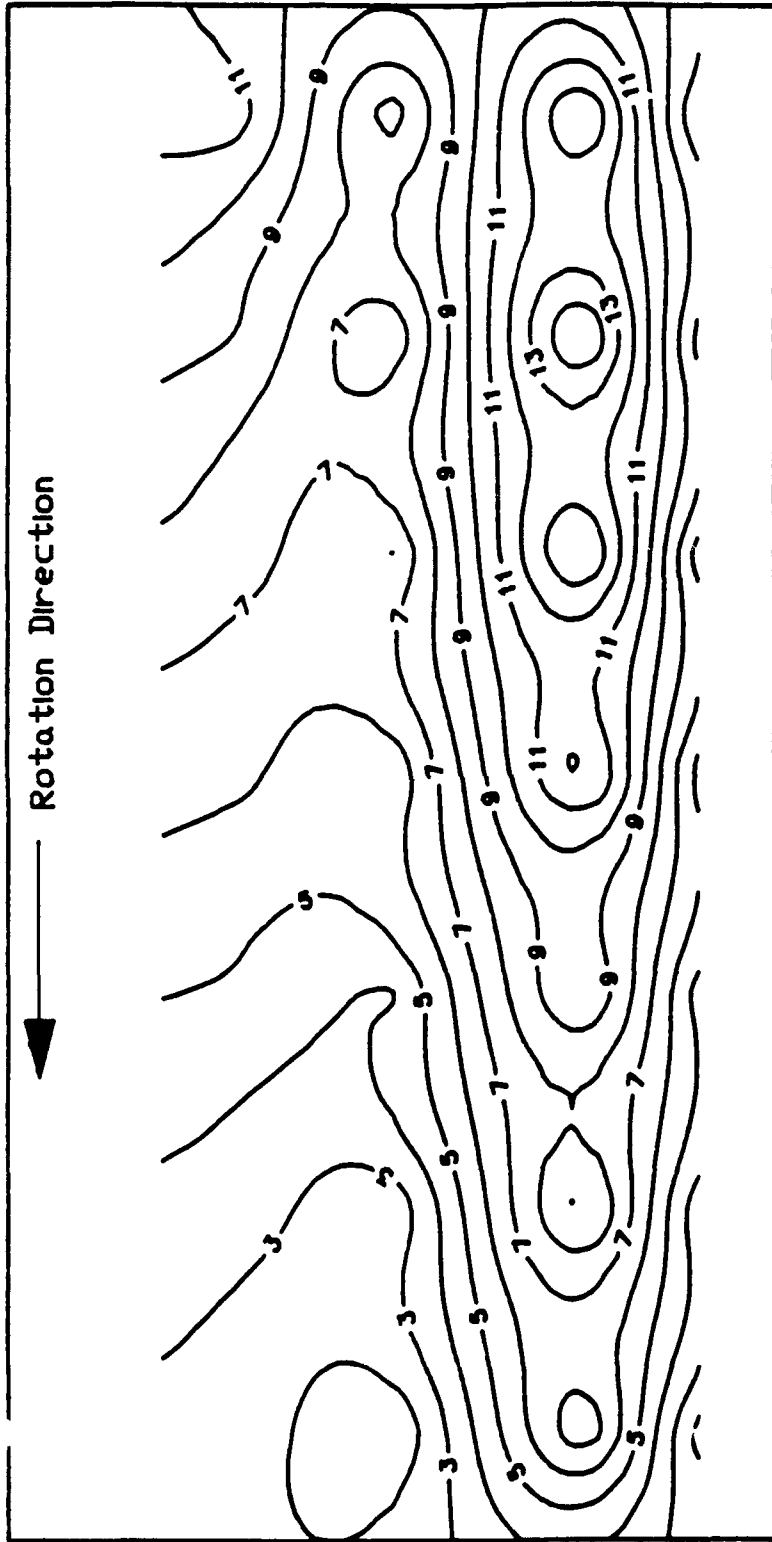


FIG. 88 STREAMWISE RELATIVE VELOCITY CONTOURS (m/s)
CROSS SECTION 1

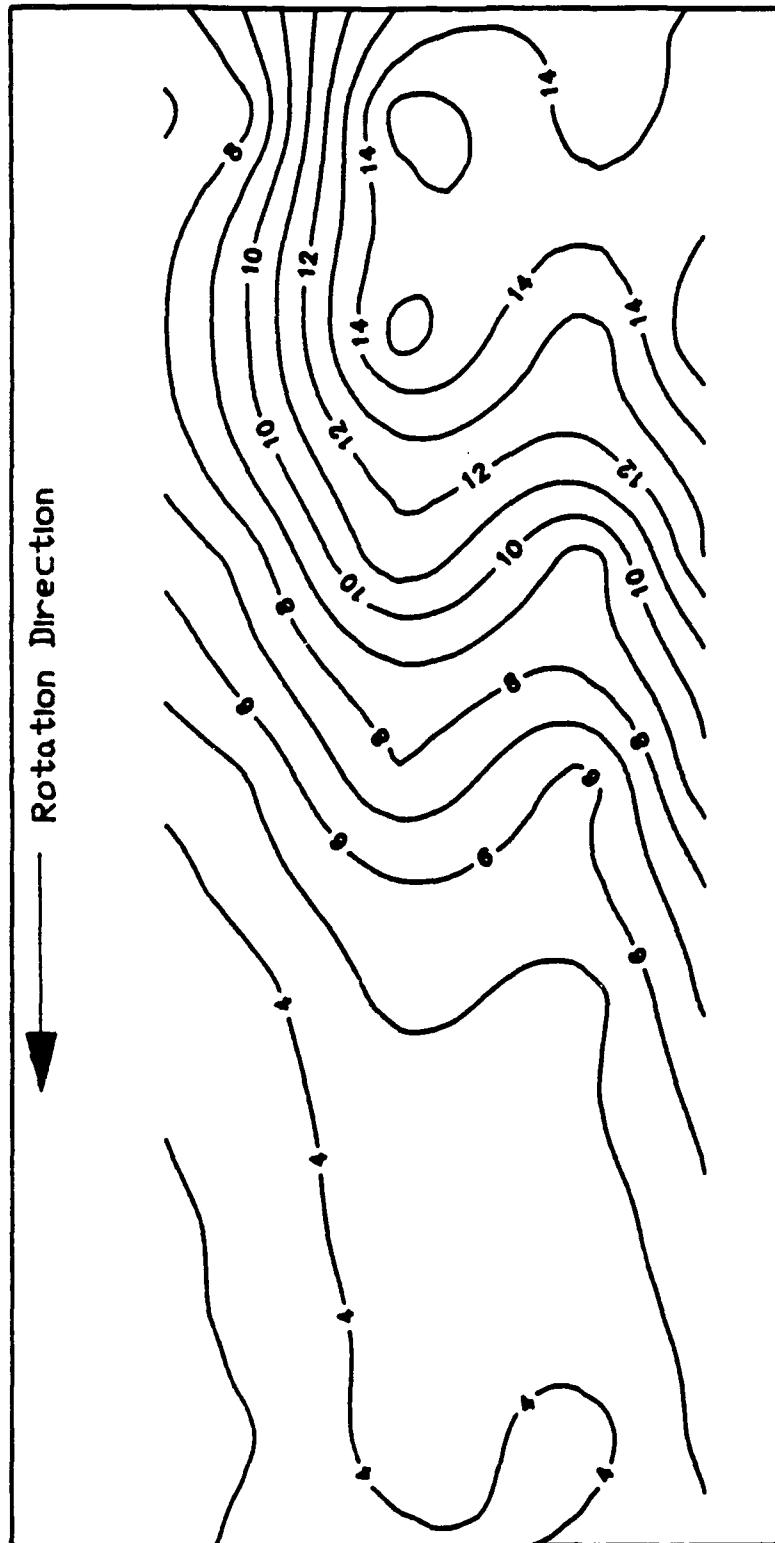


FIG. 89 TANGENTIAL RELATIVE VELOCITY CONTOURS (m/s)
CROSS SECTION 1

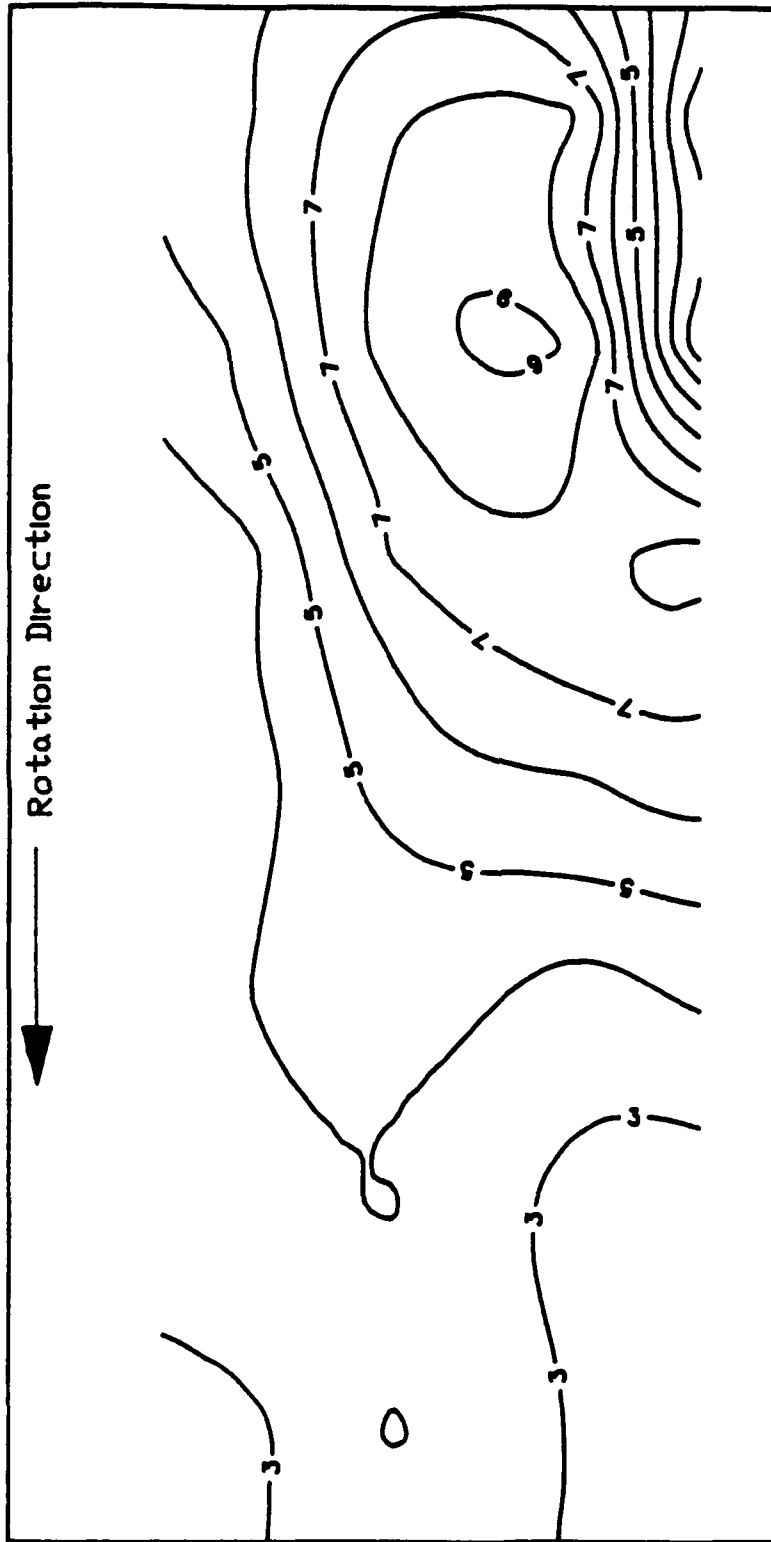


FIG. 90 STREAMWISE RELATIVE VELOCITY CONTOURS (m/s)
CROSS SECTION 2

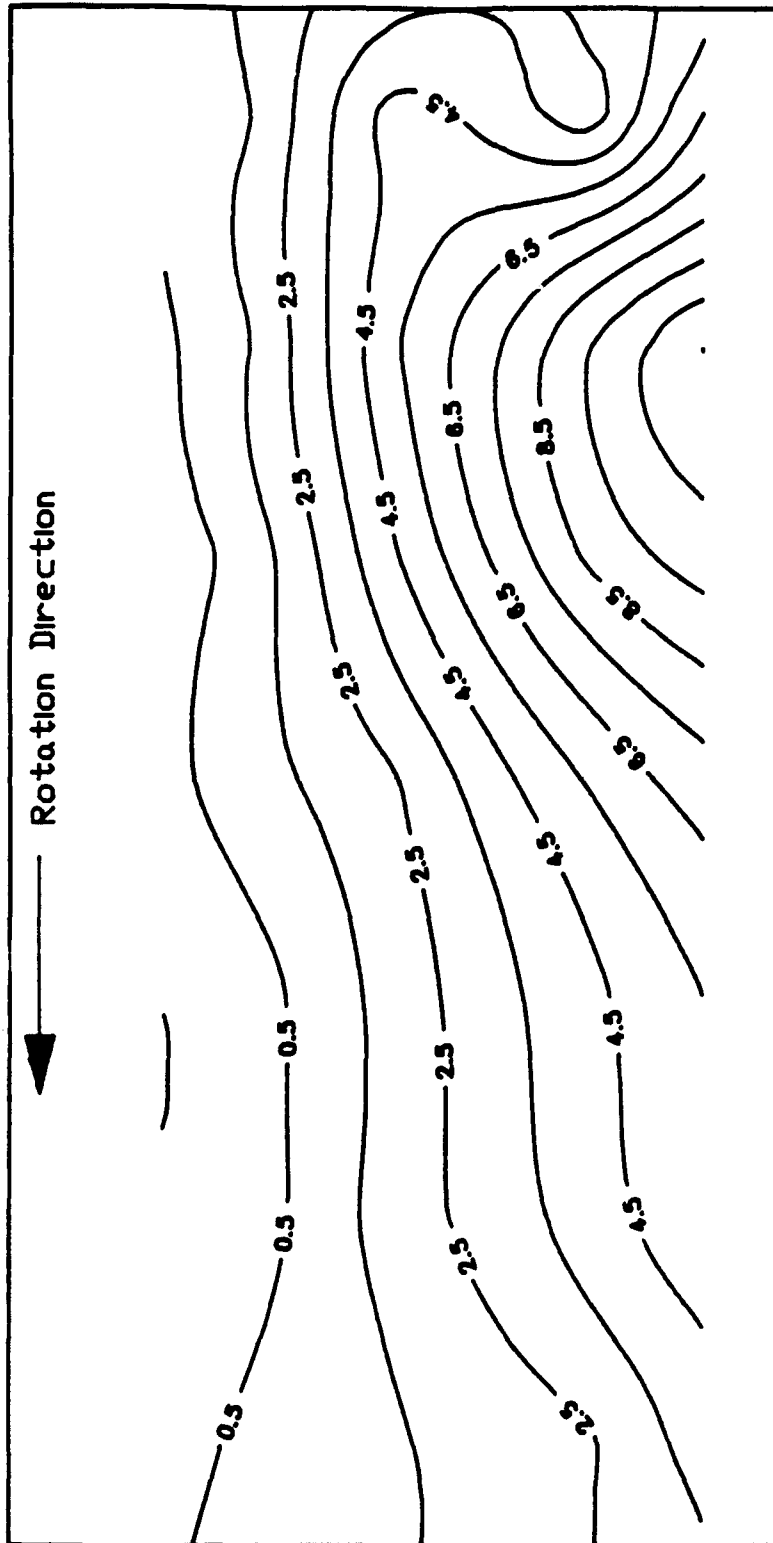


FIG. 91 TANGENTIAL RELATIVE VELOCITY CONTOURS (m/s)
CROSS SECTION 2

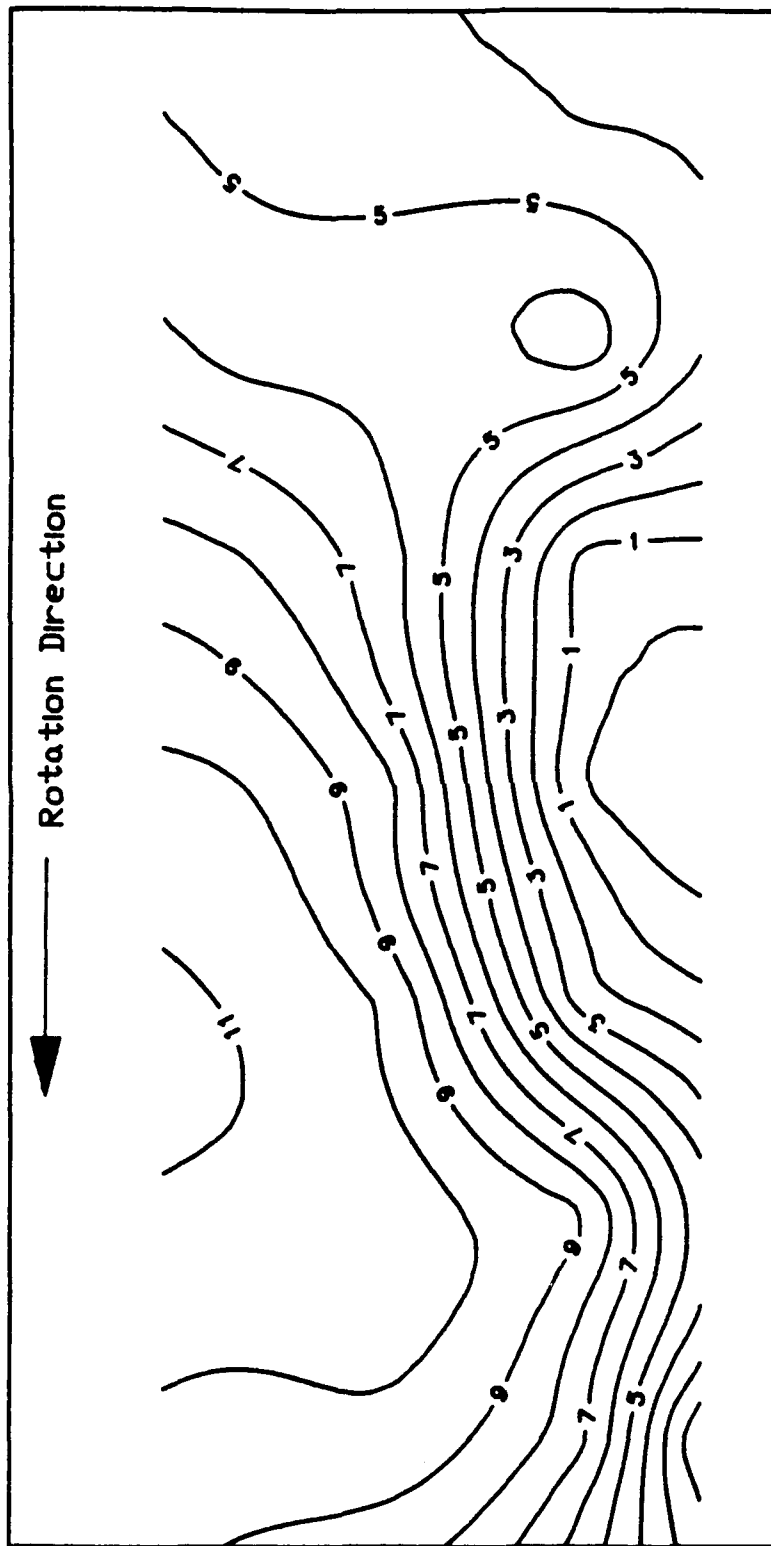


FIG. 92 STREAMWISE RELATIVE VELOCITY CONTOURS (m/s)
CROSS SECTION 3

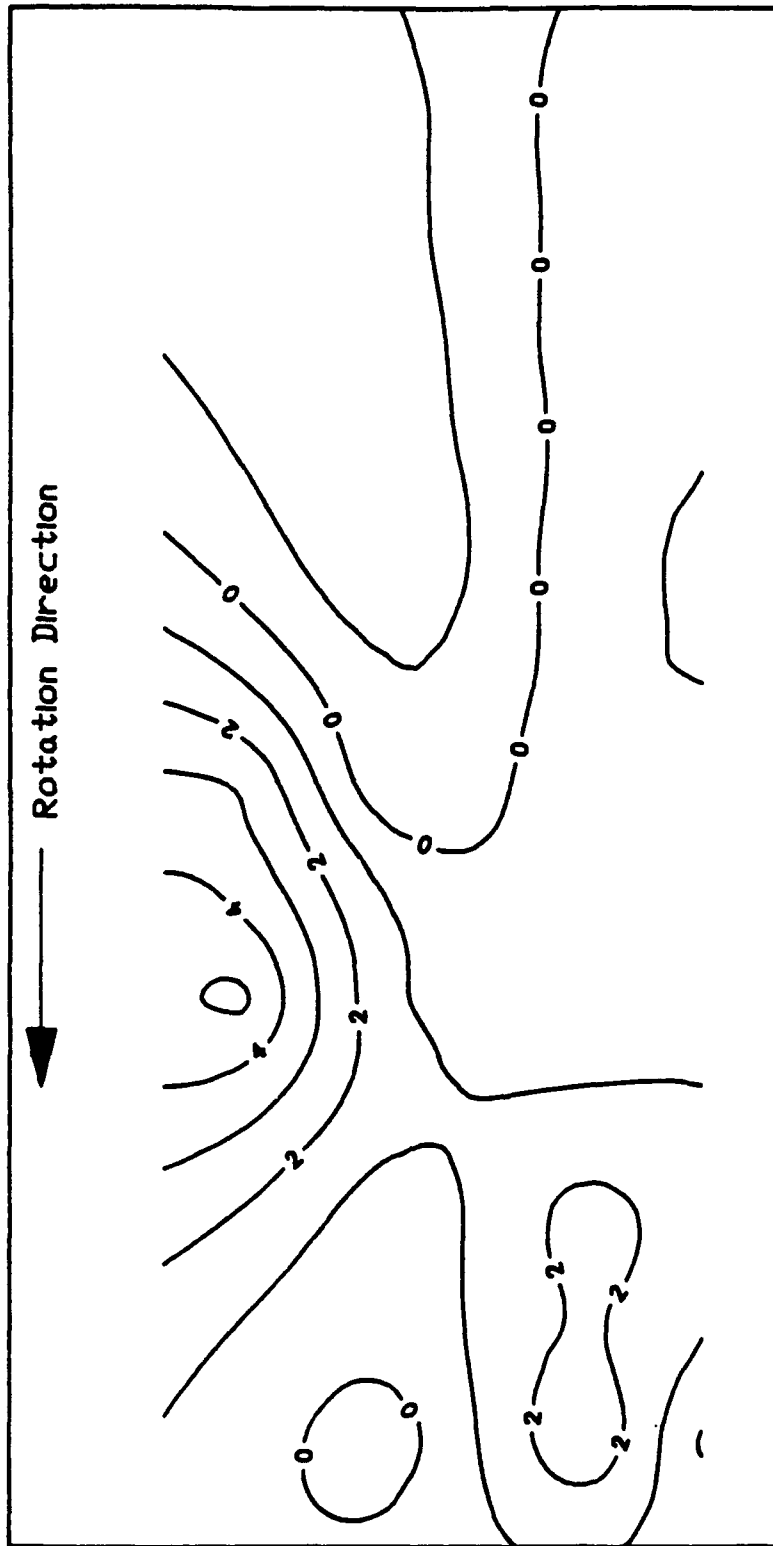


FIG. 93 TANGENTIAL RELATIVE VELOCITY CONTOURS (m/s)
CROSS SECTION 3

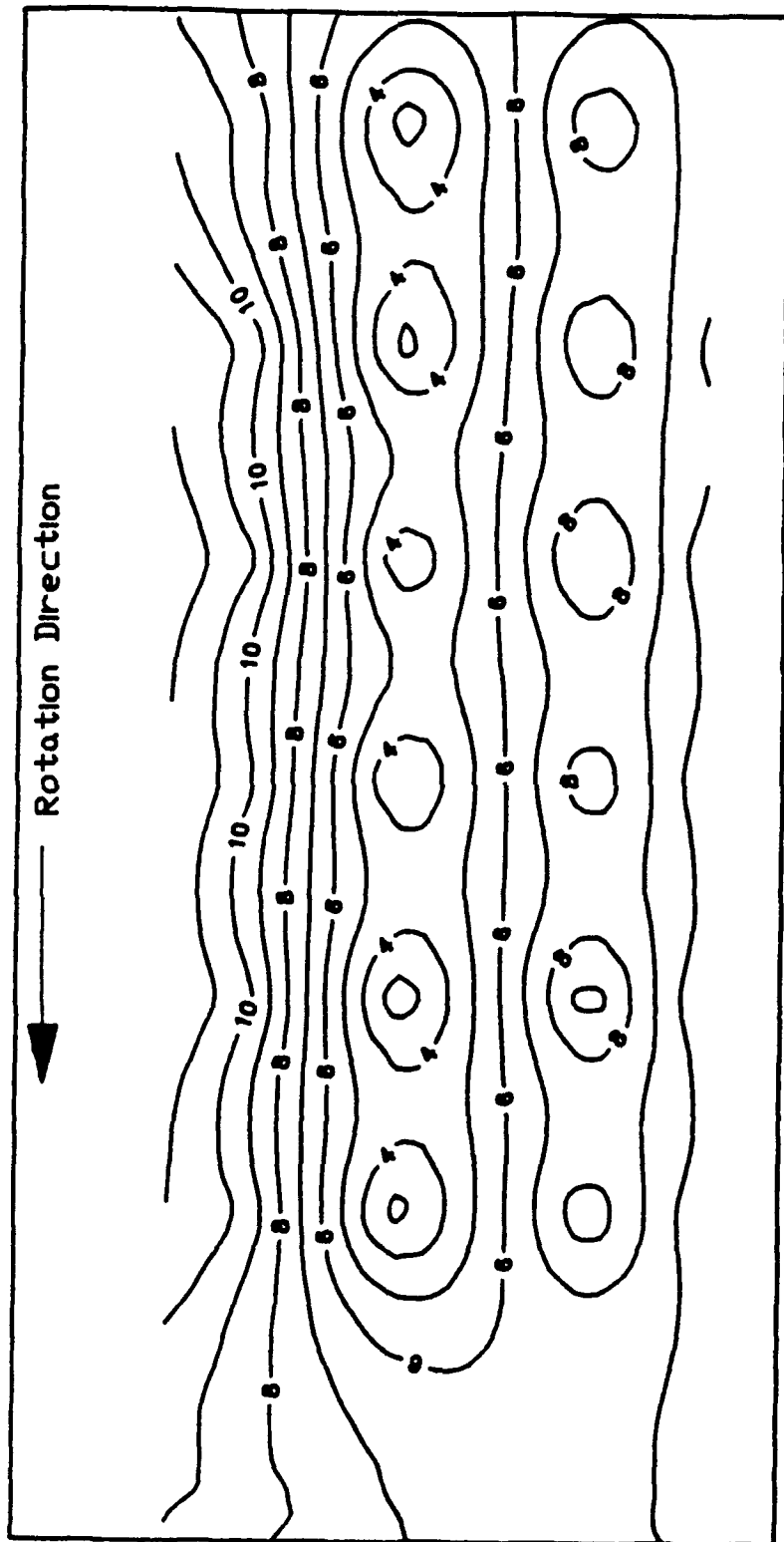


FIG. 94 STREAMWISE RELATIVE VELOCITY CONTOURS (m/s)
CROSS SECTION 4

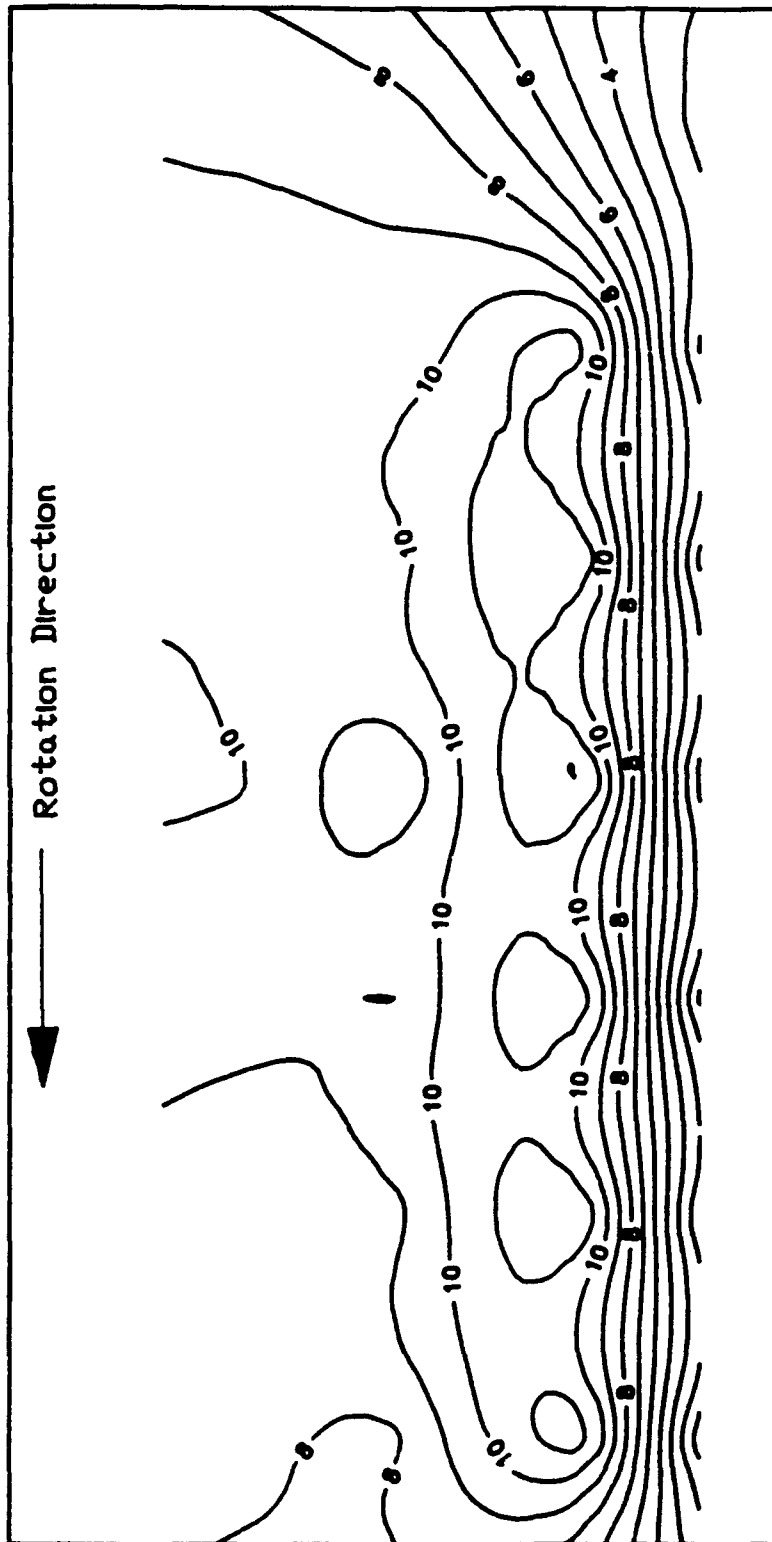


FIG. 96 STREAMWISE RELATIVE VELOCITY CONTOURS (m/s)
CROSS SECTION 5

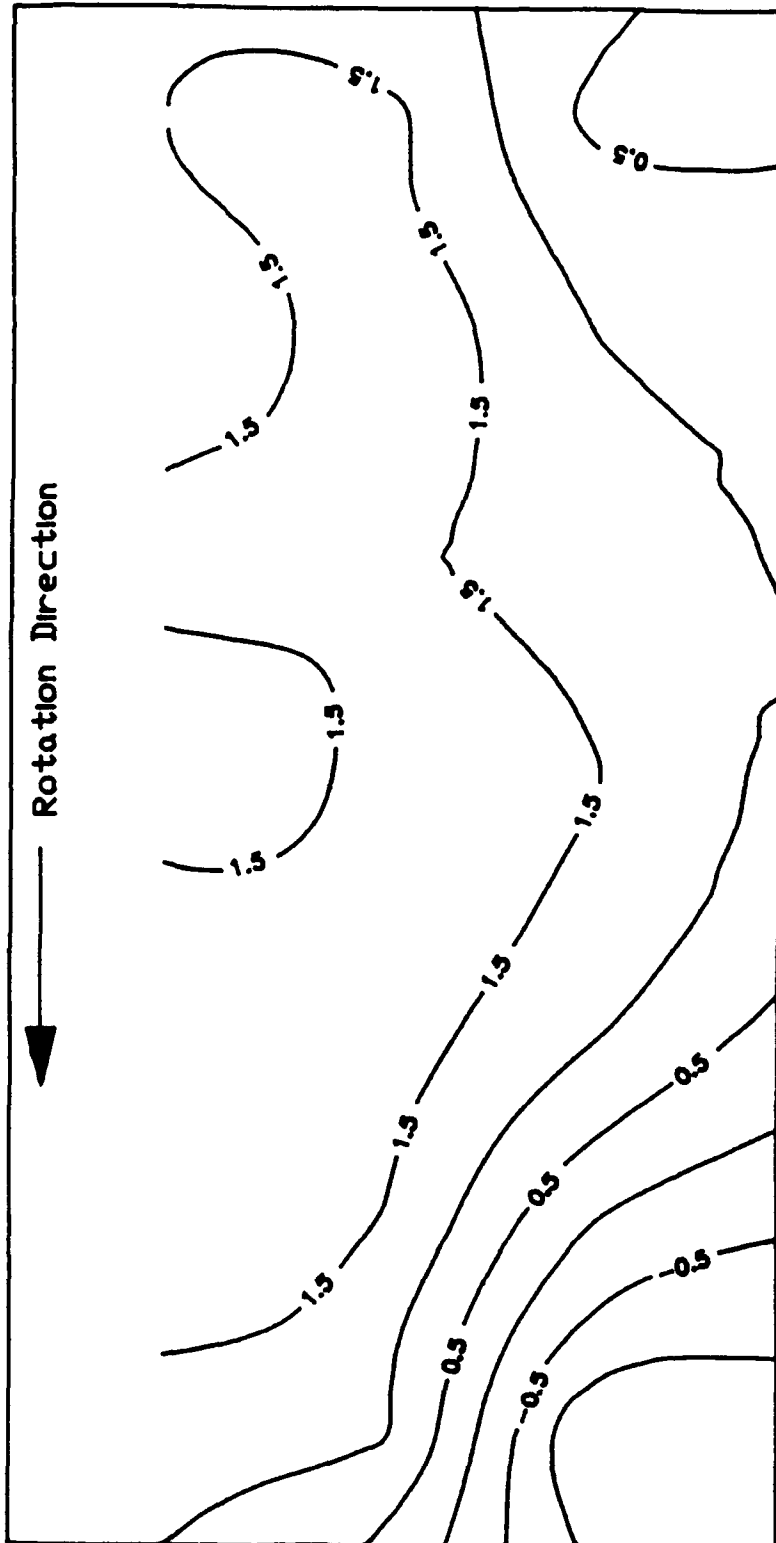


FIG. 99 TANGENTIAL RELATIVE VELOCITY CONTOURS (m/s)
CROSS SECTION 6

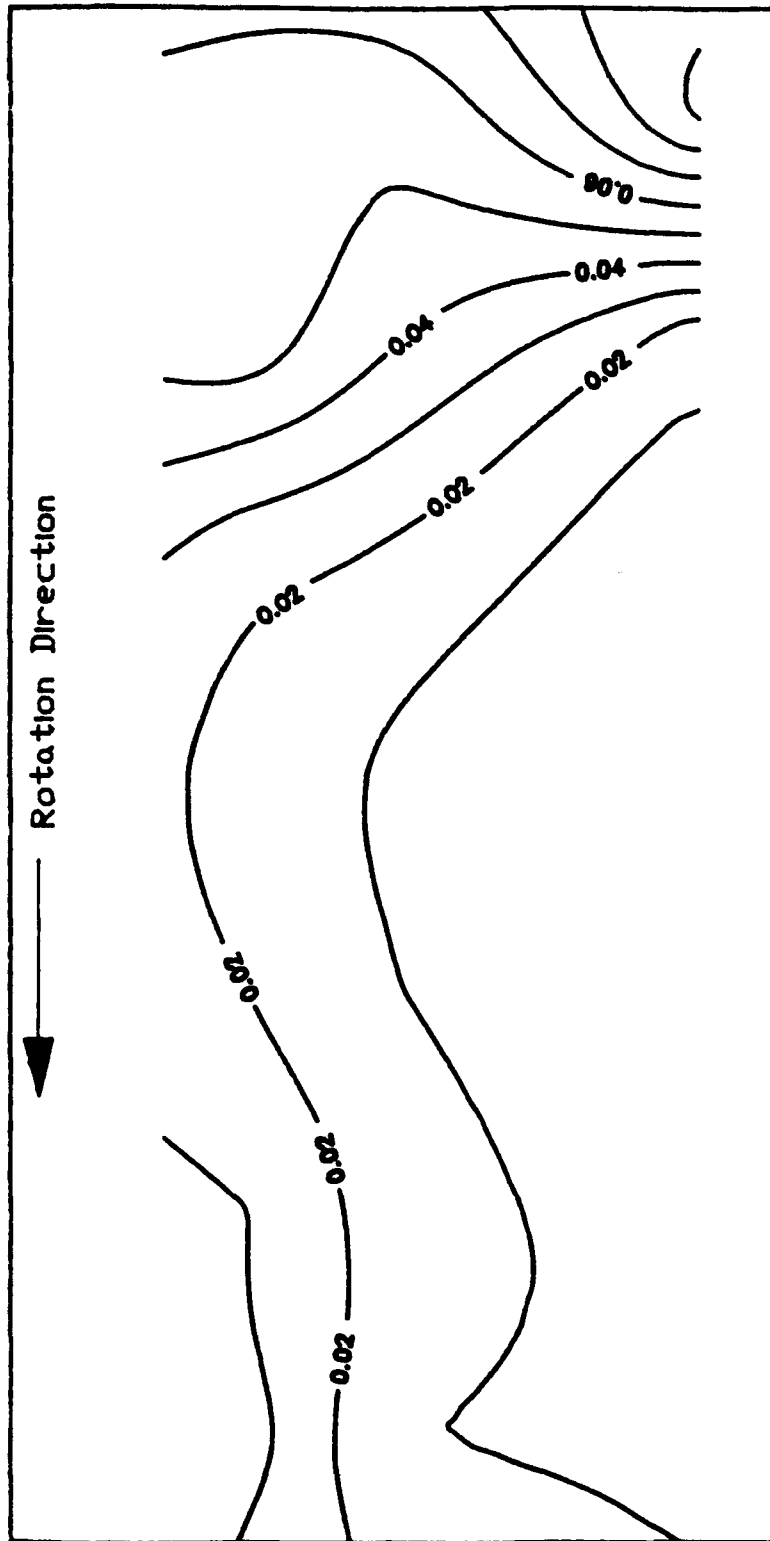


FIG. 10 TURBULENT NORMAL STRESS IN THE STREAMWISE DIRECTION
CROSS SECTION 1, $(U_i'^2/V_m^2)$

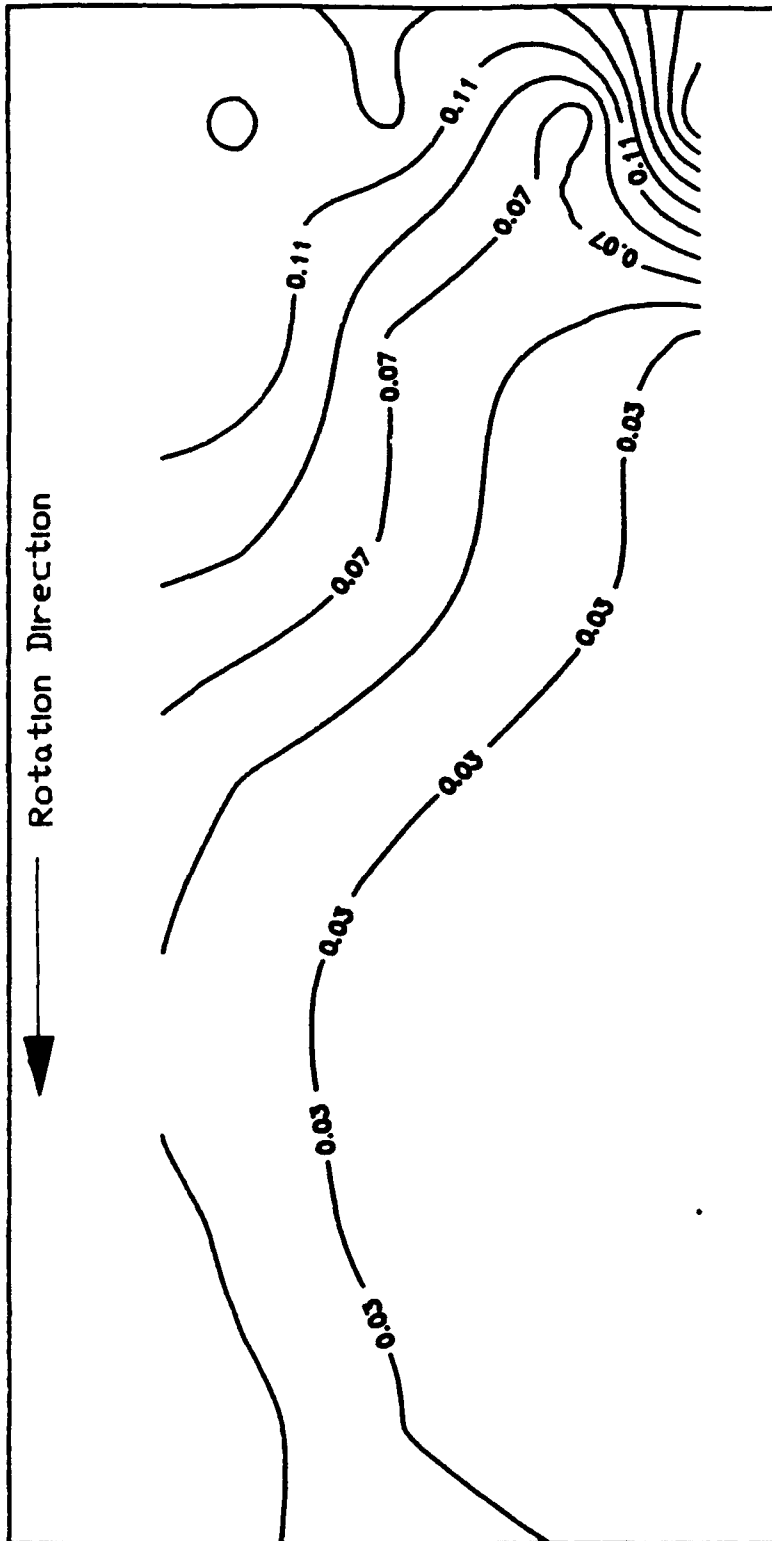


FIG. 101 TURBULENT NORMAL STRESS IN THE TANGENTIAL DIRECTION
CROSS SECTION 1, $(u'_t{}^2/v_\tau^2)$

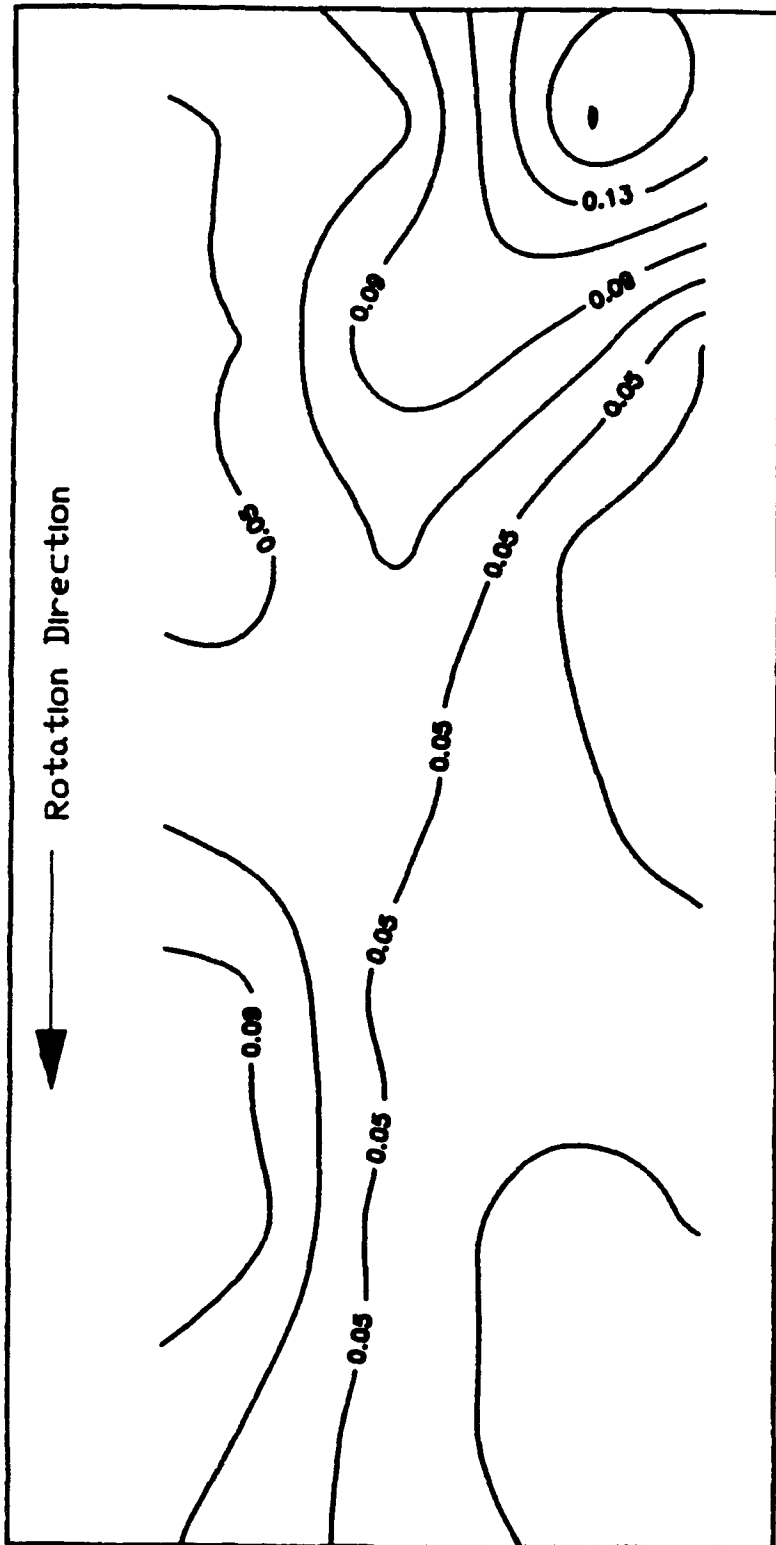


FIG.102 TURBULENT NORMAL STRESS IN THE STREAMWISE DIRECTION
 CROSS SECTION 2, $(U_i'^2/V_{\infty}^2)$

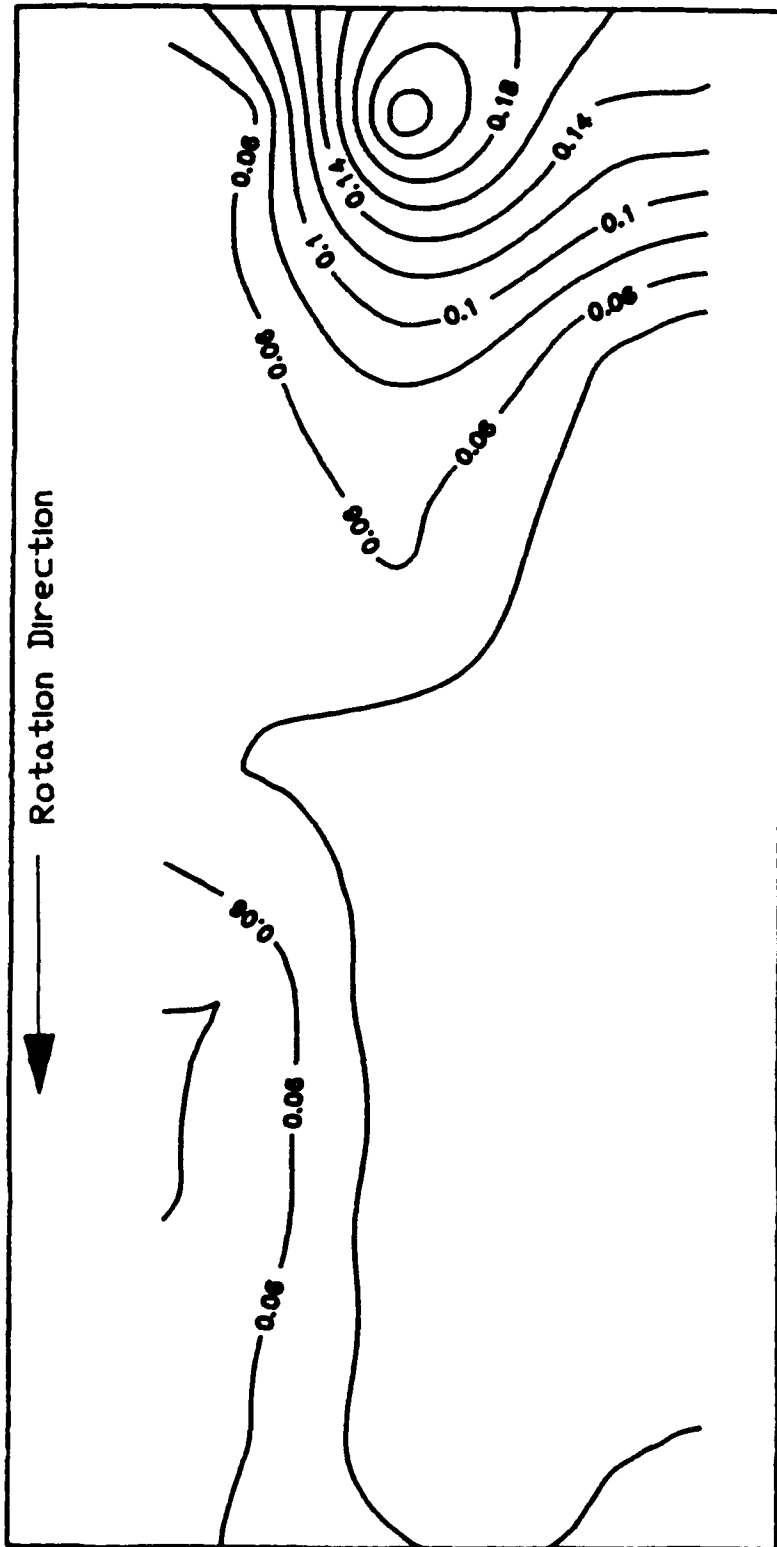


FIG.103 TURBULENT NORMAL STRESS IN THE TANGENTIAL DIRECTION
 CROSS SECTION 2, $(U_r'^2/V_m^2)$

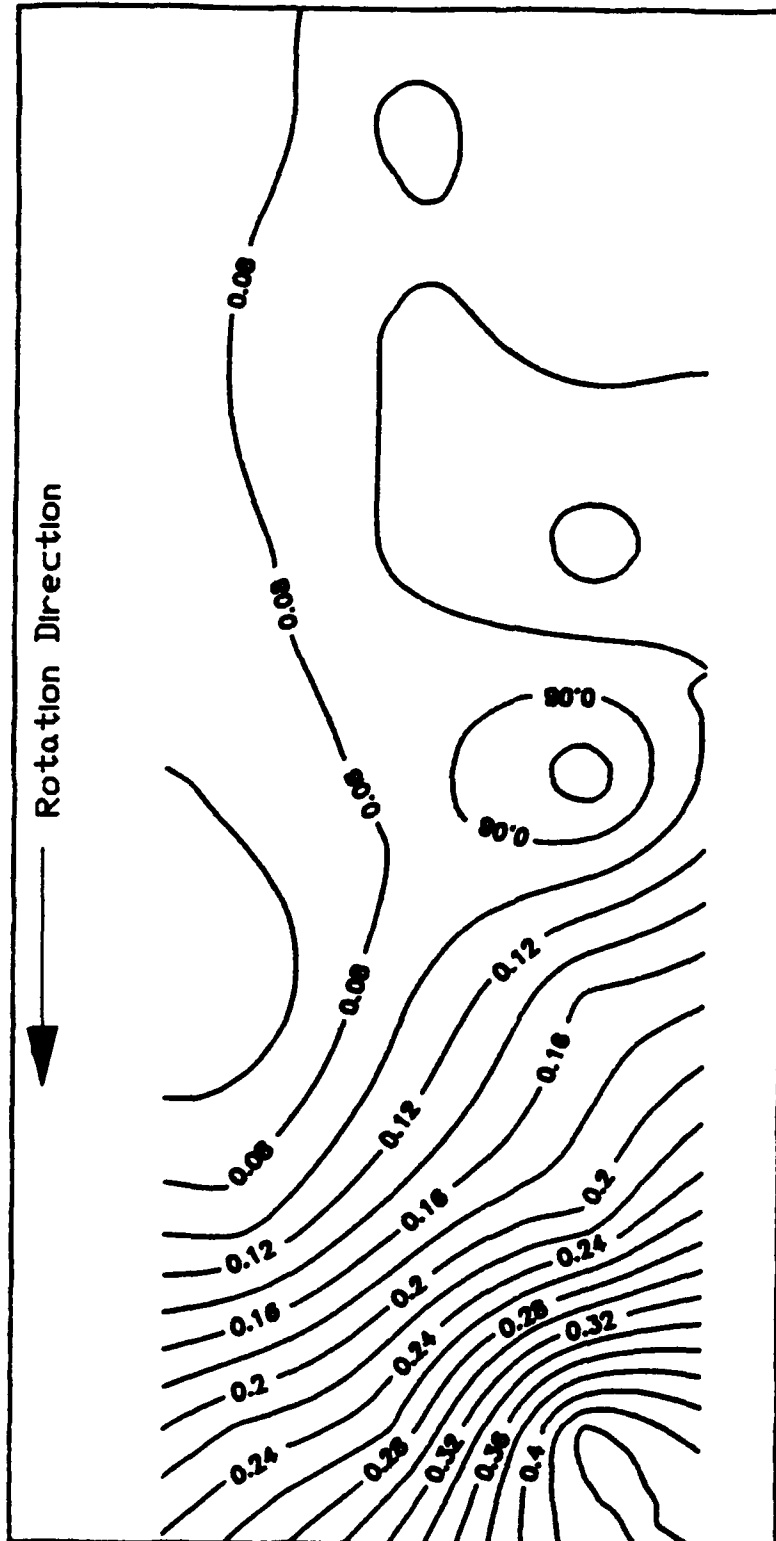


FIG. 104 TURBULENT NORMAL STRESS IN THE STREAMWISE DIRECTION
 CROSS SECTION 3, $(U_i'^2/V_m^2)$

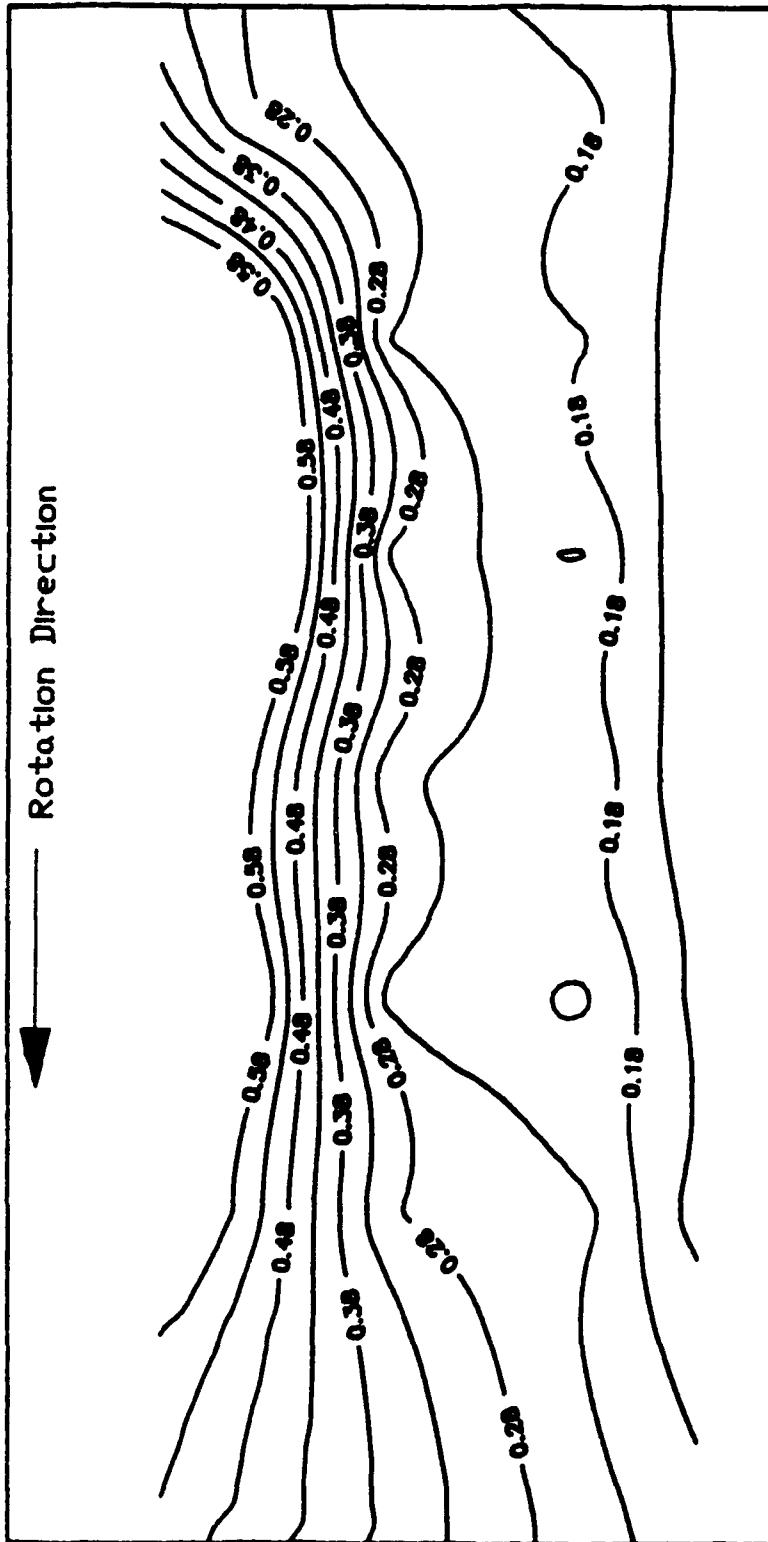


FIG.106 TURBULENT NORMAL STRESS IN THE STREAMWISE DIRECTION
 CROSS SECTION 4, $(U_r'^2/V_m^2)$

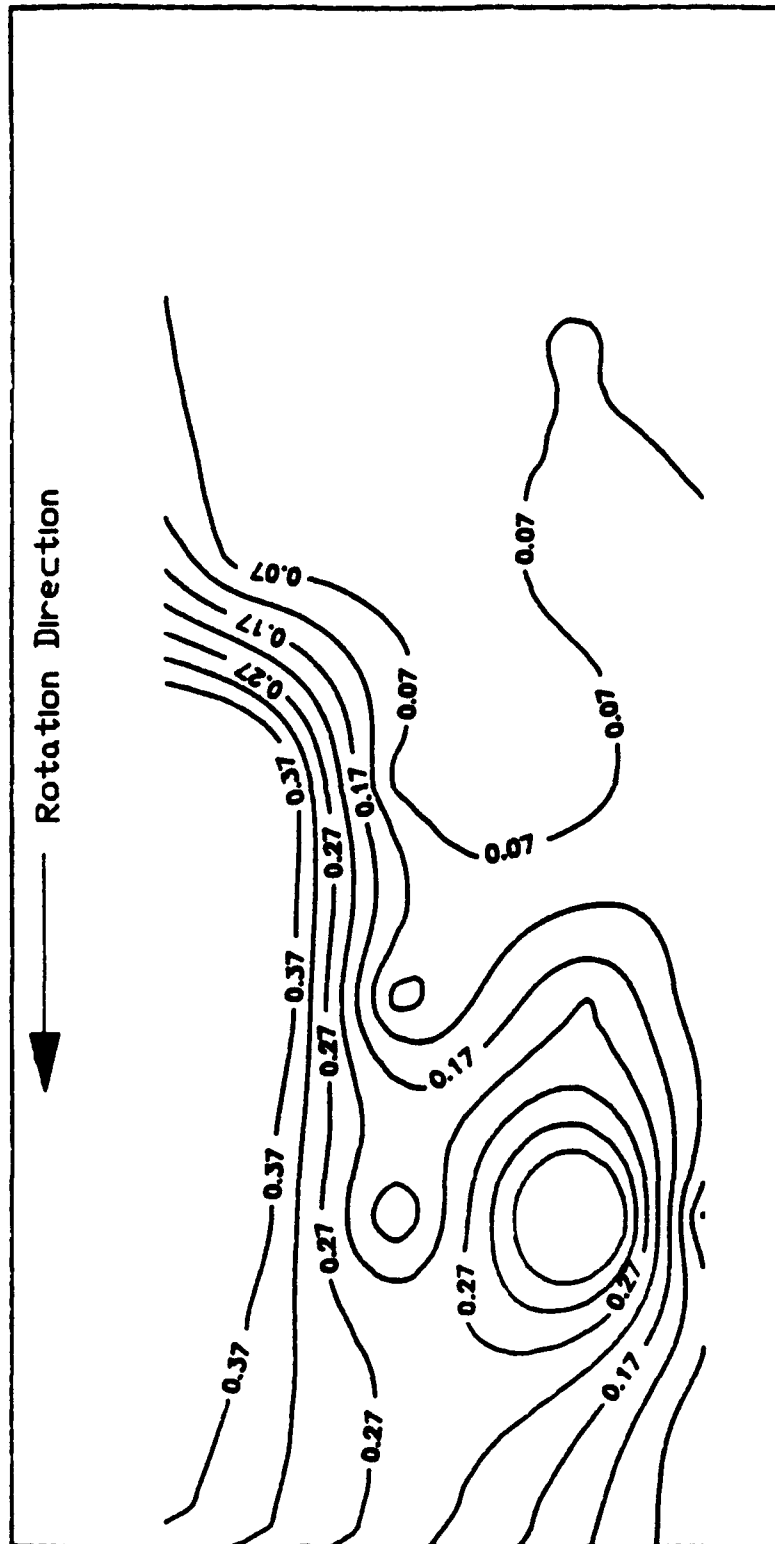


FIG.107 TURBULENT NORMAL STRESS IN THE TANGENTIAL DIRECTION
 CROSS SECTION 4, $(U_r'^2/V_m^2)$

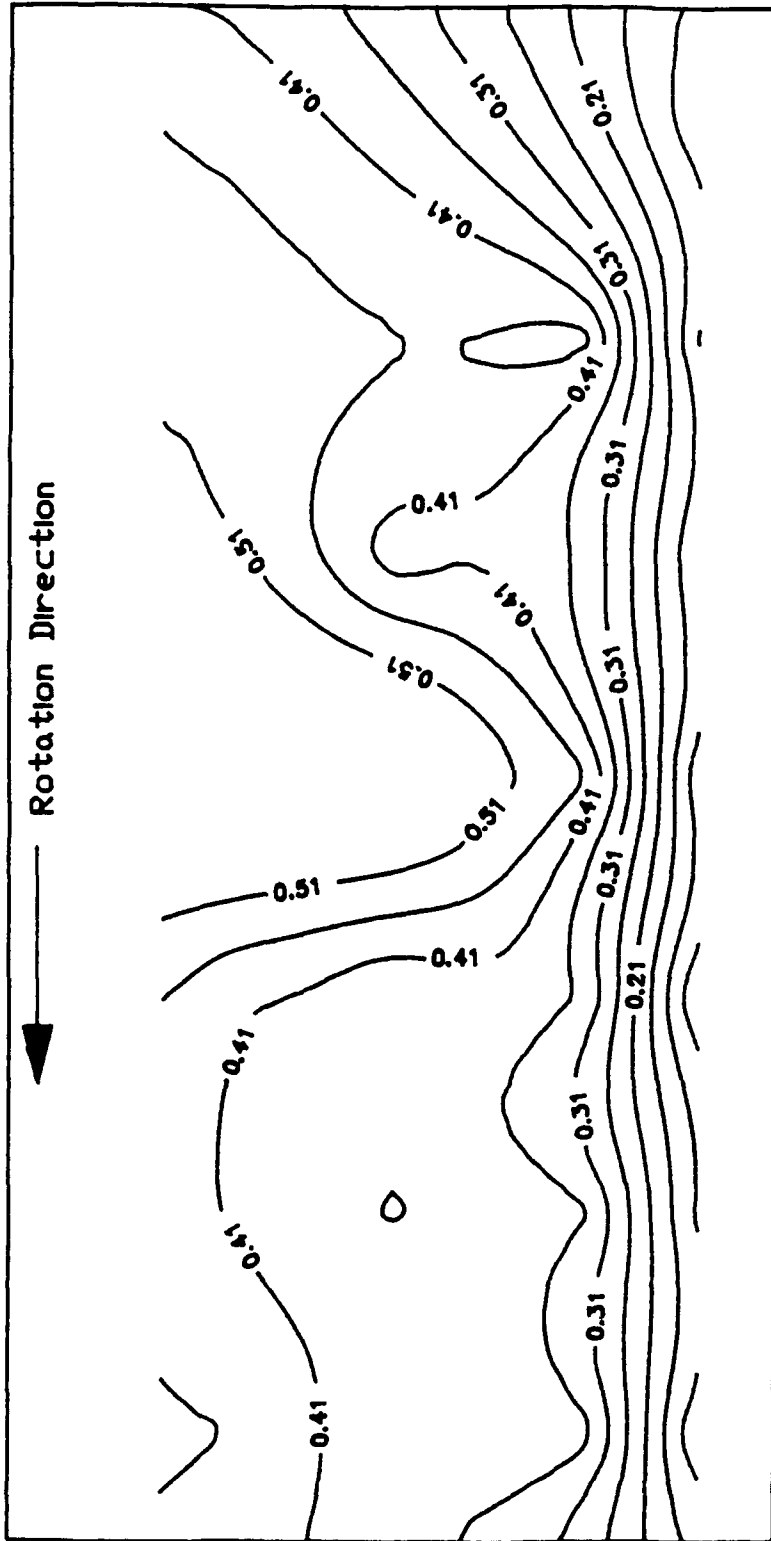


FIG. 108 TURBULENT NORMAL STRESS IN THE STREAMWISE DIRECTION
 CROSS SECTION 5, $(u_1'^2/V_m^2)$

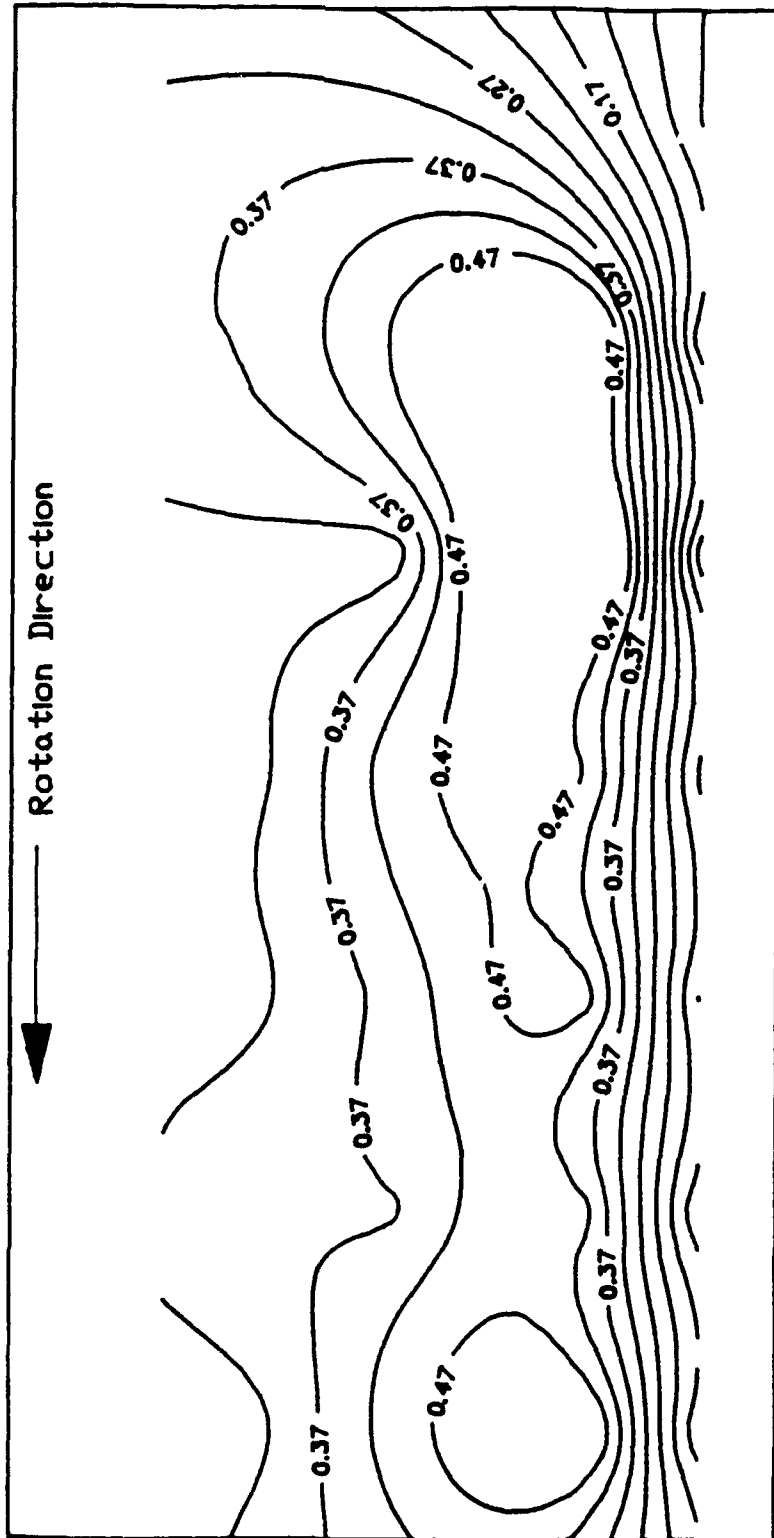


FIG. 109 TURBULENT NORMAL STRESS IN THE TANGENTIAL DIRECTION
 CROSS SECTION 5, $(U_i'^2/V_{\infty}^2)$

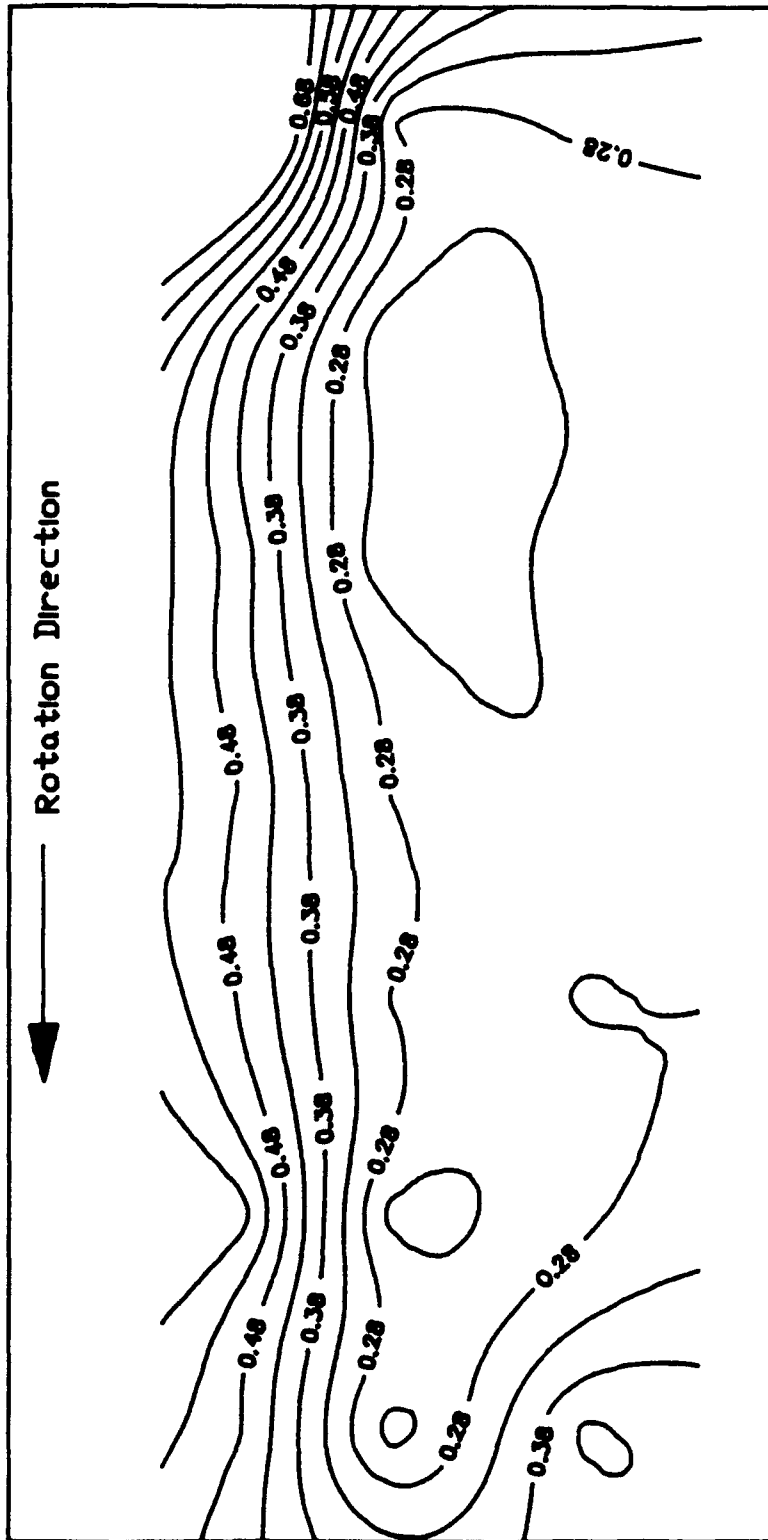


FIG.110 TURBULENT NORMAL STRESS IN THE STREAMWISE DIRECTION
CROSS SECTION 6, $(U_r'^2/V_m^2)$

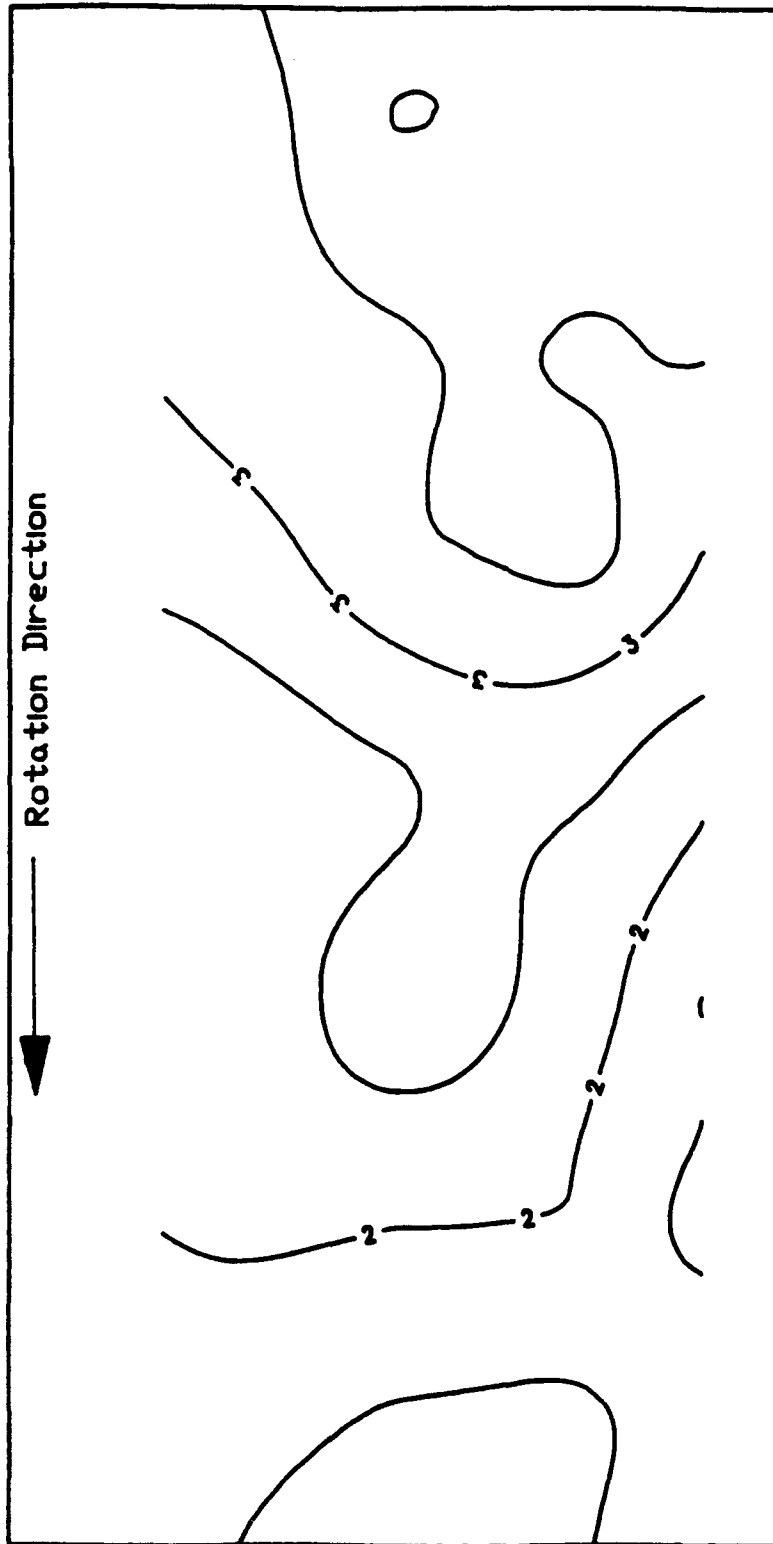


FIG.113 SPANWISE RELATIVE VELOCITY CONTOURS (m/s)
CROSS SECTION 2

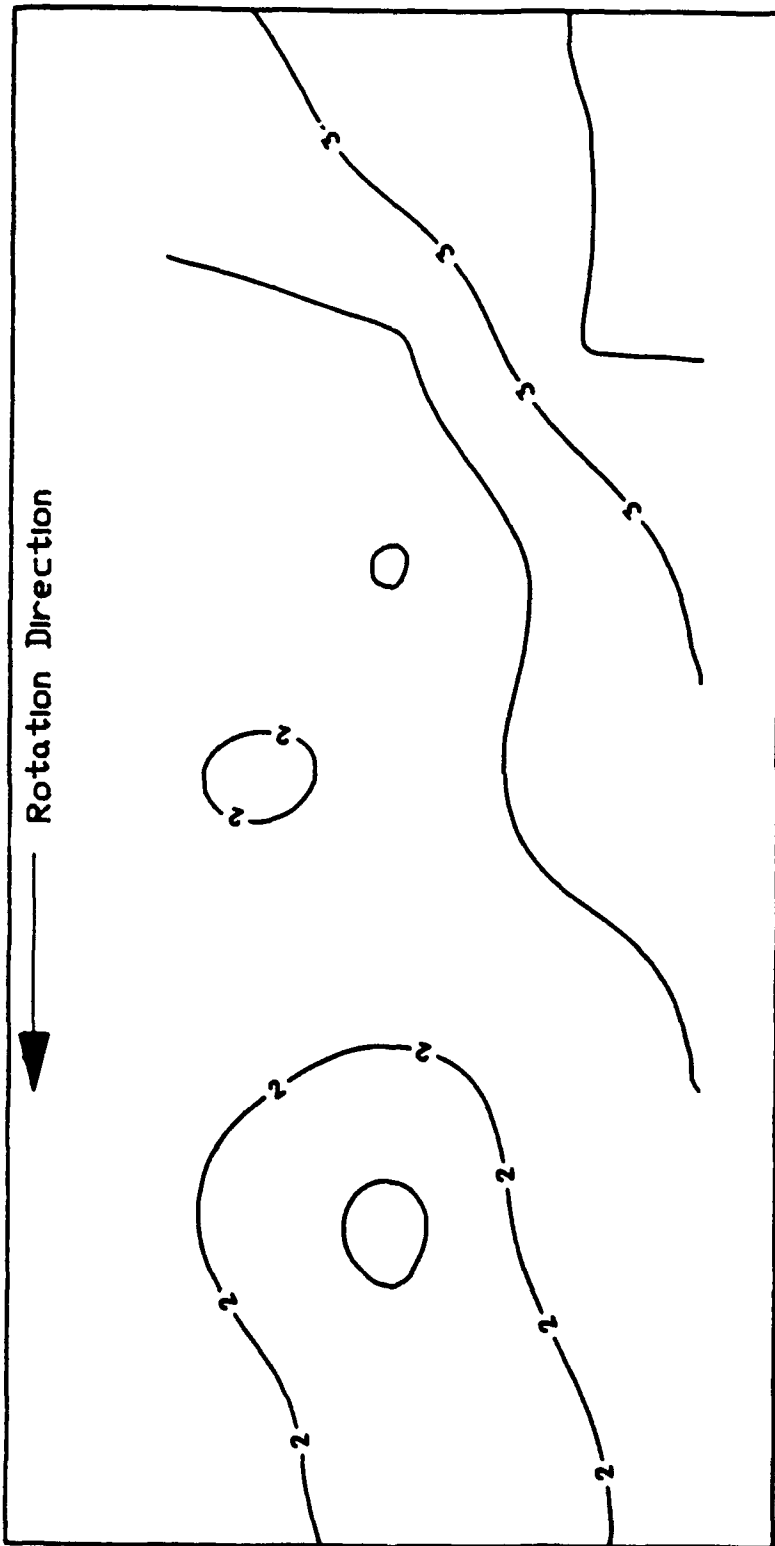


FIG.114 SPANWISE RELATIVE VELOCITY CONTOURS (m/s)
CROSS SECTION 3

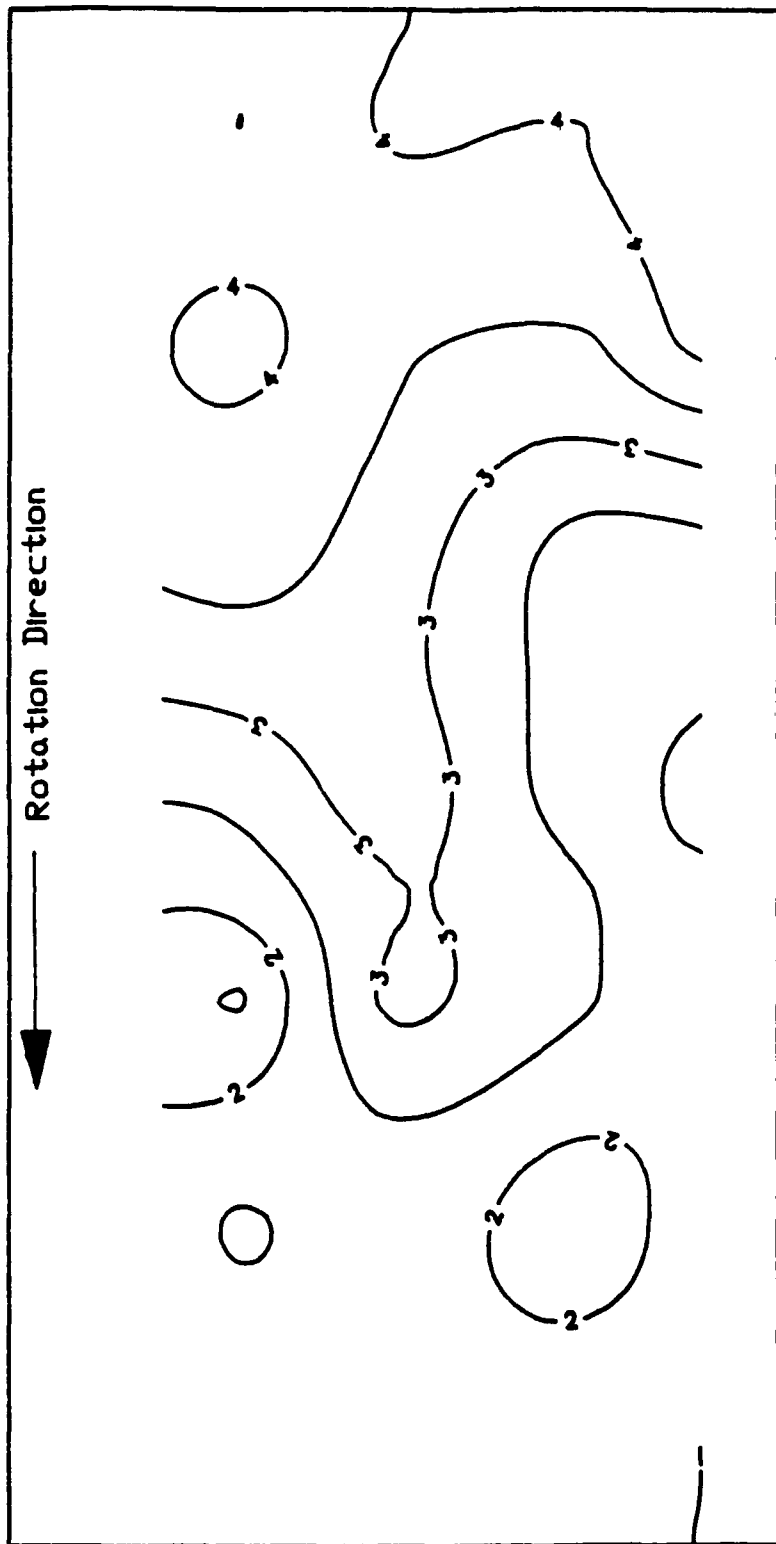


FIG.115 SPANWISE RELATIVE VELOCITY CONTOURS (m/s)
CROSS SECTION 4

APPENDIX A

- A) The following scientific and technical personnel were participating in this research project.

<u>Name</u>	<u>Title</u>
W. Tabakoff	Professor (Principal Investigators)
M. Pasin	Ph.D. Student
M. Morgan	Ph.D. Student
M. Metwally	Ph.D. Student
P. Kunkel	Electronics Technician

- B) Students working on the project and obtaining degrees.

M. Metwally, Ph.D. - 6/14/92

- C) Technical Publications:

M. Pasin, W. Tabakoff, "Laser Measurements of Flow Field in a Radial Turbine Rotor," submitted for AIAA 31st Aerospace Sciences Meeting and Exhibit, 1993.

M. Pasin, W. Tabakoff, "Unsteady Measurements of the Flow Field in Radial Turbine Guide Vanes with LDV," AIAA 18th Annual Mini-Symposium on Aerospace Science and Technology, Dayton, Ohio, March 26, 1992 (Best Paper Award).

A.N. Lakshminarasimha, W. Tabakoff and M. Metwally, "Laser Doppler Velocimeter Measurements in the Vortex Region of a Radial Inflow Turbine," AIAA Journal of Propulsion, Vol. 8, No. 1, Jan.-Feb. 1992, pp. 184-191.

M. Pasin, W. Tabakoff, "Laser Measurements of Unsteady Flow Field in a Radial Turbine Guide Vanes," AIAA 30th Aerospace Sciences Meeting and Exhibit, Reno, Nevada, 1992 (Paper No. AIAA-92-0394).

M. Pasin, W. Tabakoff, "Laser Measurements of Velocity and Flow in a Radial Turbine Guide Vanes," AIAA 17th Annual Mini-Symposium on Aerospace Science and Technology, Dayton, Ohio, 1991.